Title

New Multi-Layer Compact High-Order Finite Difference Methods with Spectral-Like Resolution for Compressible Flow Simulations

Author

Bai, Zeyu

Publication Date

2019

Peer reviewed|Thesis/dissertation

UNIVERSITY OF CALIFORNIA

Los Angeles

New Multi-Layer Compact High-Order Finite Difference Methods with Spectral-Like Resolution for Compressible Flow Simulations

A dissertation submitted in partial satisfaction of the

requirements for the degree Doctor of Philosophy

in Mechanical Engineering

by

Zeyu Bai

2019

ABSTRACT OF THE DISSERTATION

New Multi-Layer Compact High-Order Finite Difference Methods with Spectral-Like Resolution for Compressible Flow Simulations

by

Zeyu Bai

Doctor of Philosophy in Mechanical Engineering

University of California, Los Angeles, 2019

Professor Xiaolin Zhong, Chair

Numerical simulations of multi-scale flow problems such as hypersonic boundary layer transition, turbulent flows, computational aeroacoustics and other flow problems with complex physics require high-order methods with high spectral resolutions. For instance, the receptivity mechanisms in the hypersonic boundary layer are the resonant interactions between forcing waves and boundary-layer waves, and the complex wave interactions are difficult to be accurately predicted by conventional low-order numerical methods. High-order methods, which are robust and accurate in resolving a wide range of time and length scales, are required. The objective of this dissertation is to develop and analyze new very high-order numerical methods with spectral-like resolution for flow simulations on structured grids, with focus on smooth flow problems involving multiple scales. These numerical methods include: the multi-layer compact (MLC) scheme, the directional multi-layer compact (DMLC) scheme, and the least square multi-layer compact (LSMLC) scheme.

In the first place, a new upwind multi-layer compact (MLC) scheme up to seventh order is derived in a finite difference framework. By using the 'multi-layer' idea, which introduces first derivatives into the MLC schemes and approximates the second derivatives, the resolution of the MLC schemes can be significantly improved within a compact grid stencil. The auxiliary equations are introduced, and they are the only nontrivial equations. The original equation requires no approximation which contributes to good computational efficiency. In addition, the upwind MLC schemes are derived on centered stencils with adjustable parameters to control the dissipation. Fourier analysis is performed to show that the new MLC schemes have very small dissipation and dispersion in a wide range of wavenumbers in both one and two-dimensional cases, and the anisotropic error is much smaller than conventional finite difference methods in the two-dimensional case. Comparison with discontinuous-Galerkin methods is performed with Fourier analysis as well. Furthermore, stability analysis with matrix method shows that high-order boundary closure schemes are stable because of compactness of the stencils. The accuracies and rates of convergence of the new schemes are validated by numerical experiments of the linear advection equation, the nonlinear Euler equations, and the Navier-Stokes equations in both one and two-dimensional settings. The numerical results show that good computational efficiency, very high-order accuracies, and high spectral resolutions especially on coarse meshes can be attained with the MLC scheme.

On the other hand, even though the MLC scheme is promising in most test cases, it shows weak numerical instabilities for a small range of wavenumbers when it is applied to multi-dimensional flows, which are mainly triggered by the inconsistency between its one and two-dimensional formulations. The instability could lead to divergence in long-time multi-dimensional simulations. Moreover, the cross-derivative approximation in the MLC scheme

requires an ad-hoc selection of supporting grid points, and the cross-derivative approximation is relatively inefficient for very high-order cases. To address the remaining challenges of the MLC scheme and achieve better performance for multi-dimensional flow simulations, another two new schemes are developed – the directional multi-layer compact (DMLC) scheme, and the least square multi-layer compact (LSMLC) scheme.

In the second place, a new upwind directional multi-layer compact (DMLC) scheme is developed for multi-dimensional simulations. The main idea of the DMLC scheme is to introduce auxiliary equation for cross derivative in multi-dimensional cases. Consequently, the spatial discretization can be fulfilled along each dimension independently. With this directional discretization technique, the one-dimensional formulation of the MLC scheme can be applied to all spatial derivatives in a multi-dimensional governing equation. Therefore, the DMLC scheme overcomes the inconsistency between one and two-dimensional formulations of the MLC scheme, and it also avoids the ad-hoc cross-derivative approximations. Two-dimensional Fourier analysis demonstrates that all modes of the DMLC scheme are stable in the full range of wavenumbers, and it has better spectral resolution and smaller anisotropic error than the MLC scheme. Stability analysis with matrix method indicates that stable boundary closure schemes are much easier to be obtained in the DMLC scheme. Numerical tests in the linear advection equation and the nonlinear Euler equations validate that the DMLC scheme are more accurate and require less CPU time than the MLC scheme on the same mesh. In particular, the long-time simulation results reveal that the DMLC scheme is always stable for both periodic and non-periodic boundary conditions in two-dimensional cases.

In the third place, a new upwind least square multi-layer compact (LSMLC) scheme is developed for multi-dimensional simulations. The main idea of the LSMLC scheme is using the

weighted least square approximation to redesign the two-dimensional formulation for cross derivatives. It avoids the ad-hoc selection of grid points in the MLC scheme. Meanwhile, the two-dimensional upwind scheme can be derived by introducing upwind correction into the weight function. The upwind factor β can adjust the dissipation and stability of the LSMLC scheme. Lagrange multiplier is used to ensure that the LSMLC scheme satisfies both the consistency constraint at the base point and the one-dimensional constraint from the MLC scheme. The LSMLC scheme does not increase computational cost on structured meshes, and can be implemented in the same way as the MLC scheme. A parametric study based on two-dimensional Fourier analysis shows that the truncated Gaussian distribution (TGD) weight function leads to better LSMLC scheme among other weight functions because it removes the numerical instability and maintain small dissipations. The LSMLC scheme has larger dissipation than the MLC scheme, and shows similar spectral resolution. Stability analysis with matrix method indicates that a combination of an interior LSMLC scheme and MLC boundary closure schemes can improve the boundary stability while maintaining small dissipation. Numerical tests in the linear advection equation and the nonlinear Euler equations validate that the LSMLC scheme produces slightly larger errors compared with MLC scheme. The long-time simulation results reveal that the LSMLC scheme is always stable for both periodic and non-periodic boundary conditions in two-dimensional cases.

Overall, the new very high-order multi-layer compact finite difference methods have the properties of simple formulations, high-order accuracies, spectral-like resolutions, and compact stencils, and they are suitable for accurate simulation of smooth multi-scale flows with complex physics. Among the three schemes developed in this dissertation, the DMLC scheme is always the best choice for multi-dimensional simulations because it shows comprehensive

improvements from the MLC scheme with consistent stability, higher accuracy and spectral resolution, and better computational efficiency. The LSMLC scheme is also appropriate considering it has consistent stability and it is easy to be implemented.

The dissertation of Zeyu Bai is approved.

Christopher R Anderson

Jeff D Eldredge

John Kim

Xiaolin Zhong, Committee Chair

University of California, Los Angeles

2019

TABLE OF CONTENTS

LIST OF FIGURES

LIST OF TABLES

ACKNOWLEDGEMENTS

First, I would like to express my sincere gratitude to my advisor Prof. Zhong, for his recommendation on my Ph.D. program admission, valuable suggestions on my research, and continuous encouragement in the past five years. I would also like to thank my committee: Prof. Anderson, Prof. Eldredge, and Prof. Kim for their time and great advice on my research. I want to show my appreciation to Dr. Edoh for his useful suggestions on numerical methods. I also want to thank all my colleagues for creating the joyful working experience. Special thanks to Richard Abrantes and Danny Fong for their positive influence during my research, as well as those enjoyable experience about Asian food and basketball outside the campus.

There are so many people I want to thank outside my laboratory. I would like to thank my parents for their love and understanding during these years. They always believe me and encourage me to pursue my dream unhesitatingly. I could never finish this journey without their unconditional support.

I also want to give my sincere gratitude to all my friends in Los Angeles, for those good moments and food we shared together. I would also like to acknowledge all my roommates in the past five years for creating the harmonious residential life, which makes my difficult life a little bit easier.

Finally, I would like to especially thank Qing Zhang. I'm incredibly lucky to meet you and fall in love with you in this journey. You are the only person who really made my Ph.D. life colorful, and I will never forget your love, companionship, and confidence during my hard times. The story with you has become the most precious part in this journey, and it is also the most wonderful start for our long journey in the future.

VITA

2007 - 2011 B.S. in Thermal Energy and Power Engineering,
Dual B.S. in Economics,
Beijing Institute of Technology, Beijing

2011 - 2014 M.S. in Power Engineering and Engineering Thermophysics,
Beijing Institute of Technology, Beijing

2014 - 2016 M.S. in Mechanical Engineering,
UCLA, Los Angeles, California

2014 - 2019 Graduate Student Researcher in Mechanical Engineering,
UCLA, Los Angeles, California

PUBLICATIONS

- Z. Bai, X. Zhong. "New Very High-Order Upwind Directional Multi-Layer Compact (DMLC) Schemes for Multi-Dimensional Flows." Computers & Fluids (In revision)
- Z. Bai, X. Zhong. "New Very High-Order Upwind Multi-Layer Compact (MLC) Schemes with Spectral-Like Resolution for Flow Simulations." Journal of Computational Physics 378 (2019): 63-109.
- Z. Bai, X. Zhong. "Very High-Order Upwind Multi-Layer Compact (MLC) Schemes with Spectral-Like Resolution II: Two-Dimensional Case." AIAA Science and Technology Forum and Exposition. San Diego, California. Jan. 2019.

- Z. Bai, X. Zhong. “New Very High-Order Upwind Multilayer Compact Schemes with Spectral-Like Resolution for Flow Simulations.” 55th AIAA Aerospace Sciences Meeting. Grapevine, Texas. Jan. 2017.

1. Introduction

1.1. Overview

In the recent few decades, direct numerical simulation (DNS) has become one of the most important methods for the numerical study of various fluid dynamics problems with multiple scales and complex physics. An example is the prediction of the laminar-turbulent transition of hypersonic boundary layers, which is critically important to the development of hypersonic vehicles that are to be used for rapid space access [1]. In general, the transition is a result of the nonlinear response of a laminar boundary layer to various environmental disturbances, but transition mechanisms of hypersonic and supersonic boundary layers are much more complex and much less understood compared with incompressible flows. The transition of hypersonic boundary layers over blunt bodies, which are representative examples, can be affected by the additional effects of shock waves, entropy-layer instabilities, nose bluntness and thermochemical nonequilibrium at high temperatures [2]. As a natural consequence, the DNS of hypersonic boundary layer requires highly accurate numerical methods to resolve a wide range of time and length scales in the flow. At the end of the transition process, the boundary layer becomes fully turbulent, which are more complicated than laminar or transitional flows. The investigation of turbulent flows still face many difficulties because of the strong nonlinearity, the large number of degrees of freedom (DOFs), high sensitivity to small differences in flow conditions, and many other factors [3]. The numerical simulation of turbulent flows is even more challenging because of the wide range and flat distribution of energy spectrum, and the instantaneous range of scales in turbulent flows increases rapidly with the Reynolds number [4]. However, due to the

limitation of computational resources, it is impossible to resolve all the tiny structures in turbulent flows for practical Reynolds numbers. To accurately simulate the turbulent flows, it is required the numerical methods should resolve a significant portion of the scales in the flow fields on feasible grid resolutions. Computational aeroacoustics [5] is another instance which involves complex physics. The generation and propagation of acoustic waves have different features from common aerodynamic problems. In aeroacoustics, the frequency range of acoustic waves is wide, and their amplitude is very small compared with mean flow properties. Meanwhile, flows that generate noises are nonlinear, unsteady and turbulent. These features make the accurate simulation of acoustic wave propagation challenging especially in far-field that requires long-time integration [6]. A common feature of all the flow problems above is the multiple scales embedded in the fields which are difficult to be captured with schemes of low-order accuracy. In the DNS investigation of multi-scale flow problems, the schemes should have very high-order accuracy and high spectral resolution for a wide range of wavelength scales. Moreover, the numerical dissipation and dispersion of such high-order schemes should be low enough to ensure that physical wave components with small amplitude are not suppressed or distorted, which is particularly important in computational aeroacoustics. For reviews of these DNS investigations, one can read [2,4,7–9].

1.2. High-Order Numerical Methods

High-order methods have received increasing attention for flow simulations. They have the advantage of achieving the desired accuracy with fewer grid points in the computational domain, improving the computational efficiency, saving the required computer memory, and facilitating large simulations. For these reasons, the high-order methods such as spectral methods, and high-order compact schemes have been commonly used in DNS of turbulent flows [10]. There are

many high-order numerical methods developed in the past few decades. Ekaterinaris [11] presented a comprehensive review of the development of high-order methods with low numerical diffusion. Wang [12] discussed high-order methods with emphasize on unstructured grids. Roughly speaking, high-order methods can be classified as linear schemes and nonlinear schemes. Linear schemes, such as spectral methods [13–15], discontinuous-Galerkin (DG) methods [16–19], high-order finite difference methods [20–25], etc., are mainly designed for smooth flows without discontinuities. There exist other flow problems with discontinuities such as shock waves. For simulation of these flows, nonlinear schemes, such as TVD [26,27], ENO [28], WENO [29,30], etc., are designed. These are also hybridizations of linear and nonlinear schemes, which combine the advantages of both methods [31–34].

The conventional numerical methods for multi-scale problems have been the spectral methods [13–15], which are especially suitable for incompressible turbulent flow. Spectral methods use modal basis functions of orthogonal polynomials, such as Fourier series, to represent the solution in the entire computational domain, which leads to very high spectral resolutions and exponential convergence. However, high-order spectral methods have been limited to flows with simple geometries and face difficulties when dealing with complicated boundary conditions. In addition, spectral methods are less accurate for compressible flow problems, such as hypersonic boundary layer where the critical layer is important.

In an effort to simulate flows over complex geometries more accurately, many discontinuous finite element methods have been developed, such as discontinuous-Galerkin (DG) methods [16–19], spectral difference (SD) methods [35–37], and spectral volume (SV) methods [38–41], etc. These methods use the localized function representation within each element, hence they are suitable to deal with flows over very complex geometries with unstructured grids.

Among them, discontinuous-Galerkin (DG) methods may receive the most attention. DG methods combine the characteristics of finite volume methods and finite element methods by using high-order piecewise polynomials within elements and solving numerical fluxes on element interfaces. They have very high-order accuracy and there is no reconstruction needed in DG methods because the entire trial function with multiple degrees of freedom (DOFs) is evolved. Whatever the order of accuracy is, the local stencil can be attained. In other words, each element only interacts with its neighboring elements, which makes DG methods very efficient for parallel computing. However, High-order DG methods have much more degrees of freedom in trial functions, especially for multi-dimensional simulations. Storing and evolving these extra degrees of freedom require larger memory and more CPU time compared with finite volume methods, although they save some computational cost on reconstructions [10].

Compared with other high-order methods, finite difference methods have the advantages of simple formulations and high computational efficiencies with the precondition that the geometry is relatively simple and structured grid can be used. However, conventional explicit finite difference schemes face difficulty in resolving the short waves, which limits their applications in multi-scale problems such as boundary layer transition, turbulent flows, etc. To relax this constraint, finite difference schemes with spectral-like resolution have been widely investigated. The compact finite difference scheme [20,22,24,42–47] is an influential alternative. Lele [20] performed extensive analysis on compact finite difference schemes and showed that through the implicit relation between the derivatives and function values on several grid points, the error in large wavenumber region is reduced and resolutions for short waves are improved. The spectral properties can be further improved by imposing the wavenumber constraints at certain points, i.e., let the modified wavenumber equal to the exact wavenumber at these points. Simultaneously, the

maximal truncation order is abandoned on a stencil. Compared with spectral methods, compact schemes are also more flexible with complex geometries and boundary conditions. Lele's compact schemes have been extended by Chu & Fan [25,47] and Mahesh [22], by introducing the second derivatives in the implicit difference equation. The resulting scheme, which is termed the combined compact difference (CCD) scheme, can achieve higher orders in accuracy and have better spectral resolution than the normal compact schemes on the same stencils. The dispersion-relation-preserving (DRP) scheme [48–52] is another widely used finite difference scheme with spectral-like resolution. Tam and Webb [52] first proposed the DRP scheme by optimizing an explicit finite difference approximation in the wavenumber and frequency space, minimizing the L_2 norm error in modified wavenumbers, hence achieved spectral-like resolution. The general idea of these optimizing finite difference schemes is to lower the error at marginal resolution related to high-frequency wave at the expense of allowing more error for low-frequency wave [53]. Another main difficulty in applying high-order finite difference methods is the numerical instability from boundaries when used on solid wall boundary layer [54]. The stencil is usually wide for high-order finite difference methods and it is difficult to construct stable boundary closure schemes. In most DNS studies of transitional and turbulent flows of the boundary layer, the orders of numerical methods are often limited due to the numerical instability from boundaries. Many approaches have been proposed to improve the stability of boundary conditions in high-order finite difference methods. Zhong [21] showed that using an adjustable parameter to control dissipation in inner schemes would stabilize the boundary conditions. The non-uniform grid schemes proposed by Zhong and Tatineni [54] use an appropriate grid stretching and cluster grid points near the boundary to attain stable high-order boundary closure schemes. Ashcroft & Zhang [43] and Hixon [44] derived prefactored compact schemes which

require smaller stencils and offer simpler boundary condition. By narrowing the grid stencil, the boundary closure schemes can be simplified because narrower boundary stencils are required, which is commonly known as the main advantage of stencil compactness.

The high-order methods discussed above are linear schemes designed for smooth flows. They usually have difficulties in capturing discontinuities, such as shock wave, where they produce spurious oscillations known as the Gibbs phenomenon. For flows with shock, shock-capturing methods based on nonlinear schemes are required. Total-variation-diminishing (TVD) [26], essentially-nonoscillatory (ENO) [28], and weighted-essentially-nonoscillatory (WENO) [29] schemes are representative examples of nonlinear schemes. Many advanced nonlinear schemes have been developed from these ideas or their variations [10–12,55,56]. In past twenty years, WENO-based methods receive the most attention among nonlinear schemes. The core idea of WENO scheme is using low-order polynomials and adaptive stencils in reconstruction. The high-order numerical flux or conserved variable is approximated as a weighted summation of low-order polynomials. By using smoothness indicators and automatically selecting the optimal stencil, WENO scheme can achieve very high-order accuracy in the smooth region and maintain nonoscillatory property across shock waves in the discontinuous region. Shu [57] presented a detailed review of the development of high-order WENO schemes. There are three general problems exist in most nonlinear schemes. First, nonlinear schemes are usually computationally inefficient. Second, the accuracy near the shock is reduced because the shock location is only known to $O(h)$ on a finite grid [56]. Last, their performance in the smooth region is not as good as linear schemes due to excessive damping [56]. Although WENO-based schemes can achieve very high-order accuracies in a smooth region, they generate large phase error when resolving small waves in multi-scale flow simulations. In fact, spectral-like resolution can only be

achieved by linear schemes as mentioned by Hill & Pullin [58] and Taylor et al. [59]. As a result, these nonlinear schemes may not be accurate enough for DNS studies of hypersonic boundary layers, where short wavelength shock/disturbance interactions need to be resolved with high accuracy [21]. As an alternative approach to deal with shocks, shock-fitting methods [21,60–62] have been used to treat the bow shock as a computational boundary and the flow region behind the shock can be simulated with high-order linear schemes.

1.3. Transition of Hypersonic Boundary Layers

The accurate prediction of the laminar-turbulent transition of boundary layers is critically important for hypersonic vehicles because transition has a first-order impact on aerodynamic heating, drag, and vehicle operation [1]. The success of transition prediction relies on a fundamental understanding of the relevant physical mechanisms. Various physical mechanisms of boundary-layer transition have been reviewed by many authors [63–71] over the years. Most of these reviews are limited to incompressible flows. Compared to incompressible flows, transition mechanisms of hypersonic and supersonic boundary layers are much more complex and much less understood. Reed & Saric [72] reviewed the use of linear stability theory (LST) for transition predictions of compressible boundary layers. Schneider [73–80] had comprehensive reviews on experiments and flight tests of hypersonic boundary. Fedorov [81] summarized the theoretical analysis of hypersonic boundary-layer transition.

Most of our current understanding on hypersonic boundary-layer stability and transition is based on LST. Mack [82] found there exist higher acoustic instability waves, in which the second mode dominates the instability when Mach number is greater than 4. Additional effects that will affect transition and stability of hypersonic boundary layers include shock waves,

entropy-layer instabilities, nose bluntness and thermochemical nonequilibrium at high temperature conditions [2]. Fig. 1.1 presents a schematic of the wave field in a hypersonic flow induced by free-stream disturbance and surface roughness.

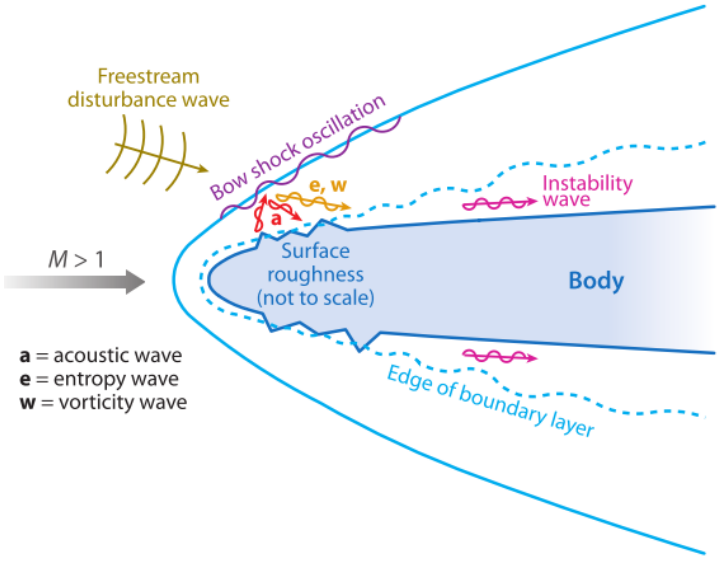

Fig. 1.1. A schematic of the wave field in a hypersonic flow induced by free-stream disturbance and surface roughness [2].

Along with the developments in high-order numerical methods and computer technologies, direct numerical simulation (DNS) has become a new approach for hypersonic boundary-layer investigations. Kleiser & Zang [83] had a review of DNS research on the transition of wall-bounded shear flows before 1991. They classified these studies into two categories: temporal DNS (TDNS) and spatial DNS (SDNS). TDNS assume the disturbance is periodic in streamwise direction so that only a small domain is need in the simulation. However, TDNS can't investigate the spatial growth effects of boundary layer. This simplification is mainly due to the limit of computational resources at that time. SDNS uses a much larger domain to conduct the simulation

so that it can take the spatial effect into consideration. With the rapid improvement of computational resource, SDNS has become the major approach and significant progress has been made on DNS of hypersonic flow regime through this approach. A recent review on hypersonic boundary-layer transition with focus on the progress of DNS studies was present by Zhong & Wang [2]. The receptivity, instability, and transition of hypersonic boundary layers are summarized. Several key points are presented below.

Zhong & Wang [2] mentioned that the main receptivity mechanisms of hypersonic boundary layers are the resonant interactions between forcing waves and boundary-layer which is different from low-speed boundary layers. Free-stream disturbances including acoustic waves, turbulence, and entropy waves are important disturbances for hypersonic vehicles, as shown in Fig. 1.1. Wall disturbances including blowing suction are also important to the receptivity and instability of hypersonic boundary layers. Together with freestream, they are the main disturbances that hypersonic vehicles experience under real flight conditions. Surface roughness can also alter boundary-layer-instability characteristics substantially and trigger transition within boundary layers. In addition, real gas effects need to be considered at high temperatures and they are found to stabilize the hypersonic boundary-layer flows. When the boundary-layer waves reach a certain amplitude, the nonlinear secondary instabilities and three-dimensional effects lead to breakdown to turbulence with the appearance of turbulent spots in transitional boundary layers. For incompressible boundary layers, secondary instabilities involving fundamental and subharmonic resonances were identified as two relevant mechanisms of boundary-layer transition [67]. For hypersonic boundary layers, although fundamental and subharmonic breakdown mechanisms are both possible, DNS studies have found that they may not be dominant mechanisms because first-mode instabilities are most unstable when they are oblique. There are still many challenging

problems in DNS studies of hypersonic boundary layers including three-dimensional and complex boundary-layer investigations, nose-bluntness/entropy-layer effects and transition reversal, theoretical analysis of DNS results, transition control, and others.

1.4. Objectives and Motivations

The objectives of the present research include: (i) developing very high-order schemes with spectral-like resolution for simulation of multi-scale flows, such as hypersonic flows which involve complex physics over simple geometries; (ii) developing new schemes specifically for multi-dimensional flow simulations using novel techniques; (iii) analyzing the properties of the new numerical methods such as stability, dissipation, spectral resolution, and anisotropy; (iv) evaluating the performances of the new numerical methods on linear advection equation, the nonlinear Euler equations and the Navier-Stokes equations in both one and two-dimensional settings including rate of convergence, computational efficiency, and numerical errors, etc.

Currently, the high-order finite difference methods for DNS studies of hypersonic flows are usually upwind schemes or compact schemes with fifth-order accuracy or lower[21]. This dissertation presents a family of new very high-order multi-layer compact (MLC) finite difference methods with spectral-like resolution. The features of these new methods include: (i) the multi-layer framework to reduce stencil size, increase order of accuracy, and improve resolution; (ii) the centered grid stencil for upwind schemes and the adjustable parameter to control numerical dissipation; (iii) the explicit finite difference formula derived on uniform structured grids; (iv) the linear approximation to maintain low computational costs and spectral-like resolution for multi-scale smooth flows; (v) the directional discretization technique for

multi-dimensional flow simulations; (vi) the weighted least square approximation for multi-dimensional flow simulations.

As the main aspect of our new methods, the multi-layer compact finite difference methods in this dissertation refers to a numerical approximation on a layered grid stencil which includes the value layer and derivative layers. Both the value and derivatives are used for approximations of higher derivatives, i.e., every grid point has multiple degrees of freedom (DOFs). Most conventional finite difference and finite volume methods can be considered as mono-layer schemes because the only DOF is the value on every grid point. In our multi-layer scheme, the auxiliary equation is introduced and both value and first derivatives are treated as unknows. There are two DOFs in one-dimensional simulations, three in two-dimensional simulations, and four in three-dimensional simulations. The original governing equation becomes an exact equation and only approximation for auxiliary equations are required, which is a benefit for computational efficiency. Details of the methods will be presented in forthcoming chapters.

Researchers have developed many numerical methods with multiple degrees of freedom, which is similar to the multi-layer idea in our new scheme. Discontinuous-Galerkin (DG) methods are a typical example, in which the degrees of freedom (DOFs) in each element is determined by the order of accuracy. Orthogonal basis functions are usually utilized to construct the high-order piecewise polynomials within the element, and all the weights of the basis are solved as unknowns. To increase the order, more DOFs are added in each element. All unknowns in DG methods are numerical quantities, so there is no exact equation in the formulations. This feature becomes a major difference in methodology with the new finite difference methods in this dissertation. Spectral difference (SD) methods [35–37] and spectral volume (SV) methods [38–41] also have multiple DOFs in each element, they are similar to DG methods but the way

the piecewise polynomials are constructed is different. SV methods define the sub-cells and the averaged conservative variables in these sub-cells are DOFs, while SD methods define the solution points within each element and point values are DOFs [12]. These point or sub-cell values are then used to construct polynomials. DG methods and other finite element methods usually have high-order accuracy and can be easily applied to flow simulations over complex geometries with unstructured grids, and they are very compact because the high-order polynomials are defined, and no reconstructions are required. However, they require a large number of memories, especially in multi-dimensional simulations. In addition, controlling of numerical oscillations in the vicinity of strong discontinuities remains one of challenging issues in these methods.

The idea of evolving multiple degrees of freedom has also appeared in finite volume or finite difference methods. Qiu and Shu, et al. developed a fifth-order Hermite WENO (HWENO) scheme [84–86] in the finite volume framework, where both function value and its first derivative is evolved in time and used in the reconstruction. Balsara et al. [87] also used HWENO approach in their hybrid RKDG+HWENO schemes, where a monotonicity preserving strategy that is scale-free and problem-independent for detecting troubled zones is proposed. They proved that they are good alternatives with lower storage and narrower stencils to Runge-Kutta Discontinuous Galerkin (RKDG) schemes. Luo et al. [88–90] did extensive work on the HWENO schemes with a focus on unstructured grids. They applied HWENO approach as limiters to both original discontinuous-Galerkin (DG) methods and reconstructed DG methods and found that it can save computational cost, enhance accuracy, and ensure linear stability. The major advantage of these HWENO approaches is compactness of stencils in reconstructions, so they are also very suitable as limiters for discontinuous-Galerkin methods.

There are still many other numerical methods where the use of multiple degrees of freedom can be found. Chang et al. [91–93] proposed the space-time conservation element and solution element (CE/SE) method which includes a unified treatment of spatial and temporal discretization in the space-time domain. The core of the CE/SE method is the two-level, explicit and non-dissipative scheme so the stencil is minimized while maintaining accuracy. Sundar and Yeo [94] designed a meshless method for attaining high-order approximation with compact support by using high-order information at nodes for solution reconstruction. They avoided the trouble of a very large set of supporting points required in conventional meshless methods, thus, successfully increased the accuracy to sixth order. Nishikawa [95–98] developed the first-order hyperbolic system (FOHS) for solving diffusion and advection-diffusion problems. By introducing an additional equation for first derivatives using a relaxation technique, the diffusion term is formulated in a hyperbolic way. An upwind scheme can be applied to the entire system, which leads to a uniform order of accuracy and faster convergence.

In general, the numerical schemes with multiple degrees of freedom (DOFs) attain benefits from their compact support stencil, leading to better efficiency for parallel computing and simpler stable boundary conditions. Most of the methods mentioned above utilized this desirable feature to improve their performance. On the other hand, using multiple DOFs in a linear scheme leads to an additional advantage of a better spectral resolution for small wave components. A prominent explanation can be obtained from Fourier analysis that the resolving ability of a linear scheme depends mainly on degrees of freedom on each grid, i.e. the upper limit of wavenumber (k_{max}) that can be resolved is determined by DOFs (K) through the relation $k_{max} = K\pi$. As mentioned in the previous part of the introduction, it has been a long history to improve spectral resolutions of finite difference methods, and most of the work follows the idea of Lele [20]. They

improve the spectral resolution through the implicit relation between derivatives and values in a stencil, but they still face a limit of $k_{max} = \pi$. At the same time, many of these methods comprise the formal order when pursuing better marginal resolution, which is not good for global accuracy. As a comparison, in finite element methods such as discontinuous-Galerkin (DG) methods, the resolution limit k_{max} increases with the order of accuracy benefit from multiple DOFs. This gives us the inspiration to construct a new finite difference method with spectral-like resolution using the multi-layer approach without comprising the order of accuracy. Also, the compact stencil is attained as other numerical methods with multiple DOFs which benefits the construction of boundary closure schemes.

It should be noted that our multi-layer idea differs from the combined compact difference (CCD) scheme [22,25,47] on the role these additional derivatives play and how they are updated. In CCD scheme, the use of second derivatives provides additional implicit relations but does not increase the DOFs. Both first and second derivatives are solved simultaneously from their implicit formulas. While in our new multi-layer compact finite difference methods, the use of the first derivative provides additional DOFs and each DOF is solved separately from a discrete equation. As a result, the multi-layer idea furtherly improves the resolution. It has been noticed that the first derivative and its auxiliary equation are also used in Nishikawa's method [95–98]. However, the auxiliary equation is derived in a relaxation technique, so the approximation still applies to the first derivatives. While in our new method, the auxiliary equation is derived directly from the original equation by taking its gradients, so the approximation will apply to the second derivatives. As for the motivation, Nishikawa used the first derivative and additional equation to unify the advection and diffusion term, while our purpose is to improve the spectral resolution.

The second aspect of the current multi-layer compact (MLC) finite difference methods is the construction of upwind scheme based on a centered grid stencil with an adjustable parameter to control dissipation. Most high-order finite difference methods used in direct numerical simulation (DNS) are central difference schemes which introduce only phase errors but no dissipative errors in numerical solutions. However, central schemes are not robust enough for convection dominated flows such as supersonic and hypersonic flows. On the other hand, upwind schemes have been widely investigated because of their robustness and they have received much attention in convection dominated flows. In our very high-order upwind MLC schemes, the idea of centered-stencil upwind schemes with an adjustable parameter proposed by Zhong [21] is followed to stabilize the MLC schemes and maintain low dissipation. The main philosophy behind this idea is to attain the upwind schemes so that the dissipative errors are smaller than the dispersive errors inherent in equivalent central schemes and are large enough to stabilize high-order inner schemes coupled with boundary closure schemes. The orders of accuracies of the upwind schemes are one order lower than the highest orders the centered stencils can achieve so that there is an adjustable parameter in the leading dissipative truncation term.

The third aspect of our methods is the use of finite difference approximation based on uniform structured grids. One of the major areas of application of our new methods is the direct numerical simulation of laminar-turbulent boundary layer transition. Although the physics is complex because of a wide range of scales in these flows, the geometries are usually relatively simple such as flat plates, conical cones and blunt bodies with circular or parabolic cross-sections. Smooth curvilinear meshes can be used to discretize the computational domain. So, our

new methods are constructed in the finite difference framework which has simple formulations and good computational efficiencies on structured grids.

The fourth aspect of our methods is the use of the linear approximation. As summarized in the previous part of the introduction, high-order linear schemes with spectral-like resolution would be ideal for DNS studies of multi-scale flows in the smooth region. They have smaller dissipation and can achieve better spectral resolution compared with nonlinear schemes. In the simulation for supersonic or hypersonic flow over blunt bodies where the bow shock exists, the smooth region behind the shock can be solved by high-order linear schemes and shock-fitting methods can be applied to capture the bow shocks. In the shock-fitting method of Zhong [21], the bow shock can be treated as a moving computational boundary so that the discontinuity across the shock is avoided. The transient shock location and movement are solved as part of the solutions together with the Navier-Stokes equations. The flow variables immediately behind the shock are determined by Rankine-Hugoniot relation and a characteristic compatibility equation from the flow field behind the shock. Different variations of shock-fitting methods are discussed in [62]. In the future, the shock-fitting methods can be used to extend the MLC schemes for direct numerical simulation of hypersonic flows.

The last two aspects of our new methods – the directional discretization and the weighted least square approximation are specifically used in the development of new schemes for multi-dimensional flow simulations. More details are given in Chapters 3 and 4.

In summary, the goal of developing the new very high-order finite difference methods with spectral-like resolution is to accurately simulate smooth multi-scale flows with complex physics but over simple geometries. Besides the laminar-turbulent boundary layer transition simulations,

these new schemes should also be valuable for other multi-scale flows such as turbulence and computational aeroacoustics. The advantages of these present schemes include, very high-order accuracy and high spectral resolution; simplicity of formulations; compact stencils and simple boundary closure schemes; good computational efficiency.

The rest of the dissertation is organized as follows. In Chapter 2, the derivations of the new very high-order upwind multi-layer compact (MLC) schemes are illustrated in one-dimensional and two-dimensional cases respectively. The MLC schemes with up to seventh-order accuracy are presented. The Fourier analysis and stability analysis for boundary closure schemes is carried out to show the high-order accuracy and spectral-like resolution of the MLC schemes. The effect of adjustable damping parameters in upwind schemes is analyzed. In Chapter 3, the DMLC scheme is illustrated on the multi-dimensional linear advection equation. The comparison with the MLC scheme is described. Two-dimensional Fourier analysis and stability analysis for boundary closure schemes are used to show the dissipative and dispersive errors, the spectral resolution, the anisotropy, and the boundary stability of the DMLC scheme in two-dimension cases. In Chapter 4, the LSMLC scheme is derived through the weighted least square approximation. The parametric study based on two-dimensional Fourier analysis is performed to investigate the effects of the 1-D constraint, weight function, upwind factor, and derivative weight factor. The stability analysis with matrix method are carried out to show the stability of boundary closure schemes. In Chapter 5, the accuracies of the three schemes are assessed on the linear advection equation, the nonlinear Euler equations, and the Navier-Stokes equations with multiple test cases in one and two dimensional settings. In Chapter 0, the summary and main conclusions of this dissertation are given. A quick discussion on future work is also given in the end.

2. New Multi-Layer Compact (MLC) Scheme

In this chapter, a new very high-order upwind multi-layer compact (MLC) scheme is derived and presented. The model equation of the inviscid Euler equations is linear advection equation, which is used for the derivation of the very high-order MLC scheme. The derivations of the MLC scheme are illustrated in one-dimensional and two-dimensional cases respectively. The implementation of the MLC scheme is discussed, where we apply it to the discretization of inviscid flux term in the Euler equations, and both the inviscid and viscous flux terms in the Navier-Stokes equations. The one and two-dimensional Fourier analysis is then carried out to show the high-order accuracy and spectral-like resolution of the MLC scheme. The effect of adjustable damping parameters in upwind schemes is analyzed, and the comparison with discontinuous-Galerkin methods are also given in one-dimensional cases. In the end, stability analysis for boundary closure schemes are investigated through matrix method.

2.1. One-Dimensional MLC Scheme

The one-dimensional advection equation is used to introduce the very high-order upwind MLC scheme for one-dimensional simulations,

$$\frac{\partial u}{\partial t} + c\frac{\partial u}{\partial x} = 0, \qquad a \le x \le b \tag{2.1}$$

where it is assumed that the wave speed c is a positive constant. Downwind schemes for $c < 0$ can be easily obtained from upwind schemes. The computational domain for one-dimensional wave propagation is a periodic domain in the range of $a \le x \le b$, where two boundaries located in

$x = a$ and $x = b$ can be either periodic or non-periodic. In the spatial discretization of Eq. (2.1), a uniform mesh with a grid spacing h is used, as presented in Fig. 2.1. Conventional finite difference schemes use only value u_i in each node to approximate the first derivative $\partial u/\partial x$. Therefore, the grid stencil is usually wide for high-order schemes which could cause difficulty on numerical stability and boundary closure schemes. There are different methods which can reduce stencil size including the influential work of Lele [20].

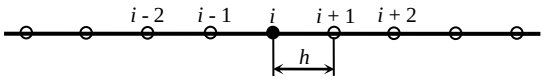

Fig. 2.1. A uniform mesh for conventional finite difference approximations.

In this chapter, we present a new MLC scheme which achieves both high-order accuracy and high spectral resolution within a compact stencil. In the new methods, the additional governing equation for the first derivatives is introduced by taking the gradient of Eq. (2.1), and the resulting Eq. (2.2) is called the auxiliary equation,

$$\frac{\partial u'}{\partial t} + c\frac{\partial u'}{\partial x} = 0 \tag{2.2}$$

Equations (2.1) and (2.2) form a system of partial differential equations in the following form,

$$\frac{\partial}{\partial t}\begin{bmatrix} u \\ u' \end{bmatrix} = -c\begin{bmatrix} u' \\ u'' \end{bmatrix} \tag{2.3}$$

where u and u' are treated as unknowns. Therefore, there are two degrees of freedom (DOFs) at each grid point. Instead of approximating the first derivative $\partial u/\partial x$ in Eq. (2.1) in conventional finite difference scheme, the MLC schemes only need the approximation of u'' in the right-hand side of Eq. (2.3) to solve the unknowns (u, u'). The original advection equation showed in Eq. (2.1) needs no spatial discretization because u' is solved at each grid point. Therefore, the

computational cost is not significantly increased although the MLC scheme involves two equations for the one-dimensional advection problem. To solve the system of equations, finite difference approximation for u'' (= $\partial u'/\partial x$) in Eq. (2.3) are needed and it can be constructed from u_i and u'_i. Because there are two DOFs at each grid point, higher-order accuracy and better spectral resolution can be obtained in a smaller stencil, which is presented in the following part of this chapter.

Same uniform mesh with grid spacing h, as shown in Fig. 2.1, is used in the MLC approximations. For a base point i, the approximation of u'' is of the form,

$$\left(\frac{\partial u'}{\partial x}\right)_i = u''_i = \frac{1}{h^2}\sum_{l=-L_1}^{L_2} a_l u_{i+l} + \frac{1}{h}\sum_{m=-M_1}^{M_2} b_m u'_{i+m} - \frac{\alpha}{(p+2)!}u_i^{p+2}h^p + \cdots \tag{2.4}$$

$$p = L_1 + L_2 + M_1 + M_2 - 1 \tag{2.5}$$

where there is a summation of u_{i+l} and u'_{i+m} with coefficients a_l and b_m, which can be derived from the Taylor series expansion with respect to base point i. In Eq. (2.4), u_{i+l}, u'_{i+m}, and u''_i are exact solutions at grid points. In the truncation error term, p is the order of accuracy, and α is the coefficient of leading truncation error term. If the truncation error term is taken out, Eq. (2.4) can be considered as a finite difference approximation and u_{i+l}, u'_{i+m}, and u''_i becomes approximate solutions. For simplicity, we use same symbols for exact and approximate variables in this chapter. The corresponding stencil is shown in Fig. 2.2, which shows a value layer and first derivative layer. A total of L_1+L_2+1 grid points are picked in the value layer, with L_1 points on the upwind side and L_2 points on the downwind side with respect to the base point i. Similarly, M_1+M_2+1 points are used in the derivative layer, with M_1 points on the upwind side and M_2 points on the downwind side. A scheme with this grid stencil is termed the L_1-L_2-M_1-M_2 scheme in this chapter. In the derivation of the inner scheme, the centered stencils (L_1=L_2, M_1=M_2) are

used, and both upwind schemes and central schemes are constructed on the same centered stencils.

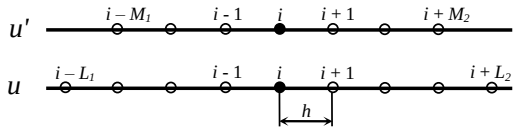

Fig. 2.2. Stencil of the L_1-L_2-M_1-M_2 scheme for second derivative approximations.

The maximum order that the approximation in Eq. (2.4) can achieve is $L_1+L_2+M_1+M_2$, while in the upwind scheme, p is set to be $L_1+L_2+M_1+M_2-1$, which means the coefficient of the leading truncation term α is a free parameter in the coefficients a_l and b_m. All schemes with nonzero α have a p-th order of accuracy, and the maximum $(p+1)$-th order is obtained when $\alpha = 0$. The choice of α is not unique, and the value and sign of α play important roles in the magnitude of numerical dissipation and stability of the numerical scheme. The stability of a high-order scheme is critical when applying it to discretize the inviscid flux terms. Meanwhile, deriving a low dissipative upwind scheme is a common goal for accuracy and spectral resolution requirement. Therefore, the value of α needs to be large enough to make the MLC scheme stable and needs to be relatively small to control the dissipation error. Positive or negative α lead to upwind or downwind schemes. It should be noted that the sign of α of upwind schemes varies with the stencils. The idea of adjustable α is similar to what is presented in [21].

Several specific MLC schemes with various orders of accuracy and grid stencils are presented in this section. First, the third-order 1-1-1-1 scheme and the seventh-order 2-2-2-2 scheme are discussed, and they are analyzed and tested comprehensively later in this dissertation.

The fifth-order 2-2-1-1 and 1-1-2-2 scheme are also presented, as examples where stencils for value and derivative layers are different.

1-1-1-1 Scheme (3rd Order)

Using a three-point stencil in both value and first derivative layers as shown in Fig. 2.3, the 1-1-1-1 scheme can be derived as,

$$\left(\frac{\partial u'}{\partial x}\right)_i = u_i'' = \frac{1}{h^2}\sum_{l=-1}^{1} a_l u_{i+l} + \frac{1}{h}\sum_{m=-1}^{1} b_m u'_{i+m} - \frac{\alpha}{5!}u_i^5 h^3 + \cdots \tag{2.6}$$

$$\begin{aligned} a_{\pm 1} &= 2 \mp \frac{3}{4}\alpha, \qquad a_0 = -4, \\ b_{\pm 1} &= \mp\frac{1}{2} + \frac{1}{4}\alpha, \qquad b_0 = \alpha. \end{aligned} \tag{2.7}$$

where α is the free parameter in coefficients a_l and b_m. The formula leads a third-order upwind scheme when $\alpha > 0$, and it recovers to the fourth-order central scheme when $\alpha = 0$. As a benefit of the multi-layer idea, compactness of grid stencil is achieved. In this case, the third-order upwind scheme or fourth-order central scheme is constructed on the three-point stencil. As a comparison, the grid for conventional finite difference schemes of the same order of accuracy is much wider. For example, a five-point stencil is required in Zhong's third-order upwind scheme or fourth-order central scheme [21].

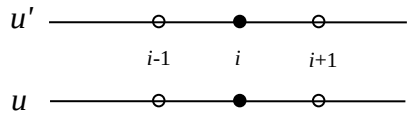

Fig. 2.3. Stencil of the 1-1-1-1 scheme (3rd order) for second derivative approximations.

Different α values lead to different stability conditions and numerical dissipation which affects accuracy and spectral resolution. Here, the recommended value of α in Eq. (2.7) is chosen based on Fourier analysis results in Section 2.4.1. The value of α for the 1-1-1-1 scheme is 1.5, and the corresponding third-order 1-1-1-1 scheme is,

$$\left(\frac{\partial u'}{\partial x}\right)_i = u_i'' = \frac{1}{h^2}\left(\frac{25}{8}u_{i-1} - 4u_i + \frac{7}{8}u_{i+1}\right) + \frac{1}{h}\left(\frac{7}{8}u_{i-1}' + \frac{3}{2}u_i' - \frac{1}{8}u_{i+1}'\right) \tag{2.8}$$

By choosing some specific α values, the 1-1-1-1 scheme can reduce to upwind schemes on bias stencils. For example, if α = 2, then b_1 in Eq. (2.7) is zero and the algorithm reduces to the 1-1-1-0 scheme. Similarly, if α = 8/3, then a_1 in Eq. (2.7) is zero and the algorithm reduces to the 1-0-1-1 scheme. Both schemes have larger α values than the recommended value 1.5. Fourier analysis in Section 2.4.1 will show that a larger α leads to more dissipation. Therefore, the upwind scheme on a bias stencil is more dissipative than the 1-1-1-1 upwind scheme on a centered stencil.

2-2-2-2 Scheme (7th Order)

Similarly, using a five-point stencil in both value and first derivative layers as shown in Fig. 2.4, the 2-2-2-2 scheme can be derived as,

$$\left(\frac{\partial u'}{\partial x}\right)_i = u_i'' = \frac{1}{h^2}\sum_{l=-2}^{2} a_l u_{i+l} + \frac{1}{h}\sum_{m=-2}^{2} b_m u_{i+m}' - \frac{\alpha}{9!}u_i^9 h^7 + \cdots \tag{2.9}$$

$$\begin{aligned} a_{\pm 2} &= \frac{7}{54} \mp \frac{25}{3456}\alpha, \qquad a_{\pm 1} = \frac{64}{27} \mp \frac{5}{108}\alpha, \qquad a_0 = -5, \\ b_{\pm 2} &= \mp\frac{1}{36} + \frac{1}{576}\alpha, \qquad b_{\pm 1} = \mp\frac{8}{9} + \frac{1}{36}\alpha, \qquad b_0 = \frac{1}{16}\alpha. \end{aligned} \tag{2.10}$$

The formula leads to a seventh-order upwind scheme when $\alpha > 0$, and it recovers to the eighth-order central scheme when α = 0. Compactness of grid stencil is significant in this 2-2-2-2

scheme compared with conventional finite difference methods. For example, a nine-point stencil is required in Zhong's seventh-order upwind scheme or eighth-order central scheme [21], while only five points are used in the MLC scheme.

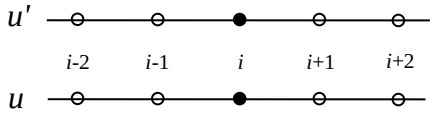

Fig. 2.4. Stencil of the 2-2-2-2 scheme (7th order) for second derivative approximations.

Again, the recommended value of α in Eq. (2.10) is chosen based on Fourier analysis results in Section 2.4.1. The recommended value of α for the 2-2-2-2 scheme is 12, and the corresponding seventh-order 2-2-2-2 scheme is,

$$\left(\frac{\partial u'}{\partial x}\right)_i = u_i'' = \frac{1}{h^2}\left(\frac{187}{864}u_{i-2} + \frac{79}{27}u_{i-1} - 5u_i + \frac{49}{27}u_{i+1} + \frac{37}{864}u_{i+2}\right) + \frac{1}{h}\left(\frac{7}{144}u'_{i-2} + \frac{11}{9}u'_{i-1} + \frac{3}{4}u'_i - \frac{5}{9}u'_{i+1} - \frac{1}{144}u'_{i+2}\right) \tag{2.11}$$

By choosing some specific α values, the 2-2-2-2 scheme can also reduce to upwind schemes on bias stencils. For example, if α = 16, then b_2 in Eq. (2.10) is zero and the algorithm reduces to the 2-2-2-1 scheme. Similarly, if α = 448/25, then a_2 in Eq. (2.10) is zero and the algorithm reduces to the 2-1-2-2 scheme. Again, both schemes has larger α values than the recommended value 12, which means they are more dissipative.

2-2-1-1 Scheme (5th Order)

The stencils in the value layer and the derivative layer can be different in the MLC schemes. For example, using five-point stencil for values and three-point stencil for first derivatives as shown in Fig. 2.5, the 2-2-1-1 scheme can be derived as,

$$\left(\frac{\partial u'}{\partial x}\right)_i = u_i'' = \frac{1}{h^2}\sum_{l=-2}^{2} a_l u_{i+l} + \frac{1}{h}\sum_{m=-1}^{1} b_m u'_{i+m} - \frac{\alpha}{7!}u_i^7 h^5 + \cdots \tag{2.12}$$

$$\begin{aligned} a_{\pm 2} &= \frac{1}{36} \pm \frac{1}{144}\alpha, \qquad a_{\pm 1} = \frac{20}{9} \pm \frac{7}{36}\alpha, \qquad a_0 = -\frac{9}{2}, \\ b_{\pm 1} &= \mp\frac{2}{3} - \frac{1}{12}\alpha, \qquad b_0 = -\frac{1}{4}\alpha. \end{aligned} \tag{2.13}$$

Here, α needs to be negative for upwind schemes. The formula leads to a fifth-order upwind scheme when $\alpha < 0$, and it recovers to the sixth-order central scheme when $\alpha = 0$. The compactness of grid stencil in this 2-2-1-1 scheme is also achieved compared with conventional finite difference schemes. For example, the seven-point stencil is required in Zhong's fifth-order upwind scheme or sixth-order central scheme [21], while only five points are used in the MLC scheme.

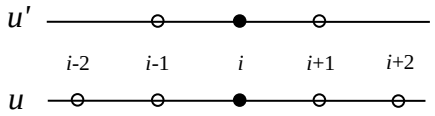

Fig. 2.5. Stencil of the 2-2-1-1 scheme (5th order) for second derivative approximations.

By choosing some specific α values, the 2-2-1-1 scheme can also reduce to upwind schemes on bias stencils. For example, if α = -4, then a_2 in Eq. (2.12) is zero and the algorithm reduces to 2-1-1-1 scheme as,

$$\left(\frac{\partial u'}{\partial x}\right)_i = u_i'' = \frac{1}{h^2}\left(\frac{1}{18}u_{i-2} + 3u_{i-1} - \frac{9}{2}u_i + \frac{13}{9}u_{i+1}\right) + \frac{1}{h}\left(u'_{i-1} + u'_i - \frac{1}{3}u'_{i+1}\right) \tag{2.14}$$

Similarly, if α = -8, then b_1 in Eq. (2.12) is zero and the algorithm reduces to 2-2-1-0 scheme as,

$$\left(\frac{\partial u'}{\partial x}\right)_i = u_i'' = \frac{1}{h^2}\left(\frac{1}{12}u_{i-2} + \frac{34}{9}u_{i-1} - \frac{9}{2}u_i + \frac{2}{3}u_{i+1} - \frac{1}{36}u_{i+2}\right) + \frac{1}{h}\left(\frac{4}{3}u'_{i-1} + 2u'_i\right) \tag{2.15}$$

1-1-2-2 Scheme (5th Order)

The stencils in the derivative layer can be wider than that in the value layer in MLC schemes. For example, using three-point stencil for values and five-point stencil for first derivatives as shown in Fig. 2.6, the 1-1-2-2 scheme can be derived as,

$$\left(\frac{\partial u'}{\partial x}\right)_i = u_i'' = \frac{1}{h^2}\sum_{l=-1}^{1} a_l u_{i+l} + \frac{1}{h}\sum_{m=-2}^{2} b_m u'_{i+m} - \frac{\alpha}{7!}u_i^7 h^5 + \cdots \tag{2.16}$$

$$\begin{aligned} a_{\pm1} &= \frac{24}{11} \pm \frac{3}{20}\alpha, \qquad & a_0 &= -\frac{48}{11}, \\ b_{\pm2} &= \pm\frac{1}{132} + \frac{1}{600}\alpha, \qquad & b_{\pm1} &= \mp\frac{20}{33} - \frac{17}{300}\alpha, \qquad b_0 = -\frac{19}{100}\alpha. \end{aligned} \tag{2.17}$$

Like the case of fifth-order 2-2-1-1 scheme, α also needs to be negative for upwind schemes. It should be noted that although both the 1-1-2-2 and 2-2-1-1 schemes have fifth-order of accuracy, their stability can be different. According to our experience in simulations, the 1-1-2-2 scheme would be less stable than 2-2-1-1 scheme. So, it is recommended to use a wider stencil in the value layer, if not the same, than that in the derivative layer.

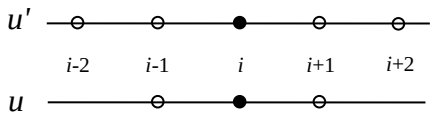

Fig. 2.6. Stencil of the 1-1-2-2 scheme (5th order) for second derivative approximations.

With one-dimensional MLC schemes, all the spatial derivatives in Eq. (2.3) can be approximated and discretized. The spatial discretization of Eq. (2.3) leads to a system of first-order ordinary differential equations,

$$\frac{d\bar{\mathbf{U}}}{dt} = \mathcal{L}\left(\bar{\mathbf{U}}, t\right) \tag{2.18}$$

where $\bar{\mathbf{U}}$ is the discretized flow field variables including function values u_i and first derivatives u'_i, and $\mathcal{L}$ is the approximate operator for spatial discretization through MLC schemes. Time-dependent boundary conditions could be included in Eq. (2.18). The explicit Runge-Kutta schemes can be used to integrate the system of equations in time. For example, the solution procedure from t^n to t^{n+1} using classical fourth-order Runge-Kutta method (RK4) is,

$$\mathbf{k}_1 = dt\mathcal{L}\left(\bar{\mathbf{U}}^n, t^n\right) \tag{2.19}$$

$$\mathbf{k}_2 = dt\mathcal{L}\left(\bar{\mathbf{U}}^n + \frac{\mathbf{k}_1}{2}, t^n + \frac{dt}{2}\right) \tag{2.20}$$

$$\mathbf{k}_3 = dt\mathcal{L}\left(\bar{\mathbf{U}}^n + \frac{\mathbf{k}_2}{2}, t^n + \frac{dt}{2}\right) \tag{2.21}$$

$$\mathbf{k}_4 = dt\mathcal{L}\left(\bar{\mathbf{U}}^n + \mathbf{k}_3, t^n + dt\right) \tag{2.22}$$

$$\bar{\mathbf{U}}^{n+1} = \bar{\mathbf{U}}^n + \frac{\mathbf{k}_1}{6} + \frac{\mathbf{k}_2}{3} + \frac{\mathbf{k}_3}{3} + \frac{\mathbf{k}_4}{6} \tag{2.23}$$

2.2. Two-Dimensional MLC Scheme

The advection equation is also used as the model equation to illustrate the construction of the very high-order upwind MLC schemes in multi-dimensional cases. The advection equation in three-dimensional flow is,

$$\frac{\partial u}{\partial t} + (\mathbf{c}\cdot\nabla)u = 0 \tag{2.24}$$

where, u is a scalar, and $\mathbf{c} = (c_1, c_2, c_3)$ is a constant vector representing the velocity. For simplicity, only the two-dimensional case is discussed here, and three-dimensional case follows the same methodology. In Cartesian grids, it can be written in scalar form as follows,

$$\frac{\partial u}{\partial t} + c_1 u_x + c_2 u_y = 0 \tag{2.25}$$

Then, two auxiliary equations are introduced by taking derivatives of Eq. (2.25) with respect to x and y,

$$\frac{\partial (u_x)}{\partial t} + c_1 u_{xx} + c_2 u_{xy} = 0 \tag{2.26}$$

$$\frac{\partial (u_y)}{\partial t} + c_1 u_{xy} + c_2 u_{yy} = 0 \tag{2.27}$$

Equations (2.25) - (2.27) form a system of partial differential equations as follows,

$$\frac{\partial}{\partial t}\begin{bmatrix} u \\ u_x \\ u_y \end{bmatrix} = -c_1 \begin{bmatrix} u_x \\ u_{xx} \\ u_{xy} \end{bmatrix} - c_2 \begin{bmatrix} u_y \\ u_{xy} \\ u_{yy} \end{bmatrix} \tag{2.28}$$

where u, u_x, u_y are treated as unknows. Therefore, there are three degrees of freedom (DOFs) at each grid point. The system of equations (2.28) is solved by the method of lines simultaneously. Same as the one-dimensional case, the original equation (2.25) needs no approximation because u_x and u_y are part of the solution. On the other hand, u_{xx}, u_{xy}, u_{yy} in auxiliary equations (2.26) and (2.27) need approximations through the MLC schemes. Thus, there are three equations to solve and three terms to approximate, while conventional finite difference method only solves Eq. (2.25) and approximates two terms (u_x, u_y). However, the computational costs are not increased significantly, because much fewer grid points are needed in multi-dimensional simulations with our MLC schemes due to their spectral-like resolutions.

The second derivative terms u_{xx}, u_{yy} in Eq. (2.28) are approximated in the same way as the one-dimensional case, and all the formulas in Section 2.1 can be applied. On the other hand, the cross-derivative term u_{xy}, which is not present in one-dimensional MLC schemes, needs to be estimated through another multi-layer approximation based on the similar idea as one-dimensional cases. Discretized function values $u_{i,j}$ and first derivatives $(u_x)_{i,j}$, $(u_y)_{i,j}$ are available for the approximation. Different from one-dimensional MLC schemes, stencils for cross derivatives in two-dimensional MLC schemes are squares in the (x, y) plane, which include the corner points. Fig. 2.7 shows the stencil of the L_1-L_2-M_1-M_2 scheme for cross derivatives, where the value layer contains $(L_1+L_2+1)^2$ grid points and the first derivative layer contains $(M_1+M_2+1)^2$ grid points. The centered stencil is used which is similar to one-dimensional stencils. In other words, the base point (i, j) is always located in the center of the square, and both u_x and u_y use the same stencil shown in Fig. 2.7(b). Consequently, the projection of this stencil on either axis is identical with the stencil for one-dimensional MLC schemes in Fig. 2.2.

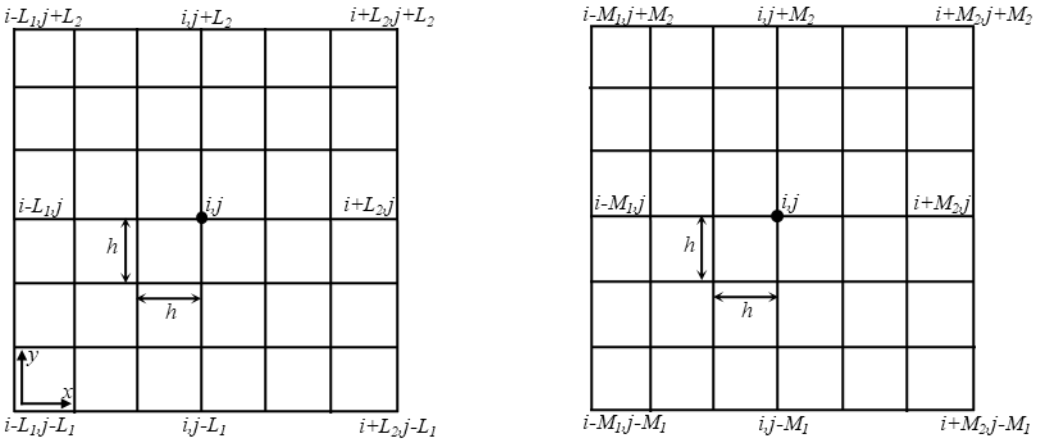

a), function value layer b), first derivative layer

Fig. 2.7. Stencil of the L_1-L_2-M_1-M_2 scheme for cross derivative approximations.

The approximation can be derived from the following equation,

$$\left(u_{xy}\right)_{i,j} = \frac{1}{h^2}\sum_{\substack{l_x=-L_1\\ l_y=-L_1}}^{L_2} a_{l_x,l_y} u_{i+l_x,j+l_y} + \frac{1}{h}\sum_{\substack{m_x=-M_1\\ m_y=-M_1}}^{M_2} b_{m_x,m_y}\left(u_x\right)_{i+m_x,j+m_y} + \frac{1}{h}\sum_{\substack{n_x=-M_1\\ n_y=-M_1}}^{M_2} c_{n_x,n_y}\left(u_y\right)_{i+n_x,j+n_y} + o\left(h^{p+1}\right) \tag{2.29}$$

where p is given in Eq. (2.5), and it is the order of corresponding one-dimensional upwind MLC scheme. It is noted that the L_1-L_2-M_1-M_2 scheme has the same maximum order of accuracy in one and two-dimensional case, which is p+1. In Eq. (2.29), the scheme with the maximum order of accuracy is derived. The truncation error term is a summation of multiple higher derivatives.

The coefficients a, b, c in Eq. (2.29) can be derived by multivariate Taylor series expansion with respect to base point (i, j). In the approximations for cross derivatives, there are many freedoms due to redundant points in a square stencil. As a result, the resulting linear system of equations from Taylor series is underdetermined, and the solution of a, b, c is not unique although the maximum order has been used in Eq. (2.29). To get a unique solution, we must preselect supporting points for both values and derivatives before solving the coefficients. In other words, only the coefficients for preselected points are unknowns, and the coefficients for other points are set to be zero. In our derivation, the goal is to find the simplest formula which contains the fewest non-zero terms and the most concise coefficients. On the other hand, only the central scheme is used to approximate the cross derivatives, because the upwind setting for cross derivatives can be cumbersome and complicated. The results of numerical tests in this dissertation show that central schemes for cross derivatives are stable when coupled with one-dimensional upwind schemes. Because they are one order higher than upwind schemes, they can maintain the overall accuracy of one-dimensional upwind schemes.

Several specific MLC schemes for cross derivatives are presented in this section. Same as the one-dimensional case, the 1-1-1-1 scheme, the 2-2-2-2 scheme, the 2-2-1-1 scheme, and the 1-1-2-2 scheme are derived. All of them are one order higher than their corresponding one-dimensional upwind schemes.

1-1-1-1 Scheme (4th Order)

The stencil to approximate the cross derivative u_{xy} for the 1-1-1-1 scheme is shown in Fig. 2.8. The maximum order of accuracy achievable in this stencil is 4. To get a unique and simplest solution of coefficients *a*, *b*, *c* in Eq. (2.29), supporting points for values and first derivatives are preselected and marked with black dots in Fig. 2.8. All the points on the corner are used to provide information of *u* and all the points along the central *x* and *y* lines are used to provide information of u_y and u_x respectively. In total, four value points, two *x* derivative points, and two *y* derivative points are preselected. It is noted that the points are distributed symmetrically, which is the requirement of central schemes.

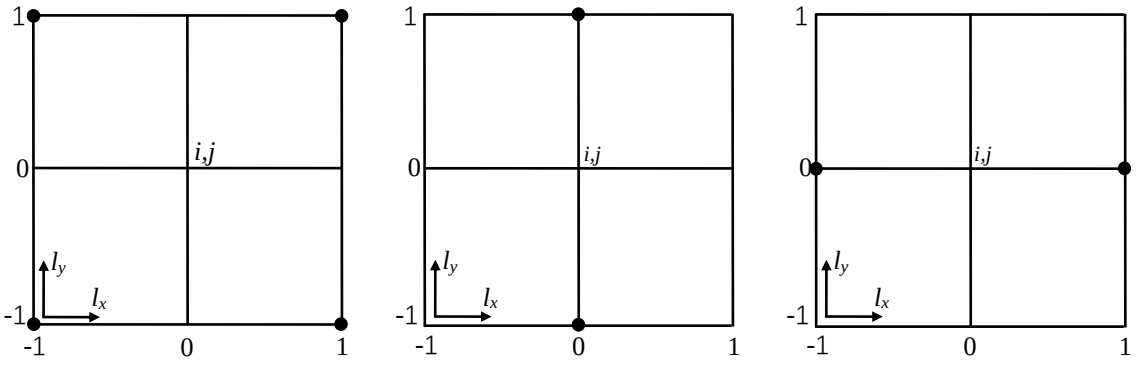

a), *u* b), u_x c), u_y

Fig. 2.8. Stencil and supporting points of the 1-1-1-1 scheme (4th order) for cross derivative approximations.

Using Taylor series expansion, the specific formula for this fourth-order 1-1-1-1 scheme is derived as follows,

$$\begin{aligned}\left(u_{xy}\right)_{i,j} = \frac{1}{h^2}\left(-\frac{1}{4}u_{i-1,j-1}+\frac{1}{4}u_{i+1,j-1}+\frac{1}{4}u_{i-1,j+1}-\frac{1}{4}u_{i+1,j+1}\right) \\ +\frac{1}{h}\left(-\frac{1}{2}\left(u_x\right)_{i,j-1}+\frac{1}{2}\left(u_x\right)_{i,j+1}\right)+\frac{1}{h}\left(-\frac{1}{2}\left(u_y\right)_{i-1,j}+\frac{1}{2}\left(u_y\right)_{i+1,j}\right)\end{aligned} \tag{2.30}$$

In the derivation of cross derivatives, all possible formulas with the fourth-order accuracy have been searched. It turns out Eq. (2.30) has the simplest form with the fewest non-zero terms and the most concise coefficients.

2-2-2-2 Scheme (8th Order)

Similarly, the stencil and preselected supporting points to approximate the cross derivative u_{xy} for the 2-2-2-2 scheme are shown in Fig. 2.9. The maximum order of accuracy achievable in this stencil is 8. A similar methodology is followed as in the 1-1-1-1 scheme to attain the simplest formula. All the points which are not on the central x and y lines are used to provide information of u, and points on central x and y lines are used to provide information of u_y and u_x respectively. In total, sixteen value points, four x derivative points, and four y derivative points are preselected.

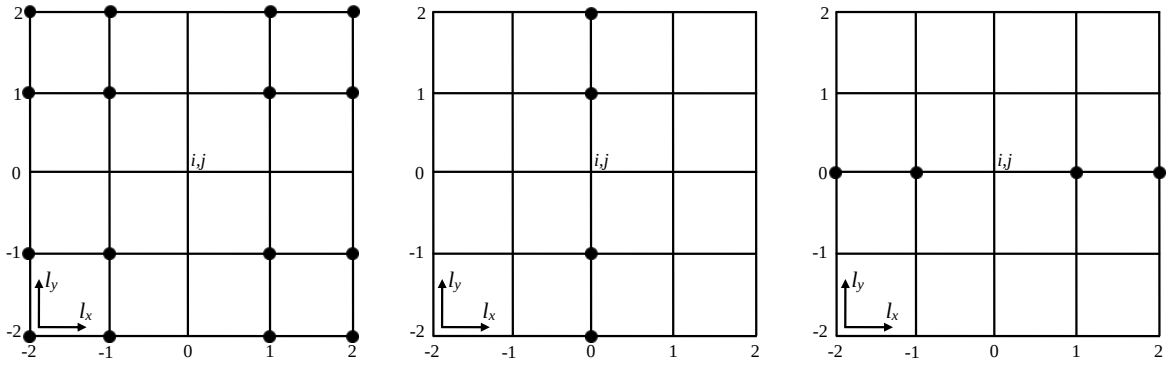

a), u b), u_x c), u_y

Fig. 2.9. Stencil and supporting points of the 2-2-2-2 scheme (8th order) for cross derivative approximations.

Using Taylor series expansion, the specific formula for this eighth-order 2-2-2-2 scheme is derived as follows,

$$\begin{aligned}\left(u_{xy}\right)_{i,j} = \frac{1}{h^2}\Bigg(&-\frac{1}{144}u_{i-2,j-2}+\frac{1}{18}u_{i-1,j-2}-\frac{1}{18}u_{i+1,j-2}+\frac{1}{144}u_{i+2,j-2}\\&+\frac{1}{18}u_{i-2,j-1}-\frac{4}{9}u_{i-1,j-1}+\frac{4}{9}u_{i+1,j-1}-\frac{1}{18}u_{i+2,j-1}\\&-\frac{1}{18}u_{i-2,j+1}+\frac{4}{9}u_{i-1,j+1}-\frac{4}{9}u_{i+1,j+1}+\frac{1}{18}u_{i+2,j+1}\\&+\frac{1}{144}u_{i-2,j+2}-\frac{1}{18}u_{i-1,j+2}+\frac{1}{18}u_{i+1,j+2}-\frac{1}{144}u_{i+2,j+2}\Bigg)\\&+\frac{1}{h}\left(\frac{1}{12}\left(u_x\right)_{i,j-2}-\frac{2}{3}\left(u_x\right)_{i,j-1}+\frac{2}{3}\left(u_x\right)_{i,j+1}-\frac{1}{12}\left(u_x\right)_{i,j+2}\right)\\&+\frac{1}{h}\left(\frac{1}{12}\left(u_y\right)_{i-2,j}-\frac{2}{3}\left(u_y\right)_{i-1,j}+\frac{2}{3}\left(u_y\right)_{i+1,j}-\frac{1}{12}\left(u_y\right)_{i+2,j}\right)\end{aligned} \tag{2.31}$$

Again, Eq. (2.31) has the simplest form with the fewest non-zero terms and the most concise coefficients among all possible formulas with eighth-order accuracy.

2-2-1-1 Scheme (6th Order)

The stencils for values and derivatives can also be different in two-dimensional MLC schemes as well. For example, 2-2-1-1 scheme has a 25-point square stencil for values and a 9-point square stencil for first derivatives. Consequently, the maximum order of accuracy achievable is 6. The stencil and preselected supporting points to approximate the cross derivative u_{xy} for the 2-2-1-1 scheme are shown in Fig. 2.10. The way the supporting points are selected here is different from the 1-1-1-1 or 2-2-2-2 schemes. Only the diagonal points are selected as supporting points. In total, eight value points, four x derivative points, and four y derivative points are preselected.

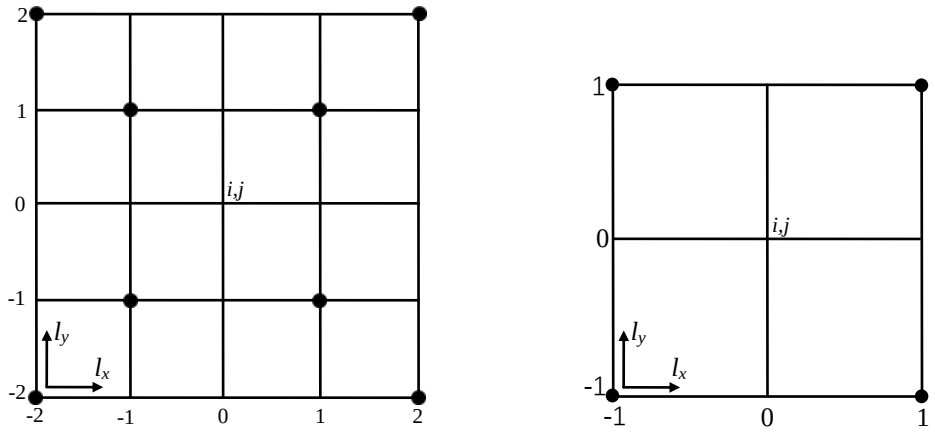

a), u b), u_x and u_y

Fig. 2.10. Stencil and supporting points of the 2-2-1-1 scheme (6th order) for cross derivative approximations.

Using Taylor series expansion, the specific formula for this sixth-order 2-2-1-1 scheme is derived as follows,

$$
\begin{aligned}
\left(u_{xy}\right)_{i,j} = \frac{1}{h^2}\left(\begin{array}{l}
\frac{1}{144}u_{i-2,j-2} - \frac{1}{144}u_{i+2,j-2} + \frac{5}{9}u_{i-1,j-1} - \frac{5}{9}u_{i+1,j-1} \\
-\frac{5}{9}u_{i-1,j+1} + \frac{5}{9}u_{i+1,j+1} - \frac{1}{144}u_{i-2,j+2} + \frac{1}{144}u_{i+2,j+2}
\end{array}\right) \\
+\frac{1}{h}\left(\frac{1}{6}\left(u_x\right)_{i-1,j-1} + \frac{1}{6}\left(u_x\right)_{i+1,j-1} - \frac{1}{6}\left(u_x\right)_{i-1,j+1} - \frac{1}{6}\left(u_x\right)_{i+1,j+1}\right) \\
+\frac{1}{h}\left(\frac{1}{6}\left(u_y\right)_{i-1,j-1} - \frac{1}{6}\left(u_y\right)_{i+1,j-1} + \frac{1}{6}\left(u_y\right)_{i-1,j+1} - \frac{1}{6}\left(u_y\right)_{i+1,j+1}\right)
\end{aligned}
\tag{2.32}
$$

1-1-2-2 Scheme (6th Order)

Similar to the situation in one-dimensional MLC schemes, we can use a wider stencil in the derivative layer than the value layer. For example, 1-1-2-2 scheme has a 9-point square stencil for values and a 25-point square stencil for first derivatives. The maximum order of accuracy achievable is 6. The stencil and preselected supporting points to approximate the cross derivative u_{xy} for the 1-1-2-2 scheme are shown in Fig. 2.11. The preselected supporting points are the same as 2-2-1-1 scheme, i.e., only the diagonal points are selected. In total, four value points, eight *x* derivative points, and eight *y* derivative points are preselected.

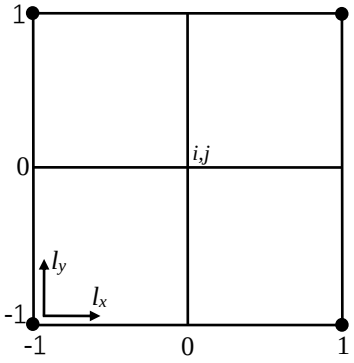

a), u

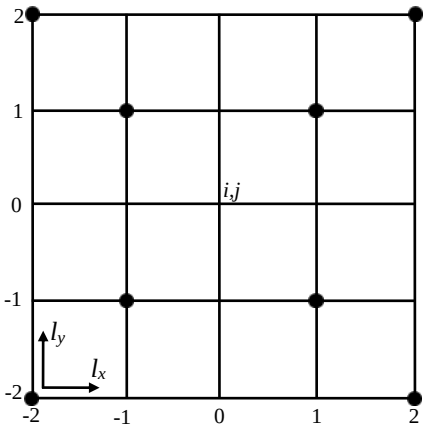

b), u_x and u_y

Fig. 2.11. Stencil and supporting points of the 1-1-2-2 scheme (6th order) for cross derivative approximations.

Using Taylor series expansion, the specific formula for this sixth-order 1-1-2-2 scheme is derived as follows,

$$\begin{aligned}\left(u_{xy}\right)_{i,j} = &\frac{1}{h^2}\left(\frac{6}{11}u_{i-1,j-1} - \frac{6}{11}u_{i+1,j-1} - \frac{6}{11}u_{i-1,j+1} + \frac{6}{11}u_{i+1,j+1}\right) \\ &+\frac{1}{h}\left(\begin{array}{l} -\frac{1}{528}\left(u_x\right)_{i-2,j-2} - \frac{1}{528}\left(u_x\right)_{i+2,j-2} + \frac{5}{33}\left(u_x\right)_{i-1,j-1} + \frac{5}{33}\left(u_x\right)_{i+1,j-1} \\ -\frac{5}{33}\left(u_x\right)_{i-1,j+1} - \frac{5}{33}\left(u_x\right)_{i+1,j+1} + \frac{1}{528}\left(u_x\right)_{i-2,j+2} + \frac{1}{528}\left(u_x\right)_{i+2,j+2}\end{array}\right) \\ &+\frac{1}{h}\left(\begin{array}{l} -\frac{1}{528}\left(u_y\right)_{i-2,j-2} + \frac{1}{528}\left(u_y\right)_{i+2,j-2} + \frac{5}{33}\left(u_y\right)_{i-1,j-1} - \frac{5}{33}\left(u_y\right)_{i+1,j-1} \\ +\frac{5}{33}\left(u_y\right)_{i-1,j+1} - \frac{5}{33}\left(u_y\right)_{i+1,j+1} - \frac{1}{528}\left(u_y\right)_{i-2,j+2} + \frac{1}{528}\left(u_y\right)_{i+2,j+2}\end{array}\right)\end{aligned} \tag{2.33}$$

Although 1-1-2-2 scheme and 2-2-1-1 scheme have the same order of accuracy, Eq. (2.33) has more terms than Eq. (2.32) which means the computational efficiency will be lower, and the coefficients are more trivial. Consistent with one-dimensional MLC scheme, it is recommended to use a wider stencil in the value layer, if not the same, than the derivative layer.

With one-dimensional and two-dimensional MLC schemes, all the spatial derivatives in Eq. (2.28) can be approximated and discretized. Same as one-dimensional case, the spatial discretization of Eq. (2.28) leads to a system of first-order ordinary differential equations. Explicit Runge-Kutta schemes can be applied to the system of equations, and solution procedures are the same as the one-dimensional case in Section 2.1.

2.3. Implementation of MLC Scheme on Euler and Navier-Stokes Equations

The compressible viscous flow problems are governed by the Navier-Stokes equations, which can be written in the following conservation-law form in the Cartesian coordinate,

$$\frac{\partial U}{\partial t}+\frac{\partial F_j}{\partial x_j}+\frac{\partial F_{vj}}{\partial x_j}=0 \tag{2.34}$$

where U, F_j, and F_{vj} are the vectors of conservative variables, inviscid convective flux, and viscous flux in the direction of x_j respectively,

$$U=\left[\rho,\ \rho u_1,\ \rho u_2,\ \rho u_3,\ E_t\right]^T \tag{2.35}$$

$$F_j=\begin{bmatrix}\rho u_j\\ \rho u_1u_j+p\delta_{1j}\\ \rho u_2u_j+p\delta_{2j}\\ \rho u_3u_j+p\delta_{3j}\\ \left(E_t+p\right)u_j\end{bmatrix} \tag{2.36}$$

$$F_{vj}=\begin{bmatrix}0\\ \tau_{1j}\\ \tau_{2j}\\ \tau_{3j}\\ \tau_{ij}u_i+q_j\end{bmatrix} \tag{2.37}$$

In a wide range of temperature and pressure, the perfect gas assumption can be used, and the total energy per unit volume E_t is calculated from,

$$E_t=\frac{p}{\gamma-1}+\frac{1}{2}\rho u_ku_k \tag{2.38}$$

In Eq. (2.37), τ_{ij} is the viscous stress which has the form,

$$\tau_{ij}=-\mu\left(\frac{\partial u_i}{\partial x_j}+\frac{\partial u_j}{\partial x_i}\right)-\lambda\frac{\partial u_k}{\partial x_k}\delta_{ij} \tag{2.39}$$

where μ is the molecular viscosity coefficient and λ is second viscous coefficient which is usually assumed to be -2μ/3. The heat flux q_j in Eq. (2.37) is calculated from,

$$q_j=-\kappa\frac{\partial T}{\partial x_j} \tag{2.40}$$

where the heat conductivity coefficient κ is computed through a constant Prandle number Pr = 0.72 as follows,

$$\kappa = \frac{C_p}{\Pr}\mu = \frac{\gamma R}{(\gamma - 1)\Pr}\mu \tag{2.41}$$

The Navier-Stokes equations reduce to the Euler equations, which are the governing equations for inviscid flows and $F_{vj} = 0$.

The method of lines can be used to discretize the governing equations by separating spatial and temporal discretization. The main difficulty in the spatial discretization is the approximation of the hyperbolic-type convective term in Eq. (2.34), which plays an important role in numerical stability. To construct a stable numerical algorithm, the high-order upwind scheme is commonly utilized to discretize the convective term. Meanwhile, the elliptic-type viscous flux term in the Navier-Stokes equations can be approximated by high-order central schemes. Therefore, in the remaining part of the chapter, the focus is mainly on the derivation and analysis of the convective term.

2.3.1 Euler Equations

Eliminating the viscous term of Navier-Stokes equations in (2.34) leads to the nonlinear Euler equations for inviscid flows. In the MLC schemes, in addition to the conservative variable U, the derivatives of U are introduced as additional degrees of freedom. Therefore, it is necessary to introduce auxiliary equations as follows,

$$\frac{\partial U_{x_k}}{\partial t} + \frac{\partial F_{jx_k}}{\partial x_j} = 0 \tag{2.42}$$

where the subscript x_k represents a directional derivative in the Cartesian coordinates (x_1, x_2, x_3). The subscript j is a dummy index. For two and three-dimensional simulation, there are two and three auxiliary equations respectively. The Euler equations and the auxiliary equations can be written in vector forms as follows,

$$\frac{\partial}{\partial t}\begin{bmatrix} U \\ U_{x_k} \end{bmatrix} = -\begin{bmatrix} A_j U_{x_j} \\ F_{j x_k x_j} \end{bmatrix} \tag{2.43}$$

where $A_j = \partial F_j / \partial U$ is the Jacobian matrix and $F_{jxk} = A_j U_{xk}$. The first equation is an exact equation, and only the term F_{jxkxj} in the auxiliary equations needs an approximation. This term is approximated from F_j and F_{jxk}, which can be calculated from U and U_{xk} exactly. Because the operation of Jacobian matrix A_j is expensive, an efficient way to compute F_j and F_{jxk} is to rewrite F_j as a function of conservative variables U as follows,

$$F_j = \begin{bmatrix} U_{1+j} \\ \dfrac{U_2 U_{1+j}}{U_1} + p\delta_{1j} \\ \dfrac{U_3 U_{1+j}}{U_1} + p\delta_{2j} \\ \dfrac{U_4 U_{1+j}}{U_1} + p\delta_{3j} \\ \dfrac{U_5 U_{1+j}}{U_1} + p\dfrac{U_{1+j}}{U_1} \end{bmatrix}, \quad p = (\gamma - 1)\left(U_5 - \frac{\sum_{i=2}^{4} U_i^2}{2U_1} \right) \tag{2.44}$$

where U_i represents the ith component of U. Then, F_{jxk} can be obtained by taking derivative of Eq. (2.44) to x_k as follows,

$$F_{j x_k} = \begin{bmatrix} U_{1+j x_k} \\ \dfrac{\left(U_{2x_k} U_{1+j} + U_2 U_{1+j x_k}\right) U_1 - U_2 U_{1+j} U_{1x_k}}{U_1^2} + p_{x_k}\delta_{1j} \\ \dfrac{\left(U_{3x_k} U_{1+j} + U_3 U_{1+j x_k}\right) U_1 - U_3 U_{1+j} U_{1x_k}}{U_1^2} + p_{x_k}\delta_{2j} \\ \dfrac{\left(U_{4x_k} U_{1+j} + U_4 U_{1+j x_k}\right) U_1 - U_4 U_{1+j} U_{1x_k}}{U_1^2} + p_{x_k}\delta_{3j} \\ \dfrac{\left(U_{5x_k} U_{1+j} + U_5 U_{1+j x_k}\right) U_1 - U_5 U_{1+j} U_{1x_k}}{U_1^2} + p_{x_k}\dfrac{U_{1+j}}{U_1} + p\dfrac{U_{1+j x_k} U_1 - U_{1+j} U_{1x_k}}{U_1^2} \end{bmatrix}$$

$$p_{x_k} = (\gamma - 1)\left(U_{5x_k} - \frac{\sum_{i=2}^{4} U_i U_{i x_k}}{U_1} + \frac{U_{1x_k} \sum_{i=2}^{4} U_i^2}{2U_1^2} \right) \tag{2.45}$$

In this form, F_{jxk} is only a function of U and U_{xk} which are the unknowns in Eq. (2.43).

After F_j and F_{jxk} are obtained from Eqs. (2.44) and (2.45), the new MLC schemes are applied to numerically approximate F_{jxkxj} in Eq. (2.43). Specifically, the one-dimensional MLC scheme in Eq. (2.4) is used when $j = k$, and the two-dimensional MLC scheme in Eq. (38) is used when $j \neq k$. For the case of $j = k$, the upwind MLC schemes are applied through flux splitting methods. In this section, a locally global Lax-Friedrichs approach is designed, which is similar to the flux splitting in Zhong's upwind schemes [21]. The inviscid flux F_j and their derivatives F_{jxk}, F_{jxkxj} are decomposed into positive and negative wave fields as follows,

$$\begin{aligned} F_j &= F_j^+ + F_j^- \\ F_{jx_k} &= F_{jx_k}^+ + F_{jx_k}^- \\ F_{jx_kx_j} &= F_{jx_kx_j}^+ + F_{jx_kx_j}^- \end{aligned} \tag{2.46}$$

The positive part $F_j{}^+{}_{xkxj}$ and negative part $F_j{}^-{}_{xkxj}$ are approximated by the upwind and downwind MLC schemes respectively, which have the same formula given in Eq. (2.4), but the opposite sign in α. It is required that the flux $F_j{}^+$ and $F_j{}^-$ contains only positive and negative eigenvalues in their Jacobian matrices respectively. A straightforward approach to construct $F_j{}^+$ and $F_j{}^-$ and their derivatives are,

$$F_j^+ = \frac{1}{2}(F_j + \Lambda U), \quad F_j^- = \frac{1}{2}(F_j - \Lambda U) \tag{2.47}$$

$$F_{jx_k}^+ = \frac{1}{2}\left(F_{jx_k} + \Lambda U_{x_k}\right), \quad F_{jx_k}^- = \frac{1}{2}\left(F_{jx_k} - \Lambda U_{x_k}\right) \tag{2.48}$$

where, λ is a positive parameter large enough to make $F_j{}^+$ and $F_j{}^-$ to contain only positive and negative eigenvalues. In Zhong's upwind schemes, λ is a local parameter, which introduces small dissipation. However, local λ causes difficulty for the new MLC schemes because λ needs to be constant for the splitting of F_{jxk} in Eq. (2.48). On the other hand, using a constant λ in the entire domain will introduce large dissipation especially for low order methods such as the third-order

1-1-1-1-1 scheme. Therefore, in our locally global Lax-Friedrichs approach, a constant λ within each stencil is used, which has the form,

$$\Lambda = \max(\lambda_i) \tag{2.49}$$

and λ_i is a positive parameter chosen to be larger than the local maximum eigenvalues of the Jacobian A_j on point i. When the Euler equations are discretized at a base point i_0, λ is set to be the largest λ_i in the grid stencil. Taking one-dimensional 2-2-2-2 scheme as an example, at the point i_0, the largest λ_i of the five supporting points (i_0-2 < i < i_0+2) in the stencil is chosen to be λ. The procedure is repeated for every base point. Compared with using a constant λ in the entire domain, the locally global Lax-Friedrichs approach has the benefit of maintaining low dissipation. For cross derivatives ($j \neq k$), the central schemes are applied to F_{jxkxj} directly for better computational efficiency. After the MLC approximations, Eq. (2.43) becomes a system of ordinary differential equations, which can be solved by the Runge-Kutta methods.

The discretization described above is performed with respect to the Cartesian coordinates (x_1, x_2, x_3), and this is straightforward for rectangular physical domains. In general case, the physical domain can have different shapes where curvilinear meshes are required. Therefore, a coordinate transformation between physical and computational domain (ξ_1, ξ_2, ξ_3) will be applied to the governing equations. The discretization with MLC schemes can be applied in the computational domain, which is very similar to the description above. The details of the transformation are not included for the sake of length.

The boundary conditions of both U and U_{xk} are needed when the MLC schemes are applied to the Euler equations (2.43) in a flow simulation with physical boundaries. Most approaches from other finite difference methods still apply to the boundary conditions of U. However, the boundary conditions of U_{xk} needs to be dealt with in different manners. It should be noted that

the boundary condition itself is a big subject, and the optimal boundary conditions for the MLC schemes still need further investigation. Here, only one practicable way from many approaches is briefly described. For simplicity, illustration is given for two-dimensional simulations.

It is usually easier to derive boundary conditions on the primitive variables $V = (\rho, u, v, p)^{\mathrm{T}}$ instead of U. Fig. 2.12 shows a physical boundary along the x-direction, where the boundary value V, the tangential derivative V_x, and the normal derivative V_y need to be determined. The derivative boundary conditions can be obtained through governing equations. The Euler equations in two-dimensional case can be written in the primitive form,

$$(A_2 T)V_y = -(A_1 T)V_x - TV_t \tag{2.50}$$

where the A_1 and A_2 are the Jacobians, and T is defined as $\partial U/\partial V$. The matrices A_1, A_2, and T are only functions of V. If the values of V, V_x, and V_t are available on the boundaries, then V_y can be obtained by solving Eq. (2.50). Therefore, the core problem in boundary conditions becomes determining V, V_x, and V_t on the boundaries. This idea can be applied to different types of boundaries. Some examples are given below.

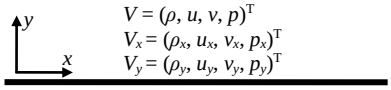

Fig. 2.12. Schematic of boundary conditions for the MLC schemes on a physical boundary.

For a supersonic inflow boundary, V is specified and imposed. Therefore, V_t and V_x can also be obtained by taking a derivative to t and x. For the subsonic inflow, only a part of the flow quantities is specified. Other quantities can be determined by solving characteristic relations, which is termed the characteristic boundary conditions [99]. The characteristic relation also leads to the equation for V_t. The tangential derivatives V_x can be approximated locally from V along the

boundary using high-order finite difference methods like Zhong's compact schemes [21]. Alternatively, we can also derive auxiliary equations for V_x from characteristic relations using the additional degrees of freedom of MLC schemes. For a supersonic outflow boundary, no flow quantities are specified. The boundary conditions are only dependent on information from interior points. They can be obtained by solving Eq. (2.43) using one-sided MLC schemes, or simply extrapolated from interior values. For a subsonic outflow boundary, p is usually specified. Other quantities are determined by solving characteristic relations. The solution procedure is similar to the case in the subsonic inflow. For a solid wall, the non-penetration condition is applied, in other words, (v, v_x, v_t) is 0. Usually, u and p can be determined from interior points by imposing $u_y = 0$ and $p_y = c$, which is a constant determined by the boundary curvature. Characteristic relations can be used to determine other unspecified quantities in V and V_t. The tangential derivatives V_x can be approximated from V by high-order finite difference methods. For all these examples, the normal derivatives V_y can be obtained through Eq. (2.50). It is straightforward to convert (V, V_x, V_y) to (U, U_x, U_y), and the details are not discussed here.

2.3.2 Navier-Stokes Equations

The Navier-Stokes equations for compressible viscous flows have been introduced in Eq. (2.34). Like the case of the Euler equations, auxiliary equations need to be derived before applying the MLC schemes. Taking gradient on Eq. (2.34), we obtain the auxiliary equations for the Navier-Stokes equations as follows,

$$\frac{\partial U_{x_k}}{\partial t} + \frac{\partial F_{j x_k}}{\partial x_j} + \frac{\partial F_{v j x_k}}{\partial x_j} = 0 \tag{2.51}$$

where the subscripts x_k and j are directional derivatives and dummy index respectively, same as in the Euler equations, and v represents viscous flux term. In vector forms, the original Navier-Stokes equations (2.34) and the auxiliary equations (2.51) can be written as,

$$\frac{\partial}{\partial t}\begin{bmatrix} U \\ U_{x_k} \end{bmatrix} = -\begin{bmatrix} A_j U_{x_j} \\ F_{j x_k x_j} \end{bmatrix} - \begin{bmatrix} F_{v j x_j} \\ F_{v j x_k x_j} \end{bmatrix} \tag{2.52}$$

Note that Eq. (2.52) have the viscous terms on the right-hand side, which is the only difference from Eq. (2.43). Therefore, the treatment of the first term on the right-hand side of Eq. (2.52) follows exactly the same procedures for the Euler equations. In the viscous part, the term F_{vjxkxj} also needs an approximation. It can be computed by high-order MLC schemes from F_{vj} and F_{vjxk}, like the treatment for the inviscid part. However, only the viscous flux F_{vj} can be calculated exactly. The first derivatives F_{vjxk} needs to be numerically approximated which is explained below. The expression of F_{vj} has been given in Eq. (2.37), and the expression of F_{vjxk} is derived by taking the derivative of Eq. (2.37) as follows,

$$F_{v j x_k} = \begin{bmatrix} 0 \\ \tau_{1 j x_k} \\ \tau_{2 j x_k} \\ \tau_{3 j x_k} \\ \tau_{ij x_k} u_i + \tau_{ij} u_{i x_k} + q_{j x_k} \end{bmatrix} \tag{2.53}$$

where the subscript i is a dummy index, and the derivatives of viscous stress, molecular viscosity coefficient, and heat flux can be obtained easily as follows,

$$\tau_{ij x_k} = -\mu_{x_k}\left(u_{i x_j} + u_{j x_i}\right) - \mu\left(u_{i x_j x_k} + u_{j x_i x_k}\right) + \frac{2}{3}\left(\mu_{x_k} u_{l x_l} + \mu u_{l x_l x_k}\right)\delta_{ij} \tag{2.54}$$

$$q_{j x_k} = -\kappa T_{x_j x_k} \tag{2.55}$$

The molecular viscosity coefficient μ and its derivative can be calculated by Sutherland's law in the form,

$$\mu = \mu_0 \left(\frac{T}{T_0} \right)^{3/2} \frac{T_0 + T_s}{T + T_s} \tag{2.56}$$

$$\mu_{x_k} = \mu_0 \left(\frac{T}{T_0} \right)^{1/2} \left(\frac{T_0 + T_s}{T + T_s} \right) \left[\frac{3}{2T_0} - \frac{T}{T_0 (T + T_s)} \right] T_{x_k} \tag{2.57}$$

Combining Eqs. (2.37) - (2.41) and (2.53) - (2.55), we find that F_{vj} and F_{vjxk} are functions of the primitive variables (u_i, T) and their derivatives in the following form,

$$\begin{aligned} F_{v\,j} &= f\left(u_i, T, u_{i x_j}, T_{x_j}\right) \\ F_{v\,j x_k} &= f'\left(u_i, T, u_{i x_j}, T_{x_j}, u_{i x_k x_j}, T_{x_k x_j}\right) \end{aligned} \tag{2.58}$$

where $i, j, k \in \{1, 2, 3\}$. At every grid point, we know U and U_{xk} from the solution, so u_i, T and their first derivatives can be obtained easily. However, u_{ixkxj} and T_{xkxj} in Eq. (2.58) needs to be approximated by finite difference methods.

The procedures of discretization for Navier-Stokes equations include three steps. Step 1 is the discretization for inviscid flux, which is described in Section 2.3.1. In Step 2, we apply the central MLC schemes to approximate (u_{ixkxj}, T_{xkxj}) from (u_i, T) and their first derivatives. Then using Eq. (2.58), the value of F_{vj} and F_{vjxk} at each point is obtained. In Step 3, we apply the same central MLC schemes to compute F_{vjxkxj} from F_{vj} and F_{vjxk}. After that, all the terms in the right-hand side of Eq. (2.52) is obtained. It should be noted that the central MLC schemes are applied twice in the approximation of viscous terms. To be consistent, the formulas for these central schemes are the same as those for F_{jxkxj} in step 1. However, $\alpha = 0$ is always used in the viscous terms due to their elliptic property. After the three steps are finished, Eq. (2.52) becomes a system of ordinary differential equations, which can be solved through the method of lines.

The boundary conditions of U and U_{xk} are needed for the Navier-Stokes simulations. For the inflow and outflow boundaries, the boundary conditions are very similar to those for the Euler equations. This topic is another important area in numerical simulations and the details are not

discussed in this dissertation. However, the solid wall condition for the Navier-Stokes equations is different, because the viscous effect is dominant near the wall. Flow quantities on the solid wall boundaries are (p, u_i, T, p_x, u_{ix}, T_x, p_y, u_{iy}, T_y), where i = 1, 2, 3. The subscript x and y represent the tangential and normal direction of the wall, which follows the schematic in Fig. 2.12. The boundary conditions for ρ can be determined through thermodynamic relations. Specifically, the physical conditions in the Navier-Stokes simulations are: the non-slip condition for u_i, and the isothermal or adiabatic condition for T. Table 2.1 summarizes the boundary conditions for the Navier-Stokes simulations with the MLC schemes. According to boundary layer equations, the zero-gradient condition for p can be derived, i.e., p_y on the wall is zero. This condition can usually be extended to the Navier-Stokes simulations. Then, a zero-gradient fitting from the interior points can be used to determine p on the wall. The non-slip boundary condition is applied to $\mathbf{u} = (u_1, u_2, u_3)$. There is no relative motion between the wall and its neighboring fluid particles, i.e., $\mathbf{u} = \mathbf{U_{wall}}$. If the wall is static, all components u_i are 0. Two types of boundary conditions of T can be used, 1) isothermal wall; 2) adiabatic wall. For isothermal case, T is a constant value; and for the adiabatic case, T_y at the wall is zero which means no heat conduction through the wall. In the adiabatic case, T is determined by the zero-gradient fitting from interior temperatures. The tangential derivatives u_{ix} and T_x in the isothermal case are set to be 0. For p_x and T_x in the adiabatic case, they are approximated by Zhong's compact schemes [21] along the tangential direction of the wall. For u_{iy} and T_y in the isothermal case, the two-layer extrapolation can be used.

Table 2.1. Summary of boundary conditions for the Navier-Stokes equations.

	Value	Tangential derivative (x)	Normal derivative (y)
p	Zero-gradient fitting	Compact finite difference approximation	Zero

u_i	Non-slip wall ($u = U_{wall}$)	Zero	Two-layer extrapolation
T	1) Isothermal wall ($T = T_{wall}$)	Zero	Two-layer extrapolation
	2) Adiabatic wall (Zero-gradient fitting)	Compact finite difference approximation	Zero

The two-layer extrapolation and the zero-gradient fitting are very similar, which follows the same multi-layer idea of the MLC schemes. In the following description, we use the T for illustration. The normal derivative is notated as T' for simplicity. For a base point i, the approximation of T' has the form,

$$T_i' = \frac{1}{h}\sum_{l=-L_1}^{L_2} a_l T_{i+l} + \sum_{\substack{m=-M_1 \\ m\neq 0}}^{M_2} b_m T_{i+m}' - \frac{\alpha}{(p+1)!} T_i^{p+1} h^p + \cdots \tag{2.59}$$

where all the coefficients are defined in the same way as in Eq. (2.4). These two formulas are very similar, both include two layers of information – value and first derivatives. However, the second derivative in Eq. (2.4) is replaced by the first derivative in Eq. (2.59). As a result, this approximation of T'_i can be considered as a combination of the interpolation/extrapolation from T'_{i+m} and the finite difference approximation from T_{i+l}. The coefficients a_l and b_m can be derived from the Taylor series expansion. On a boundary point (i = 1), one-sided stencils are used (L_1 = M_1 = 0), then the formulas for the two-layer extrapolation are obtained, as follows,

$$T_1' = \frac{1}{h}\sum_{l=0}^{L_2} a_l T_{l+1} + \sum_{m=1}^{M_2} b_m T_{m+1}' \tag{2.60}$$

For the isothermal wall, all values at the right-hand side of Eq. (2.60) are known, therefore, T'_1 on the wall can be computed. By using the first derivatives in the inner field which are already solved, the two-layer extrapolation achieved the same accuracy with fewer points compared with

finite difference approximations or conventional extrapolation of normal derivatives. Hence, it is more compatible with the MLC schemes. The formulas of the two-layer extrapolations on boundary points with different orders of accuracy are given in Appendix A.1.

In the adiabatic case, T'_1 on the wall is zero, and T_1 is the unknown. With some algebraic operations, Eq. (2.60) can be written in the following form,

$$T_1 = -\frac{1}{a_0}\left(\sum_{l=1}^{L_2} a_l T_{l+1} + h\sum_{m=1}^{M_2} b_m T'_{m+1}\right) \tag{2.61}$$

where all the coefficients keep the same values from Eq. (2.60). The approximation in Eq. (2.61) is termed the zero-gradient fitting, which also applies to the approximation of boundary pressures.

2.4. Fourier Analysis

In this section, the one-dimensional and two-dimensional Fourier analysis is performed respectively on various MLC schemes. The dissipative and dispersive errors, spectral resolution, and anisotropic error are analyzed and compared.

2.4.1 One-Dimensional Fourier Analysis

The dissipative and dispersive errors of the upwind MLC schemes applied to advection equation (2.3) are investigated by the Fourier analysis. The trial solutions in Fourier mode are of the following form,

$$\begin{bmatrix} u \\ u' \end{bmatrix} = \begin{bmatrix} \hat{u} \\ \hat{u}' \end{bmatrix} e^{\hat{a}t + i\hat{k}x} \tag{2.62}$$

where $\hat{k}$ is the wavenumber, and $\hat{a}$ is a complex characteristic parameter as a function of $\hat{k}$. If a uniform mesh with spacing h is used, the Fourier modes can also be written in discrete form as,

$$\begin{bmatrix} u_i \\ u_i' \end{bmatrix} = \begin{bmatrix} \hat{u} \\ \hat{u}' \end{bmatrix} e^{\hat{a}t + i\hat{k}x_i} \tag{2.63}$$

where $x_i = x_0 + ih$. The temporal derivative is assumed to be exact and does not introduce any error. Using the L_1-L_2-M_1-M_2 scheme given by Eq. (2.4) with the stencil in Fig. 2.2 to discretize the spatial derivative u'', the advection equation (2.3) becomes two semi-discrete equations as follows,

$$\frac{d}{dt} u_i + c u_i' = 0 \tag{2.64}$$

$$\frac{d}{dt} u_i' + \frac{c}{h}\left(\frac{1}{h} \sum_{l=-L_1}^{L_2} a_l u_{i+l} + \sum_{m=-M_1}^{M_2} b_m u_{i+m}' \right) = 0 \tag{2.65}$$

where u_{i+l} and u'_{i+m} can be represented in discrete Fourier modes according to Eq. (2.63) in this analysis,

$$u_{i+l} = \hat{u} e^{\hat{a}t + i\hat{k}(x_i + lh)} \tag{2.66}$$

$$u_{i+m}' = \hat{u}' e^{\hat{a}t + i\hat{k}(x_i + mh)} \tag{2.67}$$

Substituting Eqs. (2.66) and (2.67) into Eq. (2.64) leads to the following relation between $\hat{u}$ and $\hat{u}'$,

$$\hat{u}' = -\frac{\hat{a}}{c} \hat{u} \tag{2.68}$$

Then, substituting Eqs. (2.66) and (2.67) into Eq. (2.65) and using the relation in Eq. (2.68) results in a quadratic characteristic equation for a,

$$a^2 + Ba + C = 0 \tag{2.69}$$

where a is the non-dimensional dissipation factor defined as,

$$a = R\left(\frac{\hat{a}h}{c}\right) - i \cdot I\left(\frac{\hat{a}h}{c}\right) \tag{2.70}$$

Operators R and I represent taking real and imaginary parts respectively, and B and C are complex constants dependent on the specific choice of the MLC schemes and wavenumber $\hat{k}$, as given below,

$$B = \sum_{m=-M_1}^{M_2} b_m e^{-imh\hat{k}}, \quad C = -\sum_{l=-L_1}^{L_2} a_l e^{-ilh\hat{k}} \tag{2.71}$$

Equation (2.69) has two complex solutions,

$$a_{1,2} = \frac{-B \pm \sqrt{B^2 - 4C}}{2} \tag{2.72}$$

where one is the physical mode, and the other is spurious mode. The real part $R(a)$ is a dissipation factor which is related to stability and dissipative error, and the imaginary part $I(a)$ is the modified wavenumber and it can reveal the dispersive error. Meanwhile, the exact solution of a can be derived by substituting Eq. (2.62) into Eq. (2.3),

$$a_{exc} = i\hat{k}h = ik \tag{2.73}$$

where k is the non-dimensional wavenumber. Since there are two solutions of a for the new MLC scheme, we use a_1 to represent the physical mode, and a_2 to represent the spurious mode. The physical mode a_1 should be as close as possible to a_{exc} for better accuracy. From the following formula,

$$a_1 - a_{exc} = R(a_1) + i\left(I(a_1) - k\right) \tag{2.74}$$

it is required that $R(a_1)$ is small to reduce dissipative error, and $I(a_1)$ is close to k for small dispersive error. On the other hand, $R(a_1)$ and $R(a_2)$ should be non-positive to ensure the stability of the MLC scheme. Meanwhile, $R(a_2)$ is related to the stiffness of the MLC scheme. If its magnitude is too large, the numerical problem will be too stiff.

Before we present the Fourier analysis results for MLC schemes, the benefit of introducing the derivative layer can be briefly explained through aliasing in the discrete domain. At an arbitrary time, the Fourier mode sampled at the grid point x_i can be represented as,

$$u_i = \hat{u}e^{i(kn+\varphi)} = \hat{u}\left[\cos(kn+\varphi) + i\sin(kn+\varphi)\right] \tag{2.75}$$

where n is the index of grid point x_i, and φ is a time-dependent real number. Without the derivative layer, the Fourier mode with a different wavenumber

$$k_{alias} = k + 2N\pi \tag{2.76}$$

can produce the same samples, where N can be any integer. When the mode is reconstructed from these samples, the reconstructed wavenumber k_{rec} is the k_{alias} with the smallest magnitude. As a result, only the k in $[-\pi, \pi]$ can be corrected reconstructed from the sample values. Specifically, the following relation can be obtained,

$$k_{rec} = \begin{cases} k, & k \in (0, \pi] \\ k - 2\pi, & k \in (\pi, 2\pi] \end{cases} \tag{2.77}$$

Therefore, the wave components with $k > \pi$ cannot be resolved by a mono-layer scheme like conventional finite difference methods, because these waves cannot be represented correctly in the discrete domain. The aliasing is the main reason limiting the marginal resolution of finite difference methods. However, with the introducing of the derivative layer in our MLC schemes, another sample is generated at the grid point x_i,

$$u_i' = k\hat{u}e^{i(kn+\varphi+\pi/2)}/h = k\hat{u}\left[-\sin(kn+\varphi) + i\cos(kn+\varphi)\right]/h \tag{2.78}$$

Because the magnitude of derivatives is dependent on k, Fourier modes with different k's cannot generate the same samples. In another word, the aliasing is avoided. Therefore, the small waves with large k's can also be represented correctly in the discrete domain, which makes it possible

to resolve them with the MLC schemes. More discussion about the spectral resolution is presented in the Fourier analysis results.

Fourier Analysis of the Seventh-Order 2-2-2-2 Scheme

In the first place, the seventh-order 2-2-2-2 scheme is analyzed using the approach presented above. Fig. 2.13 presents the Fourier analysis results for the 2-2-2-2 scheme with a typical α value of 12, where the results of Zhong's sixth-order and fifth-order compact scheme with $\alpha = 0$ and -1, and Zhong's fifth-order explicit scheme with $\alpha = -6$ [21] are also presented for comparison. Here, only physical mode a_1 is plotted for the MLC scheme. Fig. 2.13(a) shows that all these schemes are stable with non-positive dissipation factors. Zhong's sixth-order central scheme with $\alpha = 0$ has no dissipation and coincides with the exact solution. With upwind setting, all schemes become dissipative for large k. Compared with Zhong's explicit scheme, Zhong's compact scheme has smaller dissipation when $k < 2.4$, however, the dissipation grows rapidly and surpass explicit scheme for large k. Both schemes have the largest dissipation when $k = \pi$. On the other hand, the 2-2-2-2 scheme is much less dissipative in all the plotted k range compared with Zhong's compact and explicit schemes, which indicates a better accuracy as well.

Fig. 2.13(b) compares the modified wavenumbers of these schemes, where the straight line represents the exact wavenumber. As expected, Zhong's compact schemes with two different α values have a better resolution than Zhong's explicit scheme. However, the accuracies of these 3 schemes decrease rapidly as k increases and drop to zero at $k = \pi$, which is the maximum resolution that most explicit and compact finite difference scheme can achieve in theory. On the other hand, the 2-2-2-2 scheme shows a very high resolution for $k > \pi$, which is similar to the

resolution of spectral methods. That means the MLC scheme is much more accurate for resolving flow with very small wavelengths. In other words, it can compute the wave solutions accurately with much fewer grid points per period. This advantage in the resolution of the new MLC schemes is due to additional degrees of freedom contained in each grid point, i.e., both the point value and its first derivative. It should be noted that both the seventh-order 2-2-2-2 scheme and Zhong's fifth-order explicit scheme use the explicit formula, but the former is constructed on a five-point grid stencil while the latter needs a seven-point stencil. In other words, the resolution of the 2-2-2-2 scheme is much better on a shorter stencil, which validates the idea that the MLC scheme can reach very high-order accuracy and spectral-like resolution within a compact stencil.

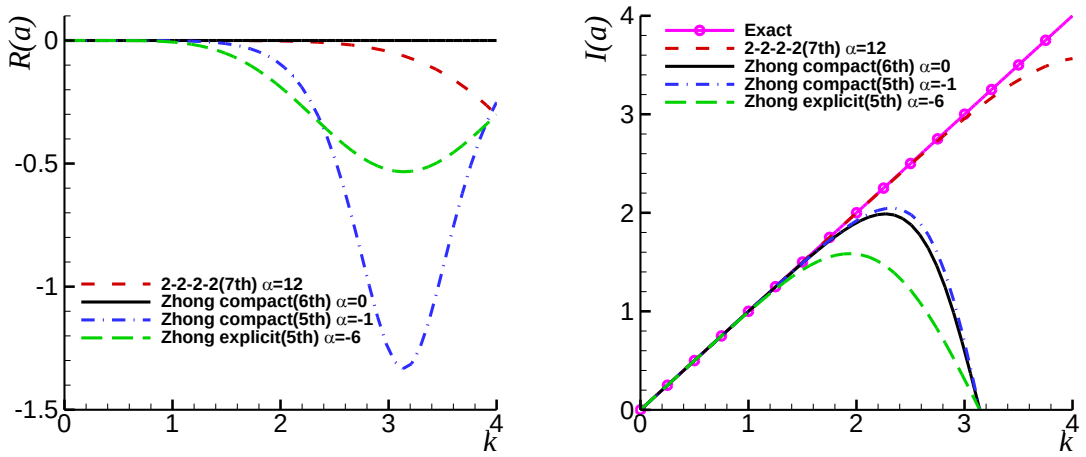

a), dissipation factor b), modified wavenumber

Fig. 2.13. Fourier analysis results of the 2-2-2-2 scheme (7th order), in comparison with Zhong's compact scheme (5th and 6th order) and Zhong's explicit scheme (5th order) [21].

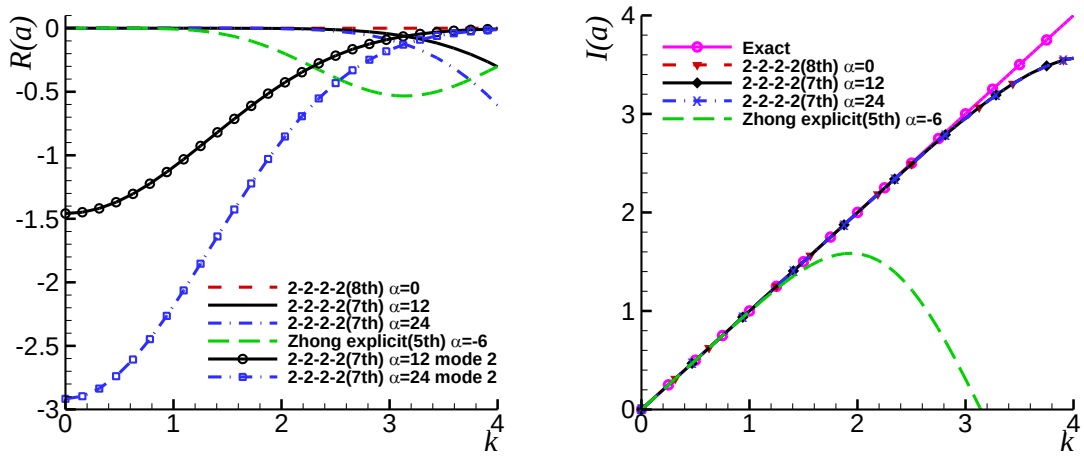

a), dissipation factor b), modified wavenumber

Fig. 2.14. Fourier analysis results of the 2-2-2-2 scheme (7th order) with different upwind coefficients.

The effect of different α values on the accuracy of the 2-2-2-2 scheme are presented. The choice of α has an impact on dissipation, dispersion, and stiffness of the numerical schemes. Fig. 2.14 presents the Fourier analysis results for three different 2-2-2-2 schemes with α = 0, 12, 24, where the result of Zhong's fifth-order explicit scheme with α = -6 is presented for comparison. To analyze the effect of α on stiffness, the dissipation factor of spurious mode – $R(a_2)$ of the 2-2-2-2 scheme is also presented. Different from $R(a_1)$, which are consistent with exact solution for small k and deviate for large k, $R(a_2)$ show large dissipation for small k. This behavior benefits the accuracy of the scheme because the spurious wave will damp out in the simulation when grid resolution is good enough. Another important information revealed by $R(a_2)$ is the restriction on the time step size in the temporal discretization or termed the stiffness of the scheme. It is well known from the numerical analysis theory that $|\hat{a}\Delta t|$ should fall into the stability region of time integration scheme if the resulting ordinary differential equation is discretized by explicit

methods such as Runge-Kutta methods. Since $R(a_2)$ is much larger than $R(a_1)$, $I(a_1)$, and $I(a_2)$ in magnitude when k is small, the stiffness of the scheme is mainly determined by $R(a_2)$. A larger magnitude of $R(a_2)$ indicates a smaller time step size Δt under the same stability condition, i.e., the integral of the resulting ordinary differential equation is more restrictive in terms of choosing time step size. Fig. 2.14 (a) shows that larger upwind coefficient α makes $R(a_2)$ much more dissipative for small k, which should result in more restrictive time step size. In addition, larger α also make $R(a_1)$ more dissipative for large k, which can affect the accuracy when small length wave is important in the flow.

On the other hand, Fig. 2.14 (b) shows that 2-2-2-2 schemes with different upwind coefficients have similar resolutions in terms of wavenumber. All of them are much better than Zhong's fifth-order explicit scheme. In summary, α should be large enough to ensure stability, but not too large to avoid stiffness and keep small dissipation. For seventh-order 2-2-2-2 scheme, $\alpha = 12$ is recommended, although other values of α could also be considered.

Fourier Analysis of the Third-Order 1-1-1-1 Scheme

In the next place, the third-order 1-1-1-1 scheme is analyzed and the impact of different values of α is discussed. Fig. 2.15 presents the Fourier analysis results of two different 1-1-1-1 schemes with $\alpha = 1.5$ and 3, where results of the seventh-order 2-2-2-2 scheme with $\alpha = 12$ and Zhong's fifth-order explicit scheme with $\alpha = -6$ are also presented for comparison. Same as Fig. 2.14, dissipation factors of both physical and spurious modes – $R(a_1)$ and $R(a_2)$ are plotted to show dissipation and stiffness of the 1-1-1-1 scheme, and modified wavenumber of spurious mode – $I(a_1)$ is plotted to show resolution. Fig. 2.15 (a) shows that the 1-1-1-1 schemes with both

α values have larger dissipation factors than the 2-2-2-2 scheme, as well as errors in modified wavenumber showed in Fig. 2.15 (b). This is reasonable that high-order MLC scheme is more accurate than low-order MLC scheme considering both dissipative and dispersive errors. Furthermore, Fig. 2.15 (b) indicates the third-order 1-1-1-1 scheme has a much better resolution for large k than Zhong's fifth-order explicit scheme though the former is two orders lower than the latter. This advantage can be explained by the additional degrees of freedom contained on each grid points. In addition, Fig. 2.15 (a) shows that the 1-1-1-1 scheme has smaller dissipation than Zhong's explicit scheme for a wide range of k as well. Specifically, the 1-1-1-1 scheme with $\alpha = 3$ are less dissipative than Zhong's fifth-order explicit scheme when $k < 2.8$; and the 1-1-1-1 scheme with $\alpha = 1.5$ are less dissipative than Zhong's fifth-order explicit scheme when $k < 3.4$, which covers the entire significant range $[0, \pi]$ of conventional finite difference scheme.

Increasing upwind coefficients α introduces more dissipation for both $R(a_1)$ and $R(a_2)$ as Fig. 2.15 (a) shows. Meanwhile, increasing α also decreases the resolving ability slightly as observed in Fig. 2.15 (b). So, larger α makes the 1-1-1-1 scheme less accurate. Similar to the discussion for the 2-2-2-2 scheme, the magnitude of $R(a_2)$ affects the stiffness of the problem, which indicates an increase of α leads to increase of stiffness. On the other hand, α should be large enough to ensure stability. Considering stability, accuracy, and stiffness, the recommended value for α is 1.5 for third-order 1-1-1-1 scheme. Again, other values could also be considered.

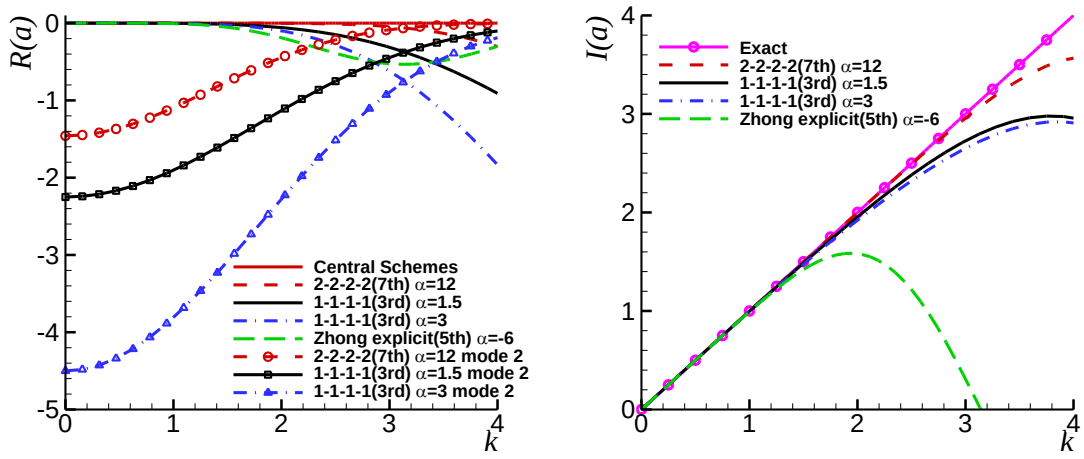

a), dissipation factor b), modified wavenumber

Fig. 2.15. Fourier analysis results of the 1-1-1-1 scheme (3rd order) with different upwind coefficients.

Fourier Analysis of MLC Schemes on Bias Stencils

MLC schemes with bias grid stencils including the 2-1-2-1, 2-1-1-1 and 1-1-2-1 schemes are also analyzed using Fourier analysis approach. Formulas of these schemes can be found in Appendix A.1. These MLC schemes follow traditional upwind schemes, where the bias stencil introduces enough numerical dissipation to control the aliasing errors and to enhance the numerical stability [21]. On the other hand, the upwind MLC schemes follow Zhong's upwind compact and explicit scheme [21] by using the centered stencil with an adjustable parameter α in the leading dissipative truncation term. Fig. 2.16 compares the Fourier analysis results of the sixth-order 2-1-2-1 scheme, the fifth-order 2-1-1-1 scheme, and the fifth-order 1-1-2-1 scheme on bias stencils, where the seventh-order 2-2-2-2 scheme on the centered stencil with α = 12 is also presented for comparison. Only physical mode a_1 is plotted to compare accuracies. Fig. 2.16

(b) shows that all the schemes have a spectral-like resolution. Specifically, the seventh-order 2-2-2-2 scheme on centered stencil has better resolution than the fifth-order 2-1-1-1 and 1-1-2-1 schemes on bias stencils, but worse than the sixth-order 2-1-2-1 scheme on bias stencil. However, Fig. 2.16 (a) shows the 2-1-2-1 scheme has the largest dissipation among all schemes while the 2-2-2-2 scheme has the smallest dissipation. Overall, the upwind 2-2-2-2 scheme is more favorable, because it has the smallest dissipation and very good spectral resolution, although lower than the resolution of the 2-1-2-1 scheme for large *k*. This observation is consistent with the conclusion in [21] that upwind scheme on centered grid stencil have smaller dissipation than those on upwind-bias grid stencil. As for the comparison of fifth-order 2-1-1-1 scheme which has bias stencil on the value layer, and fifth-order 1-1-2-1 scheme which has bias stencil on the derivative layer, there is no much difference except the latter is slightly more dispersive and less dissipative. Therefore, using bias stencil on value layer introduces slightly larger dissipation than the bias setting for the derivative layer.

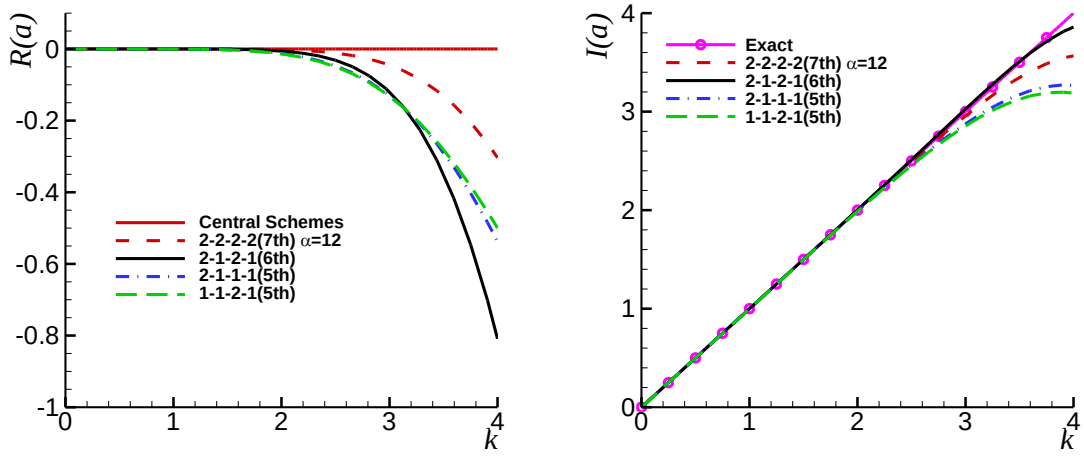

a), dissipation factor b), modified wavenumber

Fig. 2.16. Comparison of the MLC schemes on the centered and bias stencils.

Fig. 2.17 presents $R(a_1)$ and $R(a_2)$ together for the three MLC schemes on bias stencils to compare the stiffness of these different MLC schemes. The 2-1-2-1 scheme which uses bias stencil on both value and derivative layers have the largest dissipation in $R(a_1)$ and $R(a_2)$; the 2-1-1-1 scheme which uses bias stencil on the value layer has slightly larger dissipation than the 1-2-1-1 scheme which uses bias stencil on the derivative layer. Therefore, using bias stencil introduces larger dissipation in both $R(a_1)$ and $R(a_2)$, and its effect is more obvious when applied to the value layer. In addition, using bias stencil on both the value and derivative layer may introduce too much dissipation in $R(a_2)$. For example, the maximum magnitude of $R(a_2)$ is about 3.9 for 2-1-2-1 scheme. As comparison, the maximum is about 1.5 for the 2-2-2-2 scheme with α = 12 in Fig. 2.14 (a), and it is about 2.2 for 1-1-1-1 scheme with α = 1.5 in Fig. 2.15 (a). As a result, the 2-1-2-1 scheme requires smaller time step size in temporal discretization. From the above analysis, it is more appropriate to construct upwind MLC schemes on centered stencils considering stability, dissipation, and stiffness. In fact, the 2-1-1-1 and 1-1-2-1 schemes can be considered as special cases on centered stencils with some large values of α, as mentioned in Section 2.1.

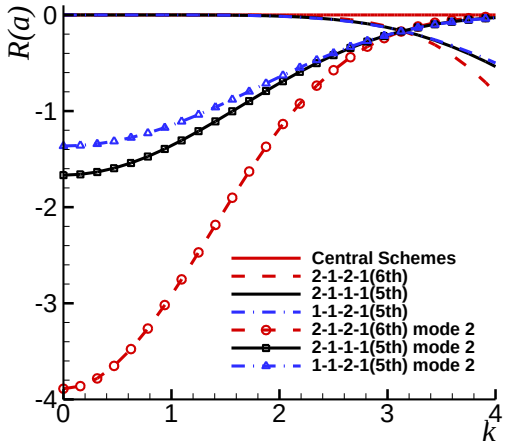

Fig. 2.17. Dissipation factors of physical and spurious modes of the MLC schemes on bias stencils.

Fourier Analysis of Pure Upwind MLC Schemes

In conventional finite difference methods, stable upwind schemes can be derived on one-sided bias stencils. For example, a second-order upwind scheme

$$u_i' = \frac{1}{2h}\left(u_{i-2} - 4u_{i-1} + 3u_i\right) \tag{2.79}$$

can be derived by using two points on the upwind side. However, the fourth-order 2-0-2-0 scheme constructed on the similar stencil is unstable. Fig. 2.18 shows the Fourier analysis results of the 2-0-2-0 scheme and other unstable pure upwind MLC schemes, where the results of the seventh-order 2-2-2-2 scheme with α = 12 is also presented for comparison. Here, only physical mode a_1 is plotted for the MLC schemes. Fig. 2.18 (a) shows that the MLC schemes on one-sided bias stencils has positive $R(a_1)$'s which indicate instability of these schemes. The numerical instability increases with the rising order of accuracy. Fig. 2.18 (b) shows their modified wavenumber $I(a_1)$'s fall on the other side of the exact solution for large k's, which is different from the 2-2-2-2 scheme. The spectral resolution of the pure upwind MLC schemes are also not as good as the 2-2-2-2 scheme.

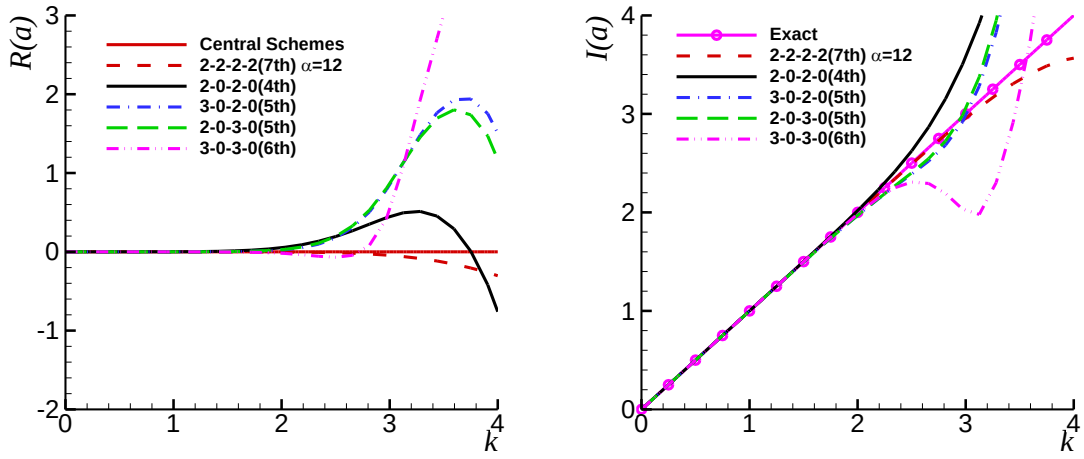

a), dissipation factor b), modified wavenumber

Fig. 2.18. Fourier analysis results of the unstable MLC schemes on one-sided bias stencils.

The instability of the pure upwind MLC schemes is unexpected because one-sided stencils usually leads to stable schemes in conventional finite difference methods. However, the MLC scheme introduces additional degrees of freedom which makes numerical stability more complicated. It is discovered through further Fourier analysis that the stability of the pure upwind MLC scheme is affected by the imbalance level of the stencils. Fig. 2.19 (a) shows that the 1-0-1-0, 2-0-1-0, and 1-0-2-0 schemes are stable, which have less imbalance than the 2-0-2-0 scheme or other pure upwind schemes in Fig. 2.18. However, the $R(a_2)$ of these pure upwind MLC schemes show much larger dissipations for small k's compared with previous examples (see Fig. 2.14, Fig. 2.15, Fig. 2.17), which should result in more restrictive time step sizes. Fig. 2.19 (b) shows that their dispersive error is also larger, and the spectral resolution reduces with the increasing imbalance level. On the other hand, any pure upwind MLC scheme with fourth or higher order of accuracy are proven to be unstable through Fourier analysis, as shown in Fig. 2.18. Therefore, the stability and accuracy of pure MLC scheme are very sensitive to the

imbalance level of stencils, and very high-order MLC scheme cannot be derived on one-sided bias stencils.

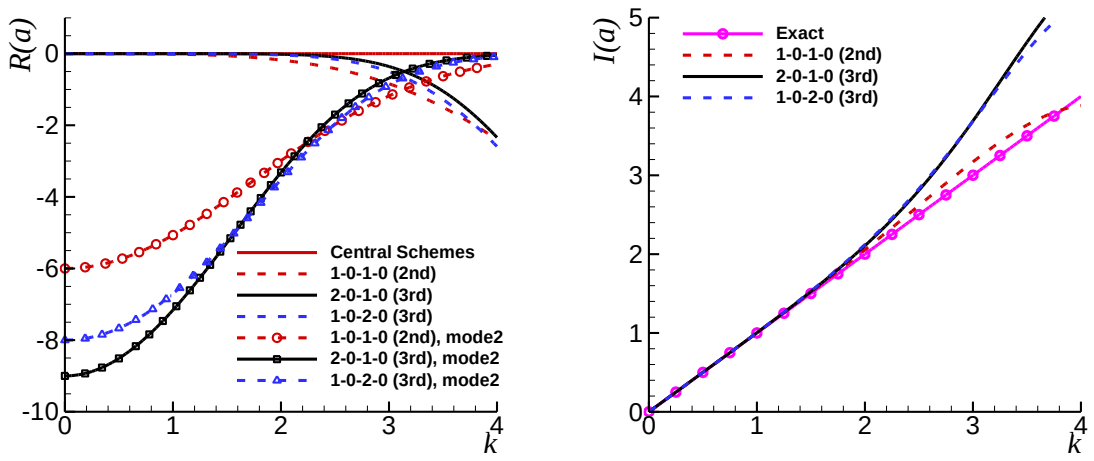

a), dissipation factor b), modified wavenumber

Fig. 2.19. Fourier analysis results of the stable MLC schemes on one-sided bias stencils.

In summary, the one-dimensional Fourier analysis in this section shows that: 1) the stable MLC scheme can be constructed on centered stencils with upwind coefficients α, or on upwind bias stencils; 2) it has very high resolution, small dissipative and dispersive errors, reasonable stiffness. Comparison of the 1-1-1-1 scheme and Zhong's fifth-order explicit scheme indicates even lower order MLC scheme can have better resolution and smaller dissipation than conventional higher-order scheme; 3) the value of α has an impact on the stability, accuracy, and stiffness of the MLC scheme. The recommended value of α is 12 for the seventh-order 2-2-2-2 scheme and 1.5 for the third-order 1-1-1-1 scheme; 4) using upwind bias stencils for MLC schemes introduces larger dissipation than using a centered stencil and adjustable parameter α, and pure upwind MLC schemes with fourth or higher order of accuracy are unstable.

2.4.2 Two-Dimensional Fourier Analysis

The dissipation and dispersive errors of the upwind MLC schemes applied to two-dimensional advection equation (2.28) are also investigated by the Fourier analysis. For multi-dimensional simulations, the approximation of the cross derivative terms given in Eq. (2.29) could lead to different stability and dissipative properties of the numerical scheme from the one-dimensional analysis. The discretization is based on Cartesian coordinates here. To be generic, the convection angle θ and Fourier wave angle φ are defined in the Fourier analysis. The governing equations are the same as Eq. (2.28), where the dimensional wave speed can be written as,

$$\begin{aligned} c_1 &= c \cdot \cos\theta \\ c_2 &= c \cdot \sin\theta \end{aligned} \tag{2.80}$$

which are functions of convection angle θ and the magnitude of wave speed c. Fourier analysis is carried out by assuming the solution in the following form,

$$\begin{bmatrix} u \\ u_x \\ u_y \end{bmatrix} = \begin{bmatrix} \hat{u} \\ \hat{u}_x \\ \hat{u}_y \end{bmatrix} e^{\hat{a}t + i\hat{k}(x\cos\varphi + y\sin\varphi)} \tag{2.81}$$

where φ is an arbitrary Fourier wave angle, the definitions of $\hat{k}$ and $\hat{a}$ are the same as one-dimensional analysis. The procedure of the two-dimensional Fourier analysis follows the same methodology as in one-dimensional analysis. Substituting the trial solution above into Eq. (2.28), a relation between $\hat{u}$, $\hat{u}_x$ and $\hat{u}_y$ can be obtained as,

$$\hat{u} = -\frac{c}{\hat{a}}\left(\hat{u}_x \cos\theta + \hat{u}_y \sin\theta\right) \tag{2.82}$$

Applying the approximations of second and cross derivatives in Eqs. (2.9) and (2.29), a cubic characteristic equation of the non-dimensional dissipation factor a defined in Eq. (2.70) can be derived,

$$a^3 + Ba^2 + Ca + D = 0 \tag{2.83}$$

Same as one-dimensional analysis, B, C, and D are complex constants dependent on the choice of the finite difference formulas and wavenumber $\hat{k}$. Meanwhile, they are also functions of θ and φ in two-dimensional analysis as given below,

$$\begin{aligned}
B &= \left(B_2 + B_3\right)\sin\theta + \left(B_1 + C_3\right)\cos\theta \\
C &= \left(B_2B_3 - A_2\right)\sin^2\theta + \left(B_1C_3 - A_1\right)\cos^2\theta + \left(\frac{1}{2}B_1B_2 - A_3\right)\sin 2\theta \\
D &= \left[A_2\left(C_3 - B_1\right) - B_2A_3\right]\sin^2\theta\cos\theta - A_2B_3\sin^3\theta \\
&\quad + \left[A_1\left(B_3 - B_2\right) - B_1A_3\right]\sin\theta\cos^2\theta - A_1C_3\cos^3\theta
\end{aligned} \tag{2.84}$$

and

$$\begin{aligned}
A_1 &= \sum_{l=-L_1}^{L_2} a_l e^{ilh\hat{k}\cos\varphi}, \qquad A_2 = \sum_{l=-L_1}^{L_2} a_l e^{ilh\hat{k}\sin\varphi} \\
B_1 &= \sum_{m=-M_1}^{M_2} b_m e^{imh\hat{k}\cos\varphi}, \quad B_2 = \sum_{m=-M_1}^{M_2} b_m e^{imh\hat{k}\sin\varphi} \\
A_3 &= \sum_{\substack{l_x=-L_1 \\ l_y=-L_1}}^{L_2} a_{l_x,l_y} e^{ih\hat{k}\left(l_x\cos\varphi + l_y\sin\varphi\right)} \\
B_3 &= \sum_{\substack{m_x=-M_1 \\ m_y=-M_1}}^{M_2} b_{m_x,m_y} e^{ih\hat{k}\left(m_x\cos\varphi + m_y\sin\varphi\right)} \\
C_3 &= \sum_{\substack{n_x=-M_1 \\ n_y=-M_1}}^{M_2} c_{n_x,n_y} e^{ih\hat{k}\left(n_x\cos\varphi + n_y\sin\varphi\right)}
\end{aligned} \tag{2.85}$$

Three roots of Eq. (2.83) correspond to one physical mode a_1 and two spurious modes a_2, a_3. The real and imaginary part of a plays the same role as in one-dimensional analysis. The exact solution of a is,

$$a_{exc} = i\hat{k}h\cos(\theta - \varphi) = ik\cos(\theta - \varphi) \tag{2.86}$$

which is a product of one-dimensional exact solution in Eq. (2.73) and a cosine function of θ and φ.

In the two-dimensional Fourier analysis as well as two-dimensional numerical simulations presented later, the one-dimensional MLC schemes with recommended α values are used for the

approximation of second derivatives, while cross derivatives are discretized by the two-dimensional MLC schemes with one order higher of accuracy than the one-dimensional scheme. Therefore, the overall accuracy depends on one-dimensional MLC schemes. Different θ and φ are considered in the two-dimensional Fourier analysis.

The two-dimensional Fourier analysis is first carried out to the third-order 1-1-1-1 scheme with $\alpha = 1.5$ as given in Eqs. (2.8) and (2.30). Fig. 2.20(a) presents the dissipation factors for the case of $\theta = 0$, and Fig. 2.20(b) shows results for the case of $\theta = \pi/4$. For each case of θ, two cases of φ are compared which also have the values of 0 and $\pi/4$. All three modes are presented, where a_1 is the physical mode and a_2, a_3 are two spurious modes. The figure shows a_1 and a_2 behave similarly as those of one-dimensional Fourier analysis, while a_3 is the distinctive mode for two-dimensional Fourier analysis. When both θ and φ are 0, the results are the same with one-dimensional Fourier results in Fig. 2.15. The value of $R(a_3)$ depends on both θ and φ. When θ is zero, it is always zero which means spurious mode will keep its initial condition during the simulation. When θ is not zero but φ is zero, $R(a_3)$ is a negative constant which means the spurious mode will be evenly decayed for all the wavenumbers. When both θ and φ is not zero, a_3 behaviors similarly to a_2. Overall, all three modes are stable in two-dimensional Fourier analysis. Similar to one-dimensional analysis, stiffness is dominated by spurious modes.

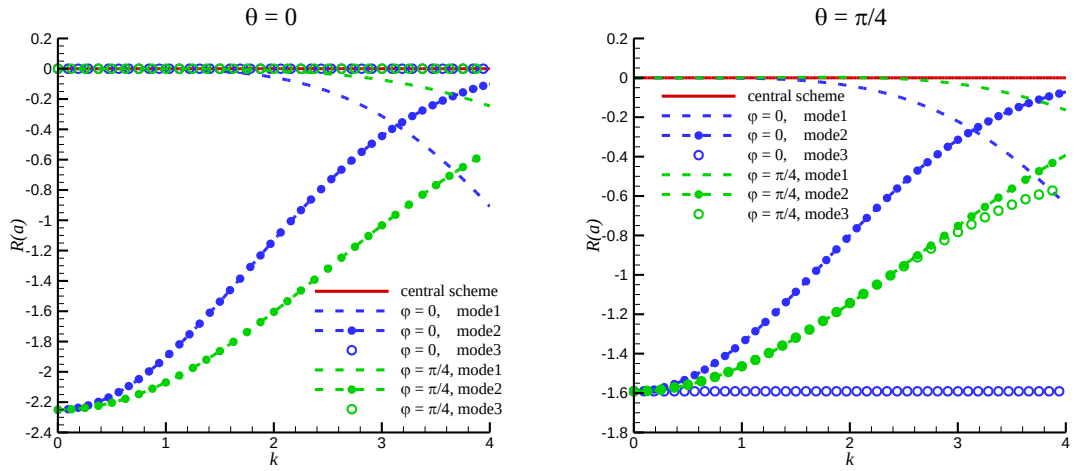

a), wave propagation in direction of $\theta = 0$ b), wave propagation in direction of $\theta = \pi/4$

Fig. 2.20. Dissipation factor $R(a_1)$, $R(a_2)$, $R(a_3)$ of the 1-1-1-1 scheme (3rd order) for two-dimensional wave propagation.

The modified wavenumber of physical mode $I(a_1)$ for the same 1-1-1-1 scheme is shown in Fig. 2.21. It should be mentioned that the spurious modes a_2 and a_3 do not affect accuracy significantly. Even though they affect the stiffness of the problem, the amplitudes of $R(a_2)$, $R(a_3)$ are much larger than those of $I(a_2)$, $I(a_3)$. Therefore, only $I(a_1)$ is plotted in two-dimensional Fourier analysis. In the figures, all the results with different combinations of θ and φ show a good resolution of the scheme for small k. When θ is zero as shown in Fig. 2.21 (a), the scheme has the best resolution. Comparing the results of (a) and (b), we can observe that the accuracy is reduced when $\theta = \pi/4$. In fact, it is true for all non-zero θ, and this property is well known as the anisotropic error of finite difference methods for multi-dimensional simulations. However, Fig. 2.21 indicates that the difference is relatively small for the MLC scheme. This favorable property is probably because our MLC schemes take information from neighboring points in all different

orientations in the approximation of cross derivatives3. On the other hand, changing of φ does not have an obvious effect on the spectral resolution.

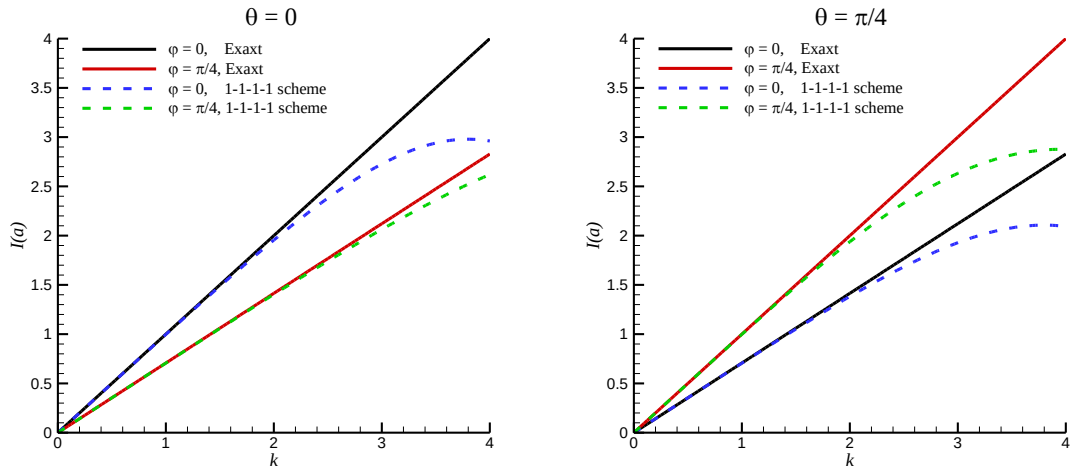

a), wave propagation in direction of $\theta = 0$ b), wave propagation in direction of $\theta = \pi/4$

Fig. 2.21. Modified wavenumber $I(a_1)$ of the 1-1-1-1 scheme (3rd order) for two-dimensional wave propagation.

The two-dimensional Fourier analysis is then carried out to the seventh-order 2-2-2-2 scheme with $\alpha = 12$ as given in Eqs. (2.11) and (2.31). Dissipation factors of all three modes are presented in Fig. 2.22, and modified wavenumber of physical mode a_1 is shown in Fig. 2.23. Comparing Fig. 2.20 and Fig. 2.22, we observe that all modes of the 2-2-2-2 scheme are less dissipative than those of 1-1-1-1 scheme. Comparing Fig. 2.21 and Fig. 2.23, we can see the resolution of the 2-2-2-2 scheme for large k is better than that of the 1-1-1-1 scheme. Both aspects indicate 2-2-2-2 scheme is much more accurate than the 1-1-1-1 scheme in two-dimensional simulations. In addition, similar effects of θ and φ on the resolution as 1-1-1-1 scheme can be observed in the results of the 2-2-2-2 scheme which indicates the anisotropic error is still very small.

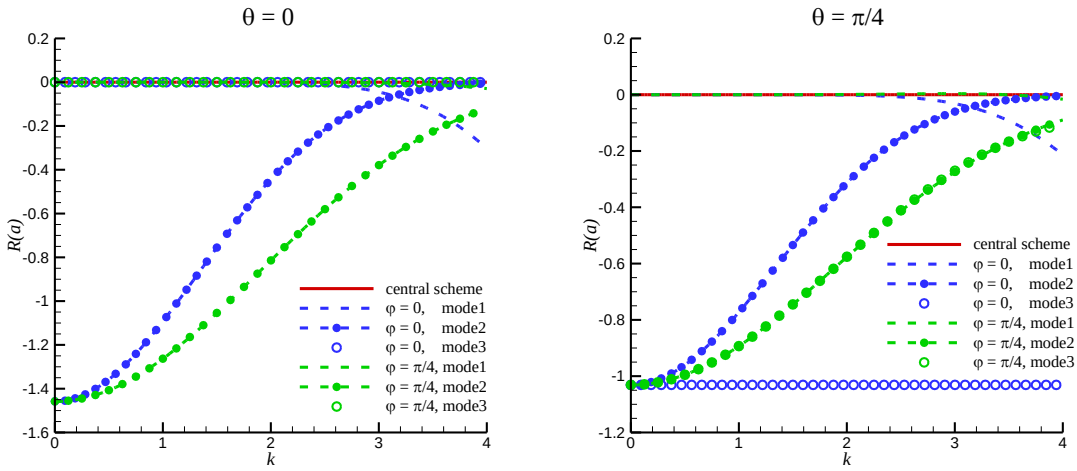

a), wave propagation in direction of $\theta = 0$ b), wave propagation in direction of $\theta = \pi/4$

Fig. 2.22. Dissipation factor $R(a_1)$, $R(a_2)$, $R(a_3)$ of the 2-2-2-2 scheme (7th order) for two-dimensional wave propagation.

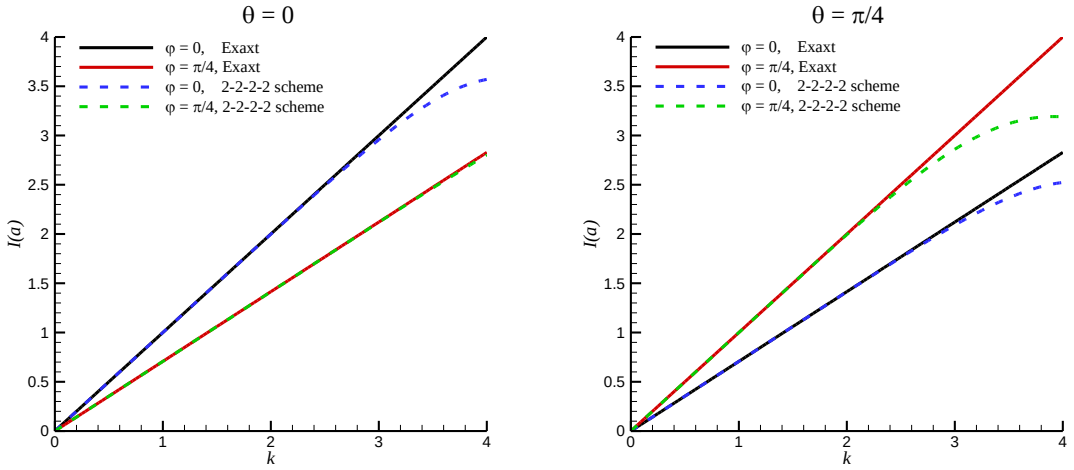

a), wave propagation in direction of $\theta = 0$ b), wave propagation in direction of $\theta = \pi/4$

Fig. 2.23. Modified wavenumber $I(a_1)$ of the 2-2-2-2 scheme (7th order) for two-dimensional wave propagation.

2.4.3 Anisotropic Analysis of Phase Speed

In order to further investigate the anisotropy, the phase speed (c_p) of MLC schemes is computed and analyzed, where c_p is defined as,

$$c_p(k,\theta) = \frac{I\left(a(k,\theta,\varphi)\right)}{k}, \text{ and } \varphi = \theta \tag{2.87}$$

where a is a function of wavenumber k, convection angle θ, and Fourier wave angle φ. The two-dimensional Fourier analysis above has shown that the effect of φ on the spectral resolution is not obvious. Therefore, we can follow Lele's approach[20] in the anisotropy analysis by assuming θ and φ have the same value. For conventional finite difference methods, c_p can be computed from the modified wavenumber k' in one-dimensional Fourier analysis as,

$$c_p(k,\theta) = \frac{\cos\theta k'(k\cos\theta) + \sin\theta k'(k\sin\theta)}{k} \tag{2.88}$$

where $k'(x)$ is a function determined by coefficients of a finite difference scheme [20].

Fig. 2.24 compares the phase speed of various upwind MLC schemes and Zhong's upwind explicit and compact schemes [21]. The phase speed contours are plotted in the range of $k = [0, \pi]$ and $\theta = [0, 2\pi]$, where each curve represents a fixed value of k. The exact value of c_p is 1 for any k and θ, which corresponds to the outer circle in the plots. Two properties can be shown from the figure; the distorted shape from a perfect circle represents the anisotropic error, and the shrink of the circle represents the dispersive error. Small k values correspond to outer contours, and contours for large k values are in the middle. As k increases from 0 to π, both anisotropic and dispersive errors increase. For a conventional finite difference scheme, the innermost curve drops to the center indicating that $k = \pi$ is the limit of spectral resolution of the scheme. Among Zhong's explicit scheme (a), (b), (c) and compact scheme (d), the fifth-order compact scheme (d) has the smallest anisotropic error which is consistent with the conclusion of Lele [20]. In the

results of MLC schemes (e), (f), (g), both the anisotropic error and dispersive error are much smaller than conventional finite difference schemes for any k and θ.

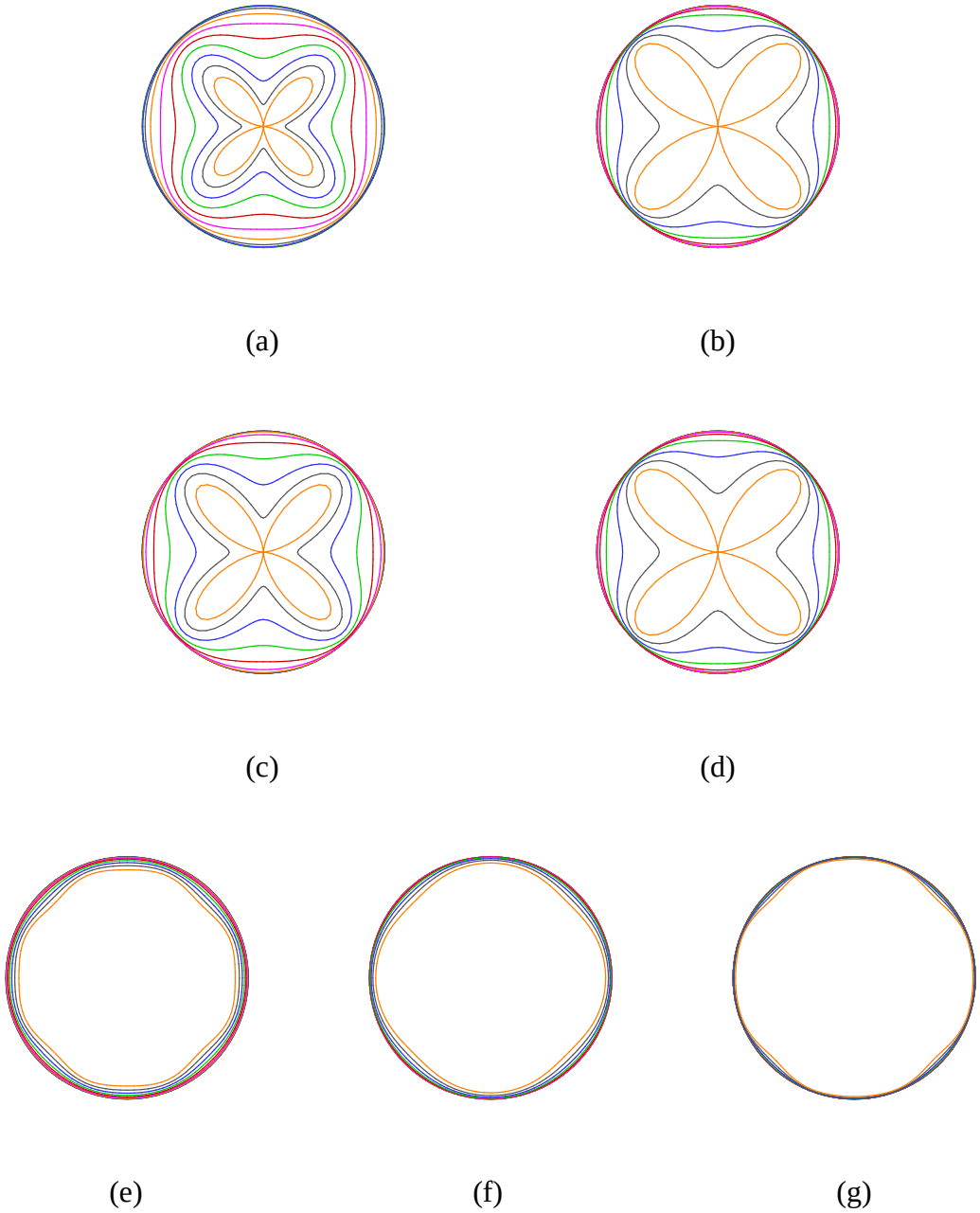

Fig. 2.24. Polar plot of phase speed anisotropy (contours are plotted at k/π = 1/50, 5/50, …, 45/50, 50/50): (a) Zhong's third-order explicit scheme; (b) Zhong's fifth-order explicit scheme; (c) Zhong's seventh-order explicit scheme; (d) Zhong's fifth-order compact scheme; (e) the

third-order 1-1-1-1 scheme; (f) the fifth-order 2-2-1-1 scheme; (g) the seventh-order 2-2-2-2 scheme.

In summary, the two-dimensional Fourier analysis in this section shows that the MLC schemes maintain very high resolution, small dissipative and dispersive errors after extended to two-dimensional cases. The anisotropy analysis indicates that anisotropic errors of current MLC schemes are much smaller than conventional finite difference schemes, which is very important in multi-dimensional flow simulations.

2.4.4 Comparison with Discontinuous-Galerkin (DG) methods

Recently, Discontinuous-Galerkin (DG) methods have received more attentions because of their high accuracy, good parallel computing efficiency, and flexibility to complex geometry with unstructured mesh. In this section, the proposed upwind MLC scheme is compared with DG methods of Cockburn and Shu [16] by Fourier analysis. Other versions of DG methods will behavior similarly. For simplicity, the derivation of DG methods on uniform structured mesh is given here. A complete derivation can be find [16].

DG methods use high-order piecewise polynomials to represent the flow quantities within each element and solve numerical fluxes on element interfaces. Orthogonal basis functions are usually utilized to construct the high-order piecewise polynomials. Standard Legendre polynomial of degree l with respect to x has the form,

$$P^{(l)}(x) = C_0^{(l)} + C_1^{(l)} x + \ldots + C_l^{(l)} x^l = \sum_{j=0}^{l} C_j^{(l)} x^j \tag{2.89}$$

where x is the local coordinate with range of [-1, 1]. $C_j^{(l)}$ are coefficients only dependent on l. Eq. (2.89) can also be written in matrix and vector form as,

$$\mathbf{P}(x) = \mathbf{A} \cdot \mathbf{x} \tag{2.90}$$

where $\mathbf{P}(x) = (P^{(0)}(x), P^{(1)}(x),\ldots, P^{(n)}(x))^T$, $\mathbf{x} = (1, x,\ldots, x^{(n)})^T$, and $\mathbf{A}$ is the lower triangular matrix containing $C_j^{(l)}$ constants, the elements up to $n = 5$ are given here,

$$\mathbf{A} = \begin{bmatrix} 1 & 0 & 0 & 0 & 0 & 0 \\ 0 & 1 & 0 & 0 & 0 & 0 \\ -\frac{1}{2} & 0 & \frac{3}{2} & 0 & 0 & 0 \\ 0 & -\frac{3}{2} & 0 & \frac{5}{2} & 0 & 0 \\ \frac{3}{8} & 0 & -\frac{30}{8} & 0 & \frac{35}{8} & 0 \\ 0 & \frac{15}{8} & 0 & -\frac{70}{8} & 0 & \frac{63}{8} \end{bmatrix} \tag{2.91}$$

The dimension for $\mathbf{P}(x)$, $\mathbf{x}$ and $\mathbf{A}$ is $(n+1)$, $(n+1)$, and $(n+1) \times (n+1)$ respectively.

In a computational cell i, Legendre polynomials are used as basis to represent the dependent variable $u_i(x, t)$ as follows,

$$u_i(x,t) = \sum_{l=0}^{n} u_i^{(l)}(t) P^{(l)}(x) = \mathbf{u}_i(t) \cdot \mathbf{P}(x) \tag{2.92}$$

where n is highest degree of Legendre polynomials, $u_i^{(l)}$ are the weight of the Legendre polynomial of degree l. $u_i(x, t)$ can also be represented in matrix form, where $\mathbf{u}_i(t) = (u_i^{(0)}(t), u_i^{(1)}(t),\ldots, u_i^{(n)}(t))$. Hence, $\mathbf{u}_i(t)$ contains all the unknowns for cell i which has $n+1$ degrees of freedom. It should be noticed that in the Nth-order DG methods, $N = n+1$, so the number of unknowns in each cell equals to the order of accuracy. If $N = 1$, the only unknown is $u_i^{(0)}(x)$ and DG methods recovers to first-order finite volume methods.

Same as the MLC schemes, the discretization of DG methods is demonstrated using the one-dimensional linear advection equation. Weak form of the advection equation is derived by first multiplying Legendre polynomials $P^{(l)}(x)$ with different degrees to advection equation in Eq. (2.1) and then integrating x from -1 to 1 in each cell,

$$\frac{d}{dt}\int_{-1}^{1} P^{(l)}(\xi) u_i(\xi,t)\, d\xi + c\int_{-1}^{1} P^{(l)}(\xi) \frac{\partial}{\partial \xi}\left[u_i(\xi,t)\right] d\xi = 0 \tag{2.93}$$

Substituting Eq. (2.92) into Eq. (2.93), then integrating the convection term by part and applying the orthogonality of Legendre polynomials,

$$\int_{-1}^{1} P^{(l)}(\xi) P^{(m)}(\xi) d\xi = \begin{cases} \dfrac{2}{2l+1} = \gamma^{(l)}, & m = l \\ 0, & m \neq l \end{cases} \tag{2.94}$$

the weak form equation can be derived as follows,

$$\gamma^{(l)} \cdot \frac{d}{dt} u_i^{(l)}(t) + c\left[P^{(l)}(1) u_i(1,t) - P^{(l)}(-1) u_i(-1,t) \right] - c\int_{-1}^{1} u_i(\xi,t) \frac{d}{d\xi}\left(P^{(l)}(\xi) \right) d\xi = 0 \tag{2.95}$$

It should be noticed that $u_i(1, t)$, $u_i(-1, t)$ are the boundary function values, which are discontinuous in cell interfaces. For linear advection equation, simple upwind setting is ideal and physical, while numerical fluxes need to be solved in nonlinear equations such as the Euler or Navier-Stokes equations. The derivative of Legendre polynomials in the last term of Eq. (2.95) can be easily represented in matrix form,

$$\frac{d}{dx}\mathbf{P}(x) = \mathbf{C} \cdot \mathbf{P}(x) \tag{2.96}$$

where **C** is a constant matrix as the operator. Combining Eqs. (2.92), (2.95), (2.96) and applying orthogonality of Legendre polynomials again, an ordinary differential equation system for cell *i* in Eq. (2.97) can be derived as,

$$\mathbf{E}\frac{d}{dt}\mathbf{u}_i(t) + c\left[\mathbf{P}(1) u_i(1,t) - \mathbf{P}(-1) u_i(-1,t) - \mathbf{D} \cdot \mathbf{u}_i(t) \right] = 0 \tag{2.97}$$

Again, both **E** and **D** is constant matrix which can be acquired with some algebraic operation.

Finally, simple upwind idea is applied to the boundary value $u_i(1, t)$, $u_i(-1, t)$, i.e., all the boundary values are determined from the left cell. Then,

$$\begin{aligned} u_i(1,t) &= \mathbf{u}_i(t) \cdot \mathbf{P}(1) \\ u_i(-1,t) &= u_{i-1}(1,t) = \mathbf{u}_{i-1}(t) \cdot \mathbf{P}(1) \end{aligned} \tag{2.98}$$

Substituting Eq. (2.98) into Eq. (2.97), a system of semi-discrete equations is derived as follows,

$$\frac{d}{dt}\mathbf{u}_i(t) = c\left[\mathbf{H}\cdot\mathbf{u}_i(t) - \mathbf{K}\cdot\mathbf{u}_{i-1}(t)\right] \tag{2.99}$$

The formula resembles a finite difference approximation but containing the coefficient matrix **H** and **K**. After **H** and **K** are derived, which are constant matrices, it's straightforward to perform Fourier analysis on DG methods. Also, it's easy to conduct numerical simulation for one-dimensional linear wave propagation using Eq. (2.99). For non-uniform grids, a coordinate transformation is needed and Eq. (2.99) can be applied in computational domain.

Fourier analysis on DG methods has similar procedures with the MLC schemes. The difference is that for DG methods with third-order or higher accuracy, there are more degrees of freedom than our MLC schemes. So, it's more general to use matrix form for the trial Fourier solution as follows,

$$\mathbf{u}(x,t) = \hat{\mathbf{u}}e^{\left(\hat{a}t + i\hat{k}x\right)} \tag{2.100}$$

Discrete form on uniform mesh is,

$$\mathbf{u}_i(t) = \hat{\mathbf{u}}e^{\left(\hat{a}t + i\hat{k}x_i\right)}, \quad \mathbf{u}_{i-1}(t) = \hat{\mathbf{u}}e^{\left(\hat{a}t + i\hat{k}(x_i - h)\right)} \tag{2.101}$$

where h is the grid spacing. Substituting Eq. (2.101) into Eq. (2.99) and following the same methodology as in Section 2.4.1, the approximate value of $a = \frac{\hat{a}h}{c}$ can be solved.

The Nth-order DG methods (DG-N) has N degrees of freedom which leads to N complex roots of a. As a result, there are a total of N Fourier modes including one physical mode and N-1 spurious modes.

The Fourier analysis results of second-order DG methods (DG-2) are shown in Fig. 2.25. Same as our MLC schemes, DG-2 have two degrees of freedom in each cell. One physical and one spurious mode are observed. For all DG methods, the dissipation factor of physical mode always starts from 0 and spurious modes always have negative dissipation factor in small

wavenumber region, which is consistent with our MLC schemes. In Fig. 2.25 (a), both modes have non-positive dissipation factors in the entire wavenumber region, which means DG-2 is stable. However, the dissipation is very large. In Fig. 2.25 (b), the modified wavenumber for physical mode overlaps on the exact solution (solid line) in a very wide wavenumber region, indicating that the resolving ability for large wavenumber region is very good even though the scheme is only second order.

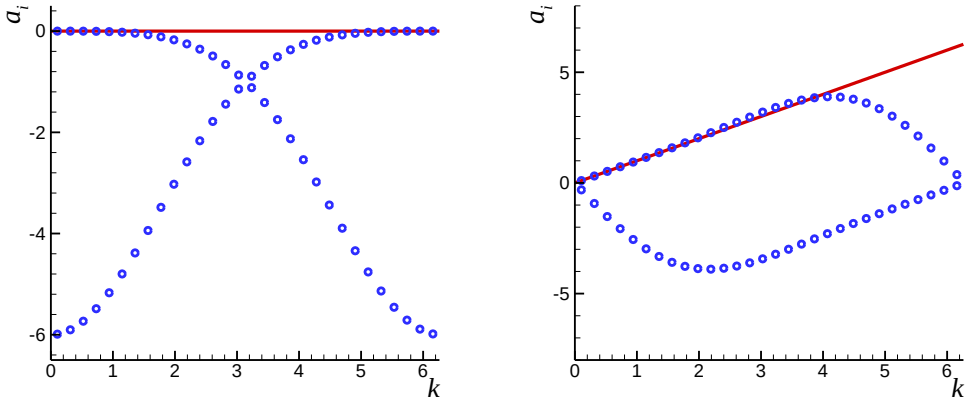

a), dissipation factor b), modified wavenumber

Fig. 2.25. Fourier analysis results of the DG-2 scheme.

Fig. 2.26 shows the results of third-order DG methods (DG-3), different from DG-2 and our MLC scheme. A second spurious mode is observed and it's very dissipative with a minimum value of -12 in dissipation factor. As comparison, the lowest point for 1-1-1-1 scheme with α = 1.5 is -2.2 and that for 2-2-2-2 scheme with α = 12 is -1.5. It is mentioned in the analysis above that the largest magnitude of $R(a)$ has impact on the time step size. Hence, based on Fourier results, DG-3 should have much more restrictive stability condition on Δt compared with our MLC scheme. The good aspect of DG-3 is that it's still stable for the linear wave. Moreover, the modified wavenumber in Fig. 2.26 (b) shows a very good resolution for large wavenumber

region. Even in the region near $k = 2\pi$ which is the upper boundary for DG-2 and our MLC scheme, DG-3 still has good accuracy. Compared with our 2-2-2-2 scheme in Fig. 2.14 and 1-1-1-1 scheme in Fig. 2.15, DG-3 shows better resolutions in the region $k > \pi$ and similar resolution in the region $k < \pi$.

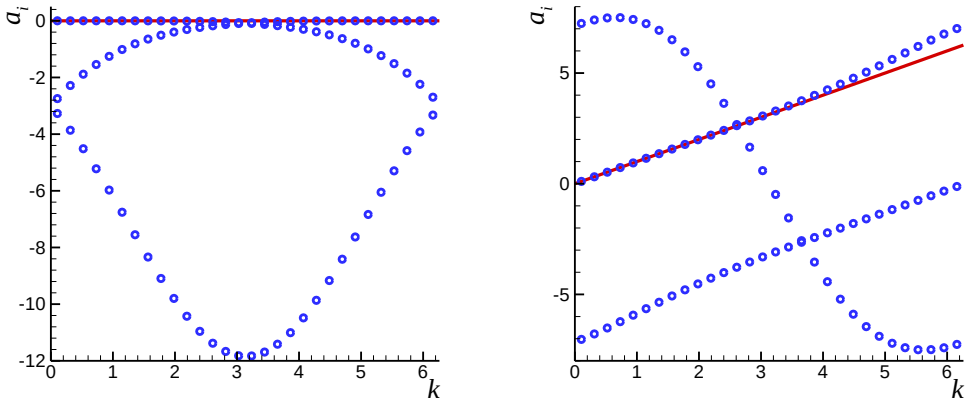

a), dissipation factor b), modified wavenumber

Fig. 2.26. Fourier analysis results of the DG-3 scheme.

The improvement of resolution in large wavenumber region is due to increase of information in each cell. A relation between the upper boundary of wavenumber (k_{max}) a numerical scheme can resolve and the degrees of freedom (K) in each cell can be given as,

$$k_{max} = K\pi \tag{2.102}$$

It can be easily concluded that, K equals to 1 for conventional finite difference and finite volume methods; K equals to 2 for our MLC scheme; and K equals to N for an Nth-order DG methods. So, high-order DG methods have the advantage of resolving very small wave length in the flow.

Comparison of different order DG methods is given in Fig. 2.27. DG-1 is same as first-order finite volume or finite difference methods and only one physical mode exists in the result. With

the increase of order, both dissipative and dispersive error is significantly decreased. Fig. 2.27 (b) shows clearly that the upper boundary of modified wavenumber for an *N*th-order DG method is $k = N\pi$.

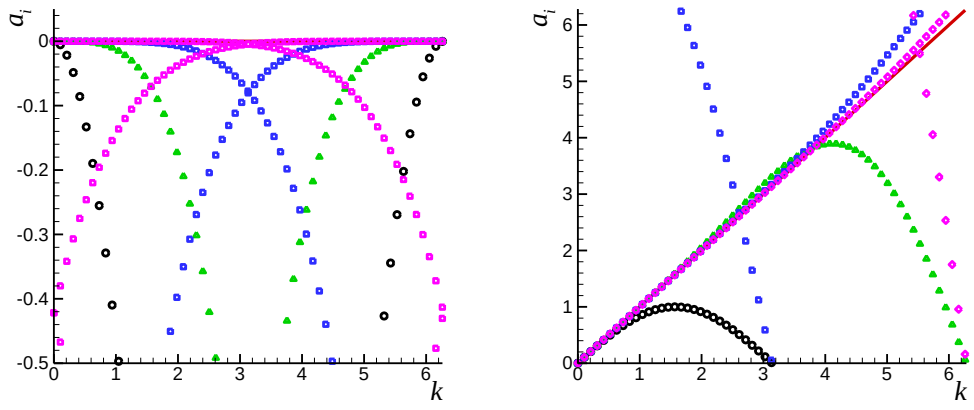

a), dissipation factor b), modified wavenumber

Fig. 2.27. Comparison of DG methods from 1st to 4th order (black: DG-1, green: DG-2, blue: DG-3, Purple: DG-4).

More Fourier analysis results of higher order DG methods indicate that DG methods are always stable for linear wave. Increasing the order will also improve the resolving ability especially for high frequency wave. This is reasonable because the maximum wavenumber a numerical scheme can approximate is mainly dependent on the degrees of freedom on each grid point or cell. However, higher orders will introduce more spurious modes and the large dissipation factors in these modes will restrict the stability condition for time integration. To give a strong demonstration on both advantage and disadvantage of DG methods, Fig. 2.28 shows the Fourier results of sixth-order DG methods (DG-6). It is clear that the modified wavenumber of physical mode perfectly overlap with exact solution in the range of $[0, 2\pi]$, indicating the high spectral resolution for very small scales. Meanwhile, the lowest point in dissipation factor is

about -38, which is about 25 times of the value in our seventh-order 2-2-2-2 scheme. Although all modes are stable, time step size will be very small to meet stability condition.

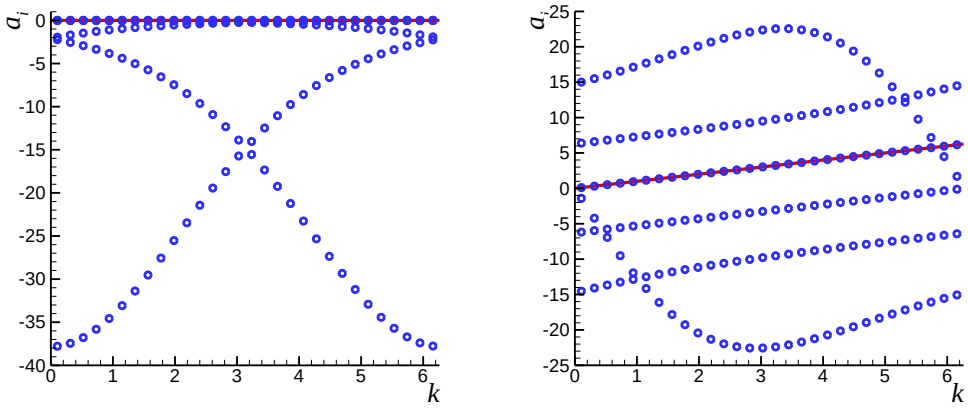

a), dissipation factor b), modified wavenumber

Fig. 2.28. Fourier analysis results of the DG-6 scheme.

In summary, Fourier analysis on the MLC schemes and DG methods indicate that, 1) the proposed upwind MLC schemes have larger error than high-order DG methods ($N > 3$) for extremely small length waves ($k > \pi$), but show comparable resolution for waves in moderate length scales ($k < \pi$); 2) the MLC schemes have much more relaxed stability condition for time integration. Other obvious advantage of our methods to DG methods is the simplicity of formulations of equations and computational efficiency on structured mesh, which is commonly used for simple geometries. With the increase of accuracy, DG methods also require more memory due to large degrees of freedom. The limitation of memory is even severer for multi-dimensional simulation. If the flow simulation requires very high accuracy and the geometry is simple, such as hypersonic boundary layer simulation over blunt body [21], our MLC scheme should be more appropriate than DG methods.

2.5. Stability Analysis of Boundary Closure Scheme

High-order finite difference methods often require boundary closure schemes at grid points on or near the boundaries of the computational domain. When the inner scheme is coupled with boundary closure schemes, the stability can be affected. It is known that for a p-th-order inner scheme, the stable boundary closure scheme can be one order lower to maintain the p-th-order global accuracy of the inner scheme. For the very high-order upwind MLC scheme, the corresponding boundary closure schemes are also expressed by the formula given in Eq. (2.4), where bias stencils are used and the adjustable parameter α is set to 0. All the formulations of the boundary closure schemes used in this dissertation are given in the Appendix A.1.

The matrix method is used here to analyze the stability of boundary closure schemes. For the MLC schemes, the matrix method is implemented on one-dimensional advection equation and its auxiliary equation as shown in Eq. (2.3). A finite domain is discretized by a uniform grid mesh as shown in Fig. 2.29, where x has the range of $[0, Nh]$. A total of N gird panels is used, and h is grid spacing. Two non-periodic boundaries are fixed at $x = 0$ and $x = Nh$, i.e., they are numbered as $i = 0$ and $i = N$. Inflow boundary condition is used at $i = 0$, and characteristic boundary condition is used from at $i = N$. For the one-dimensional linear advection, the inflow condition is specified by $u_0(t)$ and characteristic boundary condition is implemented by using one-sided MLC scheme. The upwind MLC schemes on centered stencil are used at interior grid points, and different boundary closure schemes are applied when the stencil of inner scheme goes beyond the left and right boundaries.

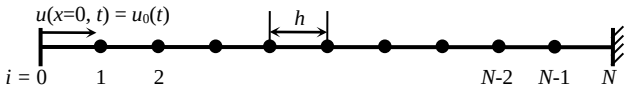

Fig. 2.29. Schematic for stability analysis on one-dimensional linear advection equation.

In matrix method, Eq. (2.3) is discretized into a system of ordinary differential equations by using the inner and boundary closure schemes. The resulting equations can be represented in matrix form,

$$\frac{d}{dt}\begin{bmatrix}\mathbf{U}\\ \mathbf{U}'\end{bmatrix}+c\begin{bmatrix}\mathbf{0} & \mathbf{I}\\ \mathbf{A} & \mathbf{B}\end{bmatrix}\cdot\begin{bmatrix}\mathbf{U}\\ \mathbf{U}'\end{bmatrix}=\begin{bmatrix}\mathbf{0}\\ \mathbf{g}(t)\end{bmatrix} \tag{2.103}$$

where $\mathbf{U} = (u_1, \ldots, u_N)^{\mathrm{T}}$, $\mathbf{U}' = (u'_1, \ldots, u'_N)^{\mathrm{T}}$ are the unknowns. The source term $\mathbf{g}(t)$ are a vector with N elements which are dependent on $u(x=0, t) = u_0(t)$ and $u'(x=0, t)$ - the inflow boundary condition given at $i = 0$. The derivative boundary condition $u'(x=0, t)$ is obtained through the advection equation,

$$u'(x=0,t)=-\frac{1}{c}\frac{d}{dt}u_0(t) \tag{2.104}$$

Matrices **A** and **B** consist of the coefficients of both inner and boundary closure schemes. Without losing generality, $c = 1$ is used in the analysis, and the equations can be written in a system of ordinary differential equations,

$$\frac{d}{dt}\overline{\mathbf{U}}=\mathbf{L}\cdot\overline{\mathbf{U}}+\mathbf{G}(t) \tag{2.105}$$

by introducing the definitions,

$$\overline{\mathbf{U}}=(\mathbf{U},\mathbf{U}')^T,\quad \mathbf{L}=-\begin{bmatrix}\mathbf{0} & \mathbf{I}\\ \mathbf{A} & \mathbf{B}\end{bmatrix},\quad \mathbf{G}(t)=\begin{bmatrix}\mathbf{0}\\ \mathbf{g}(t)\end{bmatrix} \tag{2.106}$$

The stability of Eq. (2.105) is determined by eigenvalue of matrix **L**, which only depends on the particular inner and boundary closure schemes. For asymptotic stability, the real part of all the

eigenvalues of **L** needs to be non-positive. The boundary source terms **G**(t) can be ignored in the stability analysis. Here, the eigenvalue of **L** is solved numerically, and the eigenvalue spectrum is used to show stability.

First, the stability of boundary closure schemes is performed for the third-order 1-1-1-1 scheme. Table 2.2 lists two cases with different selections of boundary closure schemes based on the same inner scheme. The 1-1-1-1 scheme uses a three-point stencil, so boundary closure scheme is required only at the right end ($i = N$). Both case 1 and 2 are supposed to have third-order global accuracy.

Table 2.2. Selections of inner and boundary closure schemes with 3rd-order expected global accuracy.

	Case 1	Case 2
$i = 0$	Inflow boundary condition	Inflow boundary condition
$i = 1$ to N-1	3rd-order 1-1-1-1 scheme (Eq. (2.7))	3rd-order 1-1-1-1 scheme
$i = N$	2nd-order 1-0-1-0 scheme (Eq. (A.5))	3rd-order 2-0-1-0 scheme (Eq. (A.9))

Fig. 2.30(a) shows the eigenvalue spectrum of case 1. The upwind coefficient α for the inner scheme can affect the boundary closure schemes. The eigenvalues show that 1-1-1-1 upwind scheme with positive α values is stable. Increasing α causes the spectrum to move towards negative direction, which means the scheme is more stable. The figure also shows that even with central scheme ($\alpha = 0$) on interior points, second-order boundary closure schemes are still stable though the real parts of eigenvalues are very close to 0. The central scheme is usually considered unstable because it contains no numerical dissipation. However, the boundary closure scheme on a bias stencil (1-0-1-0) at the right end might have stabilization effect as upwind schemes. As a

result, the central scheme becomes stable. Comparing three spectrums, we can see the recommend α value from Fourier analysis (α = 1.5) is still preferred because it has relatively low dissipation.

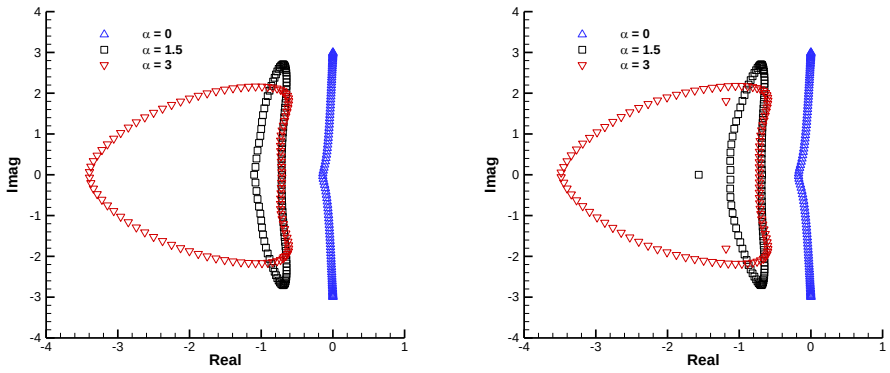

a), case 1 b), case 2

Fig. 2.30. Eigenvalue spectrum of the 3rd-order 1-1-1-1 scheme coupled with two different boundary closure schemes.

Fig. 2.30(b) shows the eigenvalue spectrum of case 2, where third-order boundary closure schemes are coupled with the 1-1-1-1 scheme. It turns out the eigenvalue spectrum is similar to case 1. No positive real part of eigenvalues is observed for all α choices. It can be concluded from Fig. 2.30 that both second-order (case 1) and third-order (case 2) boundary closure schemes can be coupled with the 1-1-1-1 scheme. The upwind setting in 1-1-1-1 scheme helps to stabilize boundary closure schemes. The value for α is still chosen to be 1.5 to keep enough dissipation and maintain accuracy at the same time.

Then, the stability of boundary closure schemes is performed for the seventh-order 2-2-2-2 scheme. Table 2.3 shows three cases with different selections of boundary closure schemes based on the same inner scheme. The 2-2-2-2 scheme uses a five-point stencil and three boundary

closure schemes are needed, one for the right boundary ($i = N$) and two for the boundary adjacent points ($i = 1, N\text{-}1$). The MLC scheme with sixth or seventh-order accuracy on bias stencil can be coupled with the 2-2-2-2 scheme to maintain a seventh-order global accuracy.

Table 2.3. Selections of inner and boundary closure schemes with 7th-order expected global accuracy.

	Case 3	Case 4	Case 5
$i = 0$	Inflow boundary condition	Inflow boundary condition	Inflow boundary condition
$i = 1$	6th-order 1-2-1-2 scheme (Eq. (A.7))	7th-order 1-3-1-2 scheme (Eq. (A.8))	7th-order 1-3-1-2 scheme
$i = 2$ to N-2	7th-order 2-2-2-2 scheme (Eq. (2.10))	7th-order 2-2-2-2 scheme	7th-order 2-2-2-2 scheme
$i = N$-1	6th-order 2-1-2-1 scheme (Eq. (A.10))	7th-order 3-1-2-1 scheme (Eq. (A.13))	7th-order 3-1-2-1 scheme
$i = N$	6th-order 3-0-3-0 scheme (Eq. (A.12))	6th-order 3-0-3-0 scheme	7th-order 4-0-3-0 scheme (Eq. (A.14))

Fig. 2.31(a) shows the eigenvalue spectrum of case 3, where sixth-order boundary closure schemes are used. Different from the 1-1-1-1 scheme, the 2-2-2-2 scheme with $\alpha = 0$ is not stable which generates positive real parts in the eigenvalue spectrum. But similarly, increasing α can stabilize the boundary closure schemes. When $\alpha = 12$, which is the recommended value from Fourier analysis above, the sixth-order boundary closure schemes are stable. When α has a value of 24, the dissipation is already very large. So, $\alpha = 12$ is still the recommended choice for the simulation with boundaries.

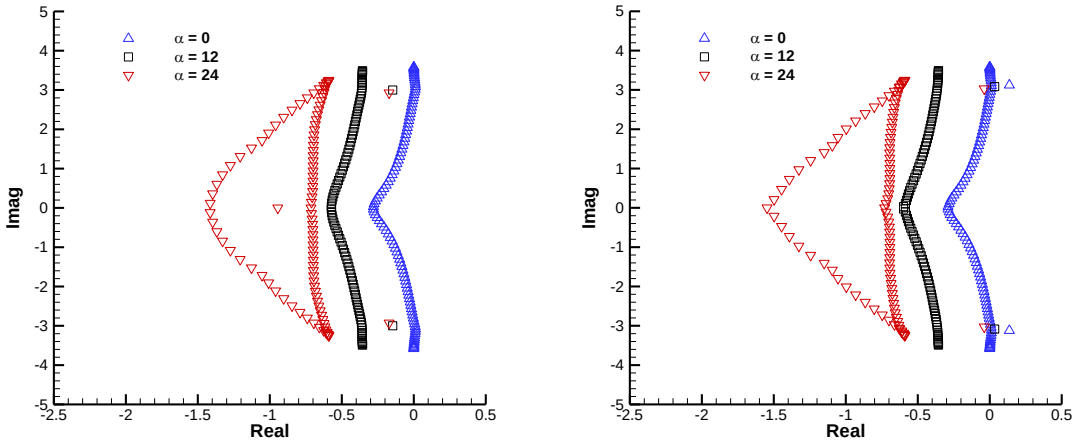

a), case 3

b), case 4

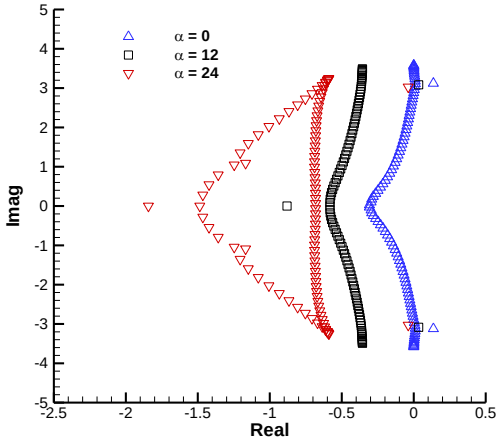

c), case 5

Fig. 2.31. Eigenvalue spectrum of the 7th-order 2-2-2-2 scheme coupled with three different boundary closure schemes.

Seventh-order boundary closure schemes can also be coupled with the seventh-order 2-2-2-2 scheme. However, from the experience of conventional finite difference methods, boundary closure schemes with the same order as the inner scheme may be unstable [21]. Fig. 2.31(b)

shows the eigenvalue spectrum of case 4, where seventh-order schemes are used on the boundary adjacent points. Compared with Fig. 2.31(a), the continue spectrum distribution does not change obviously, but the positions of discrete eigenvalue points move towards the positive direction in real axis significantly, which indicates the seventh-order boundary closure schemes causes more instability than sixth-order schemes. In Fig. 2.31(b), the two discrete eigenvalues represented by the black squares have positive real parts, indicating that the 2-2-2-2 scheme with an α value of 12 does not have enough dissipation to stabilize the system. If α is increased to 24, the eigenvalue spectrum becomes non-positive again. However, the numerical dissipation is also increased. Fig. 2.31(c) shows the eigenvalue spectrum of case 5, where seventh-order boundary closure schemes are also applied on the right boundary. The result of case 5 shows the 2-2-2-2 scheme with α values of 0 and 12 is not stable with seventh-order boundary closure schemes. From case 4 and 5, it can be concluded that the stability decreases when the order of boundary closure scheme is increased, which is consistent with previous experience from Zhong's finite difference methods [21]. From the analysis above, it is recommended to use sixth-order boundary closure schemes with the seventh-order 2-2-2-2 scheme ($\alpha = 12$), which is case 3 in Table 2.3.

Through the stability analysis with matrix method, it is observed that the high-order MLC schemes are less stable with respect to boundary closures than low-order schemes, which is a common feature of high-order finite difference schemes. But due to the compactness of stencil, there are only three boundary closure schemes required even for the seventh-order 2-2-2-2 scheme. As a comparison, Zhong's fifth-order explicit scheme needs five boundary closure schemes for flow simulations with boundaries. Therefore, the MLC schemes have an advantage

in the construction of high-order boundary closure schemes over conventional finite difference schemes.

2.6. Summary

In Chapter 2, the new very high-order upwind MLC scheme are analyzed by Fourier analysis and stability analysis with matrix methods. The aliasing in conventional finite difference methods is overcome and spectral-like resolution of the MLC scheme is observed. The dissipative, dispersive, and anisotropic error of the MLC scheme is much smaller than that of conventional finite difference methods. Compared with Zhong's fifth-order explicit scheme, both the seventh-order 2-2-2-2 scheme and third-order 1-1-1-1 scheme have a much better resolution in the large wavenumber region. Besides, the stencils are more compact because of more degrees of freedom on each grid point. Benefiting from the compactness, high-order stable boundary closure schemes can be attained. From both Fourier and stability analysis, the seventh-order 2-2-2-2 scheme with an α value of 12 is supposed to have the best accuracy, and it should be coupled with sixth-order boundary closure schemes for stability, as the case 3 in Table 2.3.

It should be emphasized that the spectral-like resolution is not simply caused by more total information, including values and derivatives, contained in the stencil. For example, the 3rd-order 1-1-1-1 scheme has a total of 6 points within a double-layer stencil. As a comparison, Zhong's 5th-order explicit scheme has a total of 7 points within a mono-layer stencil. However, the 1-1-1-1 scheme with less total information has much better spectral resolution than Zhong's 5th-order scheme, as shown in Fig. 2.15. Therefore, the multi-layer framework is the main reason for which the spectral resolution is significantly improved in the MLC schemes. In theory,

more layers can be used in the MLC schemes, which means introducing additional equations for higher derivatives. The benefit is that the spectral resolution and the order of accuracy can be further improved with more degrees of freedom. However, the resulting scheme could be very stiff, and the formulation will be too complicated for nonlinear equations such as the Euler and Navier-Stokes equations. Both the stiffness and the complexity will probably affect the computational efficiency.

Main challenges for the MLC scheme should be mentioned before in the end of this chapter. Even though the MLC scheme is promising due to very high-order of accuracy, spectral-like resolution, and consistent stability in one-dimensional cases, it shows weak numerical instabilities for a small range of wavenumbers when it is applied to multi-dimensional flows, which are mainly triggered by the inconsistency between its one and two-dimensional formulations. It is shown in the following chapter that the instability could lead to divergence in long-time multi-dimensional simulations. Moreover, the cross-derivative approximation in the MLC scheme requires an ad-hoc selection of supporting grid points, and the cross-derivative approximation is relatively inefficient for very high-order cases. To address the remaining challenges of the MLC scheme and achieve better performance for multi-dimensional flow simulations, another two new schemes are developed in the rest of the dissertation – the directional multi-layer compact (DMLC) scheme, and the least square multi-layer compact (LSMLC) scheme.

3. Directional Multi-Layer Compact (DMLC) Scheme for Multi-Dimensional Flows

The MLC scheme presented in Chapter 2 still have some drawbacks when it is applied to multi-dimensional simulations. First, even though the MLC scheme is always stable in one-dimensional cases, the Fourier analysis showed that a weak numerical instability appears in both the physical and spurious modes for a very narrow range of wavenumbers in two-dimensional cases (see Section 3.4.1 for details). The instability is mainly triggered by the inconsistency between 1-D and 2-D formulations. For example, the 1-D upwind scheme is used for the second-derivative approximation, while the 2-D central scheme is used for the cross-derivative approximation. Although the amplification factors related to the unstable modes are very small, it may still lead to potential risk of divergence in two-dimensional flow simulations, especially for long-time simulations. Second, the approximation of the cross derivative uses the square stencil where redundant information exists. Therefore, the formula for cross-derivative approximation is not unique and supporting grid points need to be selected manually. There exist difficulties in two aspects: it is difficult to select the best set of supporting points and determine the optimal formula; and it is also complicated to derive the 2-D upwind scheme that is compatible with the 1-D upwind scheme, which in turn causes the first problem of inconsistency. This ad-hoc cross-derivative approximation in the MLC scheme could also affect the accuracy and the stability of the MLC scheme. Third, the cross-derivative approximation on the square stencil is relatively inefficient compared with the second-derivative approximation. As the order

of accuracy increases, the grid stencil becomes wider, consequently, the treatment of cross derivatives is more complicated and leads to more computational costs.

In order to overcome the numerical instability and avoid the ad-hoc cross-derivative approximations in the MLC scheme, as well as to achieve better accuracy and computational efficiency in multi-dimensional flow simulations, a new directional discretization technique is presented in this Chapter. The resulting new numerical method is termed the directional multi-layer compact (DMLC) scheme, as compared with the MLC scheme developed in Chapter 2. In our directional discretization technique, the auxiliary equation for the cross derivative u_{xy} is introduced for multi-dimensional cases. Then, the cross derivative is used as an additional degree of freedom in the approximation of higher spatial derivatives. With this technique, the spatial discretization of the entire system can be fulfilled along each dimension independently. In other words, the 1-D formula can be applied to all spatial derivatives, and no special treatment is needed for cross derivatives. The significant advantage of the technique is that any inconsistency between the 1-D and 2-D formulations in the MLC scheme does not exist in the DMLC scheme, and the ad-hoc cross-derivative approximations are avoided as well. A similar idea can be found in the central Hermite WENO scheme developed by Tao et al [100], though their method is developed in the finite volume framework. In their methods, the equation of the mixed first-order momentum $\frac{1}{\Delta x \Delta y}\int u \frac{(x-x_i)(y-y_i)}{\Delta x \Delta y} dxdy$ is introduced when the dimension is higher than one. All zeroth-order and first-order moments, which are integral quantities for each cell, are used in the spatial reconstruction through a dimension-by-dimension strategy.

In this chapter, the new very high-order upwind directional multi-layer compact (DMLC) schemes are first presented using the multi-dimensional linear advection equations, which is the model equation for inviscid flows. Then, the comparison with the MLC scheme is presented. In the end, the implementation of the DMLC scheme on the nonlinear Euler equations are presented with focus on two-dimensional cases. The Fourier analysis and boundary stability analysis with matrix method are carried out to show the dissipative and dispersive errors, the spectral resolution, the anisotropy, and the stability of the DMLC scheme in two-dimensional cases.

3.1. Directional Discretization

The linear advection equation in the Cartesian coordinate can be written using Einstein notation as follows,

$$\frac{\partial u}{\partial t} = -c_j u_{x_j}, \quad j \in \{1,2,3\} \tag{3.1}$$

where u is a scalar variable, and the constant c_j is the advection speed along the x_j direction. In the first step, the gradient on Eq. (3.1) is taken, which is the same as for the MLC scheme, and a system of auxiliary equations are derived in the following form,

$$\frac{\partial u_{x_k}}{\partial t} = -c_j u_{x_j x_k}, \quad j,\ k \in \{1,2,3\} \tag{3.2}$$

In the MLC scheme, the second derivatives ($k = j$) and cross derivatives ($k \neq j$) are approximated using a 1-D finite difference formula and a 2-D finite difference formula respectively. As we mentioned in the introduction, the MLC scheme for multi-dimensional cases shows some drawbacks such as weak numerical instability, ad-hoc selection of grid points for cross derivatives, and high computational costs in very high-order cases. Because these drawbacks of the MLC scheme are related to the approximation of cross derivatives (read Section 3.2 for

details), it gives us the motivation to seek a new numerical method which can avoid cross-derivative approximations. Therefore, in the new DMLC scheme presented here, auxiliary equations for cross derivatives are introduced in the second step. Taking the derivative of Eq. (3.2) to x_l ($l \neq k$), the auxiliary equations for cross derivatives with respect to two dimensions are obtained,

$$\frac{\partial u_{x_k x_l}}{\partial t} = -c_j u_{x_j x_k x_l}, \quad j,\ k,\ l \in \{1,2,3\} \text{ and } k \neq l \tag{3.3}$$

In three-dimensional cases, the cross derivative with respect to three dimensions (u_{x1x2x3}) appears in Eq. (3.3); therefore, one more auxiliary equation for u_{x1x2x3} is needed,

$$\frac{\partial u_{x_1 x_2 x_3}}{\partial t} = -c_j u_{x_j x_1 x_2 x_3}, \quad j \in \{1,2,3\} \tag{3.4}$$

In Eqs. (3.3) and (3.4), higher cross derivatives are introduced, which seems to make the spatial discretization more complicated than the MLC scheme. However, the lower cross derivatives are solved as unknowns and can also be used to approximate higher cross derivatives. As a result, the spatial derivatives to be approximated are not significantly increased compared with the case in the MLC scheme (read Section 3.2 for more details). More importantly, with the help of auxiliary equations for cross derivatives, the spatial discretization can be performed independently along each dimension in both two and three-dimensional cases. In the following part of this section, the implementation of the DMLC schemes in two and three-dimensional cases is described in the Cartesian coordinates (x, y, z). In order to illustrate that the directional discretization is achieved in the DMLC scheme, Eqs. (3.1)- (3.4) are expanded in each dimension.

For two-dimensional cases, the linear advection equation (3.1) and its auxiliary equations (3.2) and (3.3) can be combined and written in the vector form,

$$\frac{\partial U}{\partial t} = \mathcal{L}(U), \quad U = (u, v, w, r)^T \tag{3.5}$$

where u, v ($=u_x$), w ($=u_y$), and r ($=u_{xy}$) are treated as the unknows, and the linear operator $\mathcal{L}$ is,

$$\mathcal{L} = -\begin{pmatrix} 0 & c_1 & c_2 & 0 \\ c_1 \frac{\partial}{\partial x^2} & 0 & 0 & c_2 \\ c_2 \frac{\partial}{\partial y^2} & 0 & 0 & c_1 \\ 0 & c_2 \frac{\partial}{\partial y^2} & c_1 \frac{\partial}{\partial x^2} & 0 \end{pmatrix} \tag{3.6}$$

Note that Eq. (3.4) does not exist in two-dimensional cases. In Eqs. (3.5) and (3.6), we observe that all the spatial derivatives are the second derivatives of the unknowns, and there are only four terms to be discretized, which is (u_{xx}, w_{xx}) in the x direction, and (u_{yy}, v_{yy}) in the y direction. All the cross-derivative terms vanish in Eq. (3.6). It is clear that the spatial discretization of Eq. (3.5) can be fulfilled along each dimension separately, and the discretization with the alternative formulation in Eqs. (3.5) and (3.6) is termed as the directional discretization technique in this dissertation.

The computational domain for two-dimensional advection is a square within the range of $a \le x \le b$ and $a \le y \le b$, where four boundaries can be either periodic or non-periodic. A uniform mesh is used for the computational domain, with the grid spacing h in both dimensions. Fig. 2.7 shows the stencil of the L_1-L_2-M_1-M_2 DMLC scheme for two-dimensional cases, where (i, j) is the base point. Only the grid points on the two lines passing through (i, j) are used in the DMLC scheme, which maintains a low computational cost. To discretize the system in Eq. (3.5), the following approximations is used,

$$\begin{pmatrix} u_{xx} \\ w_{xx} \end{pmatrix}_{i,j} = \frac{1}{h^2} \sum_{l=-L_1}^{L_2} a_l \begin{pmatrix} u \\ w \end{pmatrix}_{i+l,j} + \frac{1}{h} \sum_{m=-M_1}^{M_2} b_m \begin{pmatrix} v \\ r \end{pmatrix}_{i+m,j} - \frac{\alpha}{(p+2)!} \begin{pmatrix} \partial u / \partial x^{p+2} \\ \partial w / \partial x^{p+2} \end{pmatrix}_{i,j} h^p + \cdots \tag{3.7}$$

$$\begin{pmatrix} u_{yy} \\ v_{yy} \end{pmatrix}_{i,j} = \frac{1}{h^2} \sum_{l=-L_1}^{L_2} a_l \begin{pmatrix} u \\ v \end{pmatrix}_{i,j+l} + \frac{1}{h} \sum_{m=-M_1}^{M_2} b_m \begin{pmatrix} w \\ r \end{pmatrix}_{i,j+m} - \frac{\alpha}{(p+2)!} \begin{pmatrix} \partial u / \partial y^{p+2} \\ \partial v / \partial y^{p+2} \end{pmatrix}_{i,j} h^p + \cdots \tag{3.8}$$

$$p = L_1 + L_2 + M_1 + M_2 - 1 \tag{3.9}$$

where coefficients a_l and b_m can be derived from the Taylor series expansion. Both the discrete function values $u_{i,j}$, and the first derivatives $v_{i,j}$, $w_{i,j}$ are used to approximate second derivatives $(u_{xx})_{i,j}$, $(u_{yy})_{i,j}$; and the first derivatives $w_{i,j}$, $v_{i,j}$ and the cross derivatives $r_{i,j}$ are used to approximate higher cross derivatives $(w_{xx})_{i,j}$, $(v_{yy})_{i,j}$. In the truncation error term, α is an adjustable parameter. Non-zero α's lead to upwind or downwind schemes, which have a p-th order of accuracy. When $\alpha = 0$, the central scheme with the maximum (p+1)-th order is obtained. The value of α has an impact on the stability, accuracy, and stiffness of the DMLC scheme which is similar with that for the MLC scheme. Larger α leads to better stability, larger dissipation and stiffness, and it slightly increases dispersion [101]. Therefore, the value of α needs to be large enough to make the scheme stable and needs to be relatively small to control the dissipation and dispersion. In Eqs. (3.7) and (3.8), the same DMLC scheme is applied to x and y dimensions respectively.

In the next place, the extension of the DMLC scheme to three-dimensional cases are briefly described, which is straightforward. In three-dimensional cases, the linear advection equation (3.1) and its auxiliary equations (3.2) - (3.4) can be combined and written in the vector form,

$$\frac{\partial U}{\partial t} = \mathcal{L}(U), \quad U = \left(u, u_x, u_y, u_z, u_{xy}, u_{yz}, u_{xz}, u_{xyz}\right)^T \tag{3.10}$$

where the linear operator $\mathcal{L}$ is,

$$\mathcal{L} = -\begin{pmatrix} 0 & c_1 & c_2 & c_3 & 0 & 0 & 0 & 0 \\ c_1\frac{\partial}{\partial x^2} & 0 & 0 & 0 & c_2 & 0 & c_3 & 0 \\ c_2\frac{\partial}{\partial y^2} & 0 & 0 & 0 & c_1 & c_3 & 0 & 0 \\ c_3\frac{\partial}{\partial z^2} & 0 & 0 & 0 & 0 & c_2 & c_1 & 0 \\ 0 & c_2\frac{\partial}{\partial y^2} & c_1\frac{\partial}{\partial x^2} & 0 & 0 & 0 & 0 & c_3 \\ 0 & 0 & c_3\frac{\partial}{\partial z^2} & c_2\frac{\partial}{\partial y^2} & 0 & 0 & 0 & c_1 \\ 0 & c_3\frac{\partial}{\partial z^2} & 0 & c_1\frac{\partial}{\partial x^2} & 0 & 0 & 0 & c_2 \\ 0 & 0 & 0 & 0 & c_3\frac{\partial}{\partial z^2} & c_1\frac{\partial}{\partial x^2} & c_2\frac{\partial}{\partial y^2} & 0 \end{pmatrix} \tag{3.11}$$

There are eight unknowns in Eq. (3.10), which correspond to the degrees of freedom at each grid point in Fig. 2.7. Same with the two-dimensional case, all the spatial derivatives are the second derivatives of the unknowns. On the right-hand side of Eq. (3.10), there are a total of twelve spatial derivatives (u_{xx}, u_{yxx}, u_{zxx}, u_{yzxx}, u_{yy}, u_{xyy}, u_{zyy}, u_{xzyy}, u_{zz}, u_{xzz}, u_{yzz}, u_{xyzz}) to be discretized. Even though higher cross derivatives up to 4th order appear in Eq. (3.10), the lower cross derivatives (u_{xy}, u_{yz}, u_{xz}, u_{xyz}) in U are available for their approximations. As a result, the spatial discretization can be fulfilled along each dimension x, y, and z independently. For instance, using the same the L_1-L_2-M_1-M_2 DMLC scheme as in Eq. (3.7), the discretization in the x direction has the form,

$$\begin{pmatrix} u_{xx} \\ u_{yxx} \\ u_{zxx} \\ u_{yzxx} \end{pmatrix}_{i,j,k} = \frac{1}{h^2}\sum_{l=-L_1}^{L_2} a_l \begin{pmatrix} u \\ u_y \\ u_z \\ u_{yz} \end{pmatrix}_{i+l,j,k} + \frac{1}{h}\sum_{m=-M_1}^{M_2} b_m \begin{pmatrix} u_x \\ u_{xy} \\ u_{xz} \\ u_{xyz} \end{pmatrix}_{i+m,j,k} - \frac{\alpha}{(p+2)!}\begin{pmatrix} \partial u/\partial x^{p+2} \\ \partial u/\partial x^{p+2}\partial y \\ \partial u/\partial x^{p+2}\partial z \\ \partial u/\partial x^{p+2}\partial y\partial z \end{pmatrix}_{i,j,k} h^p + \cdots \tag{3.12}$$

The discretization in the y and z direction can be performed similarly, which are not repeated here.

Typical formulas for the DMLC scheme are the same with those for MLC schemes, which are presented in section 2.1. For the upwind scheme, the recommended α values are selected based on one-dimensional Fourier analysis results, which is the same as the MLC scheme. More details can be found in Chapter 2. In the MLC scheme, all formulas are described for second-derivative approximations in one-dimensional cases, but they can be naturally extended for two and three-dimensional cases with the directional discretization technique in the DMLC schemes.

3.2. Comparison of DMLC Scheme and MLC Scheme

In this section, the MLC scheme in [101] is briefly reviewed, and the comparison with the new DMLC scheme are presented.

For two-dimensional cases, the governing equations for the MLC scheme are in the following form,

$$\frac{\partial U}{\partial t} = \mathcal{L}_1(U) + \mathcal{L}_2(U), \quad U = (u, v, w)^T \tag{3.13}$$

$$\mathcal{L}_1 = -\begin{pmatrix} 0 & c_1 & c_2 \\ c_1 \frac{\partial}{\partial x^2} & 0 & 0 \\ c_2 \frac{\partial}{\partial y^2} & 0 & 0 \end{pmatrix}, \quad \mathcal{L}_2 = -\begin{pmatrix} 0 & 0 & 0 \\ c_2 \frac{\partial}{\partial x \partial y} & 0 & 0 \\ c_1 \frac{\partial}{\partial x \partial y} & 0 & 0 \end{pmatrix} \tag{3.14}$$

where $\mathcal{L}_1$ represents the second-derivative operator and $\mathcal{L}_2$ represents the cross-derivative operator. The spatial discretization for both the second and cross derivatives are needed, as shown in the two linear operators. Specifically, u_{xx}, u_{yy} are approximated with 1-D upwind schemes, and u_{xy} are approximated with 2-D central schemes. The second-derivative

approximations are the same as the DMLC scheme in Eqs. (3.7) and (3.8), and the cross derivative can be approximated using the corresponding 2-D central scheme ($\alpha_k = 0$) as follows,

$$\begin{aligned}\left(u_{xy}\right)_{i,j} = &\frac{1}{h^2}\sum_{\substack{l_x=-L_1\\ l_y=-L_1}}^{L_2} a_{l_x,l_y} u_{i+l_x,j+l_y} + \frac{1}{h}\sum_{\substack{m_x=-M_1\\ m_y=-M_1}}^{M_2} b_{m_x,m_y} v_{i+m_x,j+m_y} + \frac{1}{h}\sum_{\substack{n_x=-M_1\\ n_y=-M_1}}^{M_2} c_{n_x,n_y} w_{i+n_x,j+n_y} \\ &+ \sum_{k=0}^{p+2} \alpha_k \left(\frac{\partial u}{\partial x^k \partial y^{p+2-k}}\right)_{i,j} h^p + o\left(h^{p+1}\right)\end{aligned} \tag{3.15}$$

whose accuracy is (p + 1)-th order and is one-order higher than the 1-D upwind scheme. The approximation of $(u_{xy})_{i,j}$ use the same grid stencil in Fig. 2.7. However, all points in the square need to be considered in the approximation which leads to more computational costs.

For three-dimensional cases, the governing equations for the MLC scheme are in the following form,

$$\frac{\partial U}{\partial t} = \mathcal{L}_1(U) + \mathcal{L}_2(U), \quad U = \left(u, u_x, u_y, u_z\right)^T \tag{3.16}$$

$$\mathcal{L}_1 = -\begin{pmatrix} 0 & c_1 & c_2 & c_3 \\ c_1\frac{\partial}{\partial x^2} & 0 & 0 & 0 \\ c_2\frac{\partial}{\partial y^2} & 0 & 0 & 0 \\ c_3\frac{\partial}{\partial z^2} & 0 & 0 & 0 \end{pmatrix}, \quad \mathcal{L}_2 = -\begin{pmatrix} 0 & 0 & 0 & 0 \\ c_2\frac{\partial}{\partial x\partial y} + c_3\frac{\partial}{\partial x\partial z} & 0 & 0 & 0 \\ c_1\frac{\partial}{\partial x\partial y} + c_3\frac{\partial}{\partial y\partial z} & 0 & 0 & 0 \\ c_1\frac{\partial}{\partial x\partial z} + c_2\frac{\partial}{\partial y\partial z} & 0 & 0 & 0 \end{pmatrix} \tag{3.17}$$

Similar with two-dimensional cases, u_{xx}, u_{yy}, u_{zz} are approximated with 1-D upwind schemes, and u_{xy}, u_{yz}, u_{xz} are approximated with 2-D central schemes.

Two comments on the cross derivatives are mentioned here. First, the formula used for cross-derivative approximations are not unique because of the redundant information within the square stencil, as shown in Fig. 2.7. Although the criterion of keeping fewest non-zero terms with relatively concise coefficients in the formula is reasonable for the selection of the supporting points [101], it mainly focuses on improving the computational efficiency and

reducing the round-off error. It is unpractical to conduct rigorous analysis or numerical tests to compare the performance such as stability, dissipation, dispersion, and anisotropy among numerous candidates. Second, it is difficult to construct upwind schemes for cross derivatives. As shown in Eqs. (3.7) and (3.8), one novelty of the MLC and DMLC schemes is using an adjustable parameter α to introduce small numerical dissipation for stability, and to make a central scheme "upwind". However, there are a total of (p+3) leading truncation error terms with the same degree – h^p in the 2-D finite difference formula, as shown in Eq. (3.15). How to choose the coefficients α_k of all truncation error terms is unclear and complicated. As a result of these two reasons, the cross-derivative approximation become an ad-hoc problem. Moreover, the upwind schemes possess more complexity than the central schemes because the supporting points can be selected asymmetrically. In the current MLC schemes, the 2-D central scheme is used for two-dimensional cases to avoid the complexity of 2-D upwind schemes. Then, the resulting problem is that the 2-D central scheme may not be consistent with the 1-D upwind scheme, and even the 2-D central scheme may not be optimal because of the ad-hoc selection of supporting points for cross derivatives.

In the end of this section, the formulations of the MLC scheme and the DMLC scheme are compared. In two-dimensional cases, we can observe that there are four degrees of freedom (u, v ($=u_x$), w ($=u_y$), r ($=u_{xy}$)) at each grid point in the DMLC scheme, which slightly increases the memory compared with three degrees of freedom (u, v, w) in the MLC scheme. However, the benefit of introducing r is significant. First, only approximations for second derivatives u_{xx}, w_{xx}, u_{yy}, v_{yy} are needed in Eq. (3.5), in other words, the ad-hoc approximation of u_{xy} is avoided. Second, the discretization can be carried out along each grid line independently, and the same 1-D formula can be applied to u_{xx}, w_{xx}, u_{yy}, v_{yy}. Therefore, the spatial discretization becomes

rigorously consistent for one or two-dimensional cases. All the properties of DMLC scheme in one-dimensional cases can be generalized to two-dimensional cases; the implementation of the upwind scheme ($\alpha \neq 0$) is straightforward as well. Third, the spatial discretization becomes more computationally efficient with the directional discretization technique. As we can see in Eqs. (3.5) and (3.13), although the DMLC scheme introduces an additional equation to solve, there are only four spatial derivative terms (u_{xx}, w_{xx}, u_{yy}, v_{yy}) to deal with which is the same as the MLC scheme (u_{xx}, $2 \times u_{xy}$, u_{yy}). Note that for the MLC scheme, the same cross derivative u_{xy} appears twice in Eq. (3.2), which is just a special case for the linear advection equation. In nonlinear equations like the Euler and Navier-Stokes equations, there will be two different cross derivatives to approximate, which leads to more computations. The 2-D approximation for u_{xy} is more expensive compared with the 1-D approximations for u_{xx}, w_{xx}, u_{yy}, v_{yy}. If the stencil has n points, the time complexity for a cross-derivative approximation is $O(n^2)$, while it is $O(n)$ to approximate a second derivative. In very high-order cases where wider stencils are required, the CPU time for cross-derivative approximations increase significantly. Therefore, the DMLC schemes should lead to better computational efficiency in two-dimensional simulations. Last, the additional degree of freedom r can furtherly improve the spectral resolution, which can be shown in the two-dimensional Fourier analysis in the next chapter.

Similarly, in three-dimensional cases, there are eight degrees of freedom (u, u_x, u_y, u_z, u_{xy}, u_{yz}, u_{xz}, u_{xyz}) at each grid point in the DMLC scheme, compared with four degrees of freedom (u, u_x, u_y, u_z) in the MLC scheme. Although the memory is doubled, there are benefits from the additional degrees of freedom. In the MLC scheme with Eq. (3.16), there are three second derivatives (u_{xx}, u_{yy}, u_{zz}) and six cross derivatives $2 \times$ (u_{xy}, u_{yz}, u_{xz}) to be approximate; again, we need to consider the number of cross derivatives is doubled in nonlinear cases. As a comparison,

there are twelve second derivatives (u_{xx}, u_{yxx}, u_{zxx}, u_{yzxx}, u_{yy}, u_{xyy}, u_{zyy}, u_{xzyy}, u_{zz}, u_{xzz}, u_{yzz}, u_{xyzz}) to be approximated in the DMLC scheme with Eq. (3.10). Although the numerical tests for three-dimensional cases are not performed in this dissertation, it is reasonable to infer that the approximation of the six cross derivatives in the MLC scheme should be more time-consuming especially in very high-order cases. On the other hand, the DMLC scheme should also have much better spectral resolution than the MLC scheme in three-dimensional cases, with double degrees of freedom at each grid point.

3.3. Implementation of DMLC Scheme on Euler Equations

Fluid dynamic problems are governed by the Navier-Stokes equations. In the inviscid flow, the viscous term can be eliminated, and the resulting governing equations become the nonlinear Euler equations, which can be written in the following conservation-law form in the Cartesian coordinate,

$$\frac{\partial U}{\partial t} + \frac{\partial F_j}{\partial x_j} = 0 \tag{3.18}$$

where U and F_j are given in Eqs. (2.35) and (2.36).

To apply the DMLC scheme on the Euler equations (3.18), the auxiliary equations are required. In the spatial discretization, the locally global Lax-Friedrichs approach is first applied on the inviscid flux terms; then, the upwind and downwind schemes can be used to discretize the positive flux and negative flux. The procedures are similar with those of the MLC scheme. The main difference is that there are additional auxiliary equations for the cross derivatives of U to solve in the DMLC scheme. Therefore, the derivation and resulting formulas are more complicated. However, the numerical tests in Chapter 0 can prove that the computational

efficiency is improved due to the vanish of the cross-derivative approximations for the flux terms. The procedures for applying the DMLC scheme on the Euler equations are briefly described in the following part of this section.

In the Cartesian coordinates (x_1, x_2, x_3), the auxiliary equations for first derivatives are introduced as follows,

$$\frac{\partial U_{x_k}}{\partial t} + \frac{\partial F_{jx_k}}{\partial x_j} = 0 \tag{3.19}$$

where j, k = {1, 2, 3}, and j is a dummy index. Eq. (3.19) has two or three components in two-dimensional or three-dimensional cases respectively. For the DMLC scheme, auxiliary equations for cross derivatives are derived by taking derivatives on Eq. (3.19). For the sake of brevity, only two-dimensional cases are discussed in the following part of this section, and the extension from two-dimensional to three-dimensional cases are straightforward. The Euler equations (3.18) and the auxiliary equations (3.19) in two-dimensional cases can be written in vector forms as follows,

$$\frac{\partial}{\partial t}\begin{pmatrix} U \\ U_x \\ U_y \\ U_{xy} \end{pmatrix} = -\begin{pmatrix} F_{1x} + F_{2y} \\ F_{1xx} + F_{2xy} \\ F_{1xy} + F_{2yy} \\ F_{1yxx} + F_{2xyy} \end{pmatrix} \tag{3.20}$$

Similar as Eq. (3.5), three additional degrees of freedom can be defined as,

$$V = U_x, \quad W = U_y, \quad R = U_{xy} \tag{3.21}$$

Since F_1 and F_2 are nonlinear functions of U, the Jacobian matrices $A_1 = \partial F_1/\partial U$ and $A_2 = \partial F_2/\partial U$ are introduced. Then, the first derivatives and the cross derivatives of inviscid fluxes in Eq. (3.20) can be computed analytically as follows,

$$\begin{aligned} F_{1x} &= A_1 V, \quad F_{1y} = A_1 W, \quad F_{1xy} = A_1 R + A_{1y} V \\ F_{2x} &= A_2 V, \quad F_{2y} = A_2 W, \quad F_{2xy} = A_2 R + A_{2x} W \end{aligned} \tag{3.22}$$

Combining Eqs. (3.20) - (3.22), the system of equations used for the DMLC scheme can be obtained,

$$\frac{\partial}{\partial t}\begin{pmatrix} U \\ V \\ W \\ R \end{pmatrix} = -\begin{pmatrix} A_1 V + A_2 W \\ F_{1xx} + A_2 R + A_{2x} W \\ A_1 R + A_{1y} V + F_{2yy} \\ F_{1yxx} + F_{2xyy} \end{pmatrix} \tag{3.23}$$

Because the fluxes and their derivatives are calculated from Eqs. (2.36) and (3.22), it is clear that F_{1xx}, F_{1yxx} in Eq. (3.23) can be discretized along the x direction, and F_{2yy}, F_{2xyy} can be discretized along the y direction. The directional discretization follows the same formula as given in Eqs. (3.7) and (3.8).

Before applying the upwind DMLC schemes, the locally global Lax-Friedrichs approach [101] is used to the split the inviscid flux terms. All fluxes and their derivatives are decomposed into positive and negative wave fields as follows,

$$\begin{aligned} F_j &= F_j^+ + F_j^- \\ F_{jx_k} &= F_{jx_k}^+ + F_{jx_k}^- \\ F_{jx_kx_j} &= F_{jx_kx_j}^+ + F_{jx_kx_j}^- \\ F_{jx_kx_jx_j} &= F_{jx_kx_jx_j}^+ + F_{jx_kx_jx_j}^- \end{aligned} \tag{3.24}$$

where the subscripts $j, k = \{1, 2\}$. Note that j is not a dummy index any more in Eq. (3.24). There are four derivatives that need to be discretized in Eq. (3.23) and they are decomposed as,

$$\begin{aligned} F_{jx_jx_j} &= F_{jx_jx_j}^+ + F_{jx_jx_j}^- \\ F_{jx_kx_jx_j} &= F_{jx_kx_jx_j}^+ + F_{jx_kx_jx_j}^-, \quad j, k \in \{1, 2\}, \text{ and } j \neq k \end{aligned} \tag{3.25}$$

The positive part in Eq. (3.25) is approximated by the upwind DMLC scheme along the j direction, and the negative part is approximated by the downwind scheme in the same manner. The downwind DMLC scheme has the same formula as the upwind scheme in Eqs. (3.7) and

(3.8), but the opposite sign in α. In the locally global Lax-Friedrichs approach [101], F_j^+ and F_j^- and their first and cross derivatives are computed as follows,

$$F_j^+ = \frac{1}{2}(F_j + \Lambda U), \quad F_j^- = \frac{1}{2}(F_j - \Lambda U) \tag{3.26}$$

where, Λ is a positive parameter being a constant within each stencil, but a variant at different base points for the purpose of maintaining small dissipations. The first derivatives and cross derivatives in Eq. (3.22) can be decomposed in the same manner. Within an arbitrary stencil, Λ is determined from,

$$\Lambda = \max(\lambda_i) \tag{3.27}$$

where λ_i is a positive parameter chosen to be larger than the local maximum eigenvalues of the Jacobian A_j on the grid point i. The procedure is repeated for every base point. After the spatial discretization is finished, Eq. (3.23) becomes a system of ordinary differential equations, which can be solved by time-marching numerical methods like Runge-Kutta methods.

In summary, the DMLC scheme introduces the auxiliary equations for both first derivatives (u_x, u_y, u_z) and cross derivatives (u_{xy}, u_{yz}, u_{xz}, u_{xyz}). With the help of the additional degrees of freedom, the spatial discretization can be fulfilled along each dimension independently. Consequently, the DMLC scheme can overcome the inconsistency and the ad-hoc selection of grid points in cross-derivative approximations. Therefore, it should lead to better computational efficiency and spectral resolution than the MLC scheme.

3.4. Fourier Analysis

In this section, the two-dimensional Fourier analysis is performed first on the DMLC scheme, and the results of the MLC scheme are compared. The dissipative and dispersive errors,

spectral resolution, and anisotropic error are analyzed and compared. Then, the matrix method is used to analyze the stability of boundary closure schemes.

3.4.1 Two-Dimensional Fourier Analysis

The implementation of the two-dimensional Fourier analysis on the MLC schemes are described in Chapter 2. In this chapter, the method is implemented slightly different, where the Fourier analysis is formulated as an eigenvalue problem instead of solving the roots of a polynomial. This modification makes it easier to find the modes for the DMLC scheme.

The analysis is performed on the two-dimensional advection equation and its auxiliary equations, which is Eq. (3.5) for the DMLC scheme. To be generic, the convection angle θ and Fourier wave angle φ are distinguished, and the directional convection speed can be written as,

$$\begin{aligned} c_1 &= c \cdot \cos\theta \\ c_2 &= c \cdot \sin\theta \end{aligned} \tag{3.28}$$

where c is the magnitude of convection speed. The Fourier mode is of the following form,

$$\left(u, v, w, r\right)^T = \left(\hat{u}, \hat{v}, \hat{w}, \hat{r}\right)^T e^{\hat{a}t + i\hat{k}(x\cos\varphi + y\sin\varphi)} \tag{3.29}$$

where $\hat{k}$ is the wavenumber, $\hat{a}$ is a complex characteristic parameter as a function of $\hat{k}$, and φ is the Fourier wave angle which can be different from θ. If a uniform mesh with spacing h is used, the non-dimensional wavenumber k, the non-dimensional dissipation factor a, and the non-dimensional magnitude of the Fourier modes $\mathbf{U}$ can be defined as,

$$a = \frac{\hat{a}h}{c}, \quad k = \hat{k}h, \quad \mathbf{U} = \left(\hat{u}, h\hat{v}, h\hat{w}, h^2\hat{r}\right)^T \tag{3.30}$$

Substituting Eq. (3.29) into Eq. (3.5) and using the DMLC scheme in Eqs. (3.7) and (3.8) to discretize the spatial derivatives, an eigenvalue problem can be formulated as,

$$\mathbf{A}\mathbf{U}_{i,j} = a\mathbf{U}_{i,j} \tag{3.31}$$

where, $\mathbf{U}_{i,j}$ is the non-dimensional magnitude at the grid point (i, j), and $\mathbf{A}$ is an complex matrix dependent on θ, φ, k and the coefficients of the MLC scheme, as given below,

$$\mathbf{A} = -\cos\theta \begin{pmatrix} 0 & 1 & 0 & 0 \\ A_1 & B_1 & 0 & 0 \\ 0 & 0 & 0 & 1 \\ 0 & 0 & A_1 & B_1 \end{pmatrix} - \sin\theta \begin{pmatrix} 0 & 0 & 1 & 0 \\ 0 & 0 & 0 & 1 \\ A_2 & 0 & B_2 & 0 \\ 0 & A_2 & 0 & B_2 \end{pmatrix} \tag{3.32}$$

and the complex elements A_1, B_1, A_2, B_2 are,

$$\begin{aligned} A_1 &= \sum_{l=-L_1}^{L_2} a_l e^{ilk\cos\varphi}, \quad B_1 = \sum_{m=-M_1}^{M_2} b_m e^{imk\cos\varphi} \\ A_2 &= \sum_{l=-L_1}^{L_2} a_l e^{ilk\sin\varphi}, \quad B_2 = \sum_{m=-M_1}^{M_2} b_m e^{imk\sin\varphi} \end{aligned} \tag{3.33}$$

Four eigenvalues of $\mathbf{A}$ correspond to four modes in the two-dimensional Fourier analysis, which are the physical mode a_1, and three spurious modes a_1, a_2, a_3. The exact solution of a is,

$$a_{exc} = ik\cos(\theta - \varphi) \tag{3.34}$$

which is an imaginary number dependent on θ, φ, k. The real and imaginary part of modes a_1, a_2, a_3, a_4 play important roles in the Fourier analysis. It is required that $R(a_1)$ is small to reduce dissipative error, and $I(a_1)$ is close to a_{exc} for small dispersive error. Meanwhile, $R(a_1)$, $R(a_2)$, $R(a_3)$, $R(a_4)$ should all be non-positive to ensure the stability of the MLC scheme.

For the MLC scheme, three eigenvalues of $\mathbf{A}$ correspond to one physical mode a_1, and two spurious modes a_1, a_2. The physical and spurious modes of the MLC scheme are analyzed in the same way as the DMLC scheme.

In the following part of this section, the Fourier analysis results of the DMLC scheme are presented, and the comparison with the MLC scheme is given. As mentioned in the introduction, the Fourier analysis will show the weak numerical instability of the MLC scheme.

Fourier Analysis of the Third-Order 1-1-1-1 Scheme

First, the third-order 1-1-1-1 scheme with α = 1.5 is analyzed with the two-dimensional Fourier analysis. In Fig. 3.1, the dissipation factors of the DMLC and MLC schemes with different convection angle θ and Fourier wave angle φ are compared. All modes are presented, where $R(a_1)$ is the dissipation factor of the physical mode and $R(a_2)$, $R(a_3)$, $R(a_4)$ are dissipation factors of spurious modes.

When $\theta = \varphi = 0$, the two-dimensional Fourier analysis reduces to the one-dimensional case (see [101] for 1-D Fourier analysis), which is not presented here.

When $\theta = 0$ and $\varphi = \pi/4$, as shown in Fig. 3.1(a), the 1-1-1-1 DMLC scheme has the same behavior as the 1-1-1-1 MLC scheme. All modes are non-positive, which indicates both the 1-1-1-1 DMLC and MLC schemes are stable. Only two distinctive modes are observed, which are a physical mode a_1 and a spurious mode a_2. The dissipative error $R(a_1)$ increases with the wavenumber k, and $R(a_2)$ decreases with k. The behaviors of $R(a_1)$ and $R(a_2)$ are favorable. If the grid resolution is good enough (small k) in a flow simulation, the spurious mode should damp out due to the large dissipation factor, and the dissipative error for the physical mode should be very small. Other modes in Fig. 3.1(a) are trivial. The spurious mode a_3 in the 1-1-1-1 MLC scheme induced by the cross-derivative approximation are neutral ($R(a_3) = 0$), which means a_3 should not be changed during the simulation. For the 1-1-1-1 DMLC scheme, $R(a_3) = R(a_1)$ and $R(a_4) = R(a_2)$ are observed, indicating that the mode a_3 are the same as the physical mode a_1 and the mode a_4 are equivalent to the spurious mode a_2.

When $\theta = \pi/4$ and $\varphi = 0$ as shown in Fig. 3.1(b), the 1-1-1-1 DMLC scheme has different behaviors from the 1-1-1-1 MLC scheme in the dissipation factors. There are more distinctive

modes appearing such as a_3 in the MLC scheme and a_3, a_4 in the DMLC scheme. The behaviors of $R(a_1)$ and $R(a_2)$ are still the same as in Fig. 3.1(a). For the MLC scheme, the $R(a_3)$ is a negative constant means that the spurious mode a_3 is uniformed decayed for any wavenumber. For the DMLC scheme, $R(a_3)$ and $R(a_4)$ are similar with $R(a_1)$ and $R(a_2)$, except that the position is shifted to the negative direction. Specifically, a_4 of the DMLC scheme is more dissipative than other modes, which is related to the additional degree of freedom u_{xy}. It could increase the stiffness of the DMLC scheme.

When $\theta = \varphi = \pi/4$, as shown in Fig. 3.1(c, d), the 1-1-1-1 DMLC scheme has different behaviors from the 1-1-1-1 MLC scheme in the dissipation factors. The most noteworthy feature for the MLC scheme is the numerical instability of a_1 appearing in the neighboring region of k = 1.75. The magnitude of the positive part of $R(a_1)$, which equals to 10^{-3}, is very small compared to that of a typical unstable mode. For example, in an unstable upwind MLC scheme [101], the peak of $R(a_1)$ is usually greater than 0.5. Meanwhile, the instability only appears in a very narrow range of wavenumbers. Therefore, this specific behavior is termed as the weak numerical instability. It has been proved by numerical tests that the weak numerical instability usually does not give rise to the divergence of a flow simulation [101], however, the potential risk of divergence exists in very long-time simulations. In the 1-1-1-1 DMLC scheme, the numerical instability is removed, and all modes become stable with non-positive dissipation factors. Meanwhile, when both θ and φ is not zero, the physical mode a_1 of the DMLC scheme is slightly more dissipative than a_1 of the MLC scheme for large k's. The spurious modes a_2 and a_3 in the DMLC scheme overlap with a_2 of the MLC scheme; a_3 of the MLC scheme is very close to a_2, while a_4 of the DMLC scheme is more dissipative than other modes.

When $\theta = \pi/3$, $\varphi = \pi/6$, as shown in Fig. 3.1(e, f), the dissipation factors have similar features as Fig. 3.1(c, d) except three aspects. First, the numerical instability of the 1-1-1-1 MLC scheme is significantly reduced to the magnitude of 10^{-6}, which is three orders smaller than the case in Fig. 3.1(d). In fact, we find that the case of $\theta = \varphi = \pi/4$ has the largest instability observed. Second, the behaviors of spurious modes become more complicated. For both the 1-1-1-1 DMLC and MLC schemes, $R(a_2)$ and $R(a_3)$ are distinguishable and the latter is more dissipative. Last, all modes of the 1-1-1-1 DMLC scheme are distinguishable from the modes of the 1-1-1-1 MLC scheme, indicating that DMLC and MLC schemes should have different behaviors in cases where θ and φ are not equivalent and both non-zero.

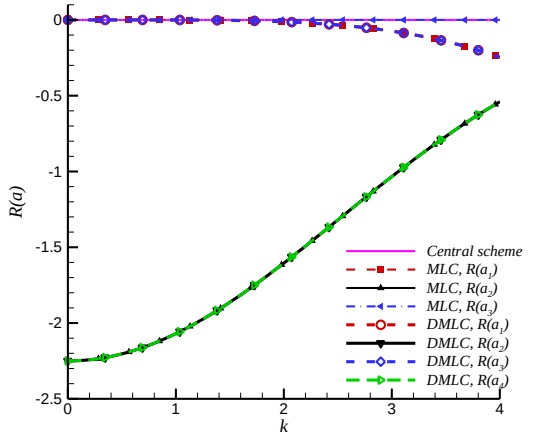

a), $\theta = 0$, $\varphi = \pi/4$

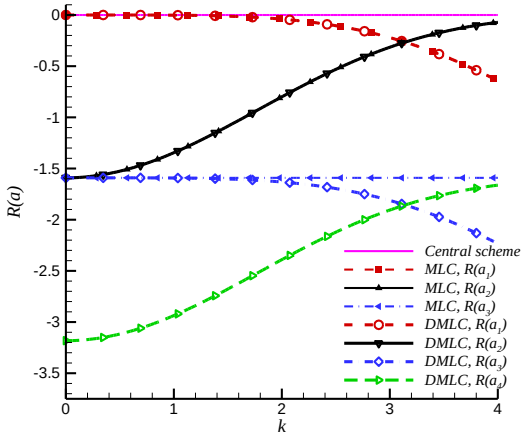

b), $\theta = \pi/4$, $\varphi = 0$

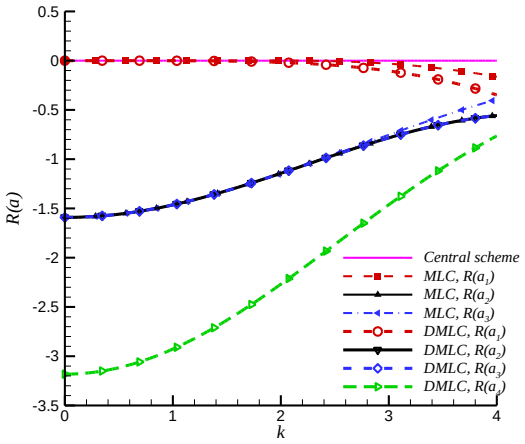

c), $\theta = \pi/4$, $\varphi = \pi/4$

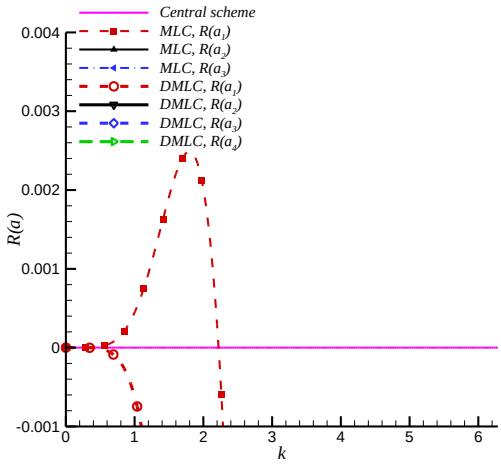

d), $\theta = \pi/4$, $\varphi = \pi/4$ (zoomed-in)

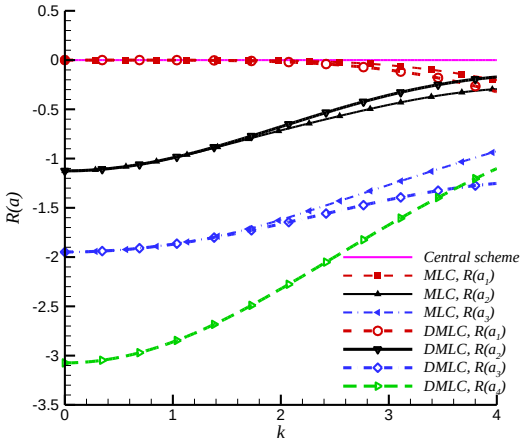

e), $\theta = \pi/3$, $\varphi = \pi/6$

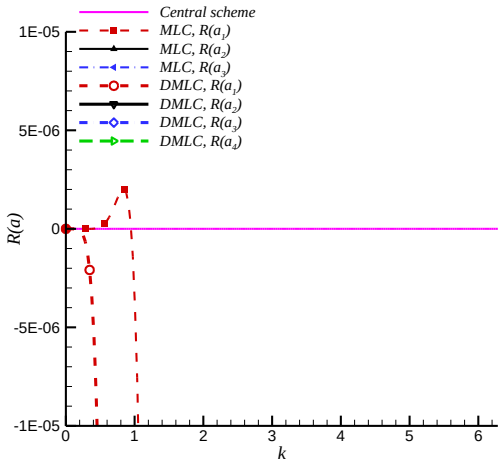

f), $\theta = \pi/3$, $\varphi = \pi/6$ (zoomed-in)

Fig. 3.1. Dissipation factors of the 1-1-1-1 DMLC and MLC schemes (3rd order) for two-dimensional cases.

The modified wavenumber $I(a_1)$ of the 1-1-1-1 DMLC and MLC schemes are presented in Fig. 3.2. Various θ and φ are analyzed, and the straight lines are exact solutions of $I(a)$ for different cases. When $\theta = 0$ or $\varphi = 0$, the 1-1-1-1 DMLC scheme generates the same $I(a_1)$ as the

1-1-1-1 MLC scheme. However, in the case of $\theta = \varphi = \pi/4$ and the case of $\theta = \pi/3$, $\varphi = \pi/6$, the DMLC scheme has much better spectral resolution than the MLC scheme. In general, the introduce of u_{xy} as the additional degree of freedom can improve the spectral resolution for the two-dimensional simulations if both θ and φ are non-zero. A noteworthy feature of the DMLC scheme is that, the spectral resolution is better in the case of $\theta = \varphi = \pi/4$ than that in the case of $\theta = \varphi = 0$, which is consistent with most conventional finite difference methods. For the MLC scheme, on the other hand, the spectral resolution is slightly decreased when $\theta = \varphi = \pi/4$ compared with the case of $\theta = \varphi = 0$. This difference is presented more clearly by the anisotropy analysis of phase speed in Section 3.4.2.

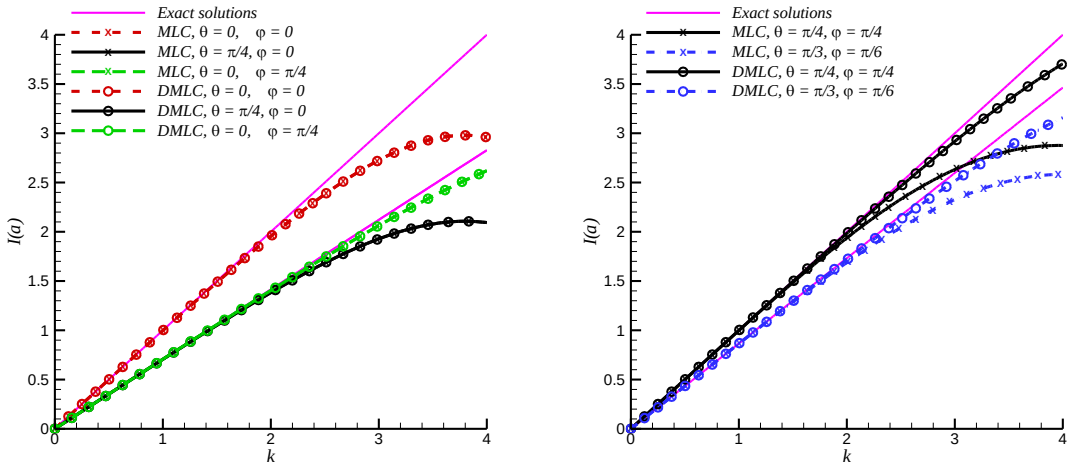

Fig. 3.2. Modified wavenumber I(a1) of the 1-1-1-1 DMLC and MLC schemes (3rd order) for two-dimensional cases.

An important observation from Fig. 3.1 and Fig. 3.2 is that, the DMLC and MLC schemes are both stable and show the same spectral resolution if either θ or φ is zero. The explanation is that the main difference of the DMLC scheme and MLC scheme is whether the cross-derivative approximations are needed. If θ or φ is zero, the cross derivative vanishes either in the governing

equation (θ = 0) or in the solution (φ = 0); therefore, the DMLC and MLC schemes behave similarly in those cases.

Fourier Analysis of the Fifth-Order 2-2-1-1 Scheme

Then, the two-dimensional Fourier analysis is carried out to the fifth-order 2-2-1-1 scheme with α = -1. In Fig. 3.3, the dissipation factors of the DMLC and MLC schemes with different convection angle θ and Fourier wave angle φ are compared. Similar behaviors of all the modes as in Fig. 3.1 are observed for both the 2-2-1-1 DMLC and MLC schemes except the following differences. First, all modes in Fig. 3.3 have much smaller dissipations for all k's within the range of [0, 4], which is more significant for the spurious modes. It indicates that reducing the stencil size in the derivative layer leads to smaller dissipation in the spurious modes. This is reasonable as the conventional finite difference method without the derivative layer does not have spurious modes, or equivalently, we can think the $R(a)$ of its spurious mode reduces to zero when the grid size in derivative layer is zero. Second, the weak numerical instability of the 2-2-1-1 MLC scheme appears in both $R(a_1)$ and $R(a_3)$ when $\theta = \varphi = \pi/4$, as shown in Fig. 3.3 (d), which is different from Fig. 3.1(d). For the case of $\theta = \pi/3$, $\varphi = \pi/6$, the 2-2-1-1 MLC scheme only generates numerical instability in $R(a_1)$, and the magnitude is much smaller than the case of $\theta = \varphi = \pi/4$. As a comparison, the 2-2-1-1 DMLC scheme is always stable in both physical and spurious modes. Third, an unusual bifurcation for small k's is observed in the spurious modes - $R(a_2)$ and $R(a_3)$. The reason behind this behavior is not clear at this moment. A possible explanation is the combined effect of the inconsistency of the 1-D and 2-D formulas and the

different stencil sizes of the value and derivative layers in the 2-2-1-1 MLC scheme. The bifurcation of the spurious modes is not observed for the 2-2-1-1 DMLC scheme.

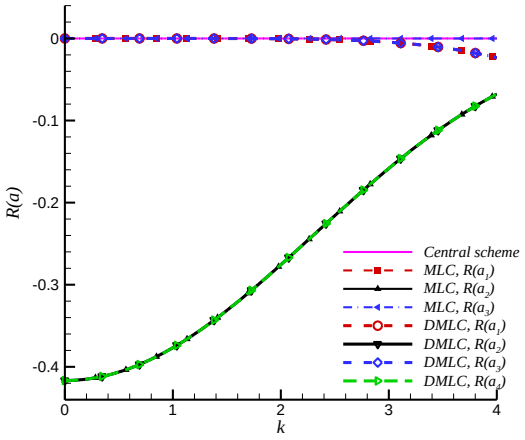

a), $\theta = 0$, $\varphi = \pi/4$

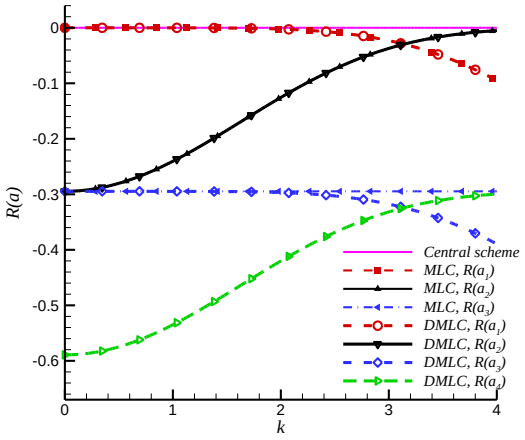

b), $\theta = \pi/4$, $\varphi = 0$

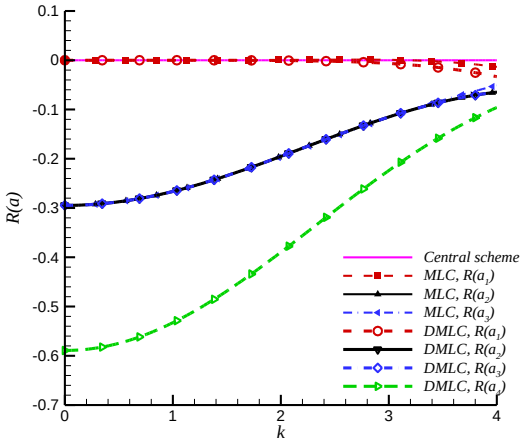

c), $\theta = \pi/4$, $\varphi = \pi/4$

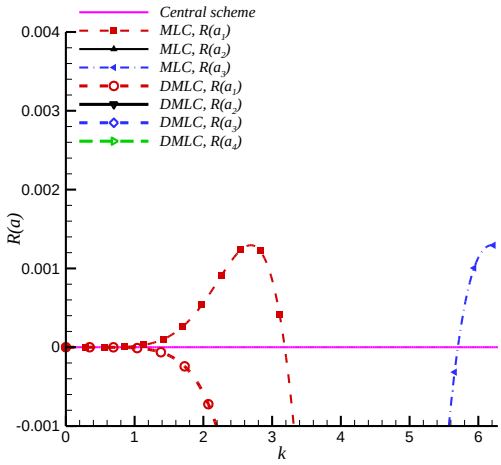

d), $\theta = \pi/4$, $\varphi = \pi/4$ (zoomed-in)

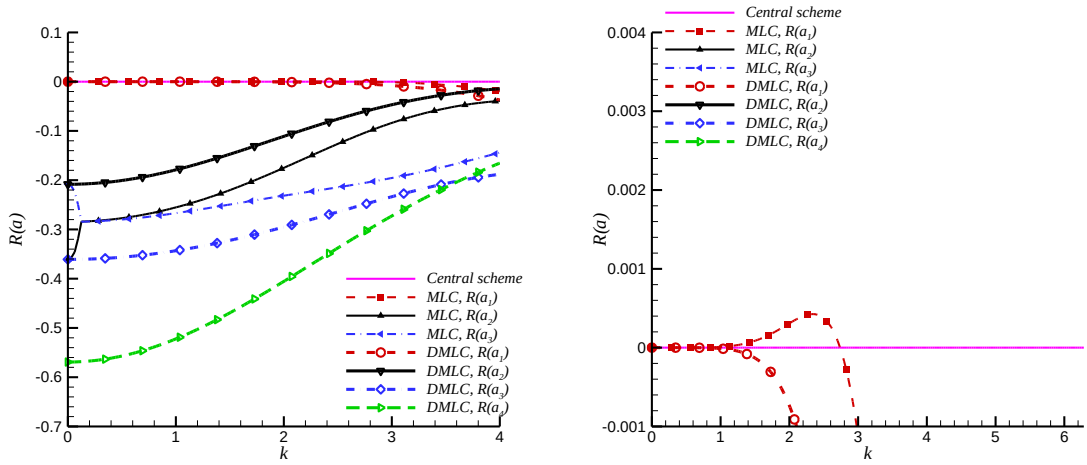

e), $\theta = \pi/3$, $\varphi = \pi/6$ f), $\theta = \pi/3$, $\varphi = \pi/6$ (zoomed-in)

Fig. 3.3. Dissipation factors of the 2-2-1-1 DMLC and MLC schemes (5th order) for two-dimensional cases.

The modified wavenumber $I(a_1)$ of the fifth-order 2-2-1-1 DMLC and MLC schemes are presented in Fig. 3.4. The 2-2-1-1 DMLC scheme and the 2-2-1-1 MLC scheme show the same spectral resolution when either θ or φ is zero; and the former has much better resolution when both θ and φ are non-zero, which is the same as the observation in Fig. 3.2. Comparing Fig. 3.2 and Fig. 3.4, we observe that the 2-2-1-1 DMLC scheme shows improved resolutions than the 1-1-1-1 DMLC scheme in all cases with different θ and φ. Similarly, the 2-2-1-1 MLC scheme also has better resolution than the 1-1-1-1 MLC scheme except in the case of $\theta = \pi/3$ and $\varphi = \pi/6$, where the spectral resolution of the 1-1-1-1 MLC scheme for large wavenumbers is slightly better.

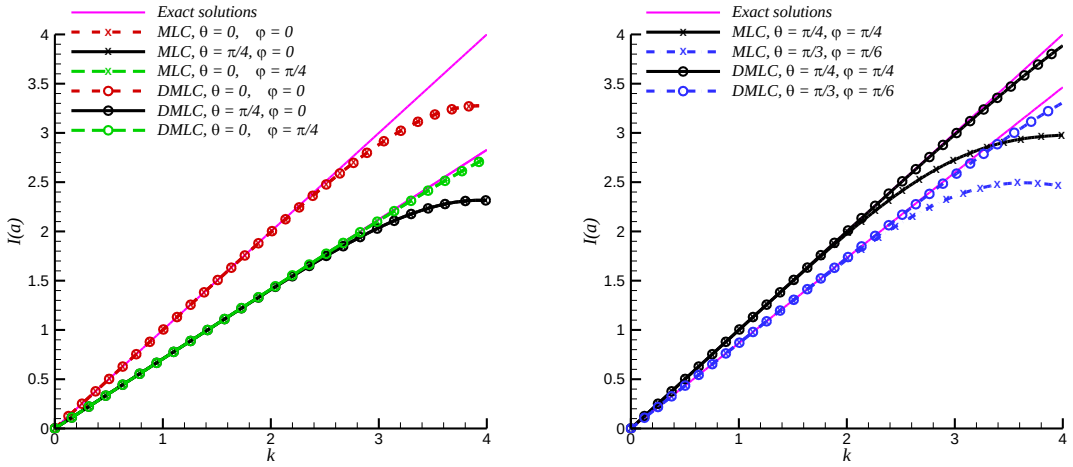

Fig. 3.4. Modified wavenumber I(a1) of the 2-2-1-1 DMLC and MLC schemes (5th order) for two-dimensional cases.

Fourier Analysis of the Seventh-Order 2-2-2-2 Scheme

Finally, the two-dimensional Fourier analysis is carried out to the seventh-order 2-2-2-2 scheme with α = 12. The dissipation factors of the DMLC and MLC schemes are given in Fig. 3.5, and the modified wavenumbers are given in Fig. 3.6. Again, various convection angle θ and Fourier wave angle φ are compared. The Fourier analysis results of the seventh-order schemes are very similar to the third and fifth-order schemes. Compared with the third-order 1-1-1-1 scheme, both the 2-2-2-2 DMLC and MLC schemes has smaller dissipation and better spectral resolutions. The 2-2-2-2 DMLC scheme is always stable and weak numerical instability exists in the 2-2-2-2 MLC scheme when both θ and φ is non-zero. Again, the case of $\theta = \varphi = \pi/4$ shows the largest instability. The magnitudes of instability of the 2-2-2-2 MLC scheme are larger than those of the 1-1-1-1 or 2-2-1-1 MLC schemes, which means the 2-2-2-2 MLC scheme is less stable. Specifically, the seventh-order 2-2-2-2 scheme has the largest magnitude of 0.0039, the

fifth-order 2-2-1-1 scheme has a magnitude of 0.0014 and the third-order 1-1-1-1 scheme has a magnitude of 0.0025.

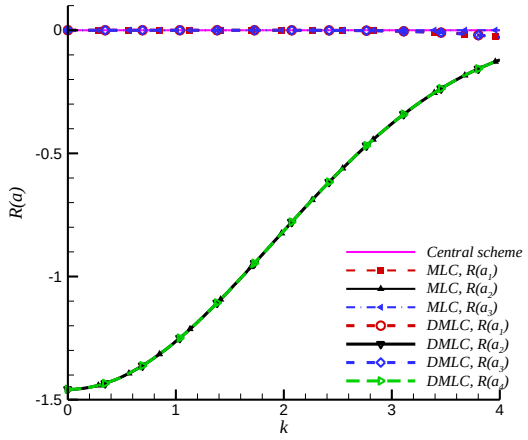

a), $\theta = 0$, $\varphi = \pi/4$

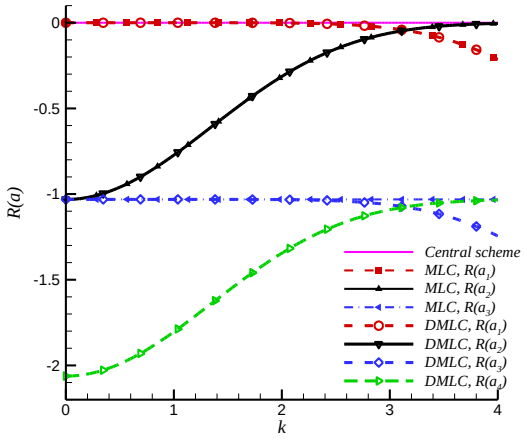

b), $\theta = \pi/4$, $\varphi = 0$

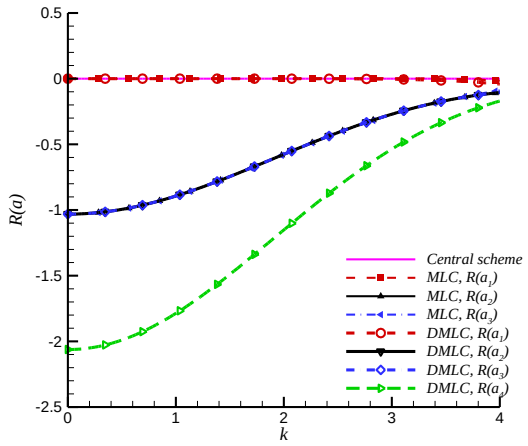

c), $\theta = \pi/4$, $\varphi = \pi/4$

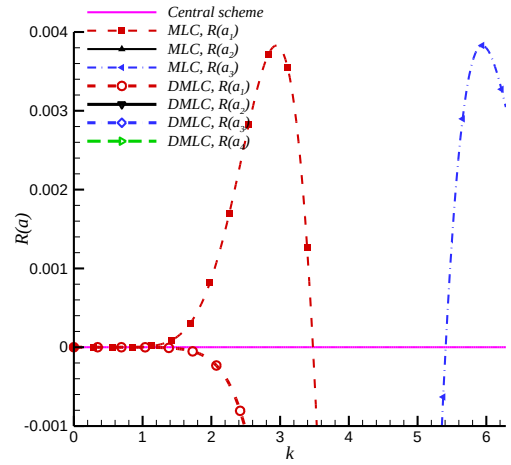

d), $\theta = \pi/4$, $\varphi = \pi/4$ (zoomed-in)

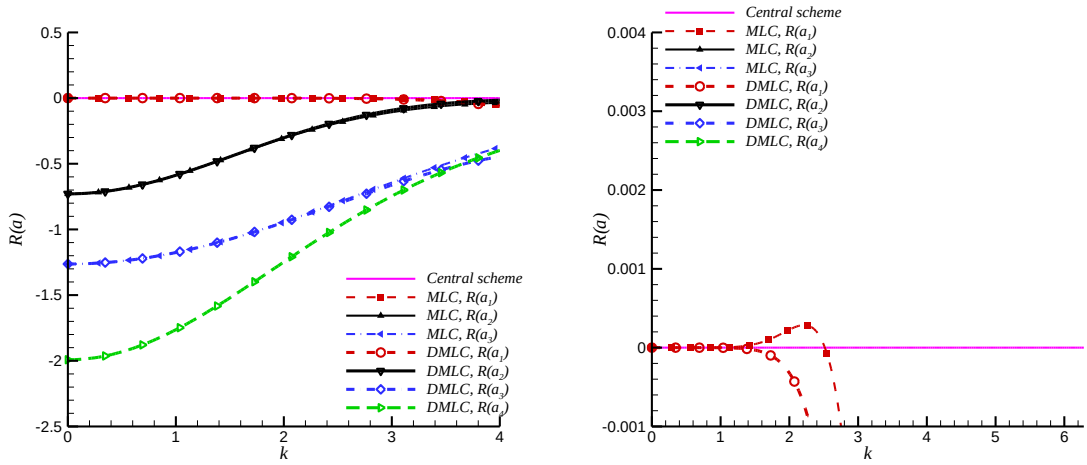

e), $\theta = \pi/3$, $\varphi = \pi/6$ f), $\theta = \pi/3$, $\varphi = \pi/6$ (zoomed-in)

Fig. 3.5. Dissipation factors of the 2-2-2-2 DMLC and MLC schemes (7th order) for two-dimensional cases.

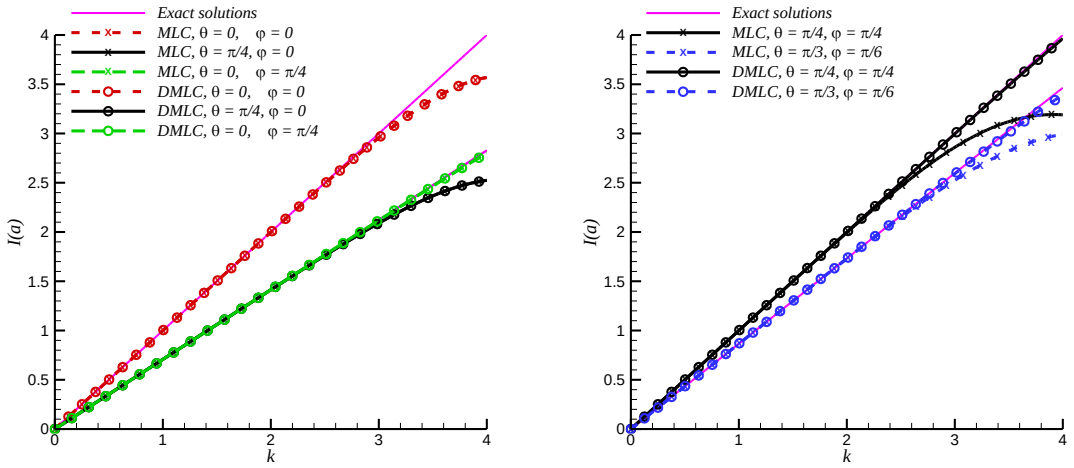

Fig. 3.6. Modified wavenumber I(a1) of the 2-2-2-2 DMLC and MLC schemes (7th order) for two-dimensional cases.

A summary of the Fourier analysis above is given to end this section:

1. The DMLC and MLC schemes have the same dissipation factors when θ is zero. When θ is not zero, the DMLC and MLC schemes both become more complicated and show different behaviors. Specifically, the DMLC scheme generates an additional spurious mode which is significantly more dissipative than other modes for small wavenumbers, which could increase its stiffness.

2. The MLC scheme shows weak numerical instabilities when both θ and φ is non-zero, where the case of $\theta = \varphi = \pi/4$ generates the largest instability. Increasing the order of accuracy usually leads to stronger numerical instability. On the other hand, the DMLC scheme is always stable benefited from the directional discretization technique.

3. When either θ or φ is zero, the DMLC and MLC schemes have the same spectral resolutions; and when both θ and φ is non-zero, the DMLC scheme shows much better spectral resolution than the MLC scheme because of the additional degree of freedom u_{xy}.

4. For both the DMLC and MLC schemes, increasing the order of accuracy leads to smaller dissipation and higher spectral resolution.

It can be inferred that the new DMLC scheme should have better accuracy than the MLC scheme, and should always be stable in two-dimensional flow simulations; while the MLC scheme could be unstable in very long-time simulations, and the 2-2-2-2 MLC scheme may be the most probable one to diverge. These inferences are validated through numerical tests in Chapter 0.

3.4.2 Anisotropic Analysis of Phase Speed

In this section, the anisotropy analysis is performed following the same approach as in the two-dimensional Fourier analysis. To investigate the anisotropic error of the DMLC schemes, the phase speed c_p is computed from the modified wavenumber $I(a_1)$,

$$c_p(k,\theta) = \frac{I(a_1)}{k} \tag{3.35}$$

where $I(a_1)$ is a function of wavenumber k, convection angle θ, and Fourier wave angle φ. Here, we follow Lele's approach [20] in the anisotropy analysis by assuming $\varphi = \theta$, so that c_p is only dependent on k and θ.

Fig. 3.7 compares the phase speed c_p of the DMLC and MLC schemes. The c_p contours are plotted in the range of $k = [0, 2\pi]$ and $\theta = [0, 2\pi]$, where each curve represents the c_p value for different θ and a constant k. The curves for $k = [0, \pi]$ and three reference values (1.3π, 1.6π, 1.9π) are plotted with solid lines, while other curves for $k = [\pi, 2\pi]$ are plotted with dashed lines. The exact value of c_p is 1 for any k and θ, which corresponds to the outermost circle in the plots. Two properties can be analyzed from the figure; the distorted shape from a perfect circle represents the anisotropic error, and the shrink of the circle represents the dispersive error. Small k values correspond to outer contours, and large k values are represented by inner contours. The figures show that both the anisotropic and dispersive errors increase as k increases from 0 to 2π. Comparing the DMLC and MLC schemes with the same order of accuracy, we find that the DMLC scheme always has smaller dispersive error than the MLC scheme except when $\theta = 0$, π, and $\pm\pi/2$. Meanwhile, the DMLC scheme also shows smaller anisotropic error for a large portion of the wavenumbers in $[0, 2\pi]$. Only when k is very large (contours close to the center), the MLC scheme shows better isotropy. This advantage of the MLC scheme on the isotropy becomes more significant when the order of accuracy increases. For example, the 2-2-2-2 DMLC scheme in (c)

shows much smaller anisotropic error than the 2-2-2-2 MLC scheme in (f) for $k < 1.6\pi$ (outside the orange solid line). The small k components are usually dominating and more important in flow simulations. Therefore, the DMLC scheme should possess better numerical isotropy than the MLC scheme for two-dimensional cases.

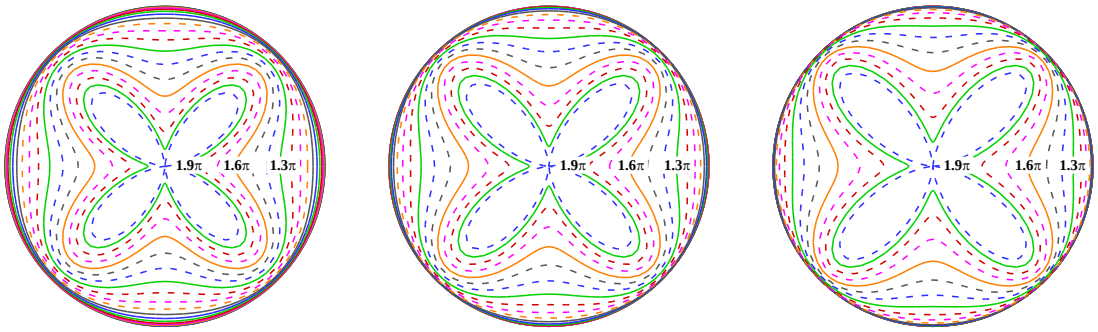

(a) (b) (c)

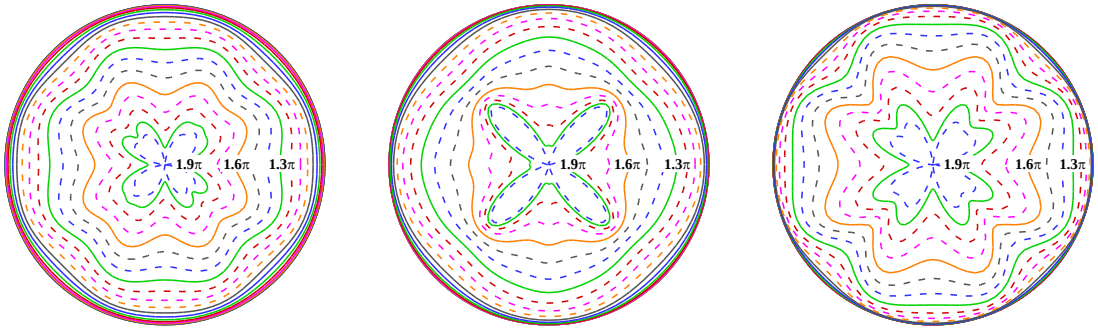

(d) (e) (f)

Fig. 3.7. Polar plot of cp for the DMLC and MLC schemes (contours are plotted at k/π = 1/50, 5/50, …, 100/50): a), third-order DMLC scheme; b), fifth-order DMLC scheme; c), seventh-order DMLC scheme; d), third-order MLC scheme; e), fifth-order MLC scheme; f), seventh-order MLC scheme.

It is also noteworthy that the contours of the DMLC and MLC schemes possess different patterns. The DMLC schemes in Fig. 3.7 (a, b, c) always have the smallest dispersive error at $\theta = \pm\pi/4$ and $\pm 3\pi/4$, and the largest error at $\theta = 0$, π, and $\pm\pi/2$. While the MLC schemes Fig. 3.7 (d, e, f) have more complicated patterns. Specifically, the 1-1-1-1 MLC scheme and the 2-2-2-2 MLC scheme have similar patterns where the smallest dispersive error seems to appear at $\theta = \pm\pi/8$, $\pm 3\pi/8$, $\pm 5\pi/8$, $\pm 7\pi/8$, and the largest error seems to locate at $\theta = 0$, π, and $\pm\pi/2$. The 2-2-1-1 MLC scheme presents an unclear pattern in the contours; a possible reason is that the stencil size for the value layer and the derivative layer are different.

The complex pattern of the MLC schemes is due to the inconsistency between the 1-D and 2-D MLC formulations. As mentioned in Section 3.1, the formulas for second derivatives and cross derivatives are derived separately in the MLC scheme, and the upwind setting is applied to second derivatives only. On the other hand, the DMLC scheme can use the same formula for all derivatives through the directional discretization technique; therefore, the upwind scheme can apply to the entire system. An evidence is from the anisotropy analysis for conventional finite difference methods. In Fig. 3.8, the phase speed c_p of Zhong's fifth-order upwind explicit scheme with $\alpha = -6$, and Zhong's fifth-order upwind compact scheme with $\alpha = -1$ [21] are analyzed in a similar way. Because a mono-layer scheme cannot resolve any wave with $k > \pi$, only k within $[0, \pi]$ is plotted. It is clearly that the both Zhong's explicit scheme and compact scheme in Fig. 3.8 shows the same pattern as the DMLC scheme in Fig. 3.7 (a, b, c), although these conventional schemes have much lower spectral resolution due to their the mono-layer framework. The phase speed anisotropy indicates that the DMLC scheme has some similar "simplicity" with conventional mono-layer schemes, which is a result of the directional discretization technique. This shared simplicity makes the DMLC scheme and conventional finite difference scheme

produce smaller dispersive error when the flow is not aligned with the coordinate axis. For the MLC scheme, the reduce of dispersive error is not obvious.

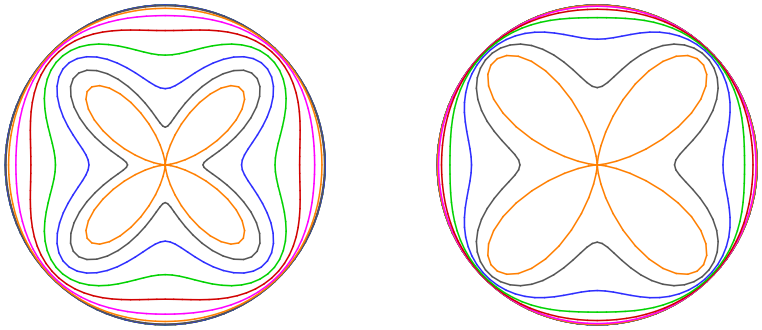

a) b)

Fig. 3.8. Polar plot of cp for conventional finite difference methods (contours are plotted at k/π = 1/50, 5/50, …, 45/50, 50/50): a), Zhong's fifth-order explicit scheme; b), Zhong's fifth-order compact scheme.

In summary, the anisotropy analysis demonstrates that the DMLC scheme has better isotropic phase speed than the MLC scheme in two-dimensional cases. Through the directional discretization technique, the dispersive error is reduced in the full range of wavenumbers, and the anisotropic error is reduced for a large portion of wavenumbers in $[0, 2\pi]$. The DMLC scheme can also achieve the consistency in the multi-layer framework. Accordingly, it has a simple and clear pattern in the anisotropy contours as the conventional finite difference method. The DMLC scheme produces much smaller dispersive error when the flow is not aligned with the coordinate axis, which is preferable for multi-dimensional simulations. On the other hand, the MLC scheme shows much more complicated patterns in the anisotropy contours.

3.5. Stability Analysis of Boundary Closure Scheme

Like other high-order finite difference methods, the DMLC scheme require boundary closure schemes for grid points on or near the boundaries of the computational domain. The stability of the inner DMLC scheme can be affected by the boundary closure schemes. In Section 2.5, the matrix method was used to analyze the stability of boundary closure schemes for the MLC schemes in one-dimensional cases [101]. This method can be extended to two-dimensional cases and applied to the stability analysis of both the MLC scheme and the new DMLC scheme.

The two-dimensional advection equation and its auxiliary equations as shown in Eq. (3.5) are used again in the matrix method. A finite domain is discretized by a uniform mesh with grid spacing h in both x and y direction, as shown in Fig. 3.9. Both x and y are in the range of $[0, Nh]$, i.e., the indexes i and j arrange from 0 to N. Inflow boundary conditions are used at $i = 0$ and $j = 0$, and characteristic boundary conditions are used at $i = N$ and $j = N$. For the linear advection, the inflow conditions are specified by $u^i_0(y, t)$ and $u^j_0(x, t)$; the characteristic boundary conditions are implemented by using one-sided scheme. The upwind schemes on centered stencil are used at interior grid points, and several boundary closure schemes are applied when the stencil of inner scheme goes beyond the left and right boundaries. For the new DMLC schemes, both the 1-D inner scheme and the 1-D boundary closure scheme can be extended to two-dimensional cases naturally without extra derivations. For the MLC schemes, formulas of boundary closure schemes for cross derivatives are derived carefully, though it is also an ad-hoc choice which may not be optimal.

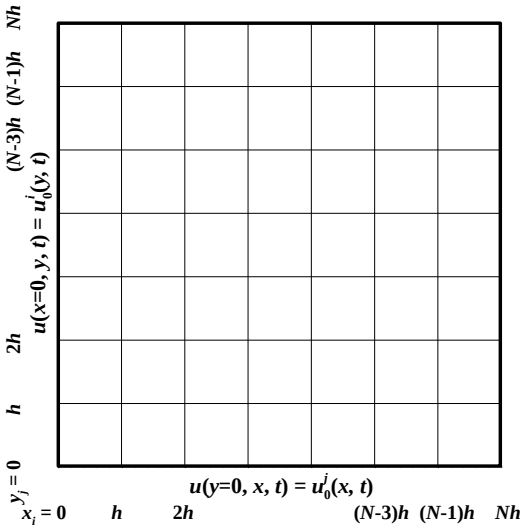

Fig. 3.9. Schematic for stability analysis on two-dimensional linear advection equation.

In the matrix method, Eq. (3.5) is discretized into a system of ordinary differential equations by using the inner and boundary closure schemes. By assuming c = 1 and defining the convection angle θ, c_1 and c_2 can be replaced by $\cos\theta$ and $\sin\theta$ respectively. The resulting equations can be written in a system of ordinary differential equations in matrix form,

$$\frac{d}{dt}\overline{\mathbf{U}} = \mathbf{L}\cdot\overline{\mathbf{U}} + \mathbf{G}(t) \tag{3.36}$$

where $\mathbf{G}(t)$ is the matrix containing all the boundary source terms which can be ignored in the stability analysis. The first normal derivatives and cross derivatives on the inflow boundary can be determined from the two-dimensional advection equation as follows,

$$
\begin{aligned}
u_y\left(x, y=0, t\right) &= -\frac{1}{c_2}\left[c_1 u_x\left(x, y=0, t\right) + u_t\left(x, y=0, t\right)\right] \\
u_{xy}\left(x, y=0, t\right) &= -\frac{1}{c_2}\left[c_1 u_{xx}\left(x, y=0, t\right) + u_{xt}\left(x, y=0, t\right)\right] \\
u_x\left(x=0, y, t\right) &= -\frac{1}{c_1}\left[c_2 u_y\left(x=0, y, t\right) + u_t\left(x=0, y, t\right)\right] \\
u_{xy}\left(x=0, y, t\right) &= -\frac{1}{c_1}\left[c_2 u_{yy}\left(x=0, y, t\right) + u_{yt}\left(x=0, y, t\right)\right]
\end{aligned}
\tag{3.37}
$$

where the temporal derivative on the right-hand side is prescribed and other terms can be calculated analytically or approximated locally on the boundaries. If the DMLC scheme is applied, $\overline{\mathbf{U}}$ and $\mathbf{L}$ in Eq. (3.36) have the form,

$$
\overline{\mathbf{U}} = \left(\mathbf{U}, \mathbf{U_x}, \mathbf{U_y}, \mathbf{U_{xy}}\right)^T, \quad \mathbf{L} = -\begin{pmatrix}
\mathbf{0} & \mathbf{I}\cos\theta & \mathbf{I}\sin\theta & \mathbf{0} \\
\mathbf{A}_1\cos\theta & \mathbf{B}_1\cos\theta & \mathbf{0} & \mathbf{I}\sin\theta \\
\mathbf{A}_2\sin\theta & \mathbf{0} & \mathbf{B}_2\sin\theta & \mathbf{I}\cos\theta \\
\mathbf{0} & \mathbf{A}_2\sin\theta & \mathbf{A}_1\cos\theta & \mathbf{B}_1\cos\theta + \mathbf{B}_2\sin\theta
\end{pmatrix} \tag{3.38}
$$

where $\mathbf{U}$, $\mathbf{U_x}$, $\mathbf{U_y}$, $\mathbf{U_{xy}}$ are vectors containing all the unknowns at the grid points, and matrices $\mathbf{A_1}$, $\mathbf{A_2}$ and $\mathbf{B_1}$, $\mathbf{B_2}$ consist of the coefficients of both the 1-D inner scheme and 1-D boundary closure schemes. If the MLC scheme is applied, $\overline{\mathbf{U}}$ and $\mathbf{L}$ in Eq. (3.36) have the form,

$$
\overline{\mathbf{U}} = \left(\mathbf{U}, \mathbf{U_x}, \mathbf{U_y}\right)^T, \quad \mathbf{L} = -\begin{pmatrix}
\mathbf{0} & \mathbf{I}\cos\theta & \mathbf{I}\sin\theta \\
\mathbf{A}_1\cos\theta + \mathbf{C}\sin\theta & \mathbf{B}_1\cos\theta + \mathbf{D}\sin\theta & \mathbf{E}\sin\theta \\
\mathbf{A}_2\sin\theta + \mathbf{C}\cos\theta & \mathbf{D}\cos\theta & \mathbf{B}_2\sin\theta + \mathbf{E}\cos\theta
\end{pmatrix} \tag{3.39}
$$

where matrices $\mathbf{A_1}$, $\mathbf{A_2}$ and $\mathbf{B_1}$, $\mathbf{B_2}$ keep the same and $\mathbf{C}$, $\mathbf{D}$, and $\mathbf{E}$ contain the coefficients of both the 2-D inner scheme and 2-D boundary closure schemes. The dimension of the vectors and matrices are as follows,

$$
\mathbf{U},\ \mathbf{U_x},\ \mathbf{U_y},\ \mathbf{U_{xy}} \in R^{N^2}, \qquad \mathbf{I},\ \mathbf{A}_1,\ \mathbf{A}_2,\ \mathbf{B}_1,\ \mathbf{B}_2,\ \mathbf{C},\ \mathbf{D},\ \mathbf{E} \in R^{N^2 \times N^2} \tag{3.40}
$$

The stability of Eq. (3.36) is determined by eigenvalue of matrix $\mathbf{L}$, which only depends on the particular inner and boundary closure schemes. For asymptotic stability, the real part of all the

eigenvalues of **L** needs to be non-positive. Here, the eigenvalues of **L** are solved numerically, and the eigenvalue spectrum is used to show stability. Different α values for the 1-D inner scheme are analyzed.

From the stability analysis of boundary closure scheme for the MLC scheme in one-dimensional cases [101], two stable configurations of inner and boundary closure schemes are obtained, which are listed in Table 5.2. In this section, the configuration is extended to two-dimensional cases. For the DMLC scheme with the spatial discretization, the same configuration can be applied. For the MLC scheme, the additional configuration for the cross derivatives are listed in Table 3.2. Note that inflow boundary conditions are applied on $i = 0$ and $j = 0$, where the values and tangential derivatives are prescribed and the normal derivatives are determined from Eq. (3.37). From the configurations in Table 5.2 and Table 3.2, it is expected that Case 1 have a third-order global accuracy and Case 2 have a seventh-order global accuracy. Both the 1-D and 2-D inner schemes are presented in Chapter 2. The formulas for the 1-D boundary closure schemes can be found in Appendix A, and the formulas for the 2-D boundary closure schemes needed by MLC schemes are given in Appendix B.

Table 3.1. Selection of the 1-D inner schemes and 1-D boundary closure schemes for second derivatives.

Case 1: 3rd-order global accuracy	Case 2: 7th-order global accuracy
	i (j) = 1: 6th-order 1-2-1-2 scheme
i (j) = 1 to *N*-1: 3rd-order 1-1-1-1 scheme	*i (j)* = 2 to *N*-2: 7th-order 2-2-2-2 scheme
i (j) = *N*: 3rd-order 2-0-1-0 scheme	*i (j)* = *N*-1: 6th-order 2-1-2-1 scheme
	i (j) = *N*: 6th-order 3-0-3-0 scheme

Table 3.2. Selection of the 2-D inner schemes and 2-D boundary closure schemes for cross derivatives in MLC schemes (see Appendix B for details).

	Scheme configuration				
		i = 1 to N-1	$i = N$		
Case 1	j = 1 to N-1	4th-order scheme	3rd-order scheme		
	$j = N$	3rd-order scheme	2nd-order scheme		
		i = 1	i = 2 to N-2	$i = N$-1	$i = N$
	j = 1	6th-order scheme	6th-order scheme	6th-order scheme	6th-order scheme
Case 2	j = 2 to N-2	6th-order scheme	8th-order scheme	6th-order scheme	6th-order scheme
	$j = N$-1	6th-order scheme	6th-order scheme	6th-order scheme	6th-order scheme
	$j = N$	6th-order scheme	6th-order scheme	6th-order scheme	6th-order scheme

Fig. 3.10 shows the eigenvalue spectrum for Case 1, where the overall order of accuracy is 3. The eigenvalue spectrums show that the third-order configuration in both the DMLC and MLC schemes are stable with all three α values. Both figures show that larger α causes the spectrum to move towards the negative direction, which means the scheme becomes more stable. When $\alpha = 3$, a large portion of the eigenvalue spectrum is significantly shifted to the negative direction, which indicates there may be excessive dissipation. Same as we suggested in the one-dimensional analysis [101], $\alpha = 1.5$ is a reasonable choice for introducing small but enough dissipation. Fig. 3.10 also shows that the DMLC scheme (b) has a more coherent pattern in the eigenvalue spectrum compared with the MLC scheme (a). The DMLC scheme has more concentrated eigenvalue spectrum for each specific α value, and the spectrums for different α values are better separated.

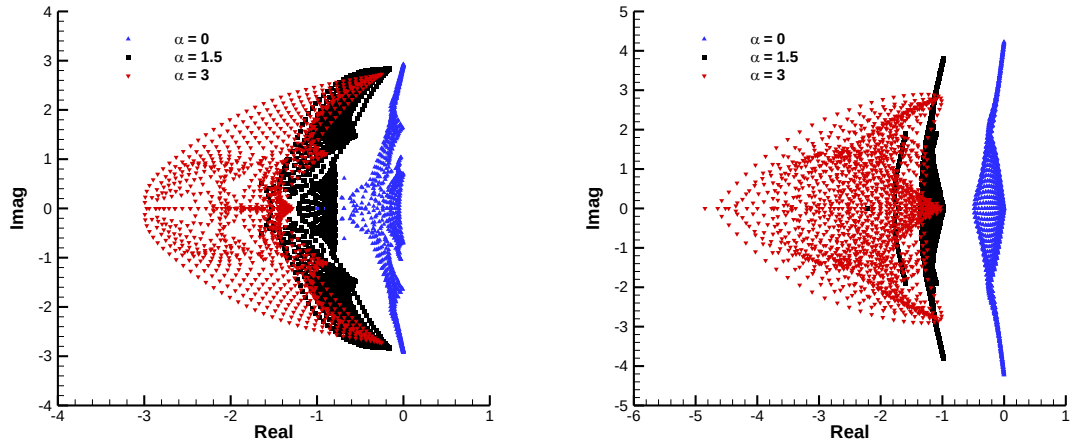

a), 1-1-1-1 MLC scheme b), 1-1-1-1 DMLC scheme

Fig. 3.10. Comparison of the eigenvalue spectrum for Case 1 (3rd-order global accuracy) with the MLC and DMLC schemes.

Similarly, Fig. 3.11 shows the eigenvalue spectrum for Case 2, where the overall order of accuracy is 7. Fig. 3.11(a) shows that the seventh-order configuration with α = 0, 12, 24 for the 1-D inner scheme are unstable in the MLC scheme. Only α = 36 leads to a stable configuration, which indicates that the very high-order MLC scheme requires large numerical dissipation to insure boundary stability. For the DMLC scheme, Fig. 3.11(b) shows the seventh-order configuration with α = 12, 24, 36 are all stable, indicating that the boundary stability is much easier to achieve in the DMLC scheme. For maintaining small dissipation, α = 12 is still a reasonable choice. Similar with Case 1 in Fig. 3.10, the DMLC scheme also shows more concentrated and better separated eigenvalue spectrums compared with the MLC scheme.

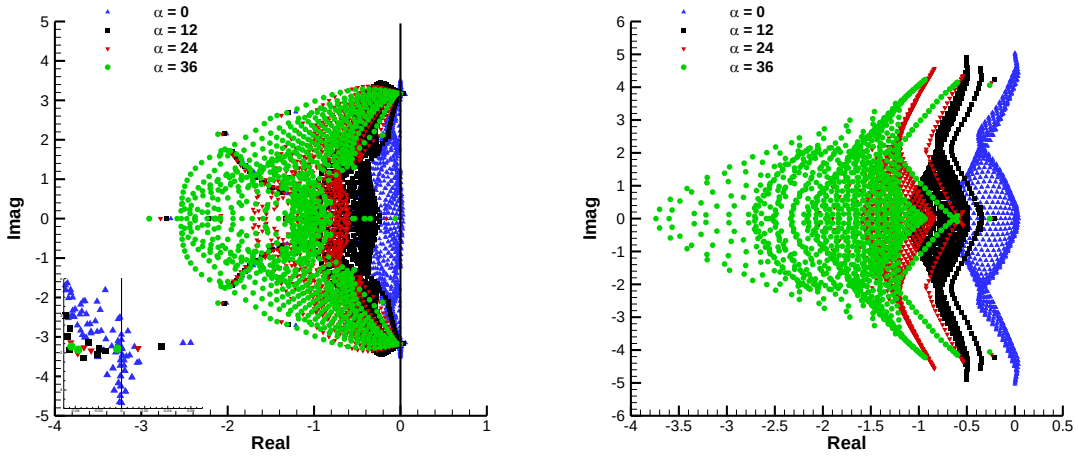

a), 2-2-2-2 MLC scheme b), 2-2-2-2 DMLC scheme

Fig. 3.11. Comparison of the eigenvalue spectrum for Case 2 (7th-order global accuracy) with the MLC and DMLC schemes.

In summary, the analysis of boundary closure schemes in two-dimensional cases demonstrates that stable boundary closure schemes can be obtained in both the DMLC and MLC schemes by choosing a reasonable α. However, in the case of very high-order inner scheme such as the 2-2-2-2 scheme, the DMLC scheme shows much better boundary stability for small α values; while the MLC scheme requires very large α values, which introduces excessive dissipation.

3.6. Summary

Chapter 3 presents the derivation of the DMLC scheme using multi-dimensional linear advection equation. The implementation of the DMLC scheme on two-dimensional Euler equations is discussed. The DMLC scheme introduces the auxiliary equations for both first

derivatives (u_x, u_y, u_z) and cross derivatives (u_{xy}, u_{yz}, u_{xz}, u_{xyz}). With the help of the additional degrees of freedom, the spatial discretization can be fulfilled along each dimension independently. By using the directional discretization technique, the DMLC scheme is consistent in one and two-dimensional cases, and it avoids the ad-hoc selection of grid points in cross-derivative approximations. Therefore, it should lead to better computational efficiency and spectral resolution than the MLC scheme. Then, the DMLC scheme is analyzed with the two-dimensional Fourier analysis and matrix method. The results demonstrate that the DMLC scheme can avoid the weak numerical instability encountered in the MLC scheme, and it also has better spectral resolution and smaller anisotropic error for a large portion of wavenumbers in [0, 2π] compared with the MLC scheme. When coupled with the boundary closure schemes, the DMLC scheme shows significantly better stability than the MLC scheme, which allows using smaller α values to avoid excessive dissipation.

4. Least Square Multi-Layer Compact (LSMLC) Scheme for Multi-Dimensional Flows

In this chapter, the one-dimensional multi-layer compact (MLC) schemes developed in Section 2.1 are extended to multi-dimensional cases with another approach – the weighted least square approximation. For the multi-dimensional approximations, there exist redundant information from the corner points. In the MLC schemes, the supporting grid points are pre-selected manually to reduce redundancy in the multi-dimensional approximations; in the DMLC scheme, the multi-dimensional approximation is avoided by introducing additional auxiliary equation for cross derivatives. With the weighted least square approach developed in this chapter, all grid points are used for the approximation. Moreover, the MLC scheme shows weak numerical instability for a small range of wavenumbers for multi-dimensional flows, which are mainly triggered by the inconsistency between its one and two-dimensional formulations. The DMLC scheme can avoid the weak numerical instabilities, and have better performance in terms of accuracy, spectral resolution, and computational efficiency than the MLC schemes. However, the auxiliary equation for cross derivative makes the implementation of the DMLC schemes more complicated than the MLC schemes.

The weighted least square approach, on the other hand, try to remove the weak numerical instability of the MLC scheme by redesign the formula of cross-derivative approximations. Meanwhile, we can prove that the approach leads to the same formula for the second derivatives as in the MLC scheme by adding the 1-D constraints through Lagrange multiplier in the

objective function. Therefore, it exactly follows the framework of the MLC scheme and can be implemented in the same way without deriving additional auxiliary equations.

In this chapter, the weighted least square approach is first introduced, which is used to derive the formula for cross-derivative approximations. The effects of several factors including the 1-D constraint, weight function, upwind factor, and derivative weight factor are investigated; and a parametric study is performed to optimize the LSMLC scheme. Same as the MLC scheme and the DMLC scheme, two-dimensional Fourier analysis on the linear advection equations are used for the parametric study. Then, the boundary stability analysis with matrix method are carried out to show the stability of the LSMLC scheme in two-dimensional cases with non-periodic boundary conditions. In the end, the implementation of the LSMLC scheme on the nonlinear Euler equations and Navier-Stokes equations are briefly discussed.

4.1. Weighted Least Square Approximation

Following the strategy of the dissertation, the weighted least square approximation is applied in the two-dimensional computational domain with a uniform mesh as well. Different from many other least square methods, which are implemented on unstructured mesh, or even meshless domain as in finite point methods[94,102–109], or element-free Galerkin methods[110,111], our LSMLC scheme does not increase the computational cost benefited from the uniform mesh. The solution of the weighted least square problem only depends on grid stencils, and it only needs to be solved once for a specific grid stencil. In other words, the solution is position-independent and can be applied to all grid points with the same grid stencil in the computational domain.

The starting point of least square approximation is defining moving least square (MLS) interpolant [110] using a polynomial with degree *m*,

$$u_i(\mathbf{x}) = \mathbf{a}_i \cdot \mathbf{p}(\mathbf{x}) = \sum_{l=0}^{m} \mathbf{a}_i^{(l)} \cdot \mathbf{p}^{(l)} \tag{4.1}$$

$$\mathbf{a}_i = \left(\mathbf{a}_i^{(0)}, \mathbf{a}_i^{(1)}, \ldots, \mathbf{a}_i^{(m)}\right), \quad \mathbf{p}(\mathbf{x}) = \left(\mathbf{p}^{(0)}, \mathbf{p}^{(1)}, \ldots, \mathbf{p}^{(m)}\right) \tag{4.2}$$

where $\mathbf{a}_i$ is the vector of undetermined coefficients which is time-dependent, $\mathbf{p}(\mathbf{x})$ is the vector of polynomial basis. The local coordinates **x** centered as every grid point *i* is used in the basis. For two-dimensional cases, the coefficients and basis related to degree l have the form,

$$\begin{aligned} \mathbf{a}_i^{(l)} &= \left(a_{i0}^{(l)}, \ldots, a_{il}^{(l)}\right) \\ \mathbf{p}^{(l)} &= \left(x^l, x^{l-1}y, \ldots, xy^{l-1}, y^l\right) \end{aligned} \tag{4.3}$$

where l ranges from 0 to *m*. Substituting (4.3) into Eqs. (4.1), we get

$$u_i(\mathbf{x}) = \mathbf{a}_i \cdot \mathbf{p}(\mathbf{x}) = \sum_{l=0}^{m} \sum_{k=0}^{l} a_{ik}^{(l)} x^{l-k} y^k \tag{4.4}$$

Taking the derivative of (4.4) to *x* and *y* leads to,

$$\begin{aligned} \frac{\partial}{\partial x} u_i(\mathbf{x}) &= \mathbf{a}_i \cdot \frac{d}{dx}\mathbf{p}(\mathbf{x}) = \sum_{l=0}^{m} \sum_{k=0}^{l-1} (l-k) a_{ik}^{(l)} x^{l-k-1} y^k \\ \frac{\partial}{\partial y} u_i(\mathbf{x}) &= \mathbf{a}_i \cdot \frac{d}{dy}\mathbf{p}(\mathbf{x}) = \sum_{l=0}^{m} \sum_{k=1}^{l} k a_{ik}^{(l)} x^{l-k} y^{k-1} \end{aligned} \tag{4.5}$$

The polynomial and their derivatives Eqs. (4.4) – (4.5) are then evaluated at the base point *i* and a set of supporting points around the base point. These supporting points and the base point *i* form the domain of influence Ω for the least square approximation. In our LSMLC scheme, the domain of influence includes all points in the square grid stencil as shown in Fig. 2.7. The discrete function value and first derivatives at the point *j* are denoted as,

$$\left(u_j, u_{xj}, u_{yj}\right), j \in \Omega \tag{4.6}$$

At the base point, we have $\mathbf{x}_i = (0,0)$, and Eqs. (4.4) – (4.5) can give the function value, and first derivatives at the base point,

$$\begin{aligned} & u_i(\mathbf{x}_i) = a_{i0}^{(0)} \\ & \frac{\partial}{\partial x} u_i(\mathbf{x}_i) = a_{i0}^{(1)}, \frac{\partial}{\partial y} u_i(\mathbf{x}_i) = a_{i1}^{(1)} \end{aligned} \tag{4.7}$$

The consistency requirement at the base point *i* gives the solution of first 3 coefficients in $\mathbf{a}_i$,

$$\left(a_{i0}^{(0)}, a_{i0}^{(1)}, a_{i1}^{(1)}\right) = \left(u_i, u_{xi}, u_{yi}\right) \tag{4.8}$$

To solve other coefficients in $\mathbf{a}_i$, we can minimize the weighted discrete L_2 norm of errors defined as,

$$J = \sum_{j \in \Omega, j \neq i} \left\{ w_{1j} \left[u_j - u_i(\mathbf{x}_j) \right]^2 + w_{2j} \left[u_{xj} - \frac{\partial}{\partial x} u_i(\mathbf{x}_j) \right]^2 + w_{3j} \left[u_{yj} - \frac{\partial}{\partial y} u_i(\mathbf{x}_j) \right]^2 \right\} \tag{4.9}$$

where w_{1j}, w_{2j}, w_{3j} are the weights for the function values, first derivatives in *x*, and first derivatives in *y* at point *j*. The weights are usually functions decaying with the Euclidean distance, which leads to larger weights on points near the base point *i*. If uniform weights are used, we get the standard least square problem. There are multiple choices of weight functions, which are discussed in detail in Section 4.2. The weights have important effect on the dissipation and stability of the LSMLC scheme, and they affect the nature of the resulting scheme as well. If larger weights are assigned to the points on the upwind side than the downwind side, the upwind LSMLC scheme is achieved; if symmetric weights are used, the central LSMLC scheme is achieved.

Substitute Eqs. (4.4) – (4.5) into (4.9), an objective function of $\mathbf{a}_i$ is obtained,

$$J(\mathbf{a}_i)=\sum_{j\in\Omega,\,j\neq i}\left\{w_{1j}\left[u_j-\mathbf{a}_i\cdot\mathbf{p}(\mathbf{x}_j)\right]^2+w_{2j}\left[u_{xj}-\mathbf{a}_i\cdot\frac{d}{dx}\mathbf{p}(\mathbf{x}_j)\right]^2+w_{3j}\left[u_{yj}-\mathbf{a}_i\cdot\frac{d}{dy}\mathbf{p}(\mathbf{x}_j)\right]^2\right\}=$$
$$\sum_{j\in\Omega,\,j\neq i}\left\{w_{1j}\left[u_j-\sum_{l=0}^{m}\sum_{k=0}^{l}a_{ik}^{(l)}x_j^{l-k}y_j^k\right]^2+w_{2j}\left[u_{xj}-\sum_{l=0}^{m}\sum_{k=0}^{l-1}(l-k)a_{ik}^{(l)}x_j^{l-k-1}y_j^k\right]^2+w_{3j}\left[u_{yj}-\sum_{l=0}^{m}\sum_{k=1}^{l}ka_{ik}^{(l)}x_j^{l-k}y_j^{k-1}\right]^2\right\} \tag{4.10}$$

The solution of the weighted least square approximation is,

$$\mathbf{a}_i=\arg\min J(\mathbf{a}_i), \tag{4.11}$$

subject to the constraints from the consistency requirement at the base point *i* as given in Eq. (4.8). After the solution $\mathbf{a}_i$ is obtained, the LSMLC scheme can be derived as,

$$\begin{aligned}\frac{\partial}{\partial x^2}u_i(\mathbf{x}_i)&=2a_{i0}^{(2)}\\ \frac{\partial}{\partial x\partial y}u_i(\mathbf{x}_i)&=a_{i1}^{(2)}\\ \frac{\partial}{\partial y^2}u_i(\mathbf{x}_i)&=2a_{i2}^{(2)}\end{aligned} \tag{4.12}$$

Obviously, they are functions of discrete functions values and first derivatives (u_j,u_{xj},u_{yj}) and the grid spacing *h*.

Equation (4.12) gives both the formula of the one-dimensional schemes and two-dimensional schemes. However, the one-dimensional schemes for the second derivatives are not guaranteed to be the same with the MLC scheme derived in Section 2.1. The second-derivative approximation in Eq. (4.12) can use any corner points in the square stencil and leads to much more complicated formulas compared with those in the MLC scheme. This gives rise to the problem of high computational costs. More importantly, the advantage of the MLC scheme can be affected, and the system becomes more difficult to be analyzed. The inconsistency between the LSMLC and MLC schemes can be overcome by introducing the 1-D constraints from the MLC scheme on $a_{i0}^{(2)}$ and $a_{i2}^{(2)}$ as follows,

$$
\begin{aligned}
a_{i0}^{(2)} &= \frac{1}{2h^2}\sum_l a_l u_l + \frac{1}{2h}\sum_m b_m u_{xm} \\
a_{i2}^{(2)} &= \frac{1}{2h^2}\sum_l a_l u_l + \frac{1}{2h}\sum_m b_m u_{ym}
\end{aligned}
\tag{4.13}
$$

where l and m represent points along the grid line passing the base point in either x or y direction, which is a subset of the domain of influence Ω. The constants a_l and b_m are coefficients of solved from Eq. (2.4), and h is the grid spacing.

The constrained optimization problem can be solved using Lagrange multipliers. In our implementation, both the consistency constraints in Eq. (4.8) and the 1-D constraints in Eq. (4.13) are added into the objective function in Eq. (4.10) through Lagrange multipliers. The new objective function becomes,

$$
\begin{aligned}
&\tilde{J}\left(\mathbf{a}_i, \lambda_1, \lambda_2, \mu_1, \mu_2, \mu_3\right) = \\
&\sum_{j\in\Omega,\, j\neq i}\left\{ w_{1j}\left[u_j - \sum_{l=0}^{m}\sum_{k=0}^{l} a_{ik}^{(l)} x_j^{l-k} y_j^k\right]^2 + w_{2j}\left[u_{xj} - \sum_{l=0}^{m}\sum_{k=0}^{l-1}(l-k)\, a_{ik}^{(l)} x_j^{l-k-1} y_j^k\right]^2 + w_{3j}\left[u_{yj} - \sum_{l=0}^{m}\sum_{k=1}^{l} k a_{ik}^{(l)} x_j^{l-k} y_j^{k-1}\right]^2 \right\} \\
&+\lambda_1\left(a_{i0}^{(2)} - \frac{1}{2h^2}\sum_l a_l u_l - \frac{1}{2h}\sum_m b_m u_{xm}\right) + \lambda_2\left(a_{i2}^{(2)} - \frac{1}{2h^2}\sum_l a_l u_l - \frac{1}{2h}\sum_m b_m u_{ym}\right) \\
&+\mu_1\left(a_{i0}^{(0)} - u_i\right) + \mu_2\left(a_{i0}^{(1)} - u_{xi}\right) + \mu_3\left(a_{i1}^{(1)} - u_{yi}\right)
\end{aligned}
\tag{4.14}
$$

where λ_1, λ_2, μ_1, μ_2, μ_3 are the Lagrange multipliers. The solution of the constrained optimization problem can be obtained by solving the following equations,

$$
\begin{aligned}
&\frac{\partial}{d\mathbf{a}_i}\tilde{J}\left(\mathbf{a}_i, \lambda_1, \lambda_2, \mu_1, \mu_2, \mu_3\right) = 0 \\
&\frac{\partial}{d\lambda_1}\tilde{J}\left(\mathbf{a}_i, \lambda_1, \lambda_2, \mu_1, \mu_2, \mu_3\right) = 0 \\
&\frac{\partial}{d\lambda_2}\tilde{J}\left(\mathbf{a}_i, \lambda_1, \lambda_2, \mu_1, \mu_2, \mu_3\right) = 0 \\
&\frac{\partial}{d\mu_1}\tilde{J}\left(\mathbf{a}_i, \lambda_1, \lambda_2, \mu_1, \mu_2, \mu_3\right) = 0 \\
&\frac{\partial}{d\mu_2}\tilde{J}\left(\mathbf{a}_i, \lambda_1, \lambda_2, \mu_1, \mu_2, \mu_3\right) = 0 \\
&\frac{\partial}{d\mu_3}\tilde{J}\left(\mathbf{a}_i, \lambda_1, \lambda_2, \mu_1, \mu_2, \mu_3\right) = 0
\end{aligned}
\tag{4.15}
$$

In the end of the section, we briefly talk about the relation between the order of accuracy of the LSMLC scheme and the weighted least square approximation. The LSMLC scheme uses the same L_1-L_2-M_1-M_2 stencil from the MLC scheme, as shown in Fig. 2.7. The degree of polynomial in Eq. (4.1) is m is set to be, and the order of accuracy of the LSMLC scheme p has the following relation with m,

$$p = \begin{cases} even(m, m-1) & \text{for centered stencil with symmetric weights} \\ m-1 & \text{for baised stencil or asymmetric weights} \end{cases} \tag{4.16}$$

On centered stencil with symmetric weights, the resulting LSMLC scheme is central scheme which have even orders, otherwise, the LSMLC scheme is one-order lower than the degree of polynomial. In our LSMLC scheme, the degree of polynomial is set to be,

$$m = \begin{cases} L_1 + L_2 + M_1 + M & \text{for interior scheme} \\ L_1 + L_2 + M_1 + M_2 - 1 & \text{for boundary closure scheme} \end{cases} \tag{4.17}$$

For the interior scheme, when m is an even number, the maximum order of accuracy the interior scheme can achieve is $p_{\max} = m$, which is consistent with the MLC scheme for two-dimensional cases.

4.2. Weight Functions with Upwind Correction

As we discussed in last section, the weights have important effect on the dissipation and stability of the LSMLC scheme, and they affect the nature of the resulting scheme as well. There are many forms of weight functions. Typical examples include exponential/Gaussian weight function [102,103,106,107,110–112], cosine weight function [113,114], spline weight function [109,115], inverse proportional function (IPF) of distance [94,108], etc.

In this section, different choices of weight functions are first discussed. Most weight functions used in the literatures are based on Euclidean distance and do not depend on orientation. In other words, they are symmetric for upwind and downwind sides, which lead to central scheme in our case. To derive upwind LSMLC schemes, the upwind correction on these weight functions are introduced. The upwind version of the truncated Gaussian Distribution (TGD) weights and the inverse proportional function (IPF) are illustrated in the following sections.

4.2.1 Truncated Gaussian Distribution (TGD) Weights

The most common choice of the weights is the truncated Gaussian distribution (TGD) function. It was used in [102,103,106,107,110–112]. Here, we follow the formulation of Boroomand [102], but represent them in a nondimensionalized fashion. Also, the upwind correction is introduced. The weight in the function value layer for a supporting grid point has the form,

$$\begin{aligned} w_1 &= w_c\left(1+\beta\cos\varphi\right) \\ w_c &= \frac{\exp\left(-\left(\xi^2+\eta^2\right)/\lambda^2\right)-\exp\left(-\rho^2/\lambda^2\right)}{1-\exp\left(\rho^2/\lambda^2\right)} \end{aligned} \tag{4.18}$$

where w_c is the weight before correction defined by the truncated Gaussian distribution, and $\beta\cos\varphi$ is the upwind correction. Nondimensionalized coordinates are used in w_c,

$$\begin{aligned} \xi &= \frac{x}{r_{\max}} \\ \eta &= \frac{y}{r_{\max}} \end{aligned} \tag{4.19}$$

where $r_{\max}$ is the maximum distance between a supporting point and the base point in a grid stencil. At the based point, w_c is normalized to 1. The constants ρ and λ are used to control the

weight at the farthest point. The recommended values $\rho = 2$ and $\lambda = 0.25$ from [102] are used here. In the upwind correction part, φ is the deviation angle of the supporting point from the upwind direction. If a point is along the upwind direction ($\varphi = 0$), its weight is maximized; and if a point is in the downwind direction ($\varphi = \pi$), its weight is minimized. The cosine of φ can be computed as,

$$\cos\varphi \approx -\frac{\xi\cos\theta + \eta\sin\theta}{\sqrt{\xi^2 + \eta^2 + \varepsilon}} \tag{4.20}$$

where θ is the convection angle and ε is a small constant of 0.0001 to avoid singularity at the base point. The level of the upwind correction is adjusted by β, which has the range of (0, 1). This range of β ensures that w_1 will always be non-negative. Following analysis in this chapter shows that the upwind factor β has the similar effect as α in the one-dimensional upwind scheme (Section 2.1), which controls the dissipation, dispersion and stability of the LSMLC scheme in two-dimensional cases. Fig. 4.1 shows an example of the truncated Gaussian distribution weight in the function value layer (w_1) on a 2-2-2-2 square stencil with the upwind factor $\beta = 0.2$ and convection angle $\theta = \frac{\pi}{4}$. The corresponding grid stencil is given in Fig. 2.9. The TGD weight has a bell shape. It shows a fast decay with the increase of distance, so the weights on distant grid points are very small. The projection on the diagonal line *y* = *x* shows that the weight is not symmetric, and it has larger values on the upwind side.

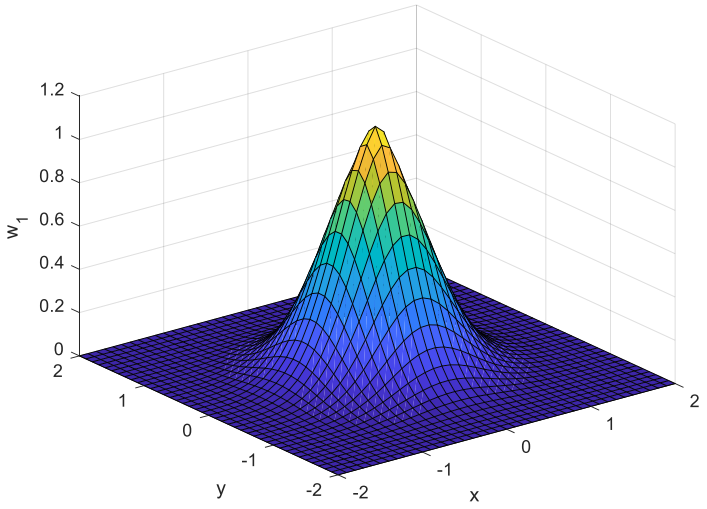

(a) 2-D plot

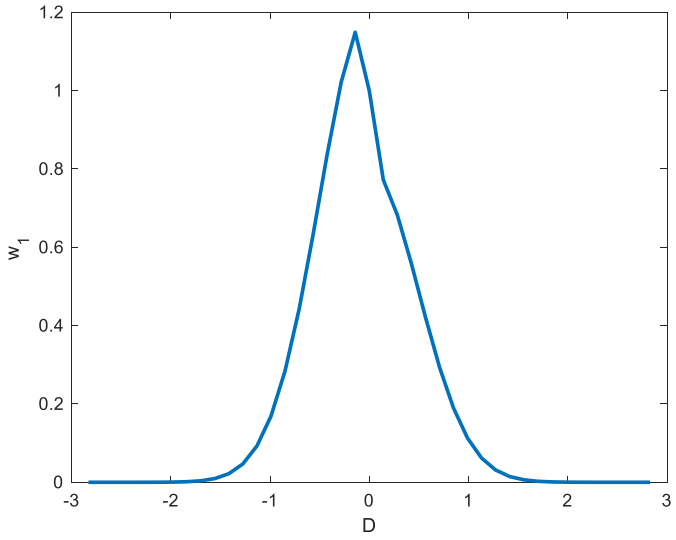

(b) projection to $y = x$ line

Fig. 4.1. TGD weight w_1 on a 2-2-2-2 stencil ($\beta = 0.2$, $\theta = \frac{\pi}{4}$).

The weights in the first derivative layers are proportional with the weight in the function value layer,

$$w_2 = w_3 = \gamma w_1 \tag{4.21}$$

where w_2 and w_3 are weights for x derivative and y derivative respectively, which are usually equivalent. The factor γ is a positive constant. If γ is 0, then the least square approximation only uses the discrete function values and the LSMLC scheme reduces to a mono-layer scheme.

4.2.2 Inverse Proportional Function (IPF) Weights

Another popular form of the weight is the inverse proportional function (IPF) of distance [94,108]. To be generic, it has the form of [108],

$$w \sim \frac{1}{d^n}, n \geq 0 \tag{4.22}$$

where d is the distance from the base point to a supporting point. In our LSMLC scheme, we designed the IPF weight in nondimensionalized fashion as follows,

$$\begin{aligned} w_1 &= w_c\left(1+\beta\cos\varphi\right) \\ w_c &= \frac{\lambda}{\sqrt{\xi^2+\eta^2}+\lambda} \end{aligned} \tag{4.23}$$

where λ, ξ, η, β, $\cos\varphi$ have the definition as in TGD weights. Again, w_c is normalized to 1 at the base point; λ can be used to control the weight at the farthest point; and β is the adjustable upwind factor. To be consistent with the TGD weight, λ is also set to be 0.25. Fig. 4.2 shows an example of the IPF weight in the function value layer (w_1) on a 2-2-2-2 square stencil with the upwind factor $\beta = 0.2$ and convection angle $\theta = \frac{\pi}{4}$. The corresponding grid stencil is given in Fig. 2.9. Compared with the TGD weight shown in Fig. 4.1, the IPF weight shows a slower decay with the increase of distance, and the weights on distant grid points are much larger. The projection on the diagonal line $y = x$ shows that the weight is not symmetric, and it has larger values on the upwind side.

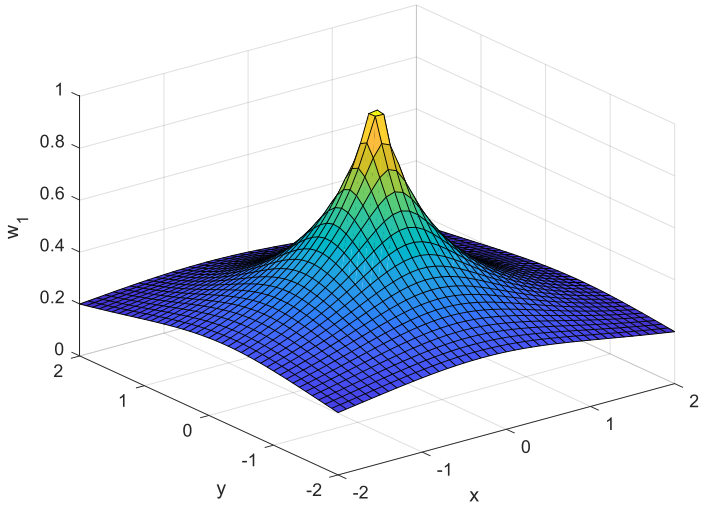

(a) 2-D plot

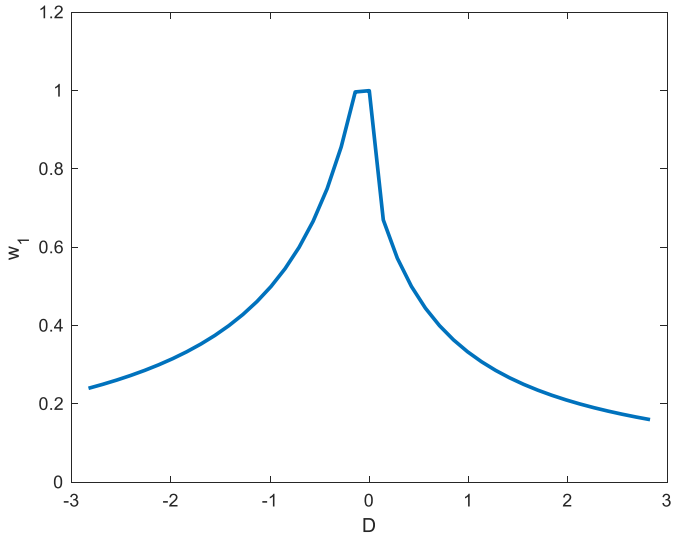

(b) projection to $y = x$ line

Fig. 4.2. IPF weight w_1 on a 2-2-2-2 stencil ($\beta = 0.2$, $\theta = \frac{\pi}{4}$).

The weights for derivative layers are also proportional with w_1, as given by Eq. (4.21).

4.3. Parametric Study of LSMLC scheme

In this section, a parametric study is performed to optimize the LSMLC scheme. The goal is to find a LSMLC scheme which have the best properties in the two-dimensional Fourier analysis. The procedures for the two-dimensional Fourier analysis is described in Section 2.4.2. Both the convection angle and Fourier phase angle are set to be $\pi/4$, which corresponds to the most unstable cases according to previous analysis (Section 3.4.1). Throughout the parametric study, the second-derivative approximation for the LSMLC scheme uses the same formula from the MLC scheme, and the cross-derivative approximation for the LSMLC scheme is derived by the weighted least square approximation, as shown in Eq. (4.12). The effects of the 1-D constraint, choices of weight functions, upwind factors in the weights, and derivative weight factors are investigated.

4.3.1 Effect of One-Dimensional Constraint

The one-dimensional constraints from the MLC scheme are given in Eq. (4.13), and are imposed in the objective function through Lagrange multiplier, as shown in Eq. (4.14). From the solution of Eq. (4.14), we can observe that Eq. (4.13) are always satisfied with the Lagrange multiplier. However, the solution of $a_{i0}^{(2)}$ and $a_{i2}^{(2)}$ becomes messy and includes many corner points from the square stencil if the 1-D constraints is removed. This difference is expected and shows that the Lagrange multiplier can impose the 1-D constraints properly.

More important, we want to investigate how the solution of $a_{i1}^{(2)}$, which gives the coefficients of cross-derivative approximations, is affected by the 1-D constraints. Table 4.1 presents the coefficients of 1-1-1-1 LSMLC schemes when we impose the 1-D constraints or not. Here, *a*, *b*, and *c* represent the coefficients in function values, first derivatives of *x*, and first derivatives of *y* respectively. It is observed that the coefficients are almost the same whether we

impose the 1-D constraints or not. Table 4.2 compares the coefficients of the 2-2-1-1, and Table 4.3 shows the coefficients of the 2-2-2-2 schemes. Similarly, imposing the 1-D constraints does not affect the cross-derivative approximations significantly. However, there exist coefficients that are slightly different in these 3 tables, which could be caused by numerical error or the 1-D constraints. To be consistent, we always apply the Lagrange multiplier for the LSMLC scheme in this dissertation.

Table 4.1. Comparison of coefficients of 1-1-1-1 LSMLC schemes with or without 1-D constraints.

a		b		c	
1-D constraint	No constraint	1-D constraint	No constraint	1-D constraint	No constraint
-2.99E-02	-2.99E-02	4.50E-02	4.50E-02	4.50E-02	4.50E-02
4.94E-03	5.01E-03	-3.77E-01	-3.77E-01	-7.53E-03	-7.51E-03
2.49E-02	2.49E-02	3.75E-02	3.75E-02	-3.75E-02	-3.75E-02
4.94E-03	5.01E-03	-7.53E-03	-7.51E-03	-3.77E-01	-3.77E-01
-2.12E-06	-2.51E-06	5.51E-02	5.52E-02	5.51E-02	5.52E-02
-4.94E-03	-5.01E-03	-7.53E-03	-7.51E-03	3.22E-01	3.22E-01
2.49E-02	2.49E-02	-3.75E-02	-3.75E-02	3.75E-02	3.75E-02
-4.94E-03	-5.01E-03	3.22E-01	3.22E-01	-7.53E-03	-7.51E-03
-1.99E-02	-1.99E-02	-3.00E-02	-3.00E-02	-3.00E-02	-3.00E-02

Table 4.2. Comparison of coefficients of 2-2-1-1 LSMLC schemes with or without 1-D constraints.

a		b		c	
1-D constraint	No constraint	1-D constraint	No constraint	1-D constraint	No constraint
8.34E-03	8.34E-03	7.85E-02	7.85E-02	7.85E-02	7.85E-02

-9.33E-03	-9.33E-03	-2.98E-01	-2.98E-01	-3.71E-03	-3.73E-03
5.99E-05	5.64E-05	7.17E-02	7.17E-02	-6.89E-02	-6.89E-02
8.37E-03	8.37E-03	-3.71E-03	-3.73E-03	-2.98E-01	-2.98E-01
-6.94E-03	-6.94E-03	3.43E-02	3.43E-02	3.43E-02	3.43E-02
-9.33E-03	-9.33E-03	-3.98E-03	-3.96E-03	2.81E-01	2.81E-01
1.18E-01	1.18E-01	-6.89E-02	-6.89E-02	7.17E-02	7.17E-02
3.21E-03	3.15E-03	2.81E-01	2.81E-01	-3.98E-03	-3.96E-03
-1.06E-01	-1.06E-01	-6.19E-02	-6.19E-02	-6.19E-02	-6.19E-02
7.68E-03	7.68E-03				
5.99E-05	5.64E-05				
3.21E-03	3.15E-03				
-8.14E-04	-6.90E-04				
-2.44E-03	-2.50E-03				
-1.94E-05	-2.22E-05				
8.37E-03	8.37E-03				
-1.06E-01	-1.06E-01				
-2.44E-03	-2.50E-03				
9.30E-02	9.30E-02				
-6.76E-03	-6.76E-03				
-6.94E-03	-6.94E-03				
7.68E-03	7.68E-03				
-1.94E-05	-2.22E-05				
-6.76E-03	-6.76E-03				
5.55E-03	5.55E-03				

Table 4.3. Comparison of coefficients of 2-2-2-2 LSMLC schemes with or without 1-D constraints.

a	b	c

1-D constraint	No constraint	1-D constraint	No constraint	1-D constraint	No constraint
-9.15E-04	-9.15E-04	1.63E-03	1.63E-03	1.63E-03	1.63E-03
1.13E-02	1.12E-02	-9.86E-03	-9.86E-03	-4.54E-03	-4.55E-03
-1.24E-03	-1.14E-03	4.53E-02	4.53E-02	3.50E-05	6.27E-05
-1.03E-02	-1.03E-02	-9.14E-03	-9.14E-03	4.12E-03	4.12E-03
7.52E-04	7.52E-04	1.35E-03	1.35E-03	-1.35E-03	-1.35E-03
1.13E-02	1.12E-02	-4.54E-03	-4.55E-03	-9.86E-03	-9.86E-03
-4.30E-01	-4.30E-01	-7.31E-03	-7.37E-03	-7.31E-03	-7.37E-03
5.69E-02	5.75E-02	-6.71E-01	-6.71E-01	1.07E-02	1.10E-02
3.68E-01	3.68E-01	-6.13E-03	-6.07E-03	-3.54E-03	-3.59E-03
-8.80E-03	-8.81E-03	-3.65E-03	-3.64E-03	8.43E-03	8.43E-03
-1.24E-03	-1.14E-03	3.50E-05	6.27E-05	4.53E-02	4.53E-02
5.69E-02	5.75E-02	1.07E-02	1.10E-02	-6.71E-01	-6.71E-01
-2.57E-04	-7.30E-04	8.14E-02	8.20E-02	8.14E-02	8.20E-02
-5.66E-02	-5.68E-02	1.06E-02	1.07E-02	5.77E-01	5.77E-01
1.18E-03	1.14E-03	4.31E-05	5.13E-05	-3.63E-02	-3.63E-02
-1.03E-02	-1.03E-02	4.12E-03	4.12E-03	-9.14E-03	-9.14E-03
3.68E-01	3.68E-01	-3.54E-03	-3.59E-03	-6.13E-03	-6.07E-03
-5.66E-02	-5.68E-02	5.77E-01	5.77E-01	1.06E-02	1.07E-02
-3.06E-01	-3.06E-01	-4.63E-03	-4.58E-03	-4.63E-03	-4.58E-03
7.87E-03	7.86E-03	3.22E-03	3.22E-03	7.68E-03	7.68E-03
7.52E-04	7.52E-04	-1.35E-03	-1.35E-03	1.35E-03	1.35E-03
-8.80E-03	-8.81E-03	8.43E-03	8.43E-03	-3.65E-03	-3.64E-03
1.18E-03	1.14E-03	-3.63E-02	-3.63E-02	4.31E-05	5.13E-05
7.87E-03	7.86E-03	7.68E-03	7.68E-03	3.22E-03	3.22E-03
-5.87E-04	-5.87E-04	-1.07E-03	-1.07E-03	-1.07E-03	-1.07E-03

4.3.2 Effect of Weight Function

In this section, 3 different weight functions: the TGD weight, the IPF weight, and the uniform weight are discussed. For the TGD weight and IPF weight, the upwind factor β is set to be 0.2, the derivative weight factor λ is set to be 0.5, the convection angle θ in the upwind correction is set to be $\pi/4$. Other details can be found in Section 4.2. For the uniform weights, $w_1 = w_2 = w_3 = 1$.

Third-Order 1-1-1-1 LSMLC Scheme

First, the third-order 1-1-1-1 LSMLC scheme is analyzed. Fig. 4.3 shows their dissipation factors with different weight functions. Figure (a) presents the physical mode and 2 spurious modes for each LSMLC scheme with different weights. It shows that the modal behaviors are very similar with different weights. Specifically, the spurious mode a_3 does not change with the weight; the physical mode a_1 and spurious mode a_2 show slightly different dissipation. The uniform weight has the smallest dissipation, the TGD weight is the middle, and the IPF weight introduces the largest dissipation. According to the analysis in Section 3.4.1, there exist a small range of *k* where the weak numerical instability appears. Figure (b) zooms in the region where the unstable modes exist, and the unstable 1-1-1-1 MLC scheme is also plotted here for comparison. It is observed that the LSMLC scheme with the uniform weight still show the weak numerical instability in a_1, although the magnitude is smaller compared with the MLC scheme. After applying the weight function, the LSMLC scheme becomes stable.

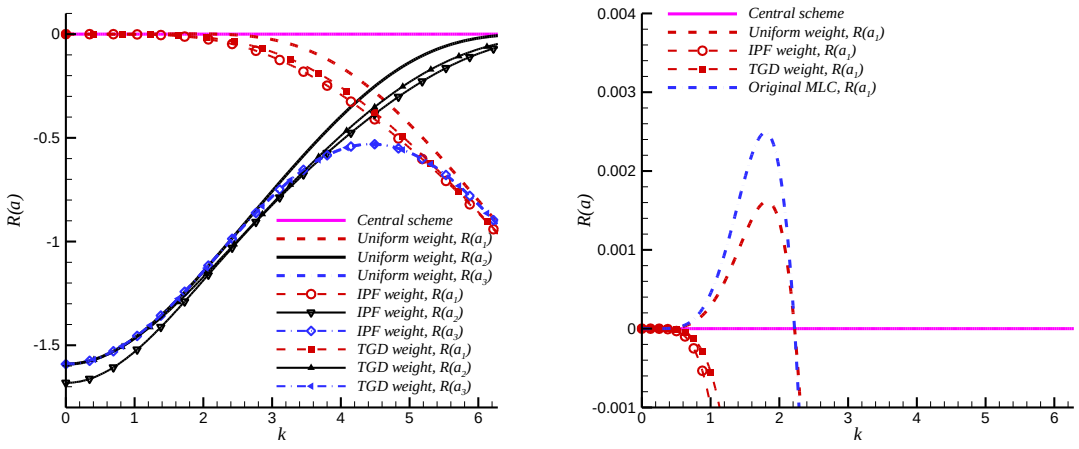

(a) (b)

Fig. 4.3. Dissipation factors of the 1-1-1-1 LSMLC schemes (3rd order) with different weight functions.

Fig. 4.4 shows the modified wavenumbers of the 1-1-1-1 LSMLC schemes with different weights. To better understand the effect of weight functions, the physical mode a_1 and two spurious modes are shown together. In terms of spectral resolution, we should only focus on the $I(a_1)$. The uniform weight and the IPF weight have very close values in all three modes. The TGD weight leads to slightly lower spectral resolution for very large *k*, and the shape of $I(a_2)$ is changed as well.

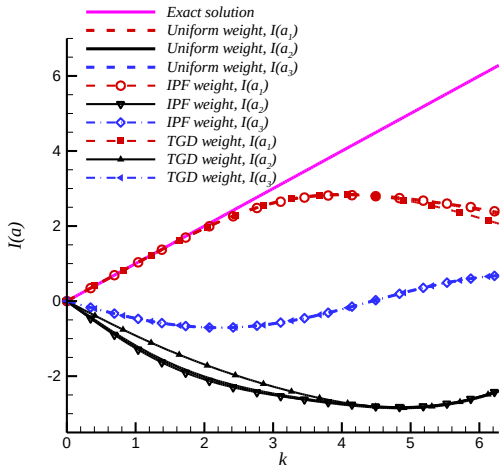

Fig. 4.4. Modified wavenumbers of the 1-1-1-1 LSMLC schemes (3rd order) with different weight functions.

Fifth-Order 2-2-1-1 LSMLC Scheme

The same procedures are repeated for the fifth-order 2-2-1-1 LSMLC scheme. The effects of the weight functions on the dissipation factors are more significant in this case, as presented in Fig. 4.5. Similar as in the 1-1-1-1 LSMLC scheme, the uniform weights have smallest dissipation in $R(a_1)$ and $R(a_2)$, but also shows weak numerical instability on $R(a_1)$ and $R(a_2)$. The TGD weight introduces more dissipation in $R(a_1)$ and $R(a_2)$, and can removes the numerical instability. The IPF weight can also leads to stable schemes but introduces more dissipation then the TGD weight.

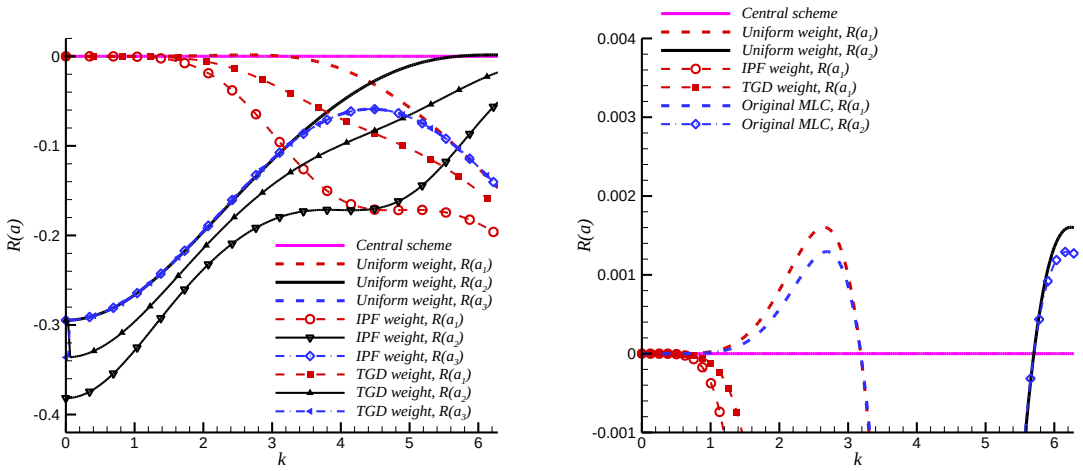

(a) (b)

Fig. 4.5. Dissipation factors of the 2-2-1-1 LSMLC schemes (5th order) with different weight functions.

Fig. 4.6 shows the modified wavenumber of the 2-2-1-1 LSMLC scheme. Different with the 1-1-1-1 scheme, the effect of weight functions on the modified wavenumber is not obvious on the 2-2-1-1 scheme.

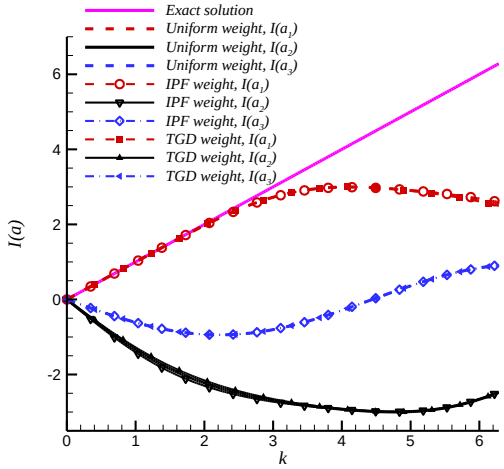

Fig. 4.6. Modified wavenumbers of the 2-2-1-1 LSMLC schemes (5th order) with different weight functions.

Seventh-Order 2-2-2-2 LSMLC Scheme

Fig. 4.7 and Fig. 4.8 show the dissipation factors and modified wavenumbers for the 2-2-2-2 LSMLC schemes with different weight functions. We found that the choice of weight functions affects both the dissipation and spectral resolution - $I(a_1)$, and the behavior is very similar with the 1-1-1-1 scheme.

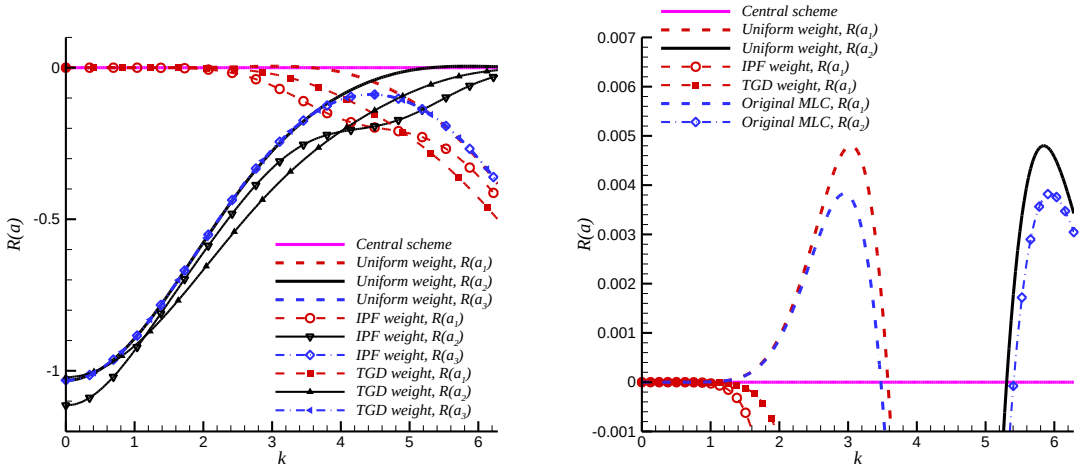

(a) (b)

Fig. 4.7. Dissipation factors of the 2-2-2-2 LSMLC schemes (7th order) with different weight functions.

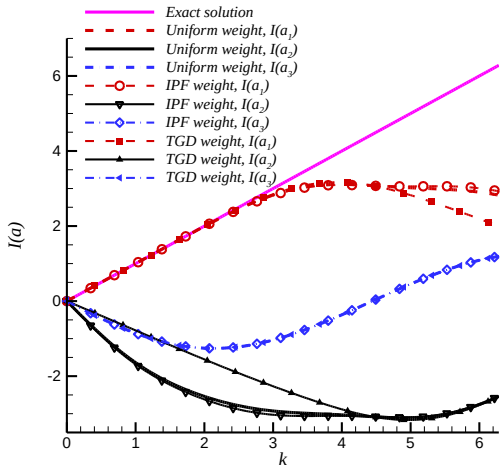

Fig. 4.8. Modified wavenumbers of the 2-2-2-2 LSMLC schemes (7th order) with different weight functions.

According to the observations from Fig. 4.3 to Fig. 4.8, the effect of weight functions can be concluded as follows,

1. The choice of weight has important effect on both the dissipation and the stability of the LSMLC scheme. Applying uniform weights leads to central schemes with the smallest dissipation, however, they are not stable which are similar with the MLC scheme. Applying the TGD and IPF weight with upwind correction leads to upwind scheme, which introduces more dissipation in the physical mode a_1 and spurious mode a_2, and it also removes the weak numerical instability.

2. The choice of weight can also affect the spectral resolution of the LSMLC scheme. The IPF weight shows similar resolution as the uniform weights, and the TGD weight slightly lowers the spectral resolution for large wavenumbers. However, the effect is not obvious on the 2-2-1-1 LSMLC scheme.

3. The TGD weight function shows the best property in our current LSMLC scheme, because it can remove the numerical instability of the uniform weight and it introduces smaller dissipation than the IPF weight function. Therefore, we mainly focus on the TGD weights in following analysis and numerical simulations.

4.3.3 Effect of Upwind Factor

In last section, the effect of TGD weight and IPF weight with upwind correction ($\beta = 0.2$) are analyzed. In this section, we try to investigate the effect of the upwind factor β in the TGD weight (Eq. (4.18)) and IPF weight (Eq. (4.23)) using the two-dimensional Fourier analysis. The level of upwind correction is adjusted by β, four values are experimented: 0.0, 0.2, 0.5, 1.0. If $\beta = 0.0$, there is no upwind correction and we get central LSMLC scheme; if $\beta = 1.0$, the LSMLC scheme has the maximal level of upwind correction.

Third-Order 1-1-1-1 LSMLC Scheme

Fig. 4.9 presents the Fourier analysis results of the third-order 1-1-1-1 LSMLC scheme with the IPF weight function. Figure (a) shows clearly that the dissipation for modes a_1 and a_2 increases with β in all range of *k*; figure (b) shows that any upwind LSMLC scheme ($\beta > 0$) is stable, and the central LSMLC scheme ($\beta = 0$) has the instability in a small range of *k*, which is similar with the MLC scheme. Figure (c) shows that the spectral resolution does not change significantly with the increase of β except in the limiting case when $\beta = 1.0$. According to Eq. (4.18) and Eq. (4.23), the weight for any point at the downwind direction is zero, which makes

the square stencil become sort of “bias”. As suggested by the one-dimensional Fourier analysis in Fig. 2.16, the upwind scheme on bias stencil has better spectral resolution. Here, similar behavior is observed in two-dimensional LSMLC scheme.

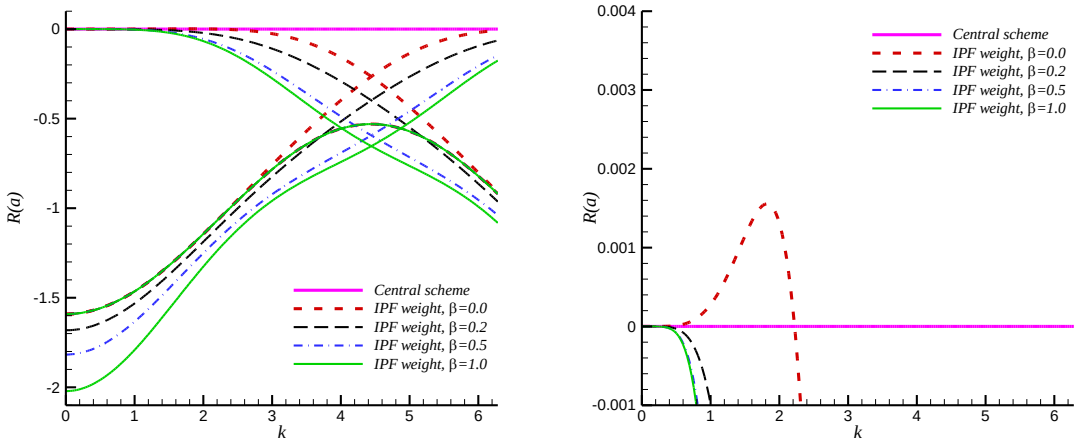

(a) Dissipation factor s (b) Unstable modes

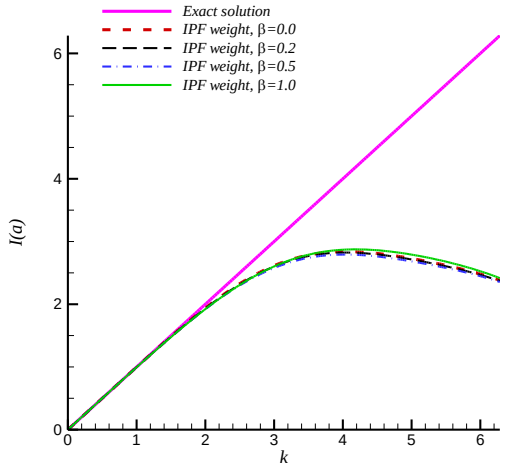

(c) Modified wavenumber

Fig. 4.9. 2-D Fourier analysis results of the 1-1-1-1 LSMLC schemes (3rd order) using IPF weight with different upwind factors (β = 0, 0.2, 0.5, 1.0).

Fig. 4.10 shows the Fourier analysis results of the third-order 1-1-1-1 LSMLC scheme with the TGD weight function. The behavior is similar with the IPF weights. However, a notable difference is that the largest dissipation in the spurious mode near $k = 0$ does not increase with β. This is favorable because the larger the dissipation is, the stiffer the numerical scheme becomes, which requires smaller time step size in numerical simulations. Therefore, we prefer to introduce more dissipation for large wavenumbers, but not for small wavenumbers. This again shows the TGD weight has the advantage over the IPF weight because it has smaller dissipation.

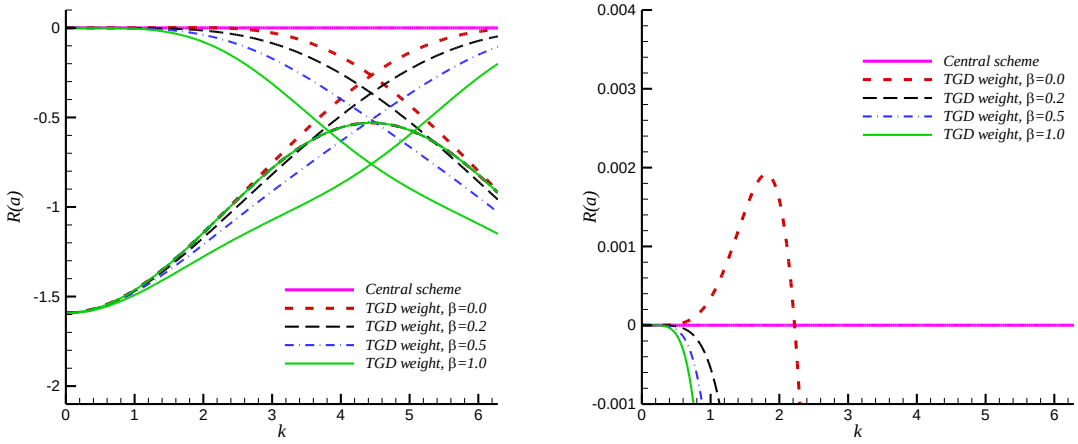

(a) Dissipation factor s (b) Unstable modes

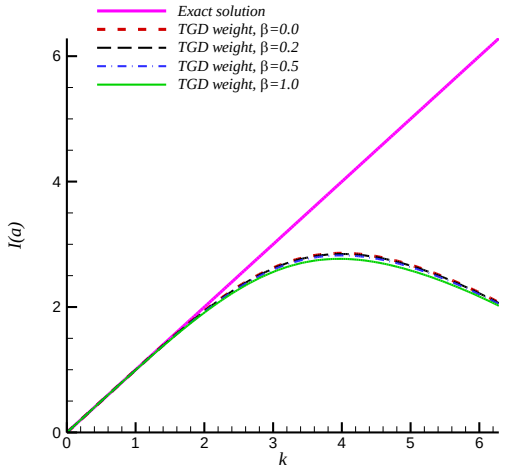

(c) Modified wavenumber

Fig. 4.10. 2-D Fourier analysis results of the 1-1-1-1 LSMLC schemes (3rd order) using TGD weight with different upwind factors (β = 0, 0.2, 0.5, 1.0).

Fifth-Order 2-2-1-1 LSMLC Scheme

Then, the effect of the upwind factor on the fifth-order 2-2-1-1 LSMLC schemes are analyzed. Fig. 4.11 presents the results with the IPF weights, and Fig. 4.12 presents the results with the TGD weights. Both figures show that the 2-2-1-1 LSMLC schemes are more sensitive to the change of β compared with the 1-1-1-1 LSMLC scheme, especially the dissipation factors. The TGD weights are less dissipative than the IPF weights, and the increase of stiffness with β is also smaller in the TGD weights. Same with the 1-1-1-1 scheme, $\beta = 0$ leads to unstable central scheme and $\beta > 0$ leads to stable upwind scheme.

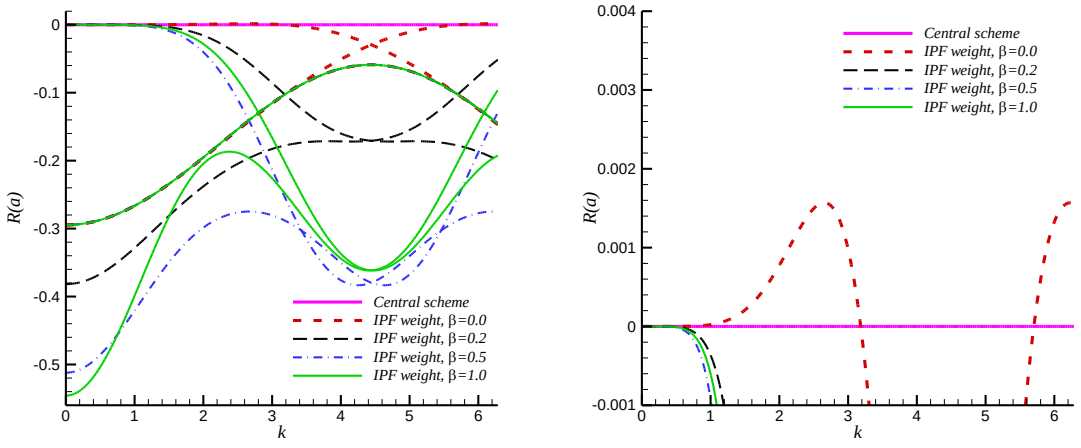

(a) Dissipation factor s (b) Unstable modes

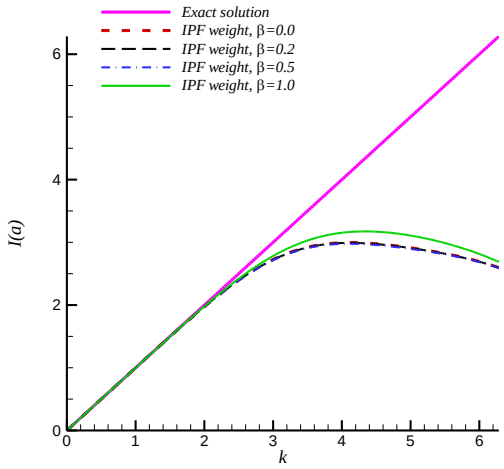

(c) Modified wavenumber

Fig. 4.11. 2-D Fourier analysis results of the 2-2-1-1 LSMLC schemes (5th order) using IPF weight with different upwind factors (β = 0, 0.2, 0.5, 1.0).

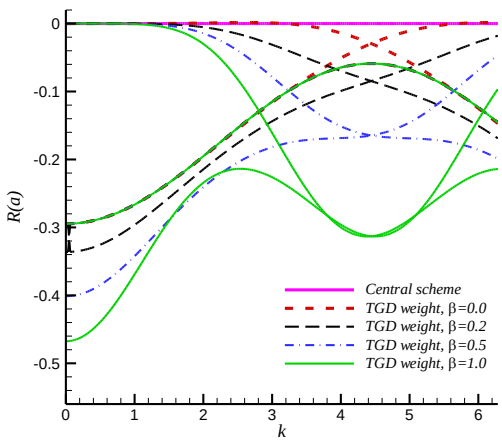

(a) Dissipation factor s

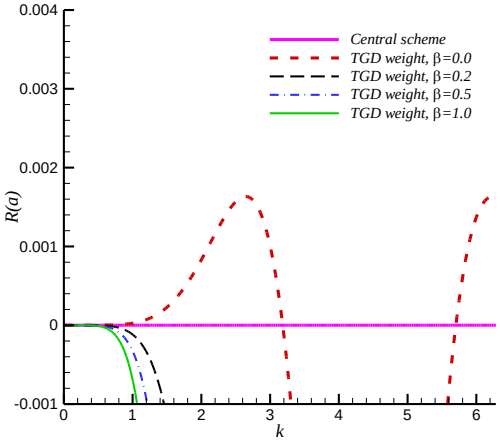

(b) Unstable modes

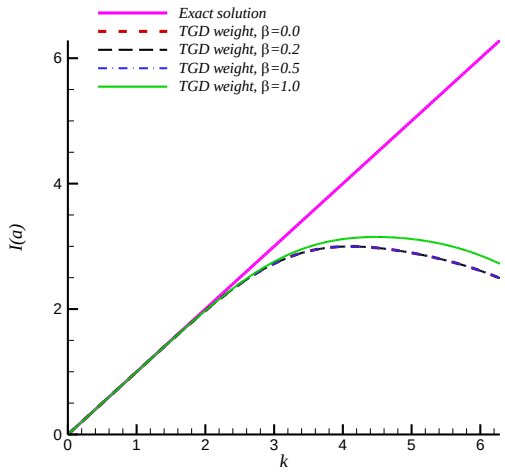

(c) Modified wavenumber

Fig. 4.12. 2-D Fourier analysis results of the 2-2-1-1 LSMLC schemes (5th order) using TGD weight with different upwind factors (β = 0, 0.2, 0.5, 1.0).

Seventh-Order 2-2-2-2 LSMLC Scheme

Last, the effect of the upwind factor on the seventh-order 2-2-1-1 LSMLC schemes with the IPF weights and TGD weights are analyzed in Fig. 4.13 and Fig. 4.14. Again, similar behaviors as in the 1-1-1-1 LSMLC scheme are observed here. The only difference is that the 2-2-2-2 LSMLC scheme are more sensitive to the change of β in terms of both dissipation and spectral resolution. In particular, the 2-2-2-2 LSMLC scheme with the TGD weight, shows a very large dissipation when $\beta = 1.0$, as shown in Fig. 4.14 (a).

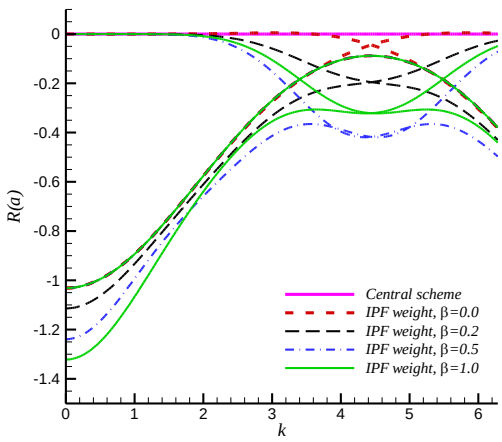

(a) Dissipation factor s

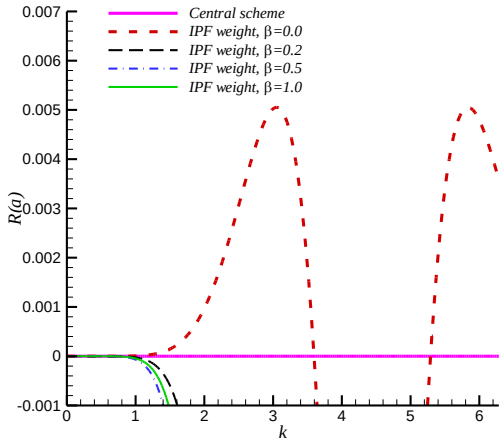

(b) Unstable modes

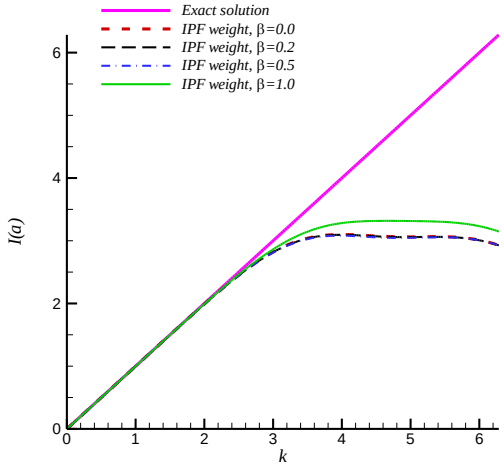

(c) Modified wavenumber

Fig. 4.13. 2-D Fourier analysis results of the 2-2-2-2 LSMLC schemes (7th order) using IPF weight with different upwind factors (β = 0, 0.2, 0.5, 1.0).

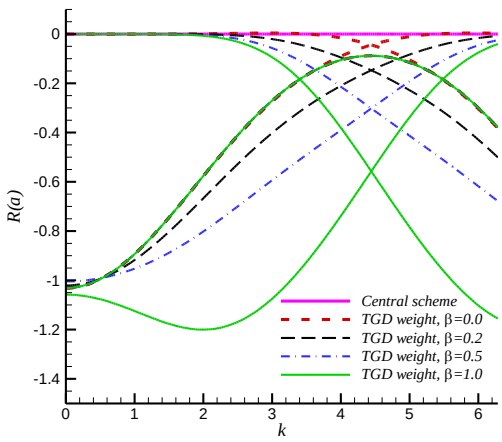

(a) Dissipation factor s

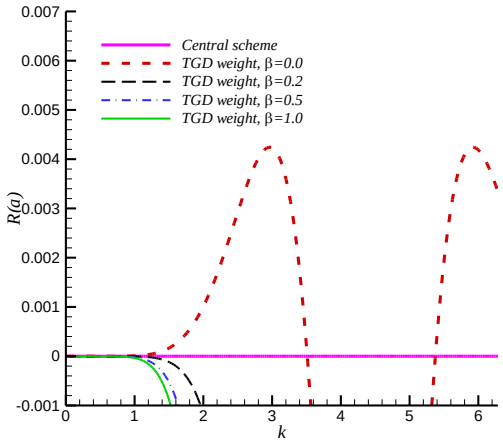

(b) Unstable modes

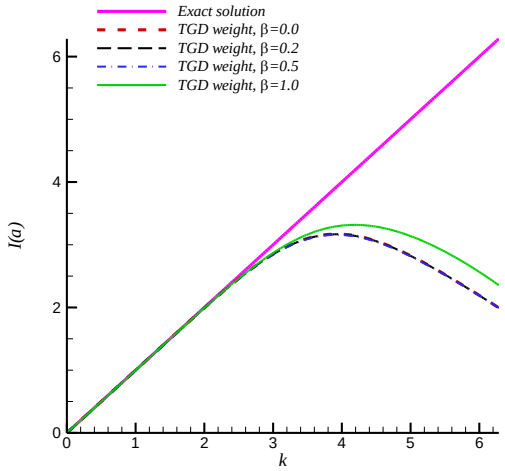

(c) Modified wavenumber

Fig. 4.14. 2-D Fourier analysis results of the 2-2-2-2 LSMLC schemes (7th order) using TGD weight with different upwind factors (β = 0, 0.2, 0.5, 1.0).

According to the observations from Fig. 4.9 to Fig. 4.14, the effect of upwind factor β can be concluded as follows,

1. For both the TGD weight function and IPF weight function, the dissipation increases with β. For the IPF weight, the dissipation for all wavenumbers in (0, 2π) increases simultaneously; while for the TGD weight, the increase of dissipation is not obvious in the region near $k = 0$, which is favorable in terms of maintaining small stiffness.

2. For both the TGD weight function and IPF weight function, the spectral resolution does not change significantly with β, except when $\beta = 1.0$. This is because that the weight on the downwind direction becomes zero and the LSMLC scheme on bias stencil has better spectral resolution.

3. For both the TGD weight function and IPF weight function, $\beta = 0$ leads to unstable central scheme and $\beta > 0$ leads to stable upwind scheme.

4. The upwind factor β has the similar effect as α in the one-dimensional upwind scheme, which can be used to adjust the dissipation and stability of the LSMLC scheme in two-dimensional cases. The recommended value for β is 0.2 according to the current analysis for interior schemes. However, we should mention here that β should be increased to 0.5 for the 2-2-2-2 LSMLC scheme according to the forthcoming analysis of boundary closure schemes in Section 4.4. The analysis on β suggests that the TGD weight function still have advantage over the IPF weight because it has smaller stiffness.

4.3.4 Effect of Derivative Weight Factor

In the last part of the parametric study, we briefly investigate the effect of derivative weight factor γ, which measures the ratio of weights in the first derivative layer over weights in the

function value layer. Three different values of γ are experimented: 0.5, 1.0, 1.5. If $\gamma < 1.0$, the LSMLC scheme put more weights on values from supporting grid points; if $\gamma > 1.0$, the LSMLC scheme put more weights on first derivatives from supporting grid points.

Fig. 4.15 presents the two-dimensional Fourier analysis results of the third-order 1-1-1-1 LSMLC scheme. The IPF weight is more sensitive to γ compared with the TGD weight. Figure (a) shows that the dissipation near k = 0 decreases with the increase of γ, which may suggest large γ works better in this case. On the other hand, figure (b) shows the spectral resolution slightly lowers with the increase of γ, which suggests small γ works better. For the TGD weight, changing γ does not affect the dissipation factor (c) or the modified wavenumber (d).

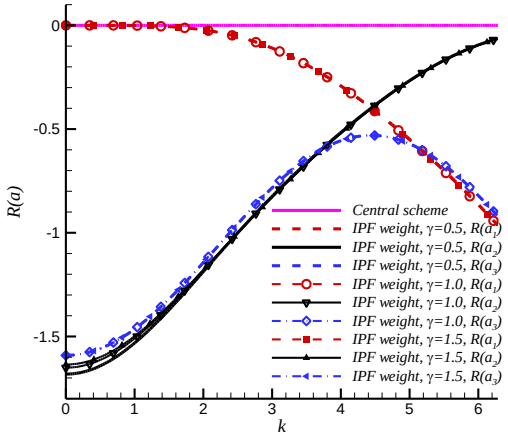

a), dissipation factor (IPF weight)

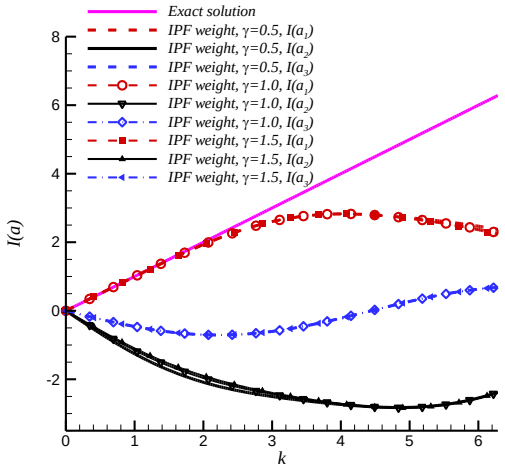

b), modified wavenumber (IPF weight)

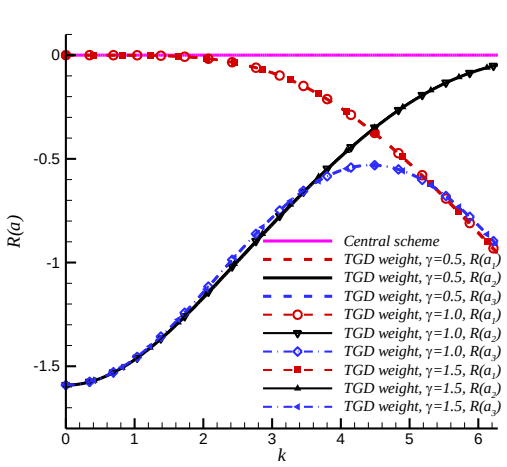

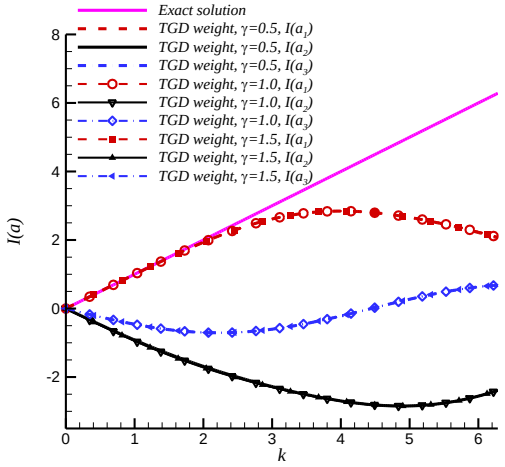

c), dissipation factor (TGD weight) d), modified wavenumber (TGD weight)

Fig. 4.15. 2-D Fourier analysis results of the 1-1-1-1 LSMLC schemes (3rd order) with various derivative weight factors (γ = 0.5, 1.0, 1.5).

Fig. 4.16 and Fig. 4.17 present the two-dimensional Fourier analysis results of the 2-2-1-1 and the 2-2-2-2 LSMLC schemes respectively. The observations are the consistent with those in the 1-1-1-1 scheme.

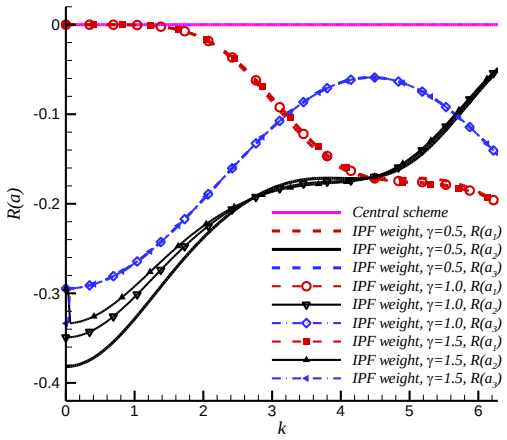

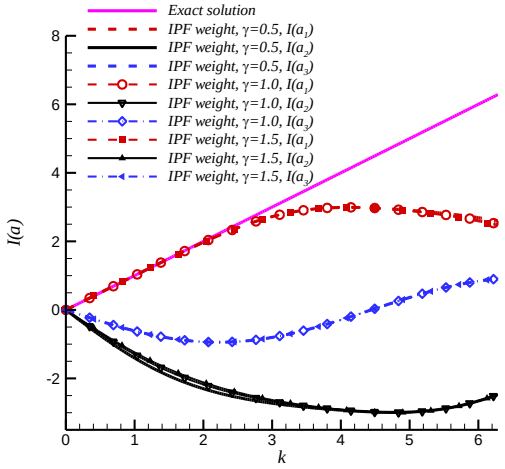

a), dissipation factor (IPF weight) b), modified wavenumber (IPF weight)

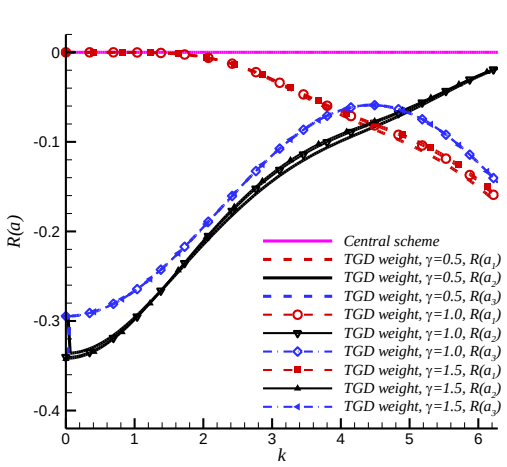

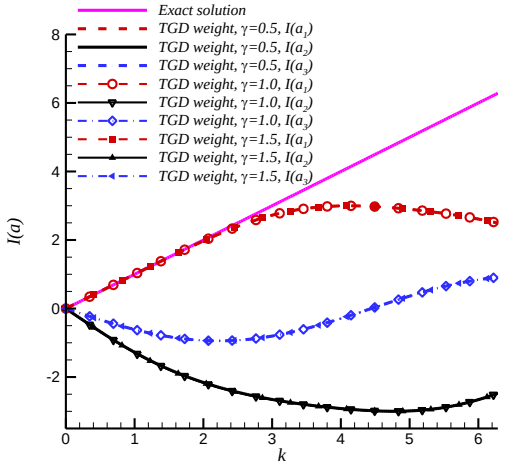

c), dissipation factor (TGD weight) d), modified wavenumber (TGD weight)

Fig. 4.16. 2-D Fourier analysis results of the 2-2-1-1 LSMLC schemes (5th order) with various derivative weight factors (γ = 0.5, 1.0, 1.5).

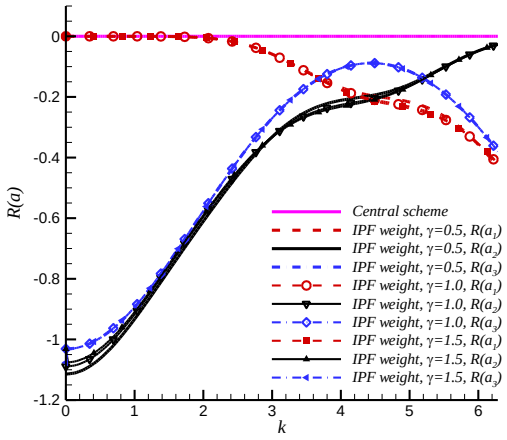

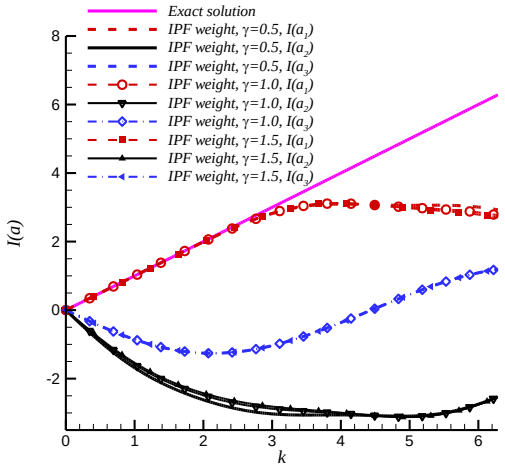

a), dissipation factor (IPF weight) b), modified wavenumber (IPF weight)

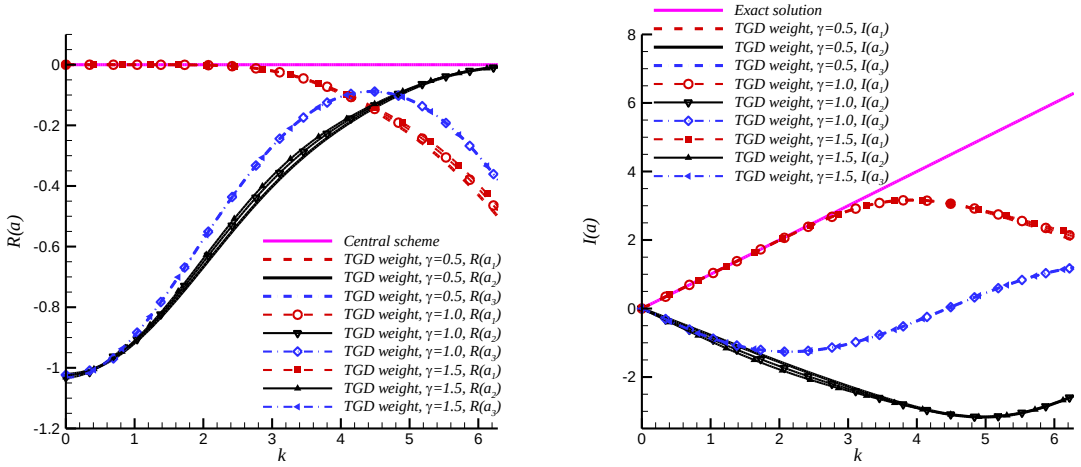

c), dissipation factor (TGD weight) d), modified wavenumber (TGD weight)

Fig. 4.17. 2-D Fourier analysis results of the 2-2-2-2 LSMLC schemes (7th order) with various derivative weight factors (γ = 0.5, 1.0, 1.5).

To conclude, the effect of the derivative weight factor γ is not significant in the LSMLC scheme with the TGD weight, while it might slightly change the stiffness and spectral resolution for the scheme with the IPF weight. Therefore, we prefer to use the TGD weight with $\gamma = 0.5$. The intuition that we should put more weights on the values are reasonable and consistent with the suggestion in [94].

4.4. Comparison of LSMLC scheme with MLC and DMLC schemes

In this section, the Fourier analysis results from three different multi-layer compact schemes developed in this dissertation are compared together. Same as last section, the convection angle and Fourier phase angle are set to be $\pi/4$. Because the spurious modes mainly affect the stability and the stiffness, only the physical mode is analyzed here to compare the accuracy of these

schemes. The dissipation factor can show the dissipation and the modified wavenumber can show the dispersion or spectral resolution of these schemes.

Fig. 4.18 compares physical mode a_1 for the third-order 1-1-1-1 schemes, the fifth-order 2-2-1-1 schemes, and the seventh-order 2-2-2-2 schemes. Figures a), c), and e) show that the MLC schemes always have the smallest dissipation. The DMLC schemes have smaller dissipations than the LSMLC schemes except that the 1-1-1-1 DMLC scheme is more dissipative than the 1-1-1-1 LSMLC scheme. Figures b), d), and f) show that the DMLC schemes always have much better resolution than the other two schemes, which is the result of additional degree of freedom u_{xy}. The resolutions of the LSMLC schemes and the MLC schemes are very similar. Fig. 4.18 also validates that all three schemes have spectral-like resolution.

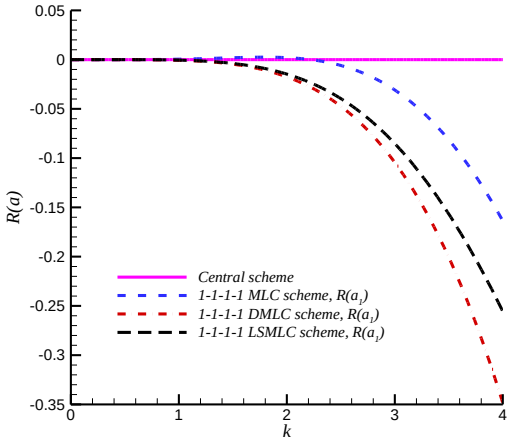

a) $R(a_1)$ for 1-1-1-1 schemes

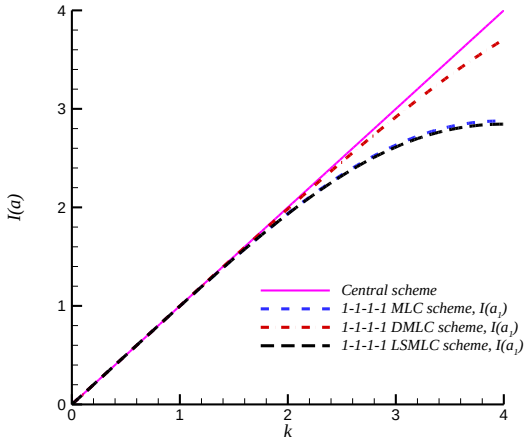

b) $I(a_1)$ for 1-1-1-1 schemes

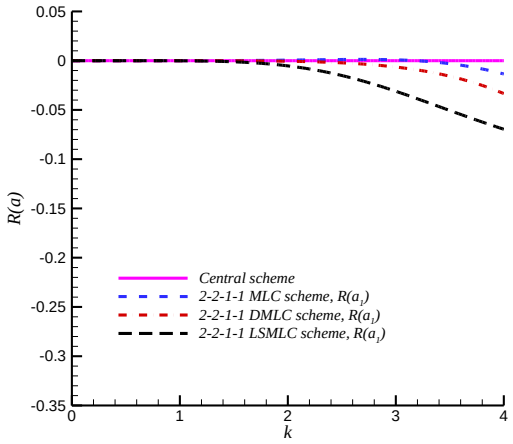

c) $R(a_1)$ for 2-2-1-1 schemes

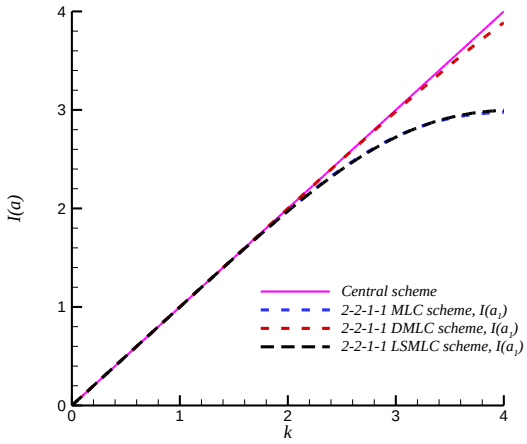

d) $I(a_1)$ for 2-2-1-1 schemes

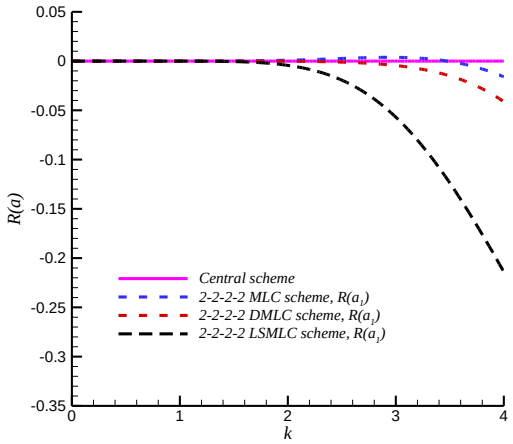

e) $R(a_1)$ for 2-2-2-2 schemes

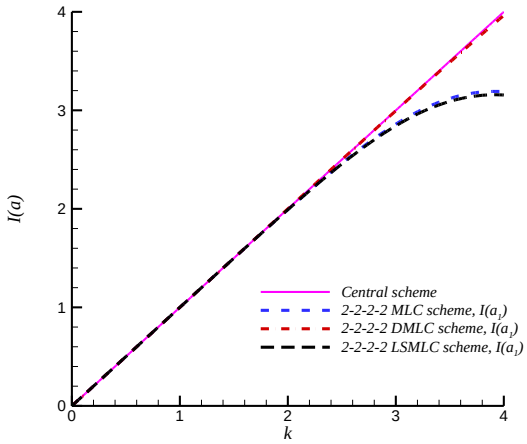

f) $I(a_1)$ for 2-2-2-2 schemes

Fig. 4.18. Comparison of the physical mode a_1 from LSMLC schemes, MLC schemes, and DMLC schemes with various orders.

To conclude, the LSMLC scheme has similar dispersion or spectral resolution with the MLC scheme, which is lower than the DMLC scheme; the LSMLC scheme has larger dissipation than the MLC scheme; the LSMLC scheme is less dissipative than the DMLC scheme in the third-

order case, but more dissipative in very high-order cases. This also implies the advantage of the DMLC scheme in very high-order cases as demonstrated by the forthcoming numerical tests in next chapter.

4.5. Stability Analysis of Boundary Closure Scheme

Like the MLC or the DMLC scheme, we also want to investigate the stability of the LSMLC scheme for two-dimensional cases when coupled with boundary closure schemes. The matrix method described in Section 3.5 is used. The analysis of the LSMLC scheme follows the same procedures and formulas as for the MLC scheme.

There are two choices for the boundary closure schemes. One natural method is deriving the boundary closure schemes from the weighted least square approximation on bias stencils. There is no special treatment required since the methodology in Section 4.1 and 4.2 works for any choice of supporting grid points. Another solution is using the same boundary closure schemes of the MLC scheme, which is given in Appendix B. This is possible because the LSMLC scheme shares the same framework of the MLC scheme in two-dimensional cases. In the following analysis, we refer the former as the pure LSMLC scheme, and the latter as the mix LSMLC scheme. The same cases given in Table 3.1 and Table 3.2 are analyzed. Case 1 has the third-order global accuracy, and Case 2 has the seventh-order global accuracy. Similar as the one-dimensional stability analysis (Section 2.5), the effect of upwind factor β are investigated in the two-dimensional stability analysis.

Fig. 4.19 shows the eigenvalue spectrum for Case 1. Both the pure LSMLC scheme and the mix LSMLC scheme are stable with all three β values, because only negative real parts exist in

the eigenvalue spectrum. However, the effect of β on the spectrum is different. Figure (a) shows that both the continuous spectrum on the right and the discrete spectrum on the left move to the negative direction with the increase of β, which means the pure LSMLC scheme becomes more stable but also has larger dissipation. On the other hand, figure (b) shows that only the continuous spectrum moves to the negative direction, and the discrete eigenvalues almost stay in the same positions when we increase β. This indicates that the mix LSMLC scheme becomes more stable with the increase of β, but it does not introduce excessive dissipation. Comparing the magnitude of real part in figures (a) and (b), it is also obvious the mix LSMLC scheme are less dissipative. Therefore, we recommend using the mix LSMLC scheme when the boundary exists in two-dimensional cases. The recommended β is still 0.2 considering the requirement in the Fourier analysis.

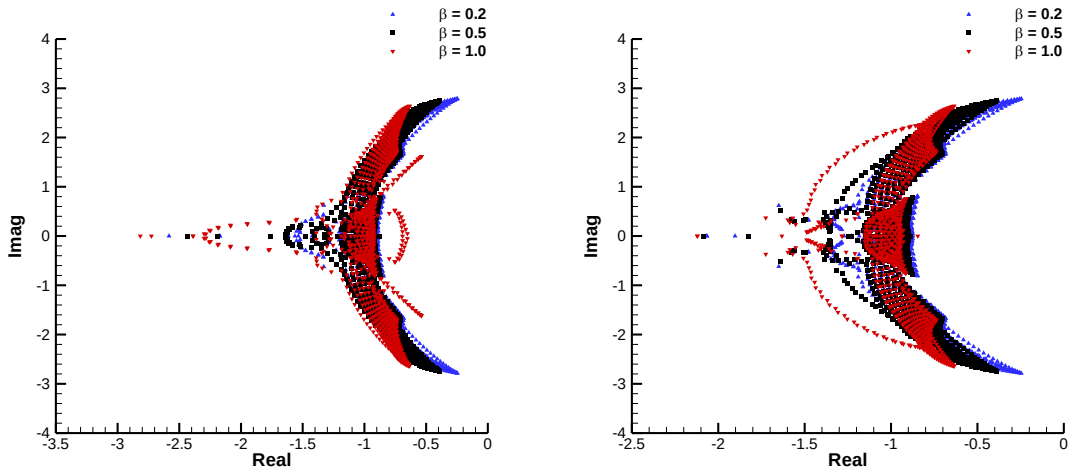

(a) pure LSMLC scheme (b) mix LSMLC scheme

Fig. 4.19. Comparison of the eigenvalue spectrum for Case 1 (3rd-order global accuracy).

Fig. 4.20 shows the eigenvalue spectrum for Case 2. Figure (a) shows that the pure LSMLC scheme is stable when $\beta = 0.2,\ 0.5$, but becomes unstable when $\beta = 1.0$. The behavior is unexpected because larger β should stabilize the LSMLC scheme and introduce more dissipations. On the other hand, the effect of β on the mix LSMLC scheme is consistent with our expectation. When $\beta = 0.2$, the mix LSMLC scheme is unstable with two discrete eigenvalues with positive real parts; when $\beta = 0.5,\ 1.0$, the mix LSMLC scheme becomes stable. Meanwhile, the mix LSMLC does not introduce excessive dissipation with the increase of β. Therefore, we still recommend using the mix LSMLC scheme for Case 2, and the recommended β is 0.5 considering the requirement of boundary stability.

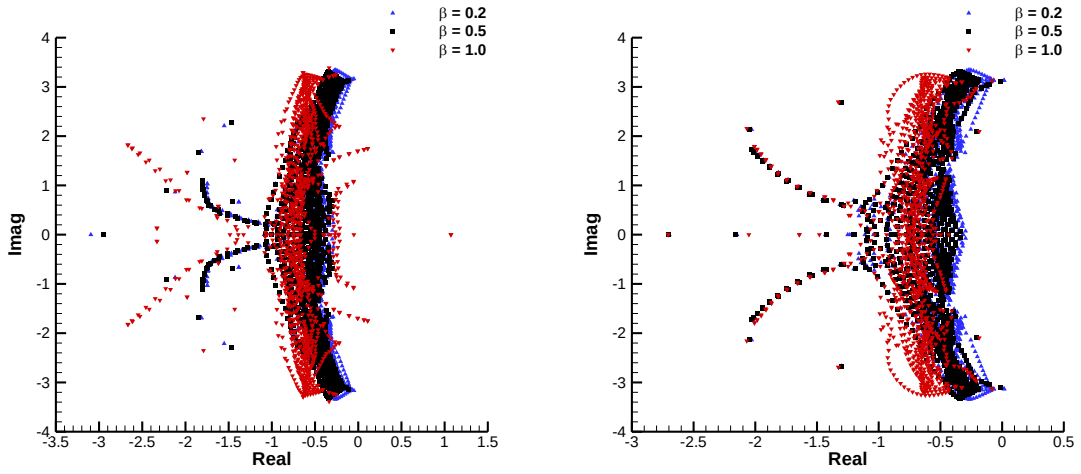

(a) pure LSMLC scheme (b) mix LSMLC scheme

Fig. 4.20. Comparison of the eigenvalue spectrum for Case 2 (7th-order global accuracy).

4.6. Implementation of LSMLC Scheme on Euler and Navier-Stokes Equations

The implementation of the LSMLC schemes on Euler equations and Navier-Stokes equations follow the same procedures of the MLC schemes as in Section 2.3. The only difference is that the cross derivatives of the convective flux should be approximated by the upwind and downwind LSMLC schemes separately, as given in Eq. (2.46). The upwind and downwind schemes only differ in the sign of upwind factor - β. For the viscous flux, the cross-derivative approximations use the central LSMLC scheme. With this approach, the second derivatives and cross derivatives of convective fluxes are both approximated by upwind schemes, which leads to consistent discretization. This approach is always stable for two-dimensional simulations, which can be shown by the numerical tests in Chapter 5.

4.7. Summary

Chapter 4 first presents the weighted least square approximation and the weight functions with upwind correction, which are used to extend the one-dimensional MLC scheme to LSMLC scheme in two-dimensional cases. The LSMLC scheme can be obtained from the solution of a constrained optimization problem. The solution is position-independent and can be applied to all grid points with the same grid stencils, which avoids high computational costs as most other least square numerical methods on unstructured meshes. The weight function has important effect on the dissipation and stability of the LSMLC scheme. The upwind scheme is derived by introducing upwind correction into the weight function.

A parametric study based on the two-dimensional Fourier analysis is performed to optimize the LSMLC scheme. Stability analysis of boundary closure scheme is performed with matrix methods. These analysis show that the 1-D constraint does not affect the formulas of cross

derivatives. The TGD weight function has the best property in our current LSMLC scheme, because it can remove the numerical instability and it maintains small dissipations. The upwind factor β has the similar effect as α in the one-dimensional upwind scheme, which can be used to adjust the dissipation and stability of the LSMLC scheme in two-dimensional cases. The recommended value for β is 0.2 for the 1-1-1-1 and 2-2-1-1 LSMLC schemes, and it is 0.5 for the 2-2-2-2 LSMLC scheme. Compared with β, the effect of the derivative weight factor γ is not significant in the LSMLC scheme with the TGD weight. The recommend value of γ is 0.5.

Like the DMLC scheme in Chapter 3, the LSMLC scheme can also overcome the inconsistency of the 1-D upwind scheme and 2-D central scheme in the MLC scheme, and it avoids the ad-hoc cross-derivative approximations by using the weighted least square approximation. The numerical instability is removed by using the weight function with a positive β and the resulting scheme is always stable in the full range of wavenumbers. For the stability of boundary closure schemes, the mix LSMLC maintains small dissipation while improving the stability. These are the main improvement in the current LSMLC scheme from the MLC scheme.

5. Evaluation and Validation of Numerical Schemes

In this chapter, the numerical tests are conducted with the schemes developed in this dissertation. The MLC scheme, the DMLC scheme and the LSMLC scheme are implemented on the 1-D and 2-D linear advection equation, the 1-D and 2-D nonlinear Euler equations, and the 2-D compressible Navier-Stokes equations. Numerical solutions are compared with corresponding analytical solutions, and the order of accuracy is evaluated by grid refinement. The numerical tests include, the 1-D and 2-D linear advection, the 1-D acoustic wave, the 1-D and 2-D entropy wave, the 2-D isentropic vortex, and the 2-D supersonic Couette flow. For one-dimensional numerical simulations, the DMLC scheme and the LSMLC scheme are equivalent with the MLC scheme; for two-dimensional numerical simulations on the Euler equations, the results of three schemes are compared. Zhong's upwind explicit schemes [21] are also used for comparison in most test cases.

For the MLC and the DMLC scheme, the adjustable parameter α follows the recommended values given in Section 2.1; for the LSMLC scheme, the TGD weight with the recommended upwind factor β given in Section 4.3.3 is used. Periodic boundary conditions are set for most cases in this chapter. In the 2-D linear advection and 2-D compressible Couette flow, the effect of boundary closure schemes for non-periodic boundaries is investigated.

The focus of the numerical tests is on the high-order accuracy and high spectral resolution property when the number of grid points per wavelength is small. Because the MLC scheme is

designed for the simulation of smooth flow fields without discontinuity, test cases with shock waves are not considered for the Euler or Navier-Stokes equations in this dissertation.

5.1. Linear Advection Equation

5.1.1 One-Dimensional Advection

In the first place, the new very high-order MLC scheme is tested on the one-dimensional linear advection equation given in Eq. (2.3), where the wave speed c is set to 1. A sinusoidal wave in x-direction is computed in the simulation, where the exact solution and initial condition ($t = 0$) is given as,

$$u(x,t) = 2\sin\left[6\pi(x-t)+0.5\right] \tag{5.1}$$

The computational domain is in an interval of $0 < x < 1$, which includes three wave periods. A uniform mesh with N grid panels is used for spatial discretization. Periodic boundary conditions are set on both ends of the domain. Various upwind MLC schemes are used to solve Eq. (2.3), along with Zhong's upwind explicit schemes [21] for comparison, as shown in Table 5.1. All calculations use the fourth-order Runge-Kutta method for time integration. To compare spatial discretization errors and estimate rates of convergence of MLC schemes, the CFL number is set to be a very small value of 0.005 so that the error from the time integration is much smaller than that from spatial discretization. In future simulations, larger CFL numbers can be used which still satisfy the stability condition.

Table 5.1. Selections of MLC schemes and Zhong's explicit schemes for 1-D linear advection equation.

MLC scheme	Zhong's explicit scheme [21]
3rd-order 1-1-1-1 MLC scheme (α = 1.5)	Zhong's 3rd-order explicit scheme (α = 0.25)
5th-order 2-2-1-1 MLC scheme (α = -1)	Zhong's 5th-order explicit scheme (α = -6)
7th-order 2-2-2-2 MLC scheme (α = 12)	Zhong's 7th-order explicit scheme (α = 36)

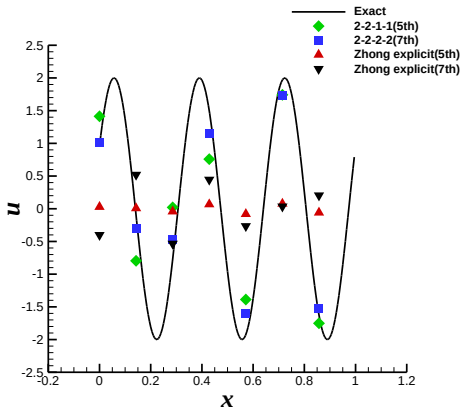

a), N = 7

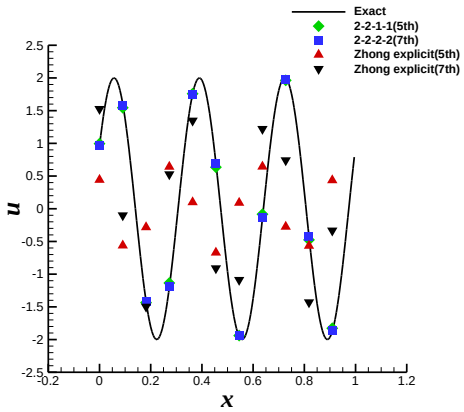

b), N = 11

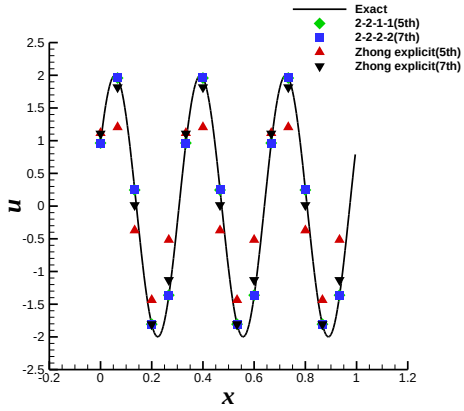

c), N = 15

Fig. 5.1. Comparison of results at t = 1 of the MLC schemes and Zhong's explicit schemes with different grid resolutions for the one-dimensional linear advection equation with periodic boundary conditions.

Fig. 5.1 compares the results of the third and fifth-order schemes mentioned in Table 5.1 with different grid resolutions (N = 7, 11, 15). The goal is to look at how these schemes perform when grid resolution is coarse. In particular, the number of grid points per wavelength is 2.33, 3.67, 5 respectively, when N = 7, 11, 15. The simulation is carried out to t = 1. As expected, the error increases when gradually decreasing the number of grid points. When N = 15 (c), the errors for Zhong's explicit schemes are observable especially with the fifth-order scheme, while the MLC schemes (both 2-2-1-1 and 2-2-2-2) can resolve the wave much better. When N = 11 (b), the MLC scheme (both 2-2-1-1 and 2-2-2-2) is still able to resolve the wave very accurately, but both Zhong's fifth and seventh-order explicit schemes show obvious deviation from the exact solution. Finally, when the grid resolution reduces to N = 7 (a), the seventh-order 2-2-2-2 scheme still have a very good resolution. The fifth-order 2-2-1-1 scheme is not as accurate as the 2-2-2-2 scheme but also generate reasonable results. In comparison, the results of Zhong's fifth and seventh-order explicit schemes show very large errors, and the solutions do not resemble the exact solution anymore on this very coarse grid. This indicates that the MLC schemes have much better accuracy than conventional finite difference methods on very coarse grids. The MLC schemes maintain excellent resolution for computing components of very small wavelengths, in other words, they can achieve a spectral-like resolution which is the ultimate purpose of the scheme.

In the next place, computational errors of the numerical schemes are calculated, and grid refinement is performed to estimate the rate of convergence. Table 5.2 to Table 5.4 compare the errors and rates of convergence of different MLC schemes and Zhong's explicit schemes in Table 5.1. First, the results show that all the schemes can achieve their expected orders of accuracy. All three tables indicate that the MLC schemes have smaller errors and higher rates of

convergence than Zhong's explicit schemes with the same designed orders. In Table 5.2 and Table 5.4, the estimated orders of the 1-1-1-1 and 2-2-2-2 schemes are almost one order higher than the expected orders (3 and 7) when N is larger than 80, which indicates the MLC scheme is very accurate in the simulation of linear waves. Second, much better accuracies are observed in the MLC schemes on the coarse mesh. For example, Table 5.2 shows that the error of the 1-1-1-1 scheme is one order smaller in magnitude than Zhong's third-order explicit scheme when N equals to 10. The advantage is even more significant for fifth and seventh-order schemes in Table 5.3 and Table 5.4, where the MLC schemes are two orders lower in error magnitudes than their counterparts. This quantitative analysis of errors further validates the spectral-like resolution of the MLC scheme.

Table 5.2. Errors and rates of convergence of the 1-1-1-1 MLC scheme (3rd order) and Zhong's explicit scheme (3rd order) for advection equation.

N	third-order 1-1-1-1 MLC scheme, α = 1.5						Zhong's third-order explicit scheme, α = 0.25					
	L1 error	Order	L2 error	Order	L∞ error	Order	L1 error	Order	L2 error	Order	L∞ error	Order
5	1.40E+00	\	1.57E+00	\	2.16E+00	\	1.45E+00	\	1.59E+00	\	2.24E+00	\
10	5.62E-01	1.31	6.42E-01	1.29	8.69E-01	1.31	1.15E+00	0.34	1.26E+00	0.34	1.77E+00	0.34
20	6.76E-02	3.06	7.56E-02	3.09	1.07E-01	3.02	5.52E-01	1.06	6.12E-01	1.04	8.62E-01	1.04
40	5.65E-03	3.58	6.28E-03	3.59	8.88E-03	3.59	4.54E-02	3.60	5.05E-02	3.60	7.15E-02	3.59
80	3.93E-04	3.85	4.37E-04	3.85	6.17E-04	3.85	4.06E-03	3.48	4.51E-03	3.49	6.37E-03	3.49
160	2.54E-05	3.95	2.82E-05	3.95	3.98E-05	3.95	4.36E-04	3.22	4.84E-04	3.22	6.85E-04	3.22

Table 5.3. Errors and rates of convergence of the 2-2-1-1 MLC scheme (5th order) and Zhong's explicit scheme (5th order) for advection equation.

N	fifth-order 2-2-1-1 MLC scheme, α = -1						Zhong's fifth-order explicit scheme, α = -6					
	L1 error	Order	L2 error	Order	L∞ error	Order	L1 error	Order	L2 error	Order	L∞ error	Order

5	2.16E+00	\	2.36E+00	\	3.33E+00	\	1.09E+00	\	1.23E+00	\	1.69E+00	\
10	6.76E-02	5.00	7.75E-02	4.93	1.05E-01	5.00	1.56E+00	-0.52	1.73E+00	-0.49	2.41E+00	-0.51
20	1.44E-03	5.56	1.59E-03	5.60	2.25E-03	5.54	1.50E-01	3.38	1.65E-01	3.39	2.31E-01	3.38
40	3.53E-05	5.35	3.92E-05	5.34	5.54E-05	5.34	4.74E-03	4.98	5.27E-03	4.97	7.44E-03	4.96
80	9.36E-07	5.24	1.04E-06	5.24	1.47E-06	5.24	1.46E-04	5.02	1.62E-04	5.02	2.30E-04	5.02
160	2.22E-08	5.40	2.47E-08	5.40	3.49E-08	5.40	4.55E-06	5.01	5.05E-06	5.01	7.14E-06	5.01

Table 5.4. Errors and rates of convergence of the 2-2-2-2 MLC scheme (7th order) and Zhong's explicit scheme (7th order) for advection equation.

N	seventh-order 2-2-2-2 MLC scheme, $\alpha = 12$						Zhong's seventh-order explicit scheme, $\alpha = 36$					
	L1 error	Order	L2 error	Order	L∞ error	Order	L1 error	Order	L2 error	Order	L∞ error	Order
5	1.33E+00	\	1.47E+00	\	2.05E+00	\	8.93E-01	\	1.01E+00	\	1.38E+00	\
10	1.87E-02	6.15	2.09E-02	6.13	2.89E-02	6.15	1.62E+00	-0.86	1.86E+00	-0.88	2.51E+00	-0.86
20	1.32E-04	7.15	1.46E-04	7.16	2.06E-04	7.13	2.13E-02	6.25	2.36E-02	6.30	3.33E-02	6.23
40	8.39E-07	7.29	9.32E-07	7.29	1.32E-06	7.29	1.35E-04	7.30	1.50E-04	7.30	2.11E-04	7.30
80	4.39E-09	7.58	4.88E-09	7.58	6.90E-09	7.58	9.20E-07	7.19	1.02E-06	7.19	1.45E-06	7.19
160	1.93E-11	7.83	2.14E-11	7.83	3.03E-11	7.83	6.87E-09	7.07	7.62E-09	7.07	1.08E-08	7.07

The parameter α in the upwind MLC scheme is determined based on the Fourier analysis and stability analysis. In Fig. 5.2, the effect of α values is also investigated in the linear advection simulation with the seventh-order 2-2-2-2 scheme, which has the recommended α value of 12. The L_2 errors with different α values on three sets of grids (N = 10, 20, 40) are presented. With the increase of α, the L_2 error grows slightly because of more numerical dissipation; however, the difference is not very significant. Therefore, in the following numerical simulations of this chapter, only the results with the recommended α values are presented. It is concluded that the choice of α is not unique as long as it satisfies the stability condition of the interior and boundary closure schemes, as discussed in Section 2.4; and the recommended α values in Section 2.1

should be appropriate for most practical numerical simulations according to the authors' experience, although it is likely that in some specific cases, the change of α value could significantly affect the results thus it needs to be carefully selected.

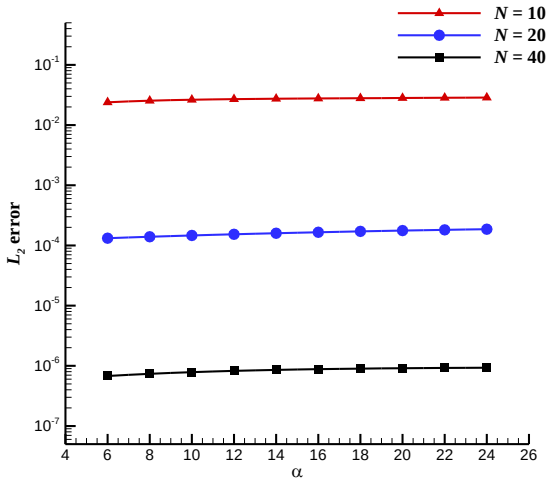

Fig. 5.2. Evolution of L_2 error with α value in the 7th-order 2-2-2-2 MLC scheme (t = 1).

There is an issue about computational efficiency of the MLC schemes because one or two auxiliary equations are introduced for one or two-dimensional simulations. However, the original equation becomes exact because the first derivative is available at a grid point, which means it does not need discretization. To show the computational efficiency, Fig. 5.3 compares the evolutions of L_2 error as a function of CPU time (a) and non-dimensional grid spacing (b) of various MLC schemes and Zhong's explicit schemes. A fixed CFL number of 0.005 is used for all simulations, and errors are measured at t = 1. Figure (a) indicates that high-order methods need less CPU time to reach the same accuracy than low-order methods. Between Zhong's explicit scheme and the MLC scheme with the same order of accuracy, the latter converges faster although it doubles the degree of freedom and number of equations at each point. When the CFL number is fixed, the time step size is proportional to the grid spacing. Therefore, the total CPU

time is dependent on the grid size and the CPU time for a single step. Figure (b) shows the evolution of L_2 error with non-dimensional grid spacing β, which is defined as,

$$\beta = k \cdot h \tag{5.2}$$

where k is the wavenumber, and h is the dimensional grid spacing. It shows that a high-order scheme allows a larger grid spacing than a low-order scheme to achieve the same accuracy. Furthermore, the MLC schemes have a clear advantage over Zhong's explicit schemes of the same order. As a result, the MLC scheme can achieve the same accuracy with much fewer grid points.

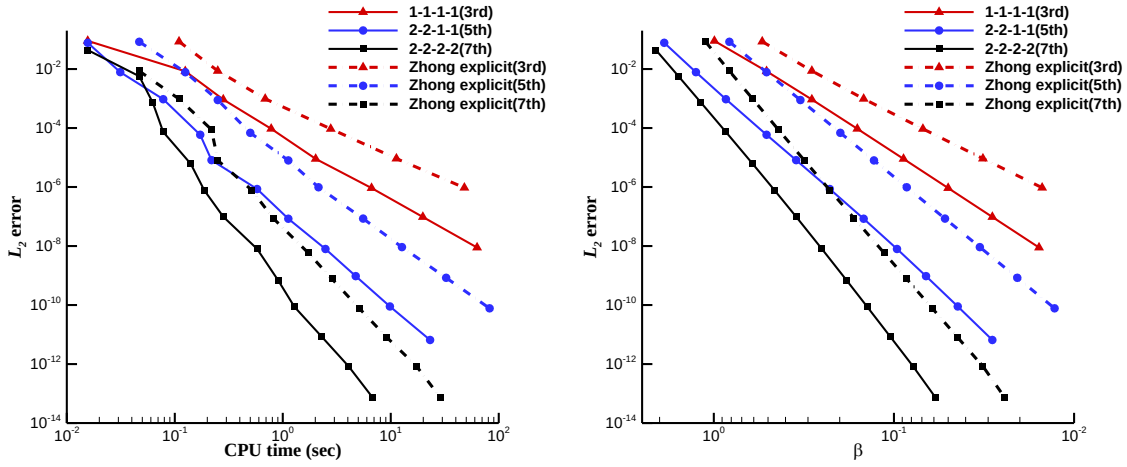

a), L_2 error versus CPU time b), L_2 error versus non-dimensional grid spacing

Fig. 5.3. Computational efficiency of the MLC schemes and Zhong's explicit schemes [21].

Table 5.5 shows the required CPU time and grid number (N) for some certain magnitudes of L_2 error. It is clear that the MLC schemes need much fewer grid points than Zhong's explicit schemes to reduce L_2 error to the same magnitude. Benefit from it, the required CPU time is significantly shortened in all MLC schemes compared with their counterparts, and this advantage becomes huge for small error magnitude. For example, to achieve the error magnitude of 1E-10,

the 2-2-1-1 scheme only needs about one-eighth CPU time of Zhong's fifth-order explicit scheme. From Fig. 5.3 and Table 5.5, it can be concluded that even the MLC schemes have more equations to solve, they still have very good computational efficiency due to the considerable reduction of grid size. This preceding comparison is for one-dimensional advection equation. In multi-dimensional flow simulations with the Euler or Navier-Stokes equations, the situation becomes more complicated and further investigation is needed.

Table 5.5. Required CPU time and grid number (N) at certain magnitudes of L_2 error.

CPU time (sec)/N	1.E-02	1.E-04	1.E-06	1.E-08	1.E-10	1.E-12
1-1-1-1 MLC scheme (3rd order)	0.13/37	0.78/118	6.64/337			
Zhong's explicit scheme (3rd order)	0.25/66	2.78/273	48.02/1253			
2-2-1-1 MLC scheme (5th order)	0.03/15	0.17/37	0.58/83	2.48/196	9.81/426	
Zhong's explicit scheme (5th order)	0.13/37	0.50/95	2.14/222	12.69/565	82.22/1469	
2-2-2-2 MLC scheme (7th order)	0.05/12	0.08/22	0.19/41	0.58/75	1.28/134	4.08/241
Zhong's explicit scheme (7th order)	0.05/23	0.22/43	0.52/83	1.72/166	5.11/308	17.36/588

5.1.2 Two-Dimensional Advection

In this section, the propagation of a sinusoidal plane wave is simulated, which is governed by Eq. (2.25). The exact solution and initial condition of the wave (t = 0) are given as,

$$u(x,y,t) = 2\sin\left[6\pi\left(x+y-(c_1+c_2)t\right)+0.5\right] \tag{5.3}$$

where c_1 and c_2 are the directional advection speeds in Eq. (2.25), and both is set to be $\sqrt{2}/2$ here. The setting is consistent with the case of $\theta = \varphi = \pi/4$ in the two-dimensional Fourier analysis (see Fig. 3.1, Fig. 3.3, Fig. 3.5) where the weak numerical stability exists.

The computational domain is a square field within the range of $0 < x < 1$ and $0 < y < 1$, which includes three wave periods. A uniform mesh with N grid panels in both dimensions is used. If the periodic boundary condition is applied, only the inner MLC scheme is needed for spatial discretization. If the non-periodic boundary condition is used, both the inner MLC scheme and boundary closure schemes are needed. The scheme configuration and spatial discretization for the non-periodic case are described in Table 3.1 and Table 3.2. The MLC scheme, the DMLC scheme, the LSMLC scheme, and Zhong's upwind explicit scheme are tested in this example. The system of equations (3.5) is used for the DMLC scheme; the system of equations (3.10) is used for the MLC and LSMLC scheme; and Zhong's upwind explicit scheme directly applies to the original equation (2.25). The fourth-order Runge-Kutta method is used for the time integration with a small CFL number of 0.01.

Results of Periodic Boundary Conditions

In the first place, the periodic boundary conditions are applied. The solution at $t = 1$ from the MLC, DMLC, and LSMLC schemes are compared to show the errors and rates of convergence. The results of the third-order 1-1-1-1 scheme, the fifth-order 2-2-1-1 scheme, and the seventh-order 2-2-2-2 scheme are presented in Table 5.6, Table 5.7, and Table 5.8. The rates of convergence demonstrate that the MLC scheme, the DMLC scheme, and the LSMLC scheme can all achieve their expected orders of accuracy. For the MLC scheme, the rates of convergence are even higher than the expected order. The higher convergence rate is related to the central scheme for cross-derivative approximations. Compared with the upwind scheme for second derivatives, the central scheme is one order higher in accuracy, while the expected order is determined by the upwind scheme. For the DMLC and the LSMLC scheme, the rates of convergence are closer to the expected order. The DMLC scheme only uses the 1-D upwind

scheme in the spatial discretization, and the LSMLC scheme uses upwind schemes with the same orders for both second and cross derivatives. On the other hand, the DMLC scheme outperforms the MLC and the LSMLC schemes with respect to accuracy, because it always shows smaller error on the same mesh. The difference in error is more obvious when N is small, which is a proof of improved spectral resolution for large wavenumbers, as indicated by the Fourier analysis (see Fig. 3.2, Fig. 3.4, and Fig. 3.6). In other words, both the numerical test and Fourier analysis prove that the DMLC scheme has better spectral resolution for large wavenumbers because of its additional degree of freedom u_{xy}. Moreover, this advantage of the DMLC scheme on accuracy becomes more significant for very high-order schemes like the 2-2-1-1 scheme in Table 5.7 and the 2-2-2-2 scheme in Table 5.8, where the error of the DMLC scheme is always one order smaller than the error of the MLC or LSMLC schemes. Since the main purpose to develop our new numerical methods is to achieve both the very high-order accuracy and the spectral-like resolution, the DMLC scheme developed in this dissertation could further realize the goal for multi-dimensional flow simulations. In terms of the MLC and LSMLC scheme, their accuracies are comparable, and their errors are at the same magnitude for most mesh settings. However, Table 5.8 shows that the 2-2-2-2 MLC scheme has smaller error than the 2-2-2-2 LSMLC scheme when N = 80 or 160, which is due to the higher order of the MLC scheme. In fact, the main advantage of the LSMLC scheme is not achieving smaller error but improving stability, which is important in long-time simulations.

Table 5.6. Errors and rates of convergence of the 1-1-1-1 MLC, DMLC, and LSMLC schemes (3rd order) for 2-D linear advection with periodic boundary conditions (t = 1).

N	1-1-1-1 MLC scheme, α = 1.5				1-1-1-1 DMLC scheme, α = 1.5				1-1-1-1 LSMLC scheme, β = 0.2			
	L_1 error	Order	L_2 error	Order	L_1 error	Order	L_2 error	Order	L_1 error	Order	L_2 error	Order

10	2.23E+00	\	2.46E+00	\	7.59E-01	\	8.32E-01	\	1.89E+00	\	2.14E+00	\
20	2.22E-01	3.33	2.46E-01	3.32	9.50E-02	3.00	1.06E-01	2.98	2.57E-01	2.88	2.85E-01	2.88
40	1.20E-02	4.21	1.33E-02	4.21	7.97E-03	3.57	8.85E-03	3.58	1.92E-02	3.74	2.13E-02	3.74
80	6.38E-04	4.23	7.09E-04	4.23	5.54E-04	3.85	6.16E-04	3.84	1.30E-03	3.88	1.45E-03	3.88
160	3.72E-05	4.10	4.14E-05	4.10	3.58E-05	3.95	3.98E-05	3.95	8.38E-05	3.96	9.30E-05	3.96

Table 5.7. Errors and rates of convergence of the 2-2-1-1 MLC, DMLC, and LSMLC schemes (5th order) for 2-D linear advection with periodic boundary conditions (t = 1).

N	2-2-1-1 MLC scheme, α = -1				2-2-1-1 DMLC scheme, α = -1				2-2-1-1 LSMLC scheme, β = 0.2			
	L_1 error	Order	L_2 error	Order	L_1 error	Order	L_2 error	Order	L_1 error	Order	L_2 error	Order
10	1.63E+00	\	1.86E+00	\	1.00E-01	\	1.10E-01	\	1.59E+00	\	1.76E+00	\
20	4.18E-02	5.28	4.63E-02	5.33	2.02E-03	5.63	2.25E-03	5.61	5.43E-02	4.87	6.01E-02	4.87
40	6.96E-04	5.91	7.74E-04	5.90	4.98E-05	5.34	5.54E-05	5.35	1.15E-03	5.56	1.27E-03	5.56
80	1.08E-05	6.01	1.20E-05	6.01	1.32E-06	5.24	1.47E-06	5.24	2.61E-05	5.46	2.90E-05	5.46
160	1.55E-07	6.12	1.73E-07	6.12	3.13E-08	5.40	3.48E-08	5.40	6.09E-07	5.42	6.76E-07	5.42

Table 5.8. Errors and rates of convergence of the 2-2-2-2 MLC, DMLC, and LSMLC schemes (7th order) for 2-D linear advection with periodic boundary conditions (t = 1).

N	2-2-2-2 MLC scheme, α = 12				2-2-2-2 DMLC scheme, α = 12				2-2-2-2 LSMLC scheme, β = 0.5			
	L_1 error	Order	L_2 error	Order	L_1 error	Order	L_2 error	Order	L_1 error	Order	L_2 error	Order
10	7.75E-01	\	8.59E-01	\	2.69E-02	\	2.95E-02	\	8.00E-01	\	9.19E-01	\
20	4.99E-03	7.28	5.54E-03	7.27	1.85E-04	7.18	2.06E-04	7.16	1.01E-02	6.30	1.12E-02	6.36
40	1.82E-05	8.10	2.02E-05	8.10	1.18E-06	7.29	1.31E-06	7.29	6.78E-05	7.22	7.54E-05	7.22
80	4.93E-08	8.53	5.48E-08	8.52	6.21E-09	7.58	6.89E-09	7.57	3.54E-07	7.58	3.93E-07	7.58
160	1.16E-10	8.73	1.29E-10	8.73	3.53E-11	7.46	3.92E-11	7.46	1.55E-09	7.83	1.72E-09	7.83

Fig. 5.4 compares the results of the 2-2-1-1 MLC scheme, the 2-2-1-1 DMLC scheme, the 2-2-1-1 LSMLC scheme, and Zhong's upwind explicit scheme [21] with different grid

resolutions (N = 10, 15, 20). All schemes have fifth-order accuracy. The numerical solutions on the diagonal in the direction of $\theta = \pi/4$ are compared with the exact solution. It shows that the DMLC scheme has the smallest error, then followed by the MLC and the LSMLC scheme, and Zhong's explicit scheme has the largest error. Even though all schemes have the same order of accuracy and are accurate on the fine mesh (N = 20), the advantage of the DMLC scheme on the coarse mesh (N = 10) is significant. The resolving ability of the DMLC scheme is a result of its spectral-like resolution. Moreover, the improvement over the MLC scheme is due to the additional degree of freedom u_{xy} in the DMLC scheme. Meanwhile, the LSMLC scheme has a comparable accuracy with the MLC scheme.

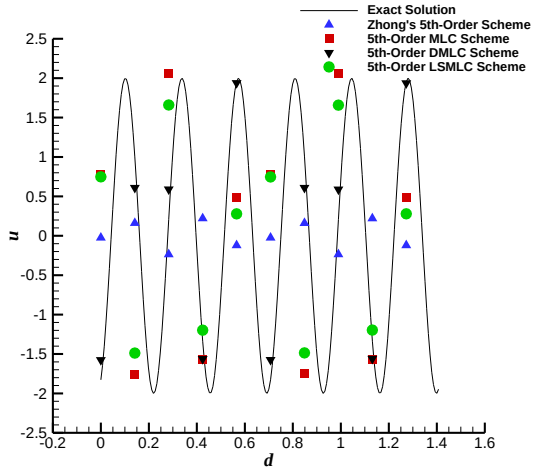

a), N = 10

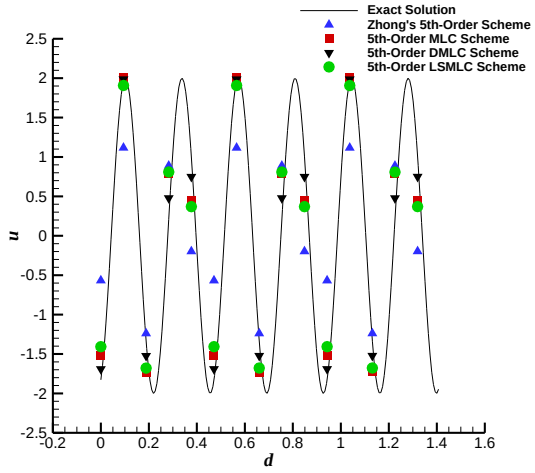

b), N = 15

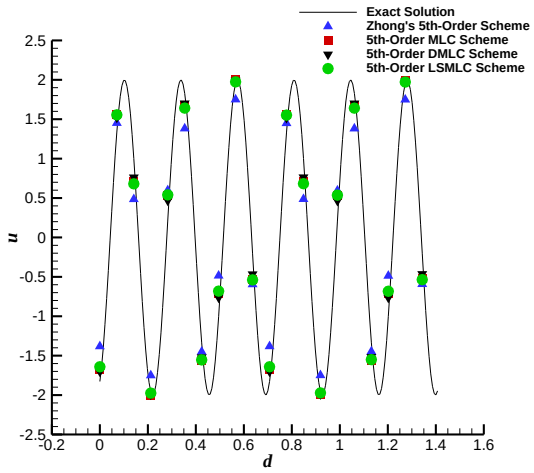

c), $N = 20$

Fig. 5.4. Comparison of solutions of the 2-2-1-1 MLC, DMLC, and LSMLC schemes (5th order) on the diagonal in the direction of $\theta = \pi/4$ for 2-D linear advection ($t = 1$).

Fig. 5.5 and Fig. 5.6 show the comparison of solutions for different third-order schemes and different five-order schemes respectively. The observations are similar with that in Fig. 5.4. The DMLC scheme has the smallest error; the MLC scheme and the LSMLC scheme are in the middle; and Zhong's upwind explicit scheme has the largest error on the same mesh.

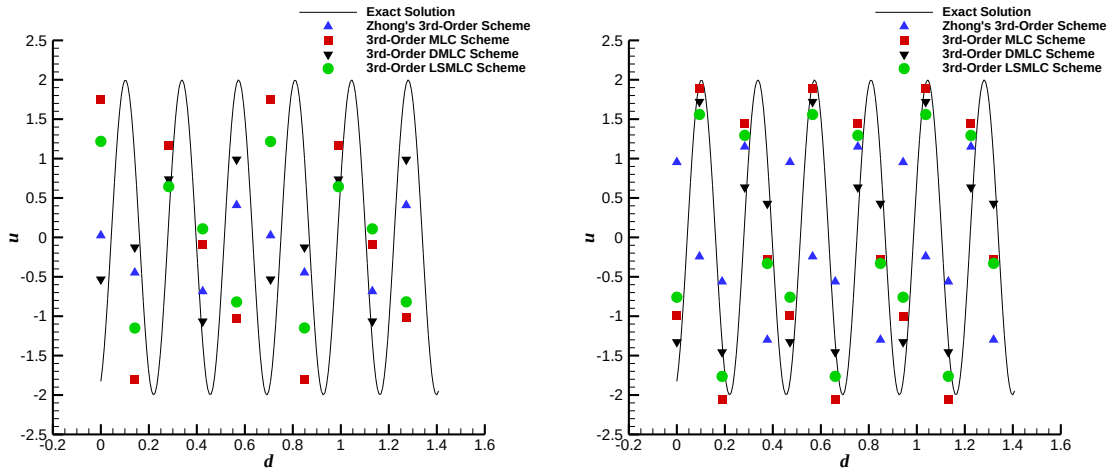

a), $N = 10$ b), $N = 15$

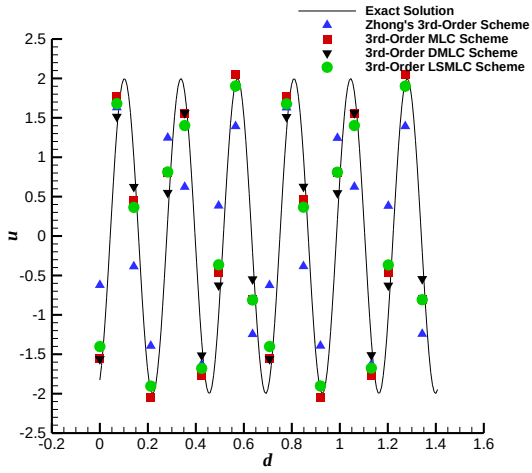

c), $N = 20$

Fig. 5.5. Comparison of solutions of the 1-1-1-1 MLC, DMLC, and LSMLC schemes (3rd order) on the diagonal in the direction of $\theta = \pi/4$ for 2-D linear advection ($t = 1$).

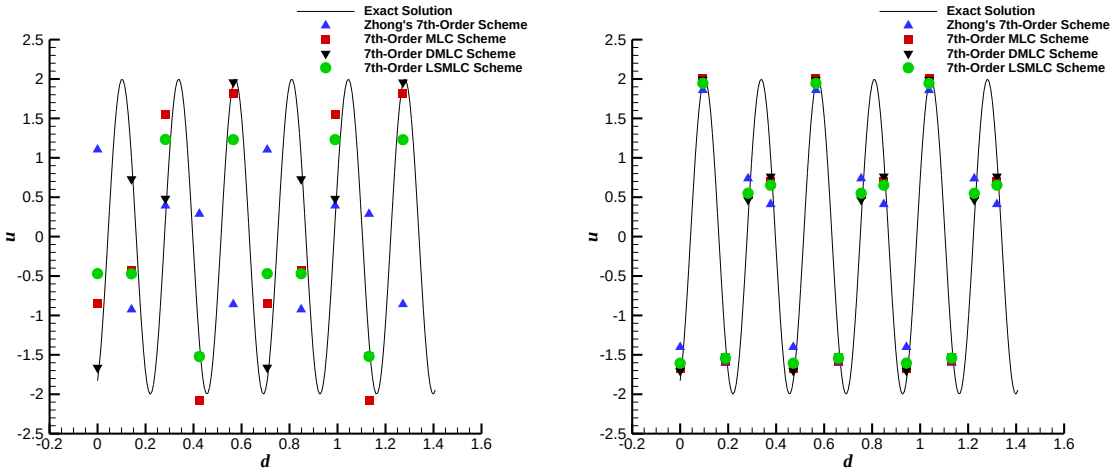

a), $N = 10$ b), $N = 15$

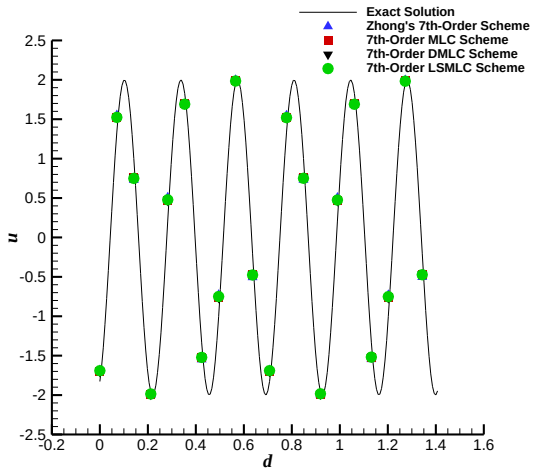

c), $N = 20$

Fig. 5.6. Comparison of solutions of the 2-2-2-2 MLC, DMLC, and LSMLC schemes (7th order) on the diagonal in the direction of $\theta = \pi/4$ for 2-D linear advection ($t = 1$).

To investigate the accuracy and stability of the MLC schemes, the long-time simulation results at $t = 100$ after the sinusoidal wave has traveled approximate 212 wavelengths are analyzed. The computational efficiency of different MLC schemes is compared as well. Fig. 5.7 compares the evolution of L_2 error with non-dimensional grid spacing β using different MLC schemes, DMLC schemes, LSMLC schemes, and Zhong's explicit schemes. The non-dimensional grid spacing β is defined as,

$$\beta = k \cdot h \tag{5.4}$$

where k is the wavenumber, and h is the dimensional grid spacing. The errors of the 1-1-1-1 MLC scheme and 2-2-2-2 MLC scheme grow abruptly during grid refinement when β is too small. This deterioration of solution is the result of the weak numerical instability of the MLC scheme presented in Section 3.4.1. In the periodic simulation, there is no boundary source term to correct the numerical error, eventually, the simulation could diverge if any numerical

instability exists. The Fourier analysis in Fig. 3.1 (d), Fig. 3.3 (d), Fig. 3.5 (d) show that the 2-2-2-2 MLC scheme has the largest magnitude of instability, then follows the 1-1-1-1 MLC scheme and 2-2-1-1 MLC scheme. It can explain why the error of the 2-2-2-2 MLC scheme increases faster than that of the 1-1-1-1 MLC scheme, and the 2-2-1-1 MLC scheme is still stable. Except the instability, different lines in each figure has similar slopes, which means they all have the same order of accuracy. The DMLC scheme is always stable during the grid refinement, and it also shows smaller error than the MLC scheme with the same grid stencil. This observation further proves the increase of spectral resolution of the DMLC scheme due to the introduce of u_{xy}. The LSMLC scheme is also stable while showing larger error than the DMLC scheme for small β. Zhong's explicit schemes are also stable during the grid refinement; however, they have larger errors than the other 3 schemes due to the limit of spectral resolution. The comparison verifies the main advantage of the numerical schemes including MLC, DMLC, and LSMLC schemes over conventional finite difference methods – the spectral-like resolution.

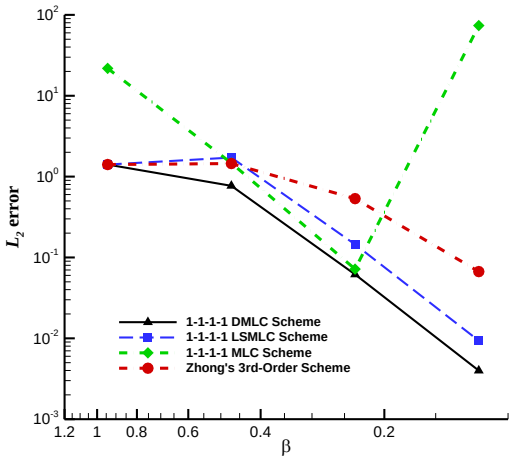

a)

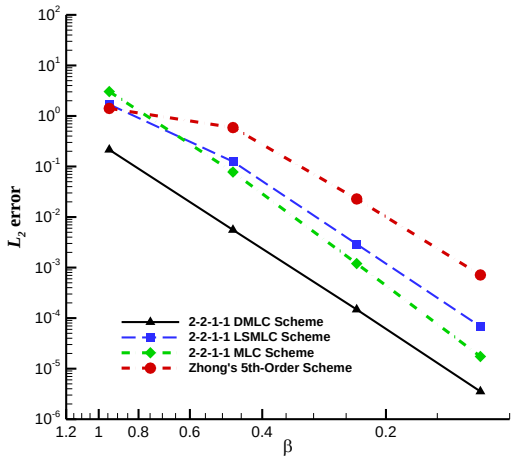

b)

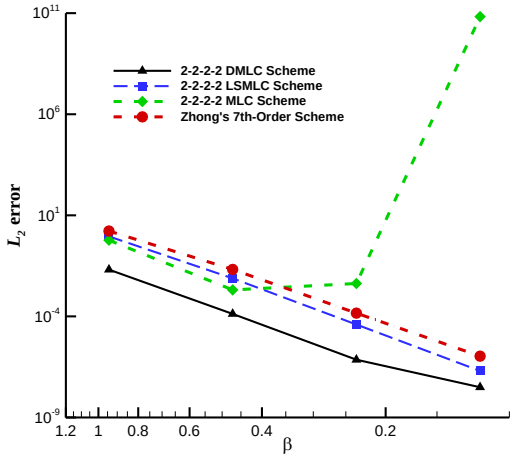

c)

Fig. 5.7. Evolution of the L_2 error versus the non-dimensional grid spacing for 2-D linear advection with periodic boundary conditions (t = 100).

Table 5.9 compares the CPU time of several DMLC schemes and MLC schemes which have the same stencils and order of accuracies. It demonstrates that the simulation with the DMLC scheme always runs faster, and the advantage of the DMLC scheme becomes more significant when the order of accuracy increases. As explained in Section 2.1, although the directional discretization technique introduces an additional equation to solve, it avoids the time-consuming approximation of cross derivatives. Overall, it leads to better computational efficiency, especially for very high-order cases. The CPU time of the LSMLC scheme is not compared here because it follows the same implementation of the MLC scheme, which leads to similar CPU time.

Table 5.9. CPU time of the MLC and DMLC schemes for 2-D linear advection with periodic boundary conditions (t = 100).

N	3rd-order 1-1-1-1 scheme, α = 1.5		5th-order 2-2-1-1 scheme, α = -1		7th-order 2-2-2-2 scheme, α = 12	
	MLC scheme	DMLC scheme	MLC scheme	DMLC scheme	MLC scheme	DMLC scheme

10	6.15E+00	4.59E+00	7.21E+00	5.30E+00	9.78E+00	5.95E+00
20	4.62E+01	3.56E+01	5.50E+01	3.96E+01	7.52E+01	4.56E+01
40	3.63E+02	2.76E+02	4.37E+02	3.09E+02	5.89E+02	3.42E+02
80	3.20E+03	2.76E+03	3.76E+03	2.99E+03	4.95E+03	3.35E+03
160	2.44E+04	2.26E+04	2.99E+04	2.45E+04	3.96E+04	2.77E+04

Results of Non-Periodic Boundary Conditions

In the next place, the results of non-periodic boundary conditions are analyzed. As described in Fig. 3.9, the inflow boundary conditions in Eq. (3.37) are enforced at the bottom and left boundaries; while the characteristic boundary conditions are applied to the top and right boundaries through the one-sided schemes. The long-time simulation results at t = 100 (212 wavelengths) are used to compare the accuracy and stability of the MLC, DMLC, and LSMLC schemes.

Table 5.10 presents the errors and rates of convergence of the 1-1-1-1 MLC scheme, the 1-1-1-1 DMLC scheme, and the 1-1-1-1 LSMLC scheme. The configuration of inner and boundary closure schemes follows Case 1 in Table 3.1 and Table 3.2. It demonstrates that all three schemes can achieve or surpass the expected third-order global accuracy. Similar with the periodic simulation results, the MLC scheme shows slightly higher rates of convergence because of the use of central scheme for cross derivatives. However, the difference is very small here because the lower order boundary closure schemes also affect the rates of convergence. On the other hand, the 1-1-1-1 DMLC scheme still shows smaller error especially for small N's due to its better spectral resolution. The 1-1-1-1 DMLC and MLC schemes with the recommended α value of 1.5 are stable as suggested in Fig. 3.10; the 1-1-1-1 LSMLC scheme with the recommended β value of 0.2 is also stable as suggested in Fig. 4.19.

Table 5.10. Errors and rates of convergence of the 1-1-1-1 MLC, DMLC, and LSMLC schemes (3rd order) for 2-D linear advection with non-periodic boundary conditions (t = 100).

N	1-1-1-1 MLC scheme, α = 1.5				1-1-1-1 DMLC scheme, α = 1.5				1-1-1-1 LSMLC scheme, β = 0.2			
	L_1 error	Order	L_2 error	Order	L_1 error	Order	L_2 error	Order	L_1 error	Order	L_2 error	Order
10	1.46E+00	\	1.42E+00	\	4.87E-01	\	4.47E-01	\	1.23E+00	\	1.21E+00	\
20	1.53E-01	3.25	1.36E-01	3.38	6.43E-02	2.92	5.73E-02	2.96	1.82E-01	2.76	1.60E-01	2.92
40	8.54E-03	4.17	7.47E-03	4.18	5.65E-03	3.51	4.95E-03	3.53	1.36E-02	3.74	1.20E-02	3.73
80	4.60E-04	4.21	4.04E-04	4.21	3.99E-04	3.82	3.51E-04	3.82	9.38E-04	3.86	8.26E-04	3.86
160	2.70E-05	4.09	2.38E-05	4.09	2.59E-05	3.94	2.28E-05	3.94	6.08E-05	3.95	5.35E-05	3.95

Similarly, Table 5.11 and Table 5.12 compare errors and rates of convergence from the 2-2-2-2 MLC scheme, the 2-2-2-2 DMLC scheme and the 2-2-2-2 LSMLC scheme. The configuration of inner and boundary closure schemes follows Case 2 in Table 3.1 and Table 3.2. The results demonstrate that the 2-2-2-2 MLC scheme with the recommended α value of 12 is unstable, as predicted by the matrix method in Fig. 3.11. It should be noted that the divergence is not merely caused by the weak numerical instability from the inner scheme, but the combined effect from the inner scheme and boundary closure schemes. If α is increased to 36, the 2-2-2-2 MLC scheme becomes stable with relatively large dissipation. The results also demonstrate that the 2-2-2-2 DMLC scheme with α value of 12 is stable, which suggests that the DMLC schemes should have better boundary stability in very high-order cases. On the other hand, the 2-2-2-2 LSMLC scheme with β value of 0.5 is stable as well, which is the main improvement of the LSMLC scheme from the MLC scheme.

Similar with the comparison in Table 5.10, the 2-2-2-2 MLC scheme shows slightly higher rates of convergence than the 2-2-2-2 DMLC scheme; however, the DMLC scheme outperforms the MLC scheme in accuracy, as its error is much smaller on the same mesh. Therefore, the

advantage of the DMLC scheme on accuracy is still significant in cases with non-periodic boundaries.

Table 5.11. Errors and rates of convergence of the 2-2-2-2 MLC schemes (7th order) for 2-D linear advection with non-periodic boundary conditions (t = 100).

N	2-2-2-2 MLC scheme, α = 12				2-2-2-2 MLC scheme, α = 36			
	L_1 error	Order	L_2 error	Order	L_1 error	Order	L_2 error	Order
10	1.18E+13	\	1.22E+13	\	1.84E+00	\	1.80E+00	\
20	6.42E+25	\	5.79E+25	\	7.63E-03	7.91	8.84E-03	7.67
40	2.09E+53	\	1.79E+53	\	2.79E-05	8.10	2.74E-05	8.33
80	1.88E+111	\	1.66E+111	\	9.44E-08	8.20	8.94E-08	8.26
160	8.90E+229	\	∞	\	4.30E-10	7.78	3.67E-10	7.93

Table 5.12. Errors and rates of convergence of the 2-2-2-2 DMLC and LSMLC schemes (7th order) for 2-D linear advection with non-periodic boundary conditions (t = 100).

N	2-2-2-2 DMLC scheme, α = 12				2-2-2-2 LSMLC scheme, β = 0.5			
	L_1 error	Order	L_2 error	Order	L_1 error	Order	L_2 error	Order
10	2.92E-02	\	2.26E-02	\	1.01E+00	\	1.05E+00	\
20	2.05E-04	7.16	1.72E-04	7.04	9.29E-03	6.77	9.52E-03	6.78
40	1.27E-06	7.33	1.00E-06	7.42	6.21E-05	7.22	5.30E-05	7.49
80	6.26E-09	7.66	4.90E-09	7.68	3.19E-07	7.60	2.69E-07	7.62
160	2.13E-10	4.88	1.87E-10	4.71	1.53E-09	7.71	1.30E-09	7.69

In summary, the numerical tests on the two-dimensional linear advection equation demonstrates that the DMLC scheme has smallest errors in cases with both the periodic or non-periodic boundary conditions due to the additional degree of freedom u_{xy}; and the advantage is more significant for very high-order schemes. Specifically, the numerical tests on coarse meshes

show that the spectral-like resolution of the DMLC scheme is further improved compared with the MLC scheme or the LSMLC scheme. The LSMLC scheme has slightly larger error than the MLC scheme due to larger dissipation. Their errors are in the same order of magnitude for most test cases; however, in very high-order cases, the increase in errors of the LSMLC scheme becomes more significantly.

The long-time simulation result demonstrates that the DMLC scheme has better computational efficiency especially for the very high-order schemes, because the directional discretization in the DMLC scheme avoids the cross-derivative approximation. The long-time simulation also verifies that the DMLC scheme and the LSMLC scheme are always stable for both periodic and non-periodic boundary conditions, while the MLC scheme could be unstable in some cases. Specifically, the deterioration of the solution is observed in the 1-1-1-1 and 2-2-2-2 MLC schemes for periodic boundary conditions; the 2-2-2-2 MLC scheme with recommended α value of 12 is unstable for non-periodic boundary conditions.

5.2. Nonlinear Euler Equations

In the following part of this section, the two-dimensional Euler equations in the Cartesian coordinates are solved with the MLC scheme, the DMLC scheme, the LSMLC scheme. Zhong's upwind explicit schemes are also used for comparison. A rectangular domain is used for simulations and periodic boundary conditions are set for all test cases. Because there is no physical boundary in the domain, uniform grid points are used, and no boundary closure schemes are required. Meanwhile, a fourth-order Runge-Kutta method is applied for time integration. The CFL number is set to be 0.1 for short-time simulation, and 0.2 for long-time simulation.

5.2.1 One-Dimensional Entropy Wave

The first test case for the Euler equations is the one-dimensional entropy wave in the *x*-direction. The same test case is used by Qiu and Shu [84]. The exact solution and initial condition (t=0) are given as follows,

$$\begin{aligned} \rho(x,t) &= 1 + 0.2\sin(\pi(x-t)) \\ u(x,t) &= 1 \\ p(x,t) &= 1 \end{aligned} \tag{5.5}$$

where the perturbation only exists in density and temperature. The problem corresponds to a passive convection of a fixed density pattern from the initial condition.

The computational domain is in an interval of $0 < x < 2$, which includes one wave period. A uniform mesh with N grid panels is used to discretize the interval, and periodic boundary conditions are applied on both ends. Both the central and upwind MLC schemes on three different centered stencils (1-1-1-1, 2-2-1-1 and 2-2-2-2) are used for spatial discretization. Same as the calculation of linear advection equation, the fourth-order Runge-Kutta method is applied. The CFL number is a small value of 0.1 to ensure stability and maintain small error from time integration.

The errors of ρ between the numerical and exact solution after simulating for one period (t = 2.0) are calculated. The rate of convergence is estimated based on grid refinements. Table 5.13 shows the results of the third-order 1-1-1-1 schemes, while Table 5.14 and Table 5.15 show the fifth-order 2-2-1-1 schemes and the seventh-order 2-2-2-2 schemes respectively. Results of the central scheme (α = 0) and upwind scheme ($\alpha \neq 0$) on the same stencil are compared. The first observation from these tables is that the error is very small. In the 1-1-1-1 scheme, the magnitude of error is about 10^{-7} when N = 80, which is about the machine epsilon in single precision. For

the 2-2-1-1 and 2-2-2-2 schemes, the error is even much smaller. The second observation is that all central schemes ($\alpha = 0$) achieve the expected orders, which is 4, 6, and 8 for the 1-1-1-1, 2-2-1-1, and 2-2-2-2 schemes respectively. The only exception is observed in Table 5.15 when the error is about than 10^{-12}, where the accumulated roundoff error could affect the results. The expected order of the upwind schemes ($\alpha \neq 0$) is one order lower than the corresponding central schemes. However, these tables show that all upwind schemes achieve or even surpass their expected orders. The error of upwind schemes is slightly larger than that of central schemes on the same stencil. This is expected because more dissipation is introduced in the upwind scheme which lowers accuracy. Despite that the central scheme does not have numerical dissipation, the simulation is stable because of the stabilization effect of the fourth-order Runge-Kutta method for time integration.

Table 5.13. Errors and rates of convergence based on ρ of the 3/4th-order 1-1-1-1 MLC scheme for the one-dimensional entropy wave.

N	1-1-1-1 MLC scheme, $\alpha = 0$				1-1-1-1 MLC scheme, $\alpha = 1.5$			
	L_1 error	Order	L_∞ error	Order	L_1 error	Order	L_∞ error	Order
5	2.23E-03	\	3.16E-03	\	1.03E-02	\	1.53E-02	\
10	1.27E-04	4.14	1.87E-04	4.08	6.81E-04	3.92	1.01E-03	3.92
20	7.42E-06	4.10	1.14E-05	4.03	4.40E-05	3.95	6.66E-05	3.92
40	4.57E-07	4.02	7.10E-07	4.01	2.74E-06	4.01	4.23E-06	3.98
80	2.84E-08	4.01	4.43E-08	4.00	1.70E-07	4.01	2.66E-07	3.99

Table 5.14. Errors and rates of convergence based on ρ of the 5/6th-order 2-2-1-1 MLC scheme for the one-dimensional entropy wave.

N	2-2-1-1 MLC scheme, α = 0				2-2-1-1 MLC scheme, α = -1			
	L_1 error	Order	L_∞ error	Order	L_1 error	Order	L_∞ error	Order
5	2.07E-04	\	2.93E-04	\	3.78E-04	\	5.77E-04	\
10	2.98E-06	6.12	4.38E-06	6.06	9.90E-06	5.26	1.54E-05	5.23
20	4.53E-08	6.04	6.90E-08	5.99	2.44E-07	5.34	3.83E-07	5.33
40	7.05E-10	6.01	1.09E-09	5.99	4.96E-09	5.62	7.73E-09	5.63
80	1.10E-11	6.01	1.87E-11	5.86	8.61E-11	5.85	1.35E-10	5.84

Table 5.15. Errors and rates of convergence based on ρ of the 7/8th-order 2-2-2-2 MLC scheme for the one-dimensional entropy wave.

N	2-2-2-2 MLC scheme, α = 0				2-2-2-2 MLC scheme, α = 12			
	L_1 error	Order	L_∞ error	Order	L_1 error	Order	L_∞ error	Order
5	1.24E-05	\	1.75E-05	\	6.72E-05	\	1.04E-04	\
10	4.95E-08	7.97	7.29E-08	7.91	3.83E-07	7.45	5.78E-07	7.49
20	1.89E-10	8.04	2.90E-10	7.97	1.66E-09	7.86	2.56E-09	7.82
40	1.28E-12	7.21	2.57E-12	6.82	7.07E-12	7.87	1.10E-11	7.86
80	2.81E-12	-1.14	3.57E-12	-0.48	6.78E-14	6.70	1.45E-13	6.24

5.2.2 Two-Dimensional Entropy Wave

The second test for the Euler equations is the two-dimensional entropy wave in (x, y) plane. The exact solution and initial condition (t=0) are given as follows,

$$\begin{aligned} \rho(x,y,t) &= 1+0.2\sin(\pi(x+y-(u+v)t)) \\ u(x,y,t) &= 0.7 \\ v(x,y,t) &= 0.3 \\ p(x,y,t) &= 1 \end{aligned} \tag{5.6}$$

To be general, there is an angle between the wave vector and convection direction. The wave vector has an angle of $\pi/4$ from the x-axis, and the convection direction is aligned with

mean flow velocity. The exact solution of two-dimensional entropy wave is a passive convection. For each location, only density and temperature change during the convection, while the density and temperature patterns from the initial condition are maintained.

The computational domain is a square field within the range of $0 < x < 2$ and $0 < y < 2$, which includes one wavelength in both x- and y-direction. A uniform mesh with N grid panels in both dimensions is used, and periodic boundary conditions on all boundaries are applied.

Table 5.16 to Table 5.18 compare the errors and rates of convergence of the MLC schemes, the DMLC schemes, the LSMLC schemes, and Zhong's upwind explicit schemes based on the solution of ρ at $t = 2$ with CFL = 0.1. Each table shows the results from the schemes with the same order of accuracy. First, the results show that the MLC, DMLC, and LSMLC schemes can surpass the expected order of accuracy by one except when the error is close to machine epsilon (see $N = 160$ in Table 5.18), and the MLC scheme shows higher convergence rate due to the use of central schemes on cross derivatives, which is obvious in Table 5.17 and Table 5.18. Zhong's upwind explicit schemes can achieve their expected order as well. Second, the DMLC scheme shows smaller error than the MLC scheme with the same order of accuracy; the advantage of the DMLC scheme over the MLC scheme is more obvious in 5th and 7th-order cases in Table 5.17 and Table 5.18 for small N, which is consistent with the observation in the linear advection results. The LSMLC scheme is less accurate than the MLC scheme but still comparable with errors in the same magnitude. This is probably because that more dissipation is introduced in the least square cross-derivative approximations. Overall, the MLC scheme, the DMLC scheme, and the LSMLC scheme are all much more accurate than the corresponding Zhong's explicit scheme due to the spectral-like resolution.

Table 5.16. Errors and rates of convergence of the 1-1-1-1 MLC scheme, the 1-1-1-1 DMLC scheme, the 1-1-1-1 LSMLC scheme, and Zhong's 3rd-order explicit scheme for 2-D entropy wave (t = 2).

N	Zhong's 3rd-order scheme, α = 0.25		1-1-1-1 MLC scheme, α = 1.5		1-1-1-1 DMLC scheme, α = 1.5		1-1-1-1 LSMLC scheme, β = 0.2	
	L_1 error	Order	L_1 error	Order	L_1 error	Order	L_1 error	Order
5	6.37E-02	\	1.41E-02	\	1.16E-02	\	1.98E-02	\
10	7.29E-03	3.13	7.66E-04	4.20	7.12E-04	4.02	1.31E-03	3.91
20	8.87E-04	3.04	4.47E-05	4.10	4.42E-05	4.01	7.95E-05	4.05
40	1.08E-04	3.04	2.74E-06	4.03	2.73E-06	4.01	4.92E-06	4.01
80	1.32E-05	3.03	1.70E-07	4.01	1.70E-07	4.01	3.06E-07	4.01
160	1.64E-06	3.01	1.06E-08	4.00	1.06E-08	4.00	1.90E-08	4.00

Table 5.17. Errors and rates of convergence of the 2-2-1-1 MLC scheme, the 2-2-1-1 DMLC scheme, the 2-2-1-1 LSMLC scheme, and Zhong's 5th-order explicit scheme for 2-D entropy wave (t = 2).

N	Zhong's 5th-order scheme, α = -6		2-2-1-1 MLC scheme, α = -1		2-2-1-1 DMLC scheme, α = -1		2-2-1-1 LSMLC scheme, β = 0.2	
	L_1 error	Order	L_1 error	Order	L_1 error	Order	L_1 error	Order
5	4.36E-02	\	4.73E-03	\	5.51E-04	\	6.51E-03	\
10	2.46E-03	4.15	7.55E-05	5.97	1.33E-05	5.38	1.71E-04	5.25
20	1.20E-04	4.36	1.08E-06	6.13	2.83E-07	5.55	3.78E-06	5.50
40	3.96E-06	4.91	1.27E-08	6.41	5.22E-09	5.76	7.07E-08	5.74
80	1.23E-07	5.01	1.37E-10	6.53	8.73E-11	5.90	1.18E-09	5.91
160	3.79E-09	5.02	1.68E-12	6.35	1.48E-12	5.88	1.83E-11	6.01

Table 5.18. Errors and rates of convergence of the 2-2-2-2 MLC scheme, the 2-2-2-2 DMLC scheme, the 2-2-2-2 LSMLC scheme, and Zhong's 7th-order explicit scheme for 2-D entropy wave (t = 2).

N	Zhong's 7th-order scheme, α = 36		2-2-2-2 MLC scheme, α = 12		2-2-2-2 DMLC scheme, α = 12		2-2-2-2 LSMLC scheme, β = 0.5	
	L_1 error	Order	L_1 error	Order	L_1 error	Order	L_1 error	Order
5	8.62E-03	\	8.13E-04	\	9.43E-05	\	2.22E-03	\
10	3.91E-04	4.46	2.06E-06	8.63	4.16E-07	7.82	1.34E-05	7.38
20	7.51E-06	5.70	4.76E-09	8.76	1.81E-09	7.85	5.89E-08	7.82
40	7.09E-08	6.73	1.60E-11	8.21	1.29E-11	7.13	2.37E-10	7.96
80	5.70E-10	6.96	4.33E-13	5.21	4.20E-13	4.94	1.03E-12	7.85
160	4.43E-12	7.01	8.42E-14	2.36	8.54E-14	2.30	6.56E-13	0.65

Similar with the analysis for the linear advection, the long-time simulation results with CFL = 0.2 at t = 100, when the mean flow has traveled for 35 domain lengths in x and 15 domain lengths in y, are presented to investigate the accuracy and stability of the MLC schemes. For the MLC schemes, the deterioration of the solution is observed in the 2-2-1-1 scheme and the 2-2-2-2 scheme as shown in Fig. 5.8 b) and c). Again, it is triggered by the weak numerical instability of the MLC scheme because there is no boundary source term in the periodic simulation. As a comparison, the DMLC scheme is always stable during the grid refinement, and it also shows smaller error than the MLC scheme on the 2-2-1-1 and 2-2-2-2 stencils. The LSMLC scheme are also stable except the 2-2-2-2 LSMLC scheme shows a small increase of error when N = 160. The increase does not imply the instability because the error of magnitude is already very small (10^{-10}). One possible reason is that the LSMLC scheme suffers larger round-off error because the coefficients of the scheme differs a lot in magnitudes. Therefore, the error could dominate when the simulation includes more and more steps, which happens in long-time simulations on very

dense meshes. Zhong's explicit schemes are stable during the grid refinement; however, due to the limit of spectral resolution, its error is much larger than other schemes with the same order. The long-time analysis validates the consistent stability of both the DMLC and MLC schemes, and the superior spectral resolution of the DMLC scheme in the nonlinear Euler equations.

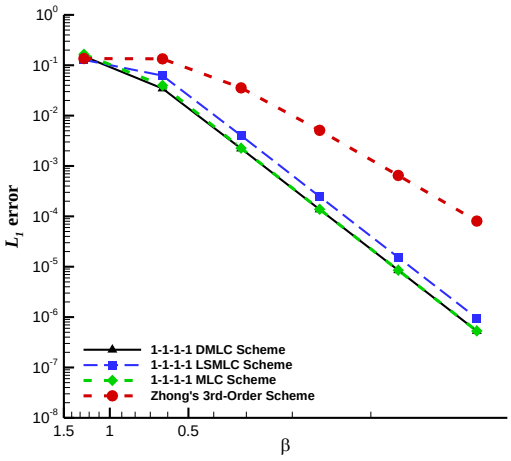

a)

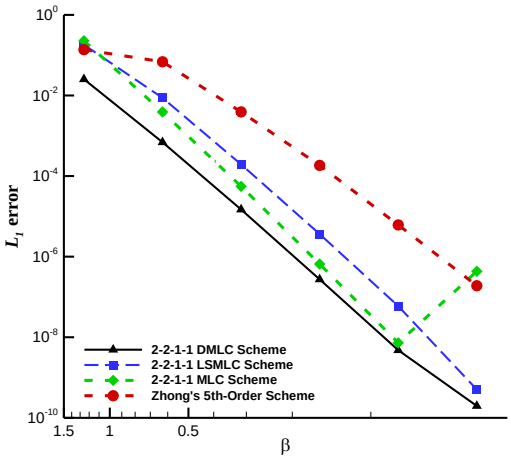

b)

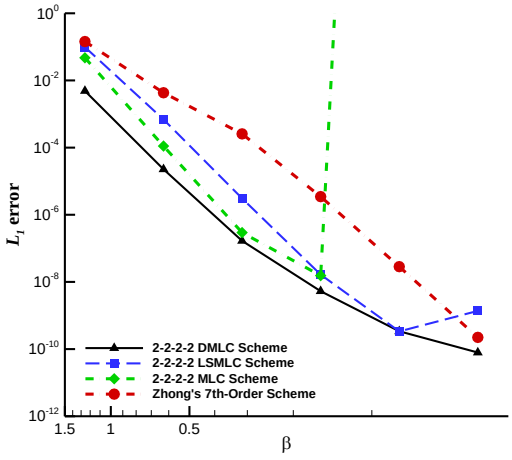

c)

Fig. 5.8. Evolution of the L_1 error versus the non-dimensional grid spacing for 2-D entropy wave (t = 100).

Table 5.19 compares the CPU time of several DMLC schemes with those of MLC schemes which have the same stencils and order of accuracies. Similar with what we observe for the linear advection equation, it shows that the simulation with the DMLC scheme also runs faster for the nonlinear Euler equation. The advantage of the DMLC scheme becomes more significant when the order of accuracy increases, because the DMLC scheme avoids the approximation of cross derivatives, which is much more expensive than the second-derivative approximations for very high-order schemes. The comparison of CPU time here is more important than that in the linear advection, since most flow dynamic problems are governed by either the Euler equations or the Navier-Stokes equations. Therefore, it is a strong proof that the DMLC scheme can have better computational efficiency than the MLC scheme in practical flow simulations. The CPU time of the LSMLC scheme is not compared here because it follows the same implementation of the MLC scheme. Considering the flux splitting of cross derivatives is required, the CPU time may slightly increase in the LSMLC scheme compared with that in the MLC scheme.

Table 5.19. CPU time of the MLC and DMLC schemes for 2-D entropy wave (t = 100).

N	3rd-order 1-1-1-1 scheme, α = 1.5		5th-order 2-2-1-1 scheme, α = -1		7th-order 2-2-2-2 scheme, α = 12	
	MLC scheme	DMLC scheme	MLC scheme	DMLC scheme	MLC scheme	DMLC scheme
10	1.72E+00	1.39E+00	2.74E+00	1.60E+00	3.29E+00	1.65E+00
20	1.40E+01	1.04E+01	2.18E+01	1.17E+01	2.55E+01	1.22E+01
40	1.15E+02	8.56E+01	1.64E+02	9.54E+01	1.95E+02	1.02E+02
80	9.70E+02	7.11E+02	1.30E+03	7.95E+02	1.60E+03	8.38E+02
160	7.67E+03	5.90E+03	1.03E+04	6.56E+03	1.30E+04	7.24E+03

5.2.3 One-Dimensional Acoustic Wave

In computational aeroacoustics, one of the main challenges is the accurate prediction of the unsteady sound wave in long-distance propagation. Small dissipation and dispersion are required at the same time to ensure the high fidelity of sound wave in the simulation. In this section, a one-dimensional acoustic wave propagation in the *x*-direction is simulated as a test case for computational aeroacoustics. The propagation medium of the acoustic wave is air in standard atmosphere pressure and room temperature. A cosine wave is superimposed to the static air flow field as the initial perturbation. The initial conditions are given as follows,

$$\begin{aligned}
&u = u_\infty + \delta u, \qquad \delta u = \varepsilon a_\infty \cos(\omega x), \quad u_\infty = 0\left[m/s\right] \\
&\rho = \rho_\infty + \delta\rho, \qquad \delta\rho = \varepsilon\rho_\infty \cos(2\omega x), \quad \rho_\infty = 1.1771\left[kg/m^3\right] \\
&\frac{p}{p_\infty} = \left(\frac{\rho}{\rho_\infty}\right)^\gamma, \qquad p_\infty = 101325\left[Pa\right] \\
&a_\infty = \sqrt{\gamma\frac{p_\infty}{\rho_\infty}}, \\
&\gamma = 1.4, \quad \omega = 6\pi, \quad \varepsilon = 10^{-5}
\end{aligned} \tag{5.7}$$

where ε is the magnitude of initial perturbation, and ω is the wavenumber of perturbations in velocity. The wavenumber of density perturbation is 2ω, and the perturbation in pressure is determined by isentropic relation. The acoustic wave described above is approximately linear because ε is small. Therefore, an analytical solution for comparison can be derived from acoustic wave equation in the following form,

$$\begin{aligned}
\rho(x,t) &= \rho_\infty + \frac{\varepsilon\rho_\infty}{2}[\cos(2\omega(x-a_\infty t)) + \cos(\omega(x-a_\infty t)) + \cos(2\omega(x+a_\infty t)) - \cos(\omega(x+a_\infty t))] \\
u(x,t) &= \frac{\varepsilon a_\infty}{2}[\cos(2\omega(x-a_\infty t)) + \cos(\omega(x-a_\infty t)) - \cos(2\omega(x+a_\infty t)) + \cos(\omega(x+a_\infty t))] \\
p(x,t) &= p_\infty + \frac{\gamma\varepsilon p_\infty}{2}[\cos(2\omega(x-a_\infty t)) + \cos(\omega(x-a_\infty t)) + \cos(2\omega(x+a_\infty t)) - \cos(\omega(x+a_\infty t))]
\end{aligned} \tag{5.8}$$

The computational domain is in an interval of $0 < x < 1/3$, which includes one period in the wavelength of initial velocity perturbation. A uniform mesh with N grid panels is used, and

periodic boundary conditions on both sides are applied. The third-order 1-1-1-1 MLC scheme (α = 1.5) and the seventh-order 2-2-2-2 MLC scheme (α = 12) are used for spatial discretization. Meanwhile, a fourth-order Runge-Kutta method is applied to time integration, and the CFL number is a small value of 0.1 to reduce temporal errors.

In the first place, the solution of ρ after computing for one period (t = 0.01s) is used to estimate the rate of convergence of the MLC schemes. The analytical solution in Eq. (5.8) is not suitable for this estimation, because it is derived from the acoustic wave equations which have embedded error from linearization. As a result, three sets of numerical results with grid refinement are used to estimate the rate of convergence. Table 5.20 shows the errors and rates of convergence of both the third-order 1-1-1-1 scheme and the seventh-order 2-2-2-2 scheme. Grid refinement results show that both schemes can achieve the expected order, which is 3 and 7 for the 1-1-1-1 and 2-2-2-2 schemes respectively. The exception appears only when the grid is too coarse, or error is already very small. Specifically, the 1-1-1-1 scheme with upwinding surpasses the expected order when $N > 80$.

Table 5.20. Errors and rates of convergence based on ρ of the 1-1-1-1 MLC scheme (3rd order) and the 2-2-2-2 MLC scheme (7th order) for the acoustic wave.

N	1-1-1-1 MLC scheme, α = 1.5				2-2-2-2 MLC scheme, α = 12			
	L_1 error	Order	L_∞ error	Order	L_1 error	Order	L_∞ error	Order
5	0.00E+00	\	0.00E+00	\	0.00E+00	\	0.00E+00	\
10	3.47E-07	\	6.24E-07	\	4.20E-06	\	5.95E-06	\
20	4.14E-06	-3.58	6.10E-06	-3.29	4.11E-08	6.68	6.35E-08	6.55
40	6.38E-07	2.70	9.81E-07	2.64	3.11E-10	7.04	4.93E-10	7.01
80	4.52E-08	3.82	7.18E-08	3.77	3.25E-12	6.58	5.14E-12	6.58
160	2.80E-09	4.01	4.47E-09	4.00	4.76E-13	2.77	6.49E-13	2.99

To evaluate the accuracy of the MLC schemes on capturing long-time solution of the unsteady acoustic wave, the simulation is carried out to 100 times of period (t = 1.0s). Fig. 5.9 shows the density distributions at three different simulation time when N = 20. It shows that a good agreement between the numerical and analytical solution is maintained in the long-time simulation. There is no visible deviation in both phase and amplitude of the acoustic wave for three different simulation time. The small discrepancy mainly appears near the peaks. In fact, the same level of deviation is also observed when N is increased to 40 and 80, which implies that the difference is caused by the embedded error from the linearization of the analytical solution. The same analysis is conducted with the 1-1-1-1 scheme, and similar behavior is observed which is not presented here.

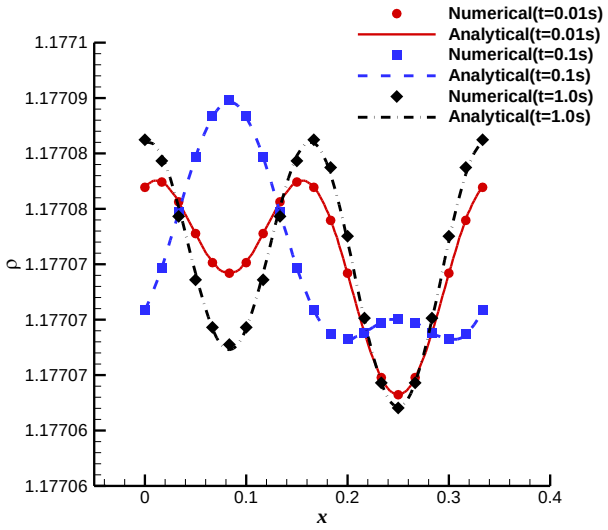

Fig. 5.9. Density distribution at different simulation time for the 2-2-2-2 MLC scheme (7th order) with N = 20.

The test case of the one-dimensional acoustic wave indicates that the current very high-order MLC schemes can maintain very small dispersive and dissipative errors at the same time. The long-time simulation results are stable and accurate which indicates the MLC schemes can be applied to computational aeroacoustics problems.

5.2.4 Two-Dimensional Isentropic Vortex

To show the performance of the current MLC schemes in vortical flow simulations, a two-dimensional inviscid isentropic vortex in (x, y) plane is simulated. The similar test case is used by Mundis and Edoh [116,117]. The vortex is superimposed to a uniform steady mean flow in the x-direction. The mean flow conditions are set as follows,

$$\begin{aligned} &p_\infty = 101325\left[Pa\right],\ \ T_\infty = 300\left[K\right],\ \ \rho_\infty = \frac{p_\infty}{RT_\infty} \\ &a_\infty = \sqrt{\gamma RT_\infty},\qquad U_\infty = Ma_\infty \\ &\gamma = 1.4,\qquad\qquad R = 286.94\left[J\cdot kg^{-1}\cdot K^{-1}\right] \end{aligned} \tag{5.9}$$

where U_∞ is the mean velocity. Mach number M is set to be 0 for stationary vortex, and 0.5 for convective vortex in the following simulations. The initial conditions (t = 0) involve the mean flow and a perturbation, which is an isentropic vortex defined as follows,

$$\begin{aligned} &\delta u = -\sqrt{RT_\infty}\,\frac{\varepsilon}{2\pi}\left(y-y_0\right)e^{\varphi\left(1-r^2\right)},\quad \delta v = \sqrt{RT_\infty}\,\frac{\varepsilon}{2\pi}\left(x-x_0\right)e^{\varphi\left(1-r^2\right)}, \\ &\delta T = -T_\infty\frac{\varepsilon^2\left(\gamma-1\right)}{16\varphi\gamma\pi^2}e^{2\varphi\left(1-r^2\right)},\qquad \frac{\delta p}{p_\infty}+1 = \left(\frac{\delta\rho}{\rho_\infty}+1\right)^\gamma = \left(\frac{\delta T}{T_\infty}+1\right)^{\gamma/\gamma-1} \end{aligned} \tag{5.10}$$

where (x_0, y_0) represents location of the vortex center, and $r^2 = (x-x_0)^2+(y-y_0)^2$. The constants ε and φ are used to describe the strength and width of the vortex. The perturbations in (u, v) and T are defined independently in Eq. (5.10), while p and ρ can be determined by isentropic relations. Here, ε =1 and φ =1 are used. Therefore, the amplitude of perturbation in density $|\delta\rho/\rho_\infty|$ is about

6.27% at the vortex center. The vortex edge is defined at the location where $|\delta\rho/\rho_\infty| = 0.1\%$, corresponding to $r = 1.15$m. The exact solution of this problem is a passive convection of the perturbed mean flow, and the vortex maintains its structure during the convection. It is appropriate for testing the performance of the numerical schemes in terms of vortex preservation, which is affected by the characteristic of dissipation, dispersion, and anisotropic errors.

The computational domain is a square field within the range of $0 < x < L$ and $0 < y < L$, where $L = 22.0$m. At $t = 0$, the vortex core is located at the center of the domain. A uniform mesh with N grid panels in both dimensions is used, and periodic boundary conditions are set on all boundaries. This domain is large enough to reduce the boundary effects because the initial perturbations on the computational boundaries are negligible. The MLC scheme, the DMLC scheme, the LSMLC scheme with various orders are used for special discretization. Zhong's upwind explicit schemes are also used for comparisons. Meanwhile, a fourth-order Runge-Kutta method is applied to time integration, and the CFL number is set to be a small value of 0.1 to reduce temporal errors.

Evaluation of the MLC scheme

Similar to the previous case of the one-dimensional acoustic wave, a short-time simulation ($t = 0.01$s) is first conducted to estimate the rate of convergence of the MLC schemes. Both the stationary vortex ($M = 0$) and convective vortex ($M = 0.5$) are tested. Table 5.21 and Table 5.22 show the errors and rates of convergence based on the solution of ρ, where Mach number is set to be 0 and 0.5 respectively. It should be noted that N is relatively larger compared with other test cases because of the larger domain in this case. However, the number of grid points within the vortex is very small, which are given in the brackets. The first observation from the tables is that

the MLC schemes can surpass their expected orders for both Mach numbers. Specifically, the 1-1-1-1 scheme shows an approximate rate of convergence of 4, while the 2-2-2-2 scheme has about 8th-order rate of convergence. Second, the simulation with $M = 0$ is more accurate than the case of with $M = 0.5$. These tables show that the errors are smaller and estimated orders are higher for stationary vortex ($M = 0$), especially when N is large. This observation indicates that convective vortex is more difficult to be accurately captured than the stationary vortex, which is expected.

Table 5.21. Errors and rates of convergence based on ρ of the 1-1-1-1 MLC scheme (3rd order) and the 2-2-2-2 MLC scheme (7th order) for the stationary vortex ($M = 0$).

N	1-1-1-1 MLC scheme, $\alpha = 1.5$				2-2-2-2 MLC scheme, $\alpha = 12$			
	L_1 error	Order	L_∞ error	Order	L_1 error	Order	L_∞ error	Order
20 (2)	1.74E-03	\	1.74E-03	\	1.46E-03	\	1.46E-03	\
40 (4)	1.59E-04	3.45	1.59E-04	3.45	5.45E-05	4.74	5.45E-05	4.74
80 (8)	8.33E-06	4.26	8.33E-06	4.26	2.95E-07	7.53	2.95E-07	7.53
160 (16)	3.77E-07	4.47	3.77E-07	4.47	7.55E-10	8.61	7.55E-10	8.61
320 (32)	2.17E-08	4.12	2.17E-08	4.12	2.95E-12	8.00	2.95E-12	8.00

Table 5.22. Errors and rates of convergence based on ρ of the 1-1-1-1 MLC scheme (3rd order) and the 2-2-2-2 MLC scheme (7th order) for the convective vortex ($M = 0.5$).

N	1-1-1-1 MLC scheme, $\alpha = 1.5$				2-2-2-2 MLC scheme, $\alpha = 12$			
	L_1 error	Order	L_∞ error	Order	L_1 error	Order	L_∞ error	Order
20 (2)	1.66E-03	\	1.37E-03	\	1.39E-03	\	1.35E-03	\
40 (4)	2.26E-04	2.88	1.86E-04	2.88	6.89E-05	4.34	5.91E-05	4.51
80 (8)	1.85E-05	3.61	1.36E-05	3.77	5.73E-07	6.91	5.25E-07	6.81
160 (16)	1.12E-06	4.04	9.79E-07	3.80	3.09E-09	7.53	2.37E-09	7.79

320 (32)	7.07E-08	3.99	6.18E-08	3.99	1.09E-11	8.14	8.36E-12	8.15

After the orders of the MLC schemes are validated in the short-time simulation, a long-time simulation is carried out in the next place. Specifically, the solution at t = 1.267s is evaluated when the vortex has traveled about 100 diameters or 10 domain lengths in space for the case of M = 0.5. Fig. 5.10 and Fig. 5.11 show the vorticity distribution along the centerline (y = 11m) for the stationary and convective vortexes respectively. Both figures show that the dissipative and dispersive errors decrease clearly when the grid resolution increases. Specifically, Fig. 5.10 compares the solution of the 1-1-1-1 and 2-2-2-2 scheme for the case of M = 0. When N = 80, the 1-1-1-1 scheme has a large dissipative error; on the other hand, the 2-2-2-2 scheme is very accurate, indicating the advantage from a seventh-order of accuracy. When N = 160, both the results of the 1-1-1-1 and 2-2-2-2 scheme show very good agreement with the exact solution. Fig. 5.11 compares these two schemes for the case of M = 0.5. The convective vortex shows similar behaviors as the stationary vortex; however, the 1-1-1-1 scheme also shows a phase shift of the vortex besides the reduced amplitude when N = 80. In the center of the vortex, the corresponding wavenumber is large. The Fourier analysis in Section 2.4 shows the MLC schemes have small dissipative and dispersive errors for large wavenumbers. As a result, the vorticity is underestimated in the vortex center for the two cases of M = 0 and M = 0.5, and the phase speed is changed during the convection in the latter case. It should be mentioned that in the meshes with N = 80 and 160, only about 8 and 16 grid points are used to resolve the vortex structure. Therefore, the results in Fig. 5.10 also validate the spectral-like resolution of the MLC schemes.

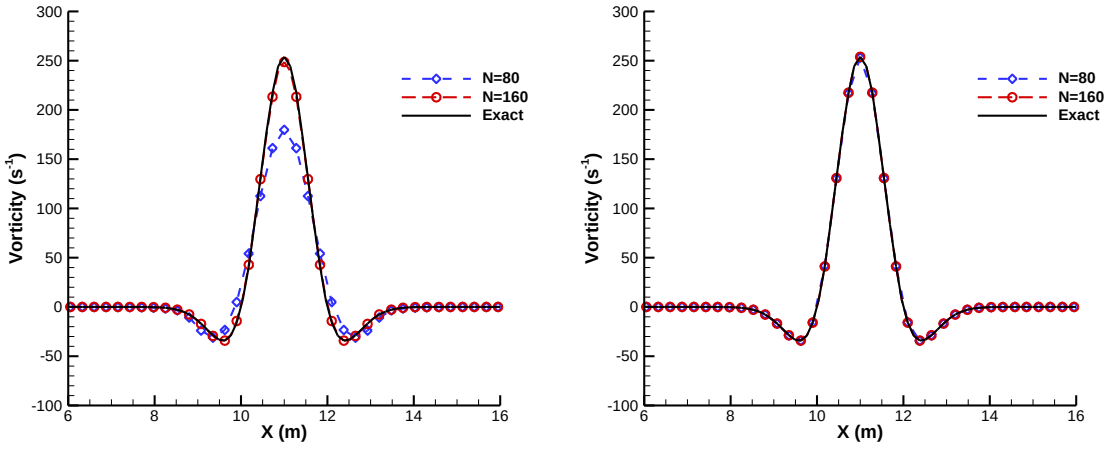

a), 1-1-1-1 MLC scheme (3rd order) b), 2-2-2-2 MLC scheme (7th order)

Fig. 5.10. Vorticity distribution on the centerline in the *x*-direction for the stationary vortex (*M* = 0) at *t* = 1.267s.

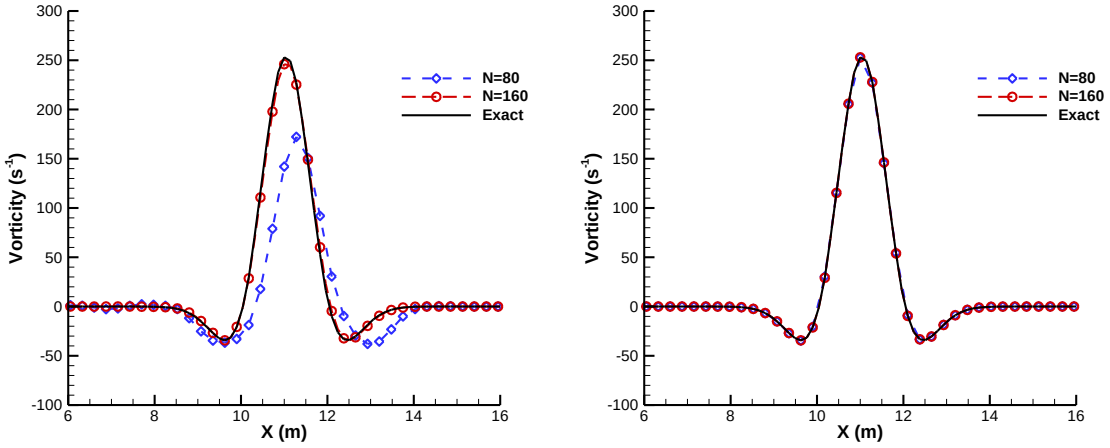

a), 1-1-1-1 MLC scheme (3rd order) b), 2-2-2-2 MLC scheme (7th order)

Fig. 5.11. Vorticity distribution on the centerline in the *x*-direction for the convective vortex (*M* = 0.5) at *t* = 1.267s.

To investigate the anisotropic errors, Fig. 5.12 and Fig. 5.13 show the density contours for the two cases of M = 0 and M = 0.5 at t = 1.267s. The results of the 1-1-1-1 scheme when N = 160 are compared with the results of the 2-2-2-2 scheme when N = 80, both of which are accurate according to Fig. 5.10. The isentropic vortex is isotropic which means the structure should be identical in any arbitrary orientation. Therefore, all density contours should be concentric circles in the exact solution. These figures show that both the 1-1-1-1 and 2-2-2-2 scheme generate isotropic density distribution after the long-time simulation, in both stationary and convective vortex cases. In particular, the seventh-order 2-2-2-2 scheme can maintain the isotropy with only 8 gird points distributed in the vortex region (N = 80).

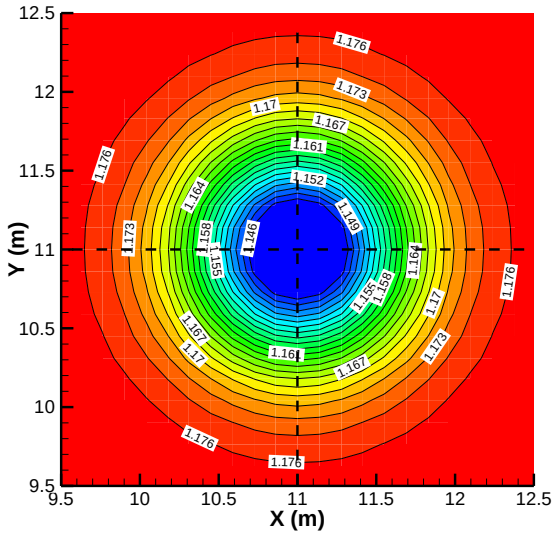

a), 1-1-1-1 MLC scheme (N = 160)

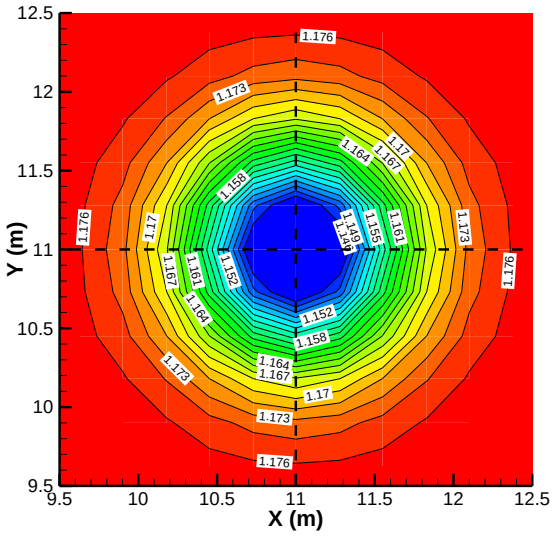

b), 2-2-2-2 MLC scheme (N = 80)

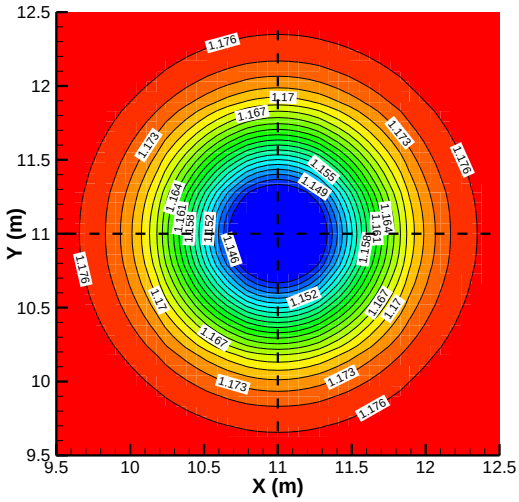

c), exact solution

Fig. 5.12. Density contours in the case of stationary vortex (M = 0) at t = 1.267s.

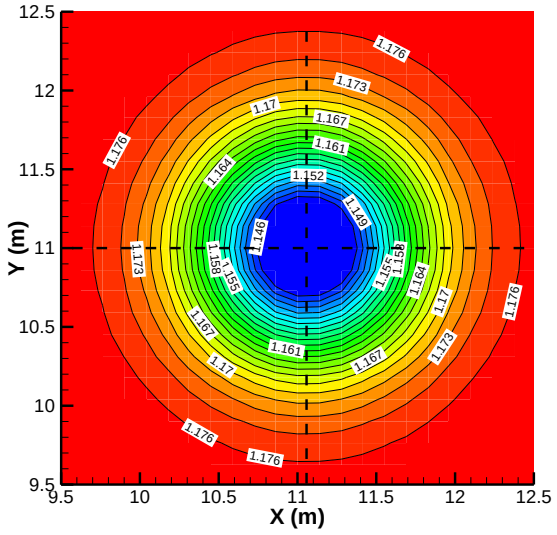

a), 1-1-1-1 MLC scheme (N = 160)

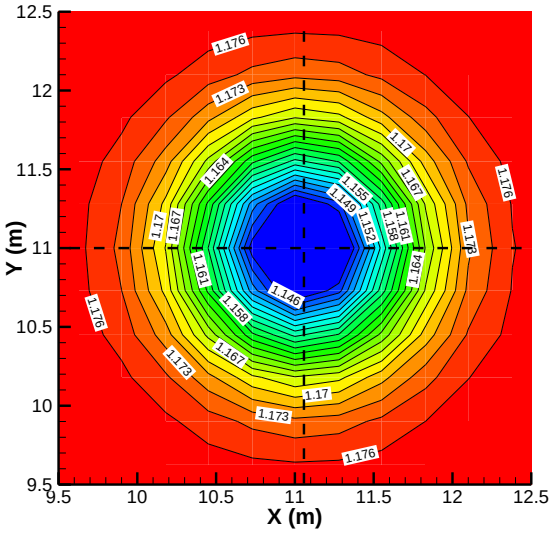

b), 2-2-2-2 MLC scheme (N = 80)

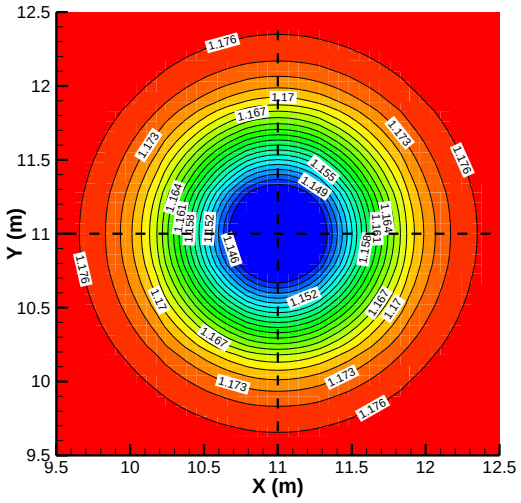

c), exact solution

Fig. 5.13. Density contours in the case of convective vortex (M = 0.5) at t = 1.267s.

Fig. 5.14 shows the density distributions in the case of M = 0.5 along two straight lines passing through the vortex core, at an angle $\theta = 0$ and $\pi/4$ with respect to the x-axis. The results of the 1-1-1-1 and 2-2-2-2 schemes are compared in the same mesh of N = 160. The figure shows that the density distributions along the two lines of $\theta = 0$ and $\theta = \pi/4$ agree very well, except that the latter shows slightly larger error at the peak. These results demonstrate that the MLC schemes have very small anisotropic errors, which is consistent with the isotropic density contours in Fig. 5.13. In the approximation of cross derivatives, our MLC schemes take information from neighboring points in different orientations, instead of doing approximation in a single x- or y-direction as many conventional finite difference methods. Hence, it has the advantage to overcome the anisotropic error.

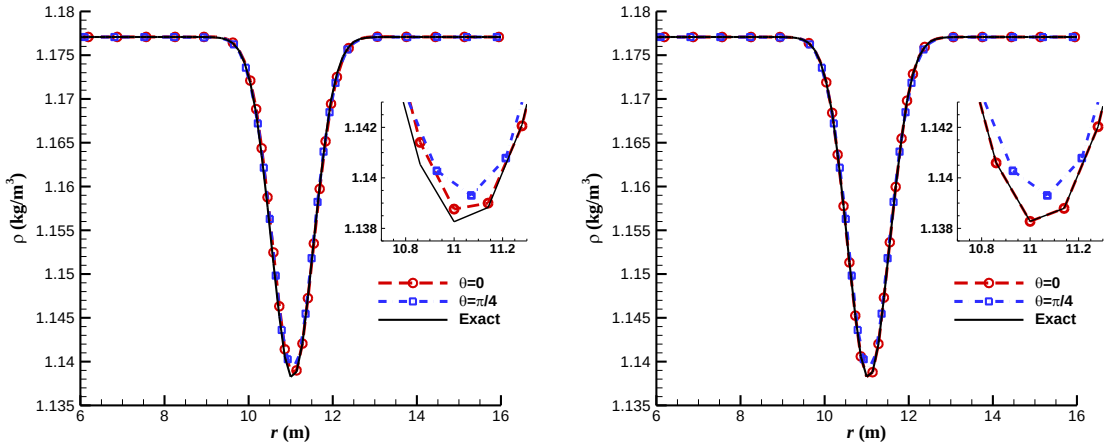

a), 1-1-1-1 MLC scheme (N = 160) b), 2-2-2-2 MLC scheme (N = 160)

Fig. 5.14. Density distribution along two centerlines in different orientations (θ = 0 and $\theta = \pi/4$) in the case of convective vortex (M = 0.5) at t = 1.267s.

Comparison of Different Schemes

Now, the convective vortex (M = 0.5) is focused for the comparison of different schemes including the MLC scheme, the DMLC scheme, the LSMLC scheme, and Zhong's explicit upwind scheme. A short-time simulation after the vortex has traveled approximate 10 diameters (t = 0.1267s, CFL = 0.1) is first conducted to estimate the rate of convergence of different schemes. The results based on the solution of ρ are compared in Table 5.23 to Table 5.25. It should be noted that N is relatively larger compared with other test cases because the computational domain is wider in this case. To be clear, the number of grid points within the vortex is given in the brackets. Similar with previous cases, the results demonstrate that all schemes can achieve the expected orders of accuracy. The DMLC scheme shows smaller error than the MLC scheme with the same order of accuracy; the LSMLC scheme shows slightly larger error than the MLC scheme in third and fifth-order cases. Overall, the MLC, DMLC, and

LSMLC schemes are all much more accurate than the corresponding Zhong's explicit scheme, which prove the advantage of spectral-like resolution.

Table 5.23. Errors and rates of convergence of the 1-1-1-1 DMLC scheme, the 1-1-1-1 MLC scheme, the 1-1-1-1 LSMLC scheme, and Zhong's 3rd-order explicit scheme for 2-D isentropic vortex after traveling 10*d*.

N	Zhong's 3rd-order scheme, α = 0.25		1-1-1-1 MLC scheme, α = 1.5		1-1-1-1 DMLC scheme, α = 1.5		1-1-1-1 LSMLC, β = 0.2	
	L_1 error	Order	L_1 error	Order	L_1 error	Order	L_1 error	Order
20 (2)	2.38E-03	\	2.03E-03	\	2.02E-03	\	2.02E-03	\
40 (4)	1.67E-03	0.51	1.02E-03	1.00	8.66E-04	1.22	1.07E-03	0.91
80 (8)	6.26E-04	1.41	1.41E-04	2.86	1.14E-04	2.93	1.54E-04	2.80
160 (16)	1.17E-04	2.42	8.33E-06	4.08	7.29E-06	3.96	8.98E-06	4.10
320 (32)	1.56E-05	2.90	4.45E-07	4.23	4.14E-07	4.14	4.75E-07	4.24

Table 5.24. Errors and rates of convergence of the 2-2-1-1 DMLC scheme, the 2-2-1-1 MLC scheme, the 2-2-1-1 LSMLC scheme, and Zhong's 5th-order explicit scheme for 2-D isentropic vortex after traveling 10*d*.

N	Zhong's 5th-order scheme, α = -6		2-2-1-1 MLC scheme, α = -1		2-2-1-1 DMLC scheme, α = -1		2-2-1-1 LSMLC, β = 0.2	
	L_1 error	Order	L_1 error	Order	L_1 error	Order	L_1 error	Order
20 (2)	2.28E-03	\	2.01E-03	\	1.61E-03	\	1.79E-03	\
40 (4)	1.34E-03	0.76	7.13E-04	1.49	1.18E-04	3.76	4.57E-04	1.97
80 (8)	2.81E-04	2.26	2.89E-05	4.63	6.17E-06	4.26	2.09E-05	4.45
160 (16)	2.63E-05	3.42	4.51E-07	6.00	1.75E-07	5.14	6.02E-07	5.12
320 (32)	1.34E-06	4.29	7.26E-09	5.95	3.69E-09	5.56	1.09E-08	5.79

Table 5.25. Errors and rates of convergence of the 2-2-2-2 DMLC scheme, the 2-2-2-2 MLC scheme, the 2-2-2-2 LSMLC scheme, and Zhong's 7th-order explicit scheme for 2-D isentropic vortex after traveling 10*d*.

N	Zhong's 7th-order scheme, $\alpha = 36$		2-2-2-2 MLC scheme, $\alpha = 12$		2-2-2-2 DMLC scheme, $\alpha = 12$		2-2-2-2 LSMLC, $\beta = 0.5$	
	L_1 error	Order	L_1 error	Order	L_1 error	Order	L_1 error	Order
20 (2)	2.08E-03	\	1.79E-03	\	1.32E-03	\	1.57E-03	\
40 (4)	8.86E-04	1.23	1.01E-04	4.14	1.15E-04	3.53	1.09E-04	3.85
80 (8)	7.25E-05	3.61	4.00E-06	4.66	2.50E-06	5.52	6.07E-06	4.17
160 (16)	2.98E-06	4.61	1.51E-08	8.05	1.02E-08	7.93	2.90E-08	7.71
320 (32)	2.84E-08	6.71	4.56E-11	8.37	3.05E-11	8.39	9.23E-11	8.29

A long-time simulation is carried out in the next place. Specifically, the solution at t = 1.267s (CFL = 0.2) is evaluated when the vortex has traveled approximate 100 diameters or 10 domain lengths in the x direction. To investigate the anisotropic errors, Fig. 5.15 compares the density contours from the 2-2-1-1 DMLC scheme, the 2-2-1-1 MLC scheme, the 2-2-1-1 LSMLC scheme, and Zhong's fifth-order explicit scheme. All schemes have the same order of accuracy. Comparing Fig. 5.15 a), b), c), and d) which share the same mesh, we can observe that the 2-2-1-1 DMLC scheme has obvious advantage over the other three schemes in terms of maintaining the vortex structure. It generates isotropic density distribution after the long-time simulation. As a comparison, the vortex from the 2-2-1-1 MLC and LSMLC scheme has an elliptic shape, which is the reflection of anisotropy. The vortex from Zhong's fifth-order explicit scheme with N = 80 has almost damped out after the long-time simulation, which is due to excessive dissipation. Even if the grid is refined as in Fig. 5.15 e), Zhong's fifth-order scheme still shows an anisotropic distribution in the density contours.

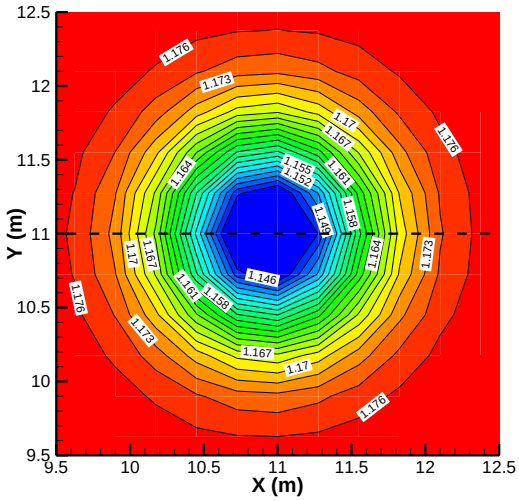

a), 2-2-1-1 DMLC scheme (N = 80)

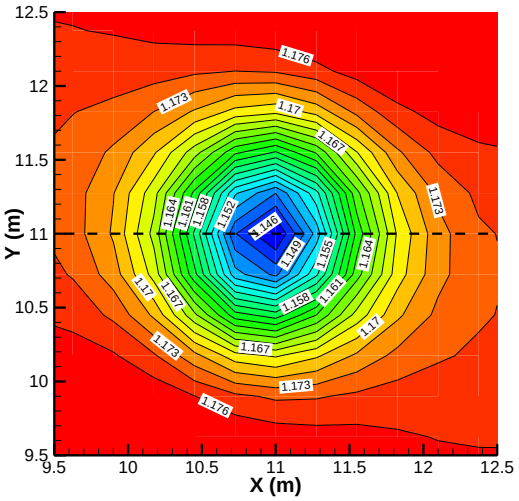

b), 2-2-1-1 MLC scheme (N = 80)

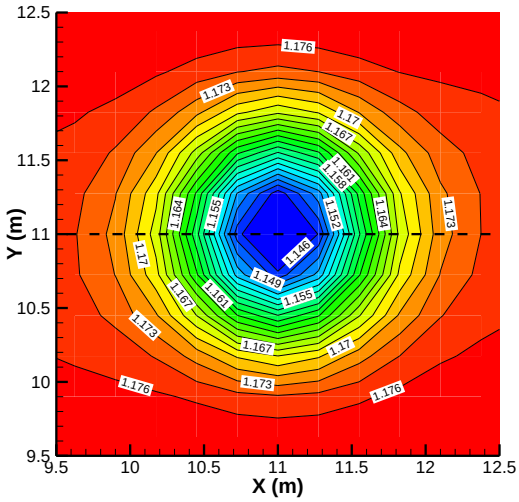

c), 2-2-1-1 LSMLC scheme (N = 80)

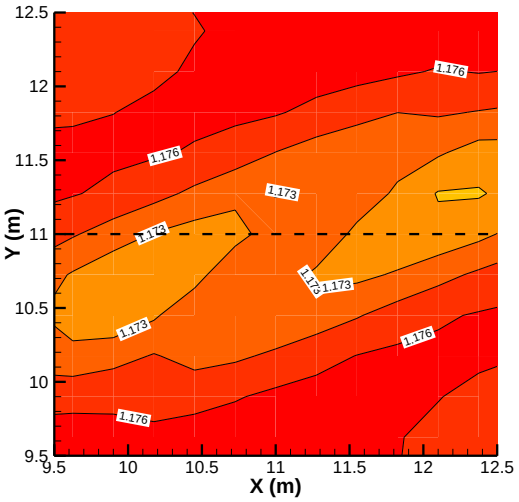

d), Zhong's 5th-order scheme (N = 80)

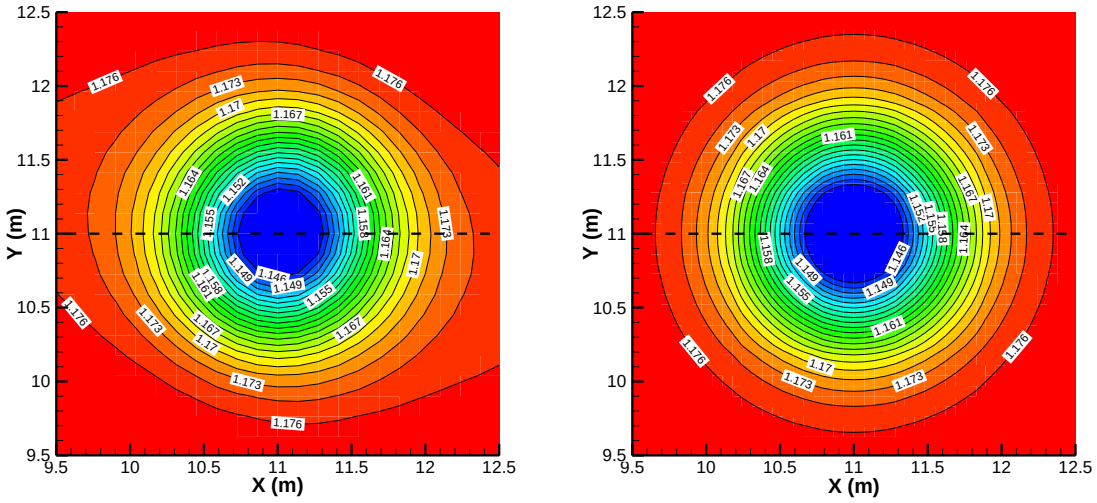

e), Zhong's 5th-order scheme (N = 160) f), exact solution

Fig. 5.15. Comparison of density contours from different schemes for 2-D isentropic vortex after traveling 100d.

Fig. 5.16 presents the vorticity distribution along the centerline (y = 11m) of the vortex, which is the black dashed line in Fig. 5.15. The fifth-order schemes are used for comparison and different mesh size (N = 40, 80, 160) are analyzed. The figures show clearly that the dissipative error which is indicated by the peak decreases when the grid resolution increases. The dispersive error is much smaller compared with the dissipation and it decreases fast when we refine the mesh. Same as the anisotropic error, Fig. 5.16 shows that the 2-2-1-1 DMLC scheme has much smaller dissipation than the 2-2-1-1 MLC or LSMLC scheme when N is 40, which is the result of the improved spectral resolution. When N is 80, the DMLC scheme becomes indistinguishable with the exact solution; the MLC scheme is more accurate than the LSMLC scheme. When N is increased to 160, the 2-2-1-1 DMLC, MLC, and LSMLC schemes are all very accurate; however, Zhong's fifth-order explicit scheme still shows observable dissipation.

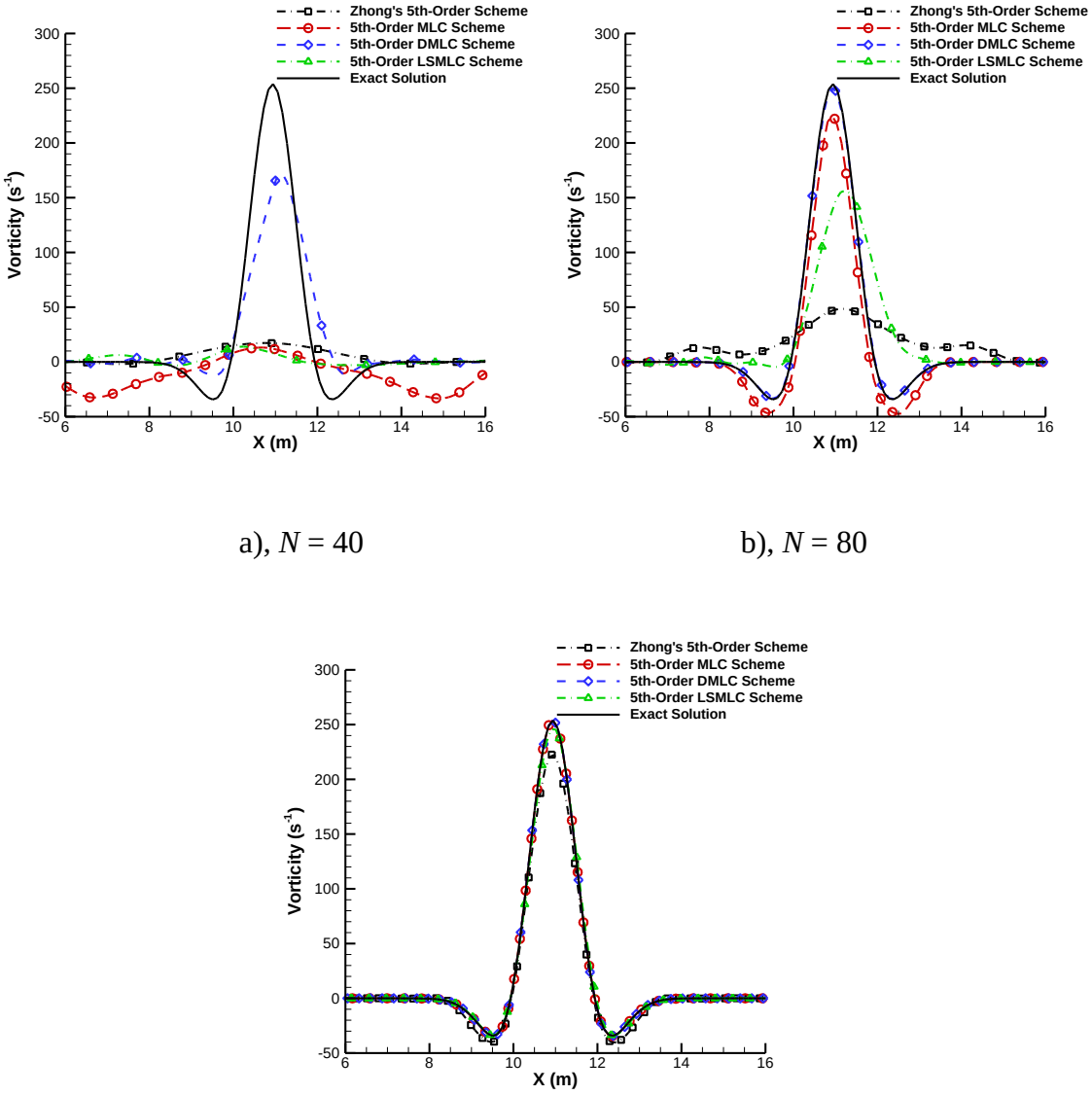

a), N = 40

b), N = 80

c), N = 160

Fig. 5.16. Comparison of vorticity distribution on the centerline in the x-direction for 2-D isentropic vortex after traveling 100d (5th-order schemes).

Same comparison for third-order schemes or seven-order schemes are presented in Fig. 5.17 and Fig. 5.18. Similar conclusions as for fifth-order schemes can be obtained for third or

seventh-order schemes, which are not repeated here. However, the seventh-order schemes do not generate obvious dispersive error even on very coarse mesh (N = 40).

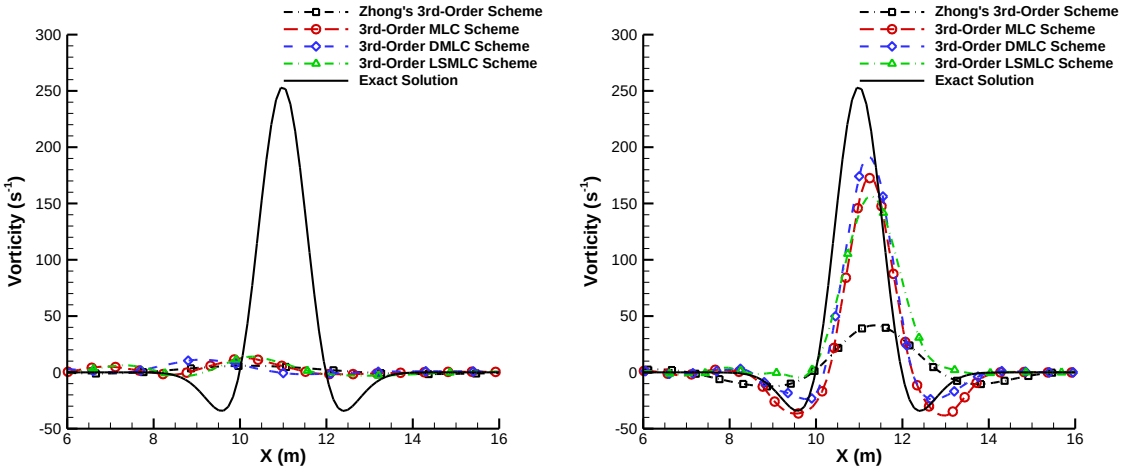

a), N = 40 b), N = 80

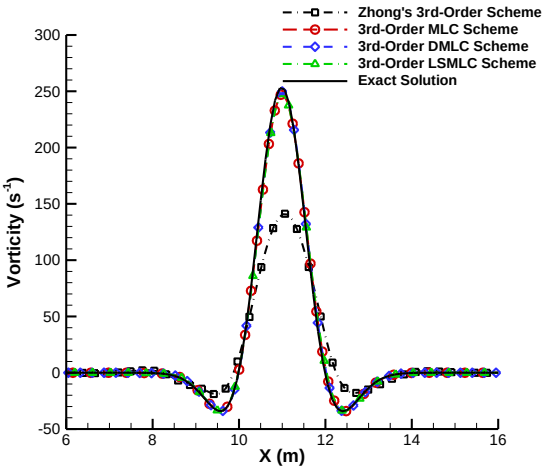

c), N = 160

Fig. 5.17. Comparison of vorticity distribution on the centerline in the x-direction for 2-D isentropic vortex after traveling 100d (3rd-order schemes).

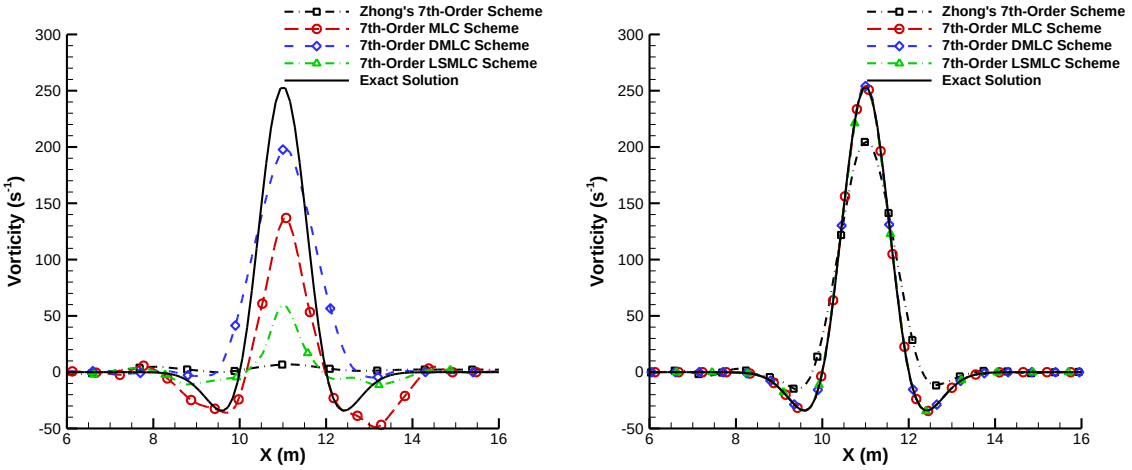

a), $N = 40$ b), $N = 80$

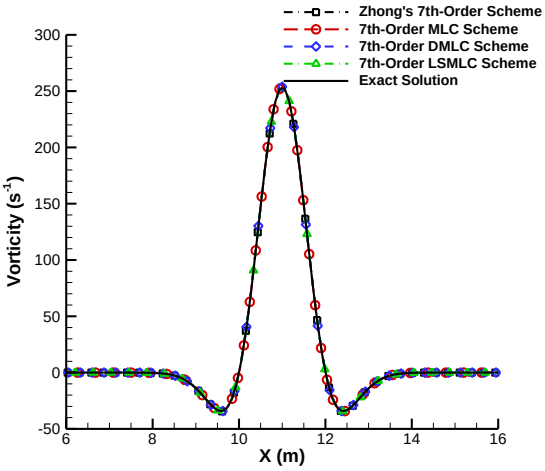

c), $N = 160$

Fig. 5.18. Comparison of vorticity distribution on the centerline in the *x*-direction for 2-D isentropic vortex after traveling 100*d* (7th-order schemes).

In previous test cases of the linear advection and the entropy wave, the deterioration or divergence of the result is observed for the MLC scheme in long-time simulations. Although the case of the isentropic vortex is quite stable compared with other cases, it turns out the MLC

scheme can also diverge in very high-order cases if the simulation is kept running. Table 5.26 shows the numerical results at t = 6.337s (CFL = 0.2), when the vortex has traveled approximate 500 diameters or 50 domain lengths in the x direction. The 2-2-2-2 MLC, DMLC, and LSMLC schemes with seventh-order of accuracy are compared. It demonstrates that on the same mesh configuration, the 2-2-2-2 DMLC scheme has the smallest error. Moreover, the 2-2-2-2 MLC scheme shows deteriorated results when N is increased to 160, which means the refined mesh generates less accurate results. When N is increased to 320, the result with the 2-2-2-2 MLC scheme diverges. This is due to the weak numerical instability of the MLC scheme. On the other hand, the DMLC and LSMLC schemes are always stable and the error decreases during the refinement of the mesh. They both overcome the instability by avoiding the cross derivative approximation or using the weighted least square approximation.

Table 5.26. Errors and rates of convergence of the 2-2-2-2 MLC, the 2-2-2-2 DMLC, and the 2-2-2-2 LSMLC schemes (7th order) after the vortex traveling for 500 diameters.

N	2-2-2-2 MLC scheme, α = 12		2-2-2-2 DMLC scheme, α = 12		2-2-2-2 LSMLC scheme, β = 0.5	
	L_1 error	L_∞ error	L_1 error	L_∞ error	L_1 error	L_∞ error
20 (2)	2.63E-03	2.50E-03	2.42E-03	2.40E-03	2.38E-03	2.39E-03
40 (4)	2.80E-03	2.22E-03	2.40E-03	2.21E-03	2.18E-03	2.35E-03
80 (8)	4.09E-04	4.20E-04	2.17E-04	2.21E-04	6.00E-04	5.20E-04
160 (16)	1.34E-03	1.48E-03	6.65E-05	6.64E-05	8.60E-05	8.64E-05
320 (32)	∞	∞	1.18E-05	1.20E-05	4.90E-05	4.98E-05

Fig. 5.19 presents the density contours for the 2-2-2-2 MLC, DMLC, and LSMLC schemes. It shows clearly that 2-2-2-2 MLC scheme (a, b) generates deteriorated results during the mesh refinement; while for the DMLC scheme (c, d) and the LSMLC scheme (e, f), the anisotropic error is reduced when N is increased from 80 to 160.

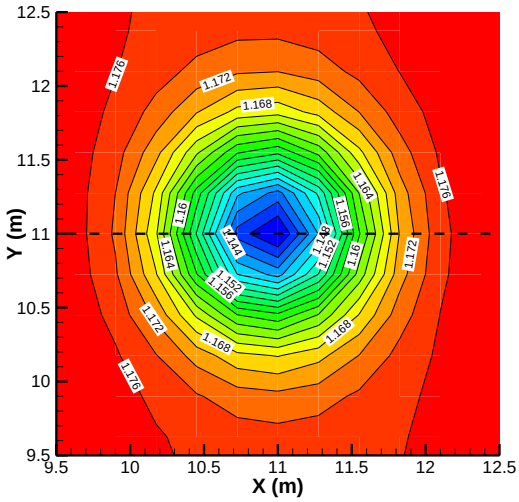

a), 2-2-2-2 MLC scheme (N = 80)

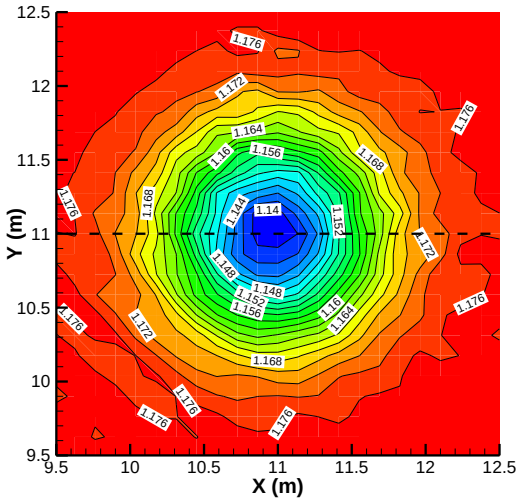

b), 2-2-2-2 MLC scheme (N = 160)

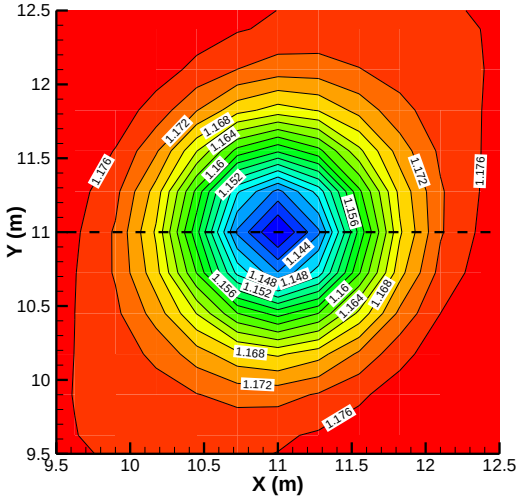

c), 2-2-2-2 DMLC scheme (N = 80)

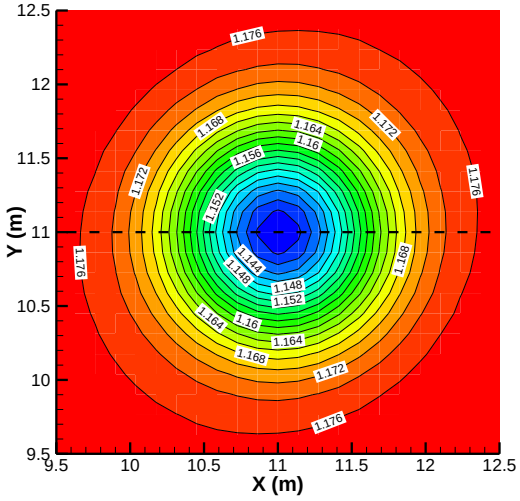

d), 2-2-2-2 DMLC scheme (N = 160)

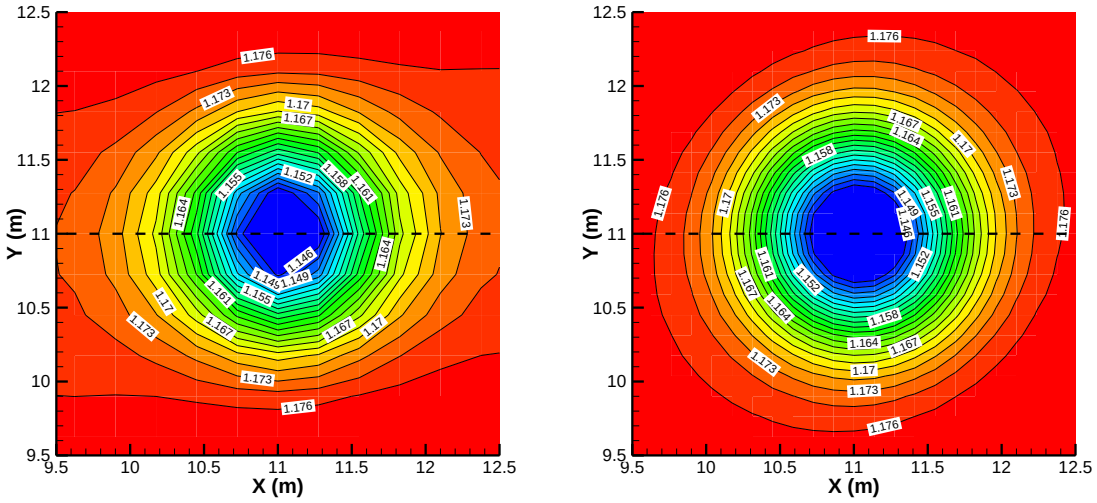

e), 2-2-2-2 LSMLC scheme (N = 80)

f), 2-2-2-2 LSMLC scheme (N = 160)

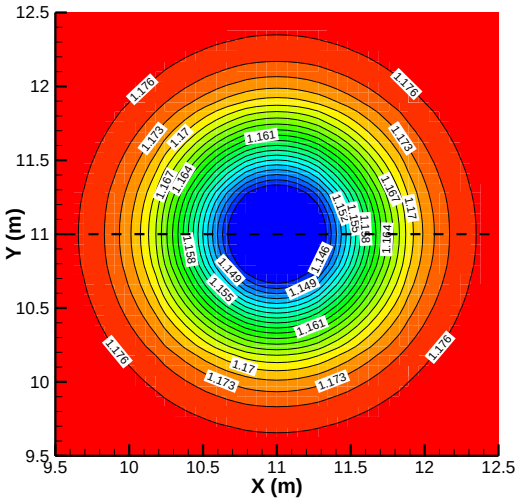

f), exact solution

Fig. 5.19. Comparison of density contours for 2-D isentropic vortex after traveling 500d (7th-order schemes).

In Section 5.2, the MLC scheme, the DMLC scheme, and the LSMLC scheme are evaluated for solving the two-dimensional Euler equations in multiple cases involving entropy, acoustic, or vorticity perturbations. In one-dimensional cases, these 3 schemes are equivalent; in two-dimensional cases, they have different performance. First, all the test cases indicate the expected order of accuracy can be achieved. Second, all three schemes developed in this dissertation generate satisfying results on coarse meshes with very few grid points, which validate the spectral-like resolution. Particularly, the result of the acoustic wave shows the high fidelity of small perturbations benefiting from the small dissipative and dispersive error of the MLC scheme; the result of the two-dimensional isentropic vortex indicates small anisotropy of these new schemes.

In two-dimensional cases, the DMLC scheme has smaller errors in both the entropy wave and isentropic vortex simulations due to the additional degree of freedom u_{xy}; the spectral-like resolution of the DMLC scheme is further improved compared with the MLC scheme; and the advantage is more significant for very high-order schemes. The LSMLC scheme has slightly larger error than the MLC scheme, and the difference is more obvious in very high-order cases. The LSMLC scheme is still much more accurate than conventional finite difference methods like Zhong's upwind explicit scheme. The analysis on long-time simulation results proves that the computational efficiency of the DMLC scheme, especially in the very high-order cases, is improved for the nonlinear Euler equations. This advantage is significant for practical flow problems. The long-time simulation also verifies that the DMLC scheme and the LSMLC scheme is always stable in both the entropy wave and isentropic vortex cases, while the MLC scheme could be unstable when the simulation is kept running. Specifically, the deterioration of the solution is observed in the 2-2-1-1 MLC scheme in the entropy wave; and the 2-2-2-2 MLC

scheme diverges in both the entropy wave and isentropic vortex simulations. The isentropic vortex also shows that the DMLC scheme has advantage over the MLC scheme or the LSMLC scheme in terms of maintaining the vortex structure, which benefits from the smaller anisotropic error and dissipation.

5.3. Navier-Stokes Equations for Compressible Flows

In the following part of this section, the two-dimensional Navier-Stokes equations in the Cartesian coordinates are solved by the MLC schemes. The results of a steady supersonic Couette flow are presented as an example. The supersonic Couette flow can be considered as a simplified model of the hypersonic boundary layer. The steady-state solutions are one-dimensional functions of wall-normal distance y, while the unsteady Couette flows are two-dimensional transient flows if disturbances exist. More details about can be found in [118].

In the two-dimensional Couette flow, the bottom wall is stationary, and the top wall is moving at a constant velocity U_∞. The flow conditions are given as follows,

$$\begin{aligned} &M_\infty = 2, \quad \mathrm{Re}_\infty = 100, \quad T_\infty = 300[\mathrm{K}] \\ &U_\infty = M_\infty \sqrt{\gamma R T_\infty}, \; p = 101325[Pa], \quad T_w = T_r \end{aligned} \tag{5.11}$$

where γ is 1.4 and the gas constant R is 286.94 $[m^2 \cdot s^{-2} \cdot K^{-1}]$. A small Reynolds number (Re_∞) is used to maintain a laminar and stable flow in the channel. The isothermal conditions are used on the boundaries. The top wall has temperature T_∞, and the bottom wall temperature T_w is set to be equivalent with the recovery temperature T_r which is calculated by,

$$T_r = T_\infty \left[1 + \frac{(\gamma - 1)}{2} \mathrm{Pr} M_\infty^2 \right] \tag{5.12}$$

with the Prandtl number (Pr) is 0.72. As a result, the bottom wall can also be considered as adiabatic. The viscosity coefficient μ is calculated by Sutherland's law in Eq. (2.56), where the constants are set as follows,

$$\mu_0 = 1.7894\times10^{-5}\left[\frac{kg}{m\cdot s}\right],\quad T_0 = 288[K],\quad T_s = 110.3333[K] \tag{5.13}$$

The exact solution of steady Couette flow can be attained by shooting methods, the details of the solution procedure can be found in [118]. The resulting solution is given in the following implicit form,

$$\begin{aligned} &U_\infty \int_0^{u^*} \mu_0 \left(\frac{T_\infty}{T_0}\right)^{1.5} \left(\frac{T}{T_\infty}\right)^{1.5} \left(\frac{T_0+T_s}{T+T_s}\right) du^* = \tau_w y \\ &T\left(u^*\right) = T_\infty \left[1+\left(\frac{T_w-T_r}{T_\infty}\right)\left(1-u^*\right)+\frac{(\gamma-1)}{2}\Pr M_\infty^2\left(1-\left(u^*\right)^2\right)\right] \end{aligned} \tag{5.14}$$

where $u^* = u/U_\infty$ is the non-dimensional velocity, and y is the distance from the bottom wall. The subscript ∞ and w represent the top and bottom wall respectively. The solution of T is a function of u^* only. The wall shear stress τ_w in the solution can be calculated from,

$$\tau_w = \frac{U_\infty}{H}\int_0^1 \mu_0 \left(\frac{T_\infty}{T_0}\right)^{1.5} \left(\frac{T}{T_\infty}\right)^{1.5} \left(\frac{T_0+T_s}{T+T_s}\right) du^* \tag{5.15}$$

where H is the height of the channel and can be calculated from Re_∞.

The computational domain is a rectangular field in $0 < x < L$ and $0 < y < H$. The length L in the x-direction is arbitrary for steady simulations because the flow is fully developed. A uniform mesh with 6 grid panels in x dimension and N grid panels in y dimension is used. Periodic boundary conditions are used on inflow and outflow boundaries; non-slip and isothermal wall conditions are applied to the bottom and top walls. The third-order 1-1-1-1 scheme with $\alpha = 1.5$ and the seventh-order 2-2-2-2 scheme with $\alpha = 12$ are applied to the two-dimensional steady

Couette flow simulations. Zhong's fifth-order explicit scheme with α = -6 [21] is also applied for comparison. A third-order Runge-Kutta method is used for time integration.

With the existence of solid walls in the Couette flow, the stencils of inner schemes could go beyond the computational domain in the region near the wall. As a result, the boundary closure schemes are also needed. It should be noted that the Navier-Stokes equations are not solved on the walls, instead, the physical boundary conditions are applied. In general, the higher-order inner schemes lead to more complicated boundary closure schemes than the lower-order schemes. For this test case, the third-order 1-1-1-1 scheme uses a three-point stencil and needs no boundary closure schemes; the seventh-order 2-2-2-2 scheme uses a seven-point stencil and needs the boundary closure scheme at the wall adjacent points. The details of boundary closure schemes coupled with the 2-2-2-2 scheme are described as follows.

The one-dimensional boundary closure schemes have been discussed in Section 2.5, and they are applied to the second derivatives terms u_{xx} and u_{yy}, where u can represent any flow quantities such as F_j, F_{vj}, u_k, and T. Specifically, the sixth-order boundary closure schemes in case 3 as described in Table 2.3 are selected for the Couette flow simulation with the seventh-order 2-2-2-2 scheme. All the formulas of boundary closure schemes are given in the Appendix A.1. For the cross derivatives terms u_{xy}, the two-dimensional boundary closure schemes are needed. Same as the inner schemes, there are many freedoms in the cross-derivative approximations. As a result, the formula of the two-dimensional boundary closure scheme on a specific stencil is not unique. However, the choice of two-dimensional boundary closure schemes become more complicated than inner schemes, because bias stencils may need to be considered. Here, only a specific sixth-order boundary closure scheme for u_{xy} is presented as an example.

The stencil and numbering of the index are shown in Fig. 5.20, where the bold line represents the wall, and the formula of this scheme is,

$$\begin{aligned}\left(u_{xy}\right)_{(i,j)=8} &= \frac{1}{h^2}\left(\frac{1}{24}u_1-\frac{1}{3}u_2+\frac{1}{3}u_4-\frac{1}{24}u_5-\frac{1}{24}u_{11}+\frac{1}{3}u_{12}-\frac{1}{3}u_{14}+\frac{1}{24}u_{15}\right)\\ &+\frac{1}{h}\left(-\frac{1}{2}\left(u_x\right)_3+\frac{1}{2}\left(u_x\right)_{13}\right)+\frac{1}{h}\left(\frac{1}{12}\left(u_y\right)_6-\frac{2}{3}\left(u_y\right)_7+\frac{2}{3}\left(u_y\right)_9-\frac{1}{12}\left(u_y\right)_{10}\right)\\ &+o\left(h^6\right)\end{aligned} \tag{5.16}$$

It shows that the stencil size is reduced to 3 points in the vertical direction, and it is still the same as the 2-2-2-2 inner scheme in the horizontal direction, which uses 5 points. Therefore, it is still symmetric about the base point 8 in the horizontal direction. It turns out this specific choice above is stable and can maintain the seventh-order accuracy of the 2-2-2-2 schemes in the Couelle flow simulations. More choices of boundary closure schemes for two-dimensional flows are given in the Appendix B.

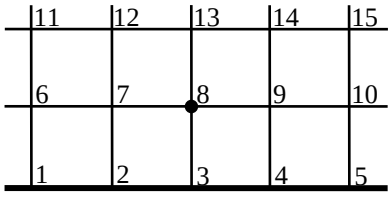

Fig. 5.20. Stencil for the boundary closure scheme (6th order) for cross derivatives.

Fig. 5.21 shows the non-dimensional temperature T^* and velocity u^* distribution generated by the 2-2-2-2 MLC scheme on a coarse mesh with 7 grid points (N = 6). A very good agreement without obvious deviation between the numerical and exact solution is achieved, indicating that the spectral-like resolution of the MLC schemes is maintained in the Navier-Stokes simulations. As we can show later, it is difficult to achieve a satisfying resolution on such a coarse mesh using conventional finite difference methods like Zhong's explicit schemes.

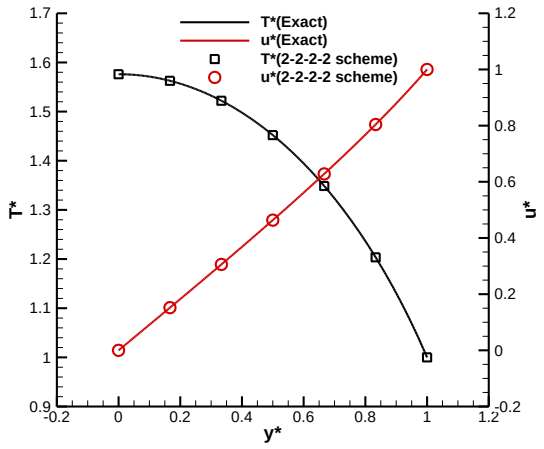

Fig. 5.21. Non-dimensional temperature and velocity distribution in the steady Couette flow simulation with the seventh-order 2-2-2-2 MLC scheme (N = 6).

To illustrate the high spectral resolution and accuracy of the MLC schemes further, the numerical errors based on T^* of Zhong's fifth-order explicit scheme, the third-order 1-1-1-1 scheme, and the seventh-order 2-2-2-2 scheme are given in Table 5.27 to Table 5.29 respectively. The first observation from these tables is that all three schemes can reach the expected orders of accuracy for Navier-Stokes calculation, which is 7 for the 2-2-2-2 scheme, 3 for the 1-1-1-1 scheme, and 5 for Zhong's explicit scheme. Next, comparing the error on the same mesh, we can observe that the 2-2-2-2 scheme shows the smallest errors for all different N values which are consistent with its seventh-order accuracy. On the other hand, a remarkable fact from Table 5.28 and Table 5.29 is that the third-order 1-1-1-1 scheme shows smaller error than Zhong's fifth-order explicit scheme when N = 8, and their errors are about the same for N = 16. Only when N = 32 and 64 cases, Zhong's explicit scheme is more accurate than the 1-1-1-1 scheme. This observation can be regarded as a further evidence of the spectral-like resolution, where the lower order MLC scheme shows better accuracy than higher order conventional finite difference

methods on coarse meshes, benefited from the additional degrees of freedom on each grid point in the MLC schemes. When the grid resolution is not fine enough, the non-dimensional wavenumber becomes large. Therefore, the accuracy of numerical results mainly depends on the resolving ability in large k region. As analyzed in Section 2.4, our MLC schemes can have very good accuracy even when k is larger than π, which is the limiting resolution of conventional finite difference methods. As a result, they have much better resolution on coarse meshes, and should significantly reduce the requirement of grid numbers for most Navier-Stokes simulations.

Table 5.27. Errors and rates of convergence based on T^* of the seventh-order 2-2-2-2 MLC scheme for steady supersonic Couette flow.

N	2-2-2-2 MLC scheme, α = 12					
	L1 error	Order	L2 error	Order	L∞ error	Order
8	1.06E-06		1.25E-06		1.97E-06	
16	1.79E-08	5.88	2.22E-08	5.81	4.13E-08	5.57
32	1.12E-10	7.32	1.37E-10	7.35	3.52E-10	6.88
64	7.29E-13	7.27	8.99E-13	7.25	1.55E-12	7.82

Table 5.28. Errors and rates of convergence based on T^* of the third-order 1-1-1-1 MLC scheme for steady supersonic Couette flow.

N	1-1-1-1 MLC scheme, α = 1.5					
	L1 error	Order	L2 error	Order	L∞ error	Order
8	7.77E-05		8.81E-05		1.28E-04	
16	7.82E-06	3.31	9.09E-06	3.28	1.42E-05	3.17
32	5.88E-07	3.73	7.07E-07	3.68	1.18E-06	3.59
64	4.05E-08	3.86	5.02E-08	3.81	8.78E-08	3.75

Table 5.29. Errors and rates of convergence based on T^* of Zhong's fifth-order explicit scheme for steady supersonic Couette flow.

N	Zhong's explicit scheme, α = -6					
	L1 error	Order	L2 error	Order	L∞ error	Order
8	1.75E-04		2.07E-04		3.76E-04	
16	6.91E-06	4.66	8.60E-06	4.59	1.74E-05	4.43
32	2.59E-07	4.74	3.41E-07	4.66	8.60E-07	4.34
64	9.96E-09	4.70	1.38E-08	4.62	4.56E-08	4.24

5.4. Summary

Chapter 5 tests the performance of the MLC scheme, with the 1-D and 2-D linear advection equations, the 1-D and 2-D nonlinear Euler equations, and the 2-D Navier-Stokes equations. The DMLC scheme and the LSMLC scheme, which are designed to improve the performance of the MLC scheme for two-dimensional flow simulations, are applied to the 2-D linear advection equations and the 2-D Euler equations as well. The one-dimensional numerical tests indicate that the MLC schemes can achieve or surpass the expected orders of accuracy. They can generate satisfying results on coarse meshes, which validate the spectral-like resolutions. This also benefits the computational efficiency because the grid numbers can be significantly saved. In two-dimensional cases, the DMLC scheme has smaller errors than the MLC scheme with the same order of accuracy, due to the better spectral resolution. With the directional discretization, the DMLC scheme has better computational efficiency than the MLC scheme in both the linear advection equation and the Euler equations. The LSMLC scheme has slightly lower accuracy compared with the MLC scheme due to its larger dissipation, but still much better than conventional finite difference methods because it has the similar spectral-like resolution with the

MLC scheme. Moreover, both the DMLC scheme and the LSMLC scheme overcomes the weak numerical instability of the MLC scheme; while the MLC scheme may show deteriorated or diverged solution in very long-time simulations.

6. Conclusions and Future Work

6.1. Conclusions

In this dissertation, a family of new very high-order multi-layer compact finite difference methods with spectral-like resolution are derived. Three different versions of the new numerical methods are developed including: the multi-layer compact (MLC) scheme, the directional multi-layer compact (DMLC) scheme, and the least square multi-layer compact (LSMLC) scheme. In particular, the DMLC and LSMLC scheme are developed for multi-dimensional flow simulations.

The goal of the MLC scheme is to solve, with very high-order of accuracy, flows involving very complex physics but over simple geometries. In the multi-layer framework, the first derivative is introduced on every grid point, and both values and derivatives are used to construct the new MLC scheme. As a result, both the accuracy and the spectral resolution can be significantly improved. Even though the MLC scheme introduces additional equations and degrees of freedom, only the auxiliary equations are nontrivial, which contributes to good computational efficiency. The upwind MLC scheme is derived based on the idea of constructing upwind schemes on centered stencils with adjustable parameters to control the dissipation. Three typical examples are the third-order 1-1-1-1 scheme with α = 1.5, the fifth-order 2-2-1-1 scheme with α = -1, and the seventh-order 2-2-2-2 scheme with α = 12.

The goal of the DMLC scheme is to resolve some drawbacks in the MLC scheme [101] for multi-dimensional simulations. Specifically, we want to overcome the weak numerical instability triggered by the inconsistency between the 1-D and 2-D MLC formulations, avoid the ad-hoc

and inefficient cross-derivative approximation, and furtherly improve the accuracy and computational efficiency in multi-dimensional cases. In the DMLC scheme presented here, a directional discretization technique is designed to extend the 1-D upwind scheme to two-dimensional cases. By introducing the auxiliary equation for the cross derivative, the spatial discretization can be fulfilled along each dimension independently. This directional discretization technique overcomes any inconsistency from the 1-D and 2-D MLC formulations, such as the difference between the 1-D upwind scheme and the 2-D central scheme. It also avoids the ad-hoc and time-consuming approximations of cross derivatives.

Similar with the DMLC scheme, the goal of the LSMLC scheme is to overcome the weak numerical instability in the MLC schemes for multi-dimensional cases, and to avoid the ad-hoc selection of grid points in the cross-derivative approximation. In the LSMLC scheme, the weighted least square approach is used to redesign the formula of cross-derivative approximations. Specifically, all grid points in a square stencil is used for cross-derivative approximation, which avoids the ad-hoc selection of grid points in the MLC schemes. Meanwhile, the 2-D upwind scheme can be derived by introducing upwind correction into the weight function. Lagrange multiplier is introduced in the objective function of the least square problem to ensure that the moving least square (MLS) interpolant satisfies both the consistency constraint at the base point and the 1-D constraint from the MLC scheme. The 1-D and 2-D upwind scheme then can be derived from the same MLS interpolant, so that they are compatible. Because the least square approximation is performed in computational domains with uniform structured meshes, the scheme is position-independent and does not increase computational costs in simulations as most other least square methods implemented on unstructured meshes.

Different with the DMLC scheme, the LSMLC scheme follows the framework of the MLC scheme and can be implemented in the same way without deriving additional auxiliary equations.

Fourier analysis is performed to investigate the accuracy and spectral resolution of the MLC schemes, and stability analysis with matrix method is conducted to analyze the boundary closure schemes. Fourier analysis results show that the dissipative, dispersive, and anisotropic errors of the MLC schemes are much smaller than those of conventional finite difference methods (Zhong's explicit and compact schemes [21]). Due to the additional degrees of freedom, which overcomes the aliasing in conventional finite difference methods, the resolution in large wavenumber region is notably improved while maintaining the compact stencil. Comparison of the 1-1-1-1 scheme and Zhong's fifth-order explicit scheme indicates that even lower order MLC scheme with less total information (values and derivatives) within the stencil can have better resolution and smaller dissipation than higher order conventional scheme. The value of α has an impact on the stability, accuracy, and stiffness of the MLC scheme. Larger α leads to better stability, larger dissipation and it slightly increases dispersion. However, the choice of α is not unique with the following criterion satisfied, which is α should be large enough to ensure the stability of both interior scheme and boundary closure schemes, and it should not be too large to keep small dissipation and avoid stiffness. From the Fourier analysis, the seventh-order 2-2-2-2 scheme with an α value of 12 has the best accuracy and spectral resolution. The eigenvalue spectrum of stability analysis shows that the stable boundary closure schemes can be derived. The upwind coefficients play an important role in stabilizing the high-order boundary closure schemes. Like most finite difference schemes, high-order MLC schemes have more severe boundary instability problem than low-order MLC schemes. The seventh-order 2-2-2-2 scheme with $\alpha = 12$ is stable only when coupled with sixth-order boundary closure schemes on the

boundary point and boundary adjacent points. The third-order 1-1-1-1 scheme with any non-negative α is stable when coupled with both third and second-order boundary closure schemes.

The two-dimensional Fourier analysis is performed to investigate the stability, accuracy, and spectral resolution of the DMLC schemes, and the matrix method is used to analyze the stability of the boundary closure schemes. The Fourier analysis demonstrates that the DMLC scheme is always stable in the full range of wavenumbers in two-dimensional cases, while the MLC scheme shows weak numerical instabilities in a small range of wavenumbers when both the convention angle and Fourier wave angle is non-zero. The DMLC scheme also has better spectral resolution than the MLC scheme for two-dimensional cases, due to its additional degree of freedom – the cross derivative. The anisotropy analysis of the phase speed shows that the DMLC scheme has much smaller dispersive error than the MLC scheme when the flow is not aligned with the coordinate axis, which is preferable for multi-dimensional simulations. Meanwhile, the anisotropic error of the DMLC scheme is also reduced for a large portion of wavenumbers in $[0, 2\pi]$. The analysis with matrix methods indicates that stable boundary closure schemes are easier to be obtained for the DMLC scheme in two-dimensional cases. The DMLC scheme shows much better boundary stability for small α values, while the MLC scheme, specifically the seventh-order 2-2-2-2 scheme, requires very large α values which could introduce excessive dissipation.

A parametric study based on two-dimensional Fourier analysis is performed to optimize the LSMLC scheme. Stability analysis of boundary closure scheme is performed with matrix methods. These analysis show that the 1-D constraint does not affect the formulas of cross derivatives. The weight function has important effect on the dissipation and stability of the LSMLC scheme. The TGD weight function has the best property in our current LSMLC scheme,

because it can remove the numerical instability and it maintains small dissipations. The upwind factor β has the similar effect as α in the one-dimensional upwind scheme, which can be used to adjust the dissipation and stability of the LSMLC scheme in two-dimensional cases. The recommended value for β is 0.2 for the 1-1-1-1 and 2-2-1-1 LSMLC schemes, and it is 0.5 for the 2-2-2-2 LSMLC scheme. Like the DMLC scheme, the LSMLC scheme is always stable in the full range of wavenumbers. Comparing with other scheme, the LSMLC scheme has similar dispersion or spectral resolution with the MLC scheme, which is lower than the DMLC scheme. The LSMLC scheme has larger dissipation than the MLC scheme, and the LSMLC scheme is less dissipative than the DMLC scheme in the third-order case, but more dissipative in very high-order cases. For the stability of boundary closure schemes, the mix LSMLC maintains small dissipation while improving the stability. These are the main improvement in the current LSMLC scheme from the MLC scheme.

Various flow problems governed by the linear advection equation and the nonlinear Euler equations are simulated with the MLC scheme, the DMLC scheme, and the LSMLC scheme. In the one-dimensional flow simulations, all three schemes developed in the dissertation are equivalent because they use the same formulas to approximate the second derivatives. In the two-dimensional flow simulations, the DMLC scheme shows the improved accuracy and stability than the MLC scheme; the LSMLC scheme shows better stability than the MLC scheme as well, but it has slightly lower accuracy due to larger dissipation. The MLC scheme and Zhong's explicit scheme are also used for comparison. The main conclusions from numerical tests are listed below.

1. All the test cases indicate the MLC schemes can achieve or surpass the expected orders of accuracy. They can generate satisfying results on coarse meshes with very few grid

points, which validate the spectral-like resolutions. The computational efficiency is tested on the advection equation, and the results show the MLC scheme can significantly save grid numbers compared with Zhong's explicit scheme, which also leads to shorter CPU time. Particularly, the results of acoustic wave show the small dissipative and dispersive error can be attained at the same time; the results of two-dimensional isentropic vortex indicate that the MLC schemes have small anisotropy; and the steady Couette flow results show that the application of high-order MLC schemes to the Navier-Stokes equations is successful, which is a good start for simulations of transient flows with more complex physics in the future.

2. The two-dimensional simulations on the linear advection equation, and the Euler equations demonstrate that the DMLC scheme produces smaller errors compared with the MLC schemes due to the additional degree of freedom – the cross derivative. Specifically, the isentropic vortex case shows that the DMLC scheme has significant advantage in terms of maintaining the vortex structure, which benefits from the smaller anisotropy and dissipation. By avoiding the time-consuming cross-derivative approximation, the DMLC scheme also has better computational efficiency than the MLC scheme. Both the advantage on accuracy and computational efficiency of the DMLC scheme is more significant in very high-order cases, which is desirable for complex flow simulations that require high-order accurate numerical methods.

3. The two-dimensional simulations on the linear advection equation, and the Euler equations demonstrate that the LSMLC scheme produces slightly larger errors compared with the MLC scheme, which is due to its larger dissipation according to the 2-D Fourier analysis. The increase of error in the LSMLC scheme becomes less obvious with the

decrease of order schemes, which may suggest the LSMLC scheme is more appropriate in third-order or fifth-order cases. On the other hand, the LSMLC scheme is much more accurate than conventional finite difference methods because it has the similar spectral-like resolution with the MLC scheme.

4. The long-time simulation verifies that the MLC scheme could be unstable in some cases. Specifically, the deterioration of the solution is observed in the 1-1-1-1 and 2-2-2-2 MLC schemes in the linear advection with periodic boundary conditions; the 2-2-2-2 MLC scheme with recommended α value of 12 is unstable in the linear advection with non-periodic boundary conditions; the deterioration of the solution is observed in the 2-2-1-1 and 2-2-2-2 MLC schemes in the Euler equations. On the other hand, both the DMLC schemes and the LSMLC schemes with various orders of accuracy are always stable for both periodic and non-periodic boundary conditions, which is consistent with the Fourier analysis and boundary stability analysis.

In summary, all 3 versions of the new very high-order multi-layer compact finite difference methods (the MLC, DMLC, LSMLC schemes) have the properties of simple formulations, high-order accuracies, compact stencils, and spectral-like resolutions in both one and two-dimensional cases. The MLC scheme shows weak numerical instability in two-dimensional flows, which triggered the development of the DMLC scheme and LSMLC scheme for multi-dimensional flow simulations. The DMLC scheme shows comprehensive improvement from the MLC scheme in stability, accuracy, spectral resolution, and computational efficiency. The improvement becomes even more significant when the scheme order increases. However, the introduce of additional auxiliary equations make the implementation more complicated compared with the MLC scheme. The LSMLC scheme shows consistent stability and slightly

lower accuracy than the MLC scheme. The difference in accuracy is not obvious in lower-order cases. Moreover, the LSMLC schemes can be implemented in the same way as the MLC scheme. Therefore, we conclude that the DMLC scheme is always the best choice for multi-dimensional simulations though it requires additional auxiliary equations. The LSMLC scheme is also appropriate considering it is easier to be implemented and still maintains the very high-order accuracy and spectral-like resolution of the MLC scheme.

6.2. Future Work

The future work on this research falls into two categories: the implementation of the current new methods, and the further investigation on the numerical method.

The new numerical methods are initially designed for solving viscous flow problems such as hypersonic boundary-layer transition. This dissertation mainly focuses on the development of the numerical methods, which is already completed and validated. A natural next step will be applying them to investigate flow mechanisms in complex viscous flow problems. As we mentioned in the conclusion, the DMLC scheme is the best candidate for multi-dimensional simulations. However, the implementation on the Navier-Stokes equations is challenging because it requires the derivation of additional auxiliary equations, which can be derived by taking a cross derivative on the Navier-Stokes equations. In addition, the new numerical methods can be also applied to turbulent flows, or computational aeroacoustics with wide ranges of wavelengths and magnitudes. More details on implementations need to be figured out.

On the other hand, the new numerical methods still have potential for further improvement. For instance, the LSMLC scheme can be applied for the simulation on unstructured mesh. In fact,

most least square scheme is used on unstructured mesh to maximize its advantage. In this dissertation, we only utilize least square approach to redesign the cross-derivative approximation on the structured mesh. If the LSMLC scheme can be implemented on unstructured mesh, it will be much more flexible for flow problems with complex geometries. Besides, there is a possibility to apply the stability criterion in the least square objective function directly to derive a stable LSMLC scheme for multi-dimensional cases. Moreover, all three new numerical methods developed in this dissertation are restricted to smooth flows. Therefore, developing the limiters for these new numerical methods are also important. In the presence of discontinuity such as shock waves, the limiting of our current schemes is essential in compressible flow simulations.

Appendix A

A.1. Schemes for Second Derivatives on Bias Stencils

All the coefficients in Appendix A.1 are defined in accordance with Eq. (2.4).

0-1-0-1 Scheme (2nd Order)

$$\begin{aligned} a_0 &= -6, \qquad a_1 = 6, \\ b_0 &= -4, \qquad b_1 = -2. \end{aligned} \tag{A.1}$$

0-2-0-1 Scheme (3rd Order)

$$\begin{aligned} a_0 &= -\frac{17}{2}, \qquad a_1 = 8, \qquad a_2 = \frac{1}{2}, \\ b_0 &= -5, \qquad b_1 = -4. \end{aligned} \tag{A.2}$$

0-3-0-3 Scheme (6th Order)

$$\begin{aligned} a_0 &= -\frac{97}{6}, \qquad a_1 = 0, \qquad a_2 = \frac{27}{2}, \qquad a_3 = \frac{8}{3}, \\ b_0 &= -\frac{22}{3}, \qquad b_1 = -18, \quad b_2 = -9, \qquad b_3 = -\frac{2}{3}. \end{aligned} \tag{A.3}$$

0-4-0-3 Scheme (7th Order)

$$\begin{aligned} a_0 &= -\frac{145}{8}, \qquad a_1 = -8, \qquad a_2 = 18, \qquad a_3 = 8, \qquad a_4 = \frac{1}{8}, \\ b_0 &= -\frac{47}{6}, \qquad b_1 = -24, \qquad b_2 = -18, \qquad b_3 = -\frac{8}{3}. \end{aligned} \tag{A.4}$$

1-0-1-0 Scheme (2nd Order)

$$a_{-1} = 6, \qquad a_0 = -6,$$
$$b_{-1} = 2, \qquad b_0 = 4. \tag{A.5}$$

1-1-2-1 Scheme (5th Order)

$$a_{-1} = \frac{63}{22}, \qquad a_0 = -\frac{48}{11}, \qquad a_1 = \frac{3}{2},$$
$$b_{-2} = -\frac{1}{66}, \qquad b_{-1} = \frac{19}{22}, \qquad b_0 = \frac{19}{22}, \qquad b_1 = -\frac{23}{66}. \tag{A.6}$$

1-2-1-2 Scheme (6th Order)

$$a_{-1} = \frac{28}{27}, \qquad a_0 = -\frac{11}{2}, \qquad a_1 = 4, \qquad a_2 = \frac{25}{54},$$
$$b_{-1} = \frac{2}{9}, \qquad b_0 = -2, \qquad b_1 = -2, \qquad b_2 = -\frac{1}{9}. \tag{A.7}$$

1-3-1-2 Scheme (7th Order)

$$a_{-1} = \frac{59}{72}, \qquad a_0 = -\frac{115}{18}, \qquad a_1 = \frac{9}{2}, \qquad a_2 = \frac{19}{18}, \qquad a_3 = \frac{1}{72},$$
$$b_{-1} = \frac{1}{6}, \qquad b_0 = -\frac{8}{3}, \qquad b_1 = -3, \qquad b_2 = -\frac{1}{3}. \tag{A.8}$$

2-0-1-0 Scheme (3rd Order)

$$a_{-2} = \frac{1}{2}, \qquad a_{-1} = 8, \qquad a_0 = -\frac{17}{2},$$
$$b_{-1} = 4, \qquad b_0 = 5. \tag{A.9}$$

2-1-2-1 Scheme (6th Order)

$$a_{-2} = \frac{25}{54}, \qquad a_{-1} = 4, \qquad a_0 = -\frac{11}{2}, \qquad a_1 = \frac{28}{27},$$
$$b_{-2} = \frac{1}{9}, \qquad b_{-1} = 2, \qquad b_0 = 2, \qquad b_1 = -\frac{2}{9}. \tag{A.10}$$

2-1-1-1 Scheme (5th Order)

$$a_{-2} = \frac{1}{18}, \quad a_{-1} = 3, \quad a_0 = -\frac{9}{2}, \quad a_1 = \frac{13}{9},$$
$$b_{-1} = 1, \quad b_0 = 1, \quad b_1 = -\frac{1}{3}. \tag{A.11}$$

3-0-3-0 Scheme (6th Order)

$$a_{-3} = \frac{8}{3}, \quad a_{-2} = \frac{27}{2}, \quad a_{-1} = 0, \quad a_0 = -\frac{97}{6},$$
$$b_{-3} = \frac{2}{3}, \quad b_{-2} = 9, \quad b_{-1} = 18, \quad b_0 = \frac{22}{3}. \tag{A.12}$$

3-1-2-1 Scheme (7th Order)

$$a_{-3} = \frac{1}{72}, \quad a_{-2} = \frac{19}{18}, \quad a_{-1} = \frac{9}{2}, \quad a_0 = -\frac{115}{18}, \quad a_1 = \frac{59}{72},$$
$$b_{-2} = \frac{1}{3}, \quad b_{-1} = 3, \quad b_0 = \frac{8}{3}, \quad b_1 = -\frac{1}{6}. \tag{A.13}$$

4-0-3-0 Scheme (7th Order)

$$a_{-4} = \frac{1}{8}, \quad a_{-3} = 8, \quad a_{-2} = 18, \quad a_{-1} = -8, \quad a_0 = -\frac{145}{8},$$
$$b_{-3} = \frac{8}{3}, \quad b_{-2} = 18, \quad b_{-1} = 24, \quad b_0 = \frac{47}{6}. \tag{A.14}$$

A.2. Formulas for Two-Layer Extrapolations and Zero-Gradient Fittings

All the coefficients in Appendix A.2 are defined in accordance with Eqs. (2.59) - (2.61). The boundary point is numbered as $i = 0$; L_1 and M_1 are 0 which means only points on the inner side of the boundary are used for approximations.

1st Order

$$a_0 = -1, \quad a_1 = 1, \quad b_1 = 0. \tag{A.15}$$

2nd Order

$$a_0 = -2, \quad a_1 = 2, \quad b_1 = -1. \tag{A.16}$$

3rd Order

$$a_0 = -\frac{5}{2}, \quad a_1 = 2, \quad a_2 = \frac{1}{2}, \quad b_1 = -2. \tag{A.17}$$

4th Order

$$a_0 = -3, \quad a_1 = 0, \quad a_2 = 3, \quad b_1 = -4, \quad b_2 = -1. \tag{A.18}$$

5th Order

$$a_0 = -\frac{10}{3}, \quad a_1 = -3, \quad a_2 = 6, \quad a_3 = \frac{1}{3}, \quad b_1 = -6, \quad b_2 = -3. \tag{A.19}$$

6th Order

$$a_0 = -\frac{11}{3}, \quad a_1 = -9, \quad a_2 = 9, \quad a_3 = \frac{11}{3}, \quad b_1 = -9, \quad b_2 = -9, \quad b_3 = -1. \tag{A.20}$$

7th Order

$$a_0 = -\frac{47}{12}, \quad a_1 = -16, \quad a_2 = 9, \quad a_3 = \frac{32}{3}, \quad a_4 = \frac{1}{4}, \tag{A.21}$$
$$b_1 = -12, \quad b_2 = -18, \quad b_3 = -4.$$

8th Order

$$a_0 = -\frac{25}{6}, \quad a_1 = -\frac{80}{3}, \quad a_2 = 0, \quad a_3 = \frac{80}{3}, \quad a_4 = \frac{25}{6}, \tag{A.22}$$
$$b_1 = -16, \quad b_2 = -36, \quad b_3 = -16, \quad b_4 = -1.$$

Appendix B

The 2-D boundary closures scheme used in Table 5.2 for cross derivatives are presented in this appendix. For Case 1, only two boundary closure schemes at ($i = N$, $j = 1$ to N-1) and ($i = N$, $j = N$) are needed; For Case 2, five boundary closure schemes at ($i = N$-1, $j = 2$ to N-2), ($i = N$, $j = 2$ to N-2), ($i = N$-1, $j = N$-1), ($i = N$, $j = N$-1), ($i = N$, $j = N$) are needed. For other grid points, the scheme formulas can be easily derived from symmetry.

B.1. Boundary Closure Schemes in Case 1

i = N, j = 1 to N-1 (3rd-order scheme)

$$\begin{aligned}\left(u_{xy}\right)_{i,j} = &\frac{1}{h^2}\left(-\frac{1}{2}u_{i-1,j-1}+\frac{1}{2}u_{i,j-1}+\frac{1}{2}u_{i-1,j+1}-\frac{1}{2}u_{i,j+1}\right)\\ &+\frac{1}{h}\left(-\frac{1}{2}\left(u_x\right)_{i,j-1}+\frac{1}{2}\left(u_x\right)_{i,j+1}\right)+\frac{1}{h}\left(-\left(u_y\right)_{i-1,j}+\left(u_y\right)_{i,j}\right)\end{aligned} \tag{B.1}$$

i = N, j = N (2nd-order scheme)

$$\begin{aligned}\left(u_{xy}\right)_{i,j} = &\frac{1}{h^2}\left(-u_{i-1,j-1}+u_{i,j-1}+u_{i-1,j}-u_{i,j}\right)\\ &+\frac{1}{h}\left(-\left(u_x\right)_{i,j-1}+\left(u_x\right)_{i,j}\right)+\frac{1}{h}\left(-\left(u_y\right)_{i-1,j}+\left(u_y\right)_{i,j}\right)\end{aligned} \tag{B.2}$$

B.2. Boundary Closure Schemes in Case 2

i = N-1, j = 2 to N-2 (6th-order scheme)

$$\begin{aligned}\left(u_{xy}\right)_{i,j} = \frac{1}{h^2}\Bigg(&\frac{1}{24}u_{i-1,j-2} - \frac{1}{24}u_{i+1,j-2} - \frac{1}{3}u_{i-1,j-1} + \frac{1}{3}u_{i+1,j-1} + \frac{1}{3}u_{i-1,j+1} - \frac{1}{3}u_{i+1,j+1} - \frac{1}{24}u_{i-1,j+2} + \frac{1}{24}u_{i+1,j+2}\Bigg) \\ &+ \frac{1}{h}\left(\frac{1}{12}\left(u_x\right)_{i,j-2} - \frac{2}{3}\left(u_x\right)_{i,j-1} + \frac{2}{3}\left(u_x\right)_{i,j+1} - \frac{1}{12}\left(u_x\right)_{i,j+2}\right) + \frac{1}{h}\left(-\frac{1}{2}\left(u_y\right)_{i-1,j} + \frac{1}{2}\left(u_y\right)_{i+1,j}\right)\end{aligned} \tag{B.3}$$

i = N, j = 2 to N-2 (6th-order scheme)

$$\begin{aligned}\left(u_{xy}\right)_{i,j} = \frac{1}{h^2}\Bigg(&-\frac{1}{24}u_{i-2,j-2} + \frac{1}{6}u_{i-1,j-2} - \frac{1}{8}u_{i,j-2} + \frac{1}{3}u_{i-2,j-1} - \frac{4}{3}u_{i-1,j-1} + u_{i,j-1} \\ &-\frac{1}{3}u_{i-2,j+1} + \frac{4}{3}u_{i-1,j+1} - u_{i,j+1} + \frac{1}{24}u_{i-2,j+2} - \frac{1}{6}u_{i-1,j+2} + \frac{1}{8}u_{i,j+2}\Bigg) \\ &+ \frac{1}{h}\left(\frac{1}{12}\left(u_x\right)_{i,j-2} - \frac{2}{3}\left(u_x\right)_{i,j-1} + \frac{2}{3}\left(u_x\right)_{i,j+1} - \frac{1}{12}\left(u_x\right)_{i,j+2}\right) + \frac{1}{h}\left(\frac{1}{2}\left(u_y\right)_{i-2,j} - 2\left(u_y\right)_{i-1,j} + \frac{3}{2}\left(u_y\right)_{i,j}\right)\end{aligned} \tag{B.4}$$

i = N-1, j = N-1 (6th-order scheme)

$$\begin{aligned}\left(u_{xy}\right)_{i,j} = \frac{1}{h^2}\Bigg(&\frac{25}{108}u_{i-2,j-2} - \frac{25}{108}u_{i,j-2} + 2u_{i-1,j-1} - 2u_{i,j-1} - \frac{25}{108}u_{i-2,j} - 2u_{i-1,j} + \frac{11}{8}u_{i,j} - \frac{14}{27}u_{i+1,j} - \frac{14}{27}u_{i,j+1} + \frac{14}{27}u_{i+1,j+1}\Bigg) \\ &+ \frac{1}{h}\left(\frac{1}{18}\left(u_x\right)_{i-2,j-2} + \left(u_x\right)_{i-1,j-1} - \frac{1}{18}\left(u_x\right)_{i-2,j} - \left(u_x\right)_{i-1,j} + \frac{1}{9}\left(u_x\right)_{i+1,j} - \frac{1}{9}\left(u_x\right)_{i+1,j+1}\right) \\ &+ \frac{1}{h}\left(\frac{1}{18}\left(u_y\right)_{i-2,j-2} - \frac{1}{18}\left(u_y\right)_{i,j-2} + \left(u_y\right)_{i-1,j-1} - \left(u_y\right)_{i,j-1} + \frac{1}{9}\left(u_y\right)_{i,j+1} - \frac{1}{9}\left(u_y\right)_{i+1,j+1}\right)\end{aligned} \tag{B.5}$$

i = N, j = N-1 (6th-order scheme)

$$\begin{aligned}\left(u_{xy}\right)_{i,j} = \frac{1}{h^2}\Bigg(&\frac{1}{24}u_{i-3,j-3} - \frac{3}{16}u_{i-2,j-3} + \frac{3}{8}u_{i-1,j-3} - \frac{11}{48}u_{i,j-3} - \frac{1}{9}u_{i-3,j-2} + \frac{1}{2}u_{i-2,j-2} - u_{i-1,j-2} + \frac{11}{18}u_{i,j-2} \\ &-\frac{1}{12}u_{i-3,j-1} + \frac{3}{8}u_{i-2,j-1} - \frac{3}{4}u_{i-1,j-1} + \frac{11}{24}u_{i,j-1} + \frac{11}{72}u_{i-3,j+1} - \frac{11}{16}u_{i-2,j+1} + \frac{11}{8}u_{i-1,j+1} - \frac{121}{144}u_{i,j+1}\Bigg) \\ &+ \frac{1}{h}\left(\frac{1}{8}\left(u_x\right)_{i,j-3} - \frac{1}{3}\left(u_x\right)_{i,j-2} - \frac{1}{4}\left(u_x\right)_{i,j-1} + \frac{11}{24}\left(u_x\right)_{i,j+1}\right) \\ &+ \frac{1}{h}\left(-\frac{1}{3}\left(u_y\right)_{i-3,j} + \frac{3}{2}\left(u_y\right)_{i-2,j} - 3\left(u_y\right)_{i-1,j} + \frac{11}{6}\left(u_y\right)_{i,j}\right)\end{aligned} \tag{B.6}$$

i = N, j = N (6th-order scheme)

$$
\begin{aligned}
\left(u_{xy}\right)_{i,j} = \frac{1}{h^2}\Bigg(& \frac{4}{3}u_{i-3,j-3} - \frac{4}{3}u_{i,j-3} + \frac{27}{4}u_{i-2,j-2} - \frac{27}{4}u_{i,j-2} - \frac{4}{3}u_{i-3,j} - \frac{27}{4}u_{i-2,j} + \frac{97}{12}u_{i,j} \Bigg) \\
& + \frac{1}{h}\Bigg(\frac{1}{3}\left(u_x\right)_{i-3,j-3} + \frac{9}{2}\left(u_x\right)_{i-2,j-2} + 9\left(u_x\right)_{i-1,j-1} - \frac{1}{3}\left(u_x\right)_{i-3,j} - \frac{9}{2}\left(u_x\right)_{i-2,j} - 9\left(u_x\right)_{i-1,j} \Bigg) \\
& + \frac{1}{h}\Bigg(\frac{1}{3}\left(u_y\right)_{i-3,j-3} - \frac{1}{3}\left(u_y\right)_{i,j-3} + \frac{9}{2}\left(u_y\right)_{i-2,j-2} - \frac{9}{2}\left(u_y\right)_{i,j-2} + 9\left(u_y\right)_{i-1,j-1} - 9\left(u_y\right)_{i,j-1} \Bigg)
\end{aligned}
\tag{B.7}
$$

REFERENCES

[1] R.L. Kimmel, Aspects of Hypersonic Boundary-Layer Transition Control, in: 41st Aerosp. Sci. Meet. Exhib., American Institute of Aeronautics and Astronautics, Reno, Nevada, 2003: p. 772. doi:10.2514/6.2003-772.

[2] X. Zhong, X. Wang, Direct Numerical Simulation on the Receptivity, Instability, and Transition of Hypersonic Boundary Layers, Annu. Rev. Fluid Mech. 44 (2012) 527–561. doi:10.1146/annurev-fluid-120710-101208.

[3] T. Ishihara, T. Gotoh, Y. Kaneda, Study of High–Reynolds Number Isotropic Turbulence by Direct Numerical Simulation, Annu. Rev. Fluid Mech. 41 (2009) 165–180. doi:10.1146/annurev.fluid.010908.165203.

[4] P. Moin, K. Mahesh, DIRECT NUMERICAL SIMULATION: A Tool in Turbulence Research, Annu. Rev. Fluid Mech. 30 (1998) 539–578. doi:10.1146/annurev.fluid.30.1.539.

[5] C.K.W. Tam, Computational Aeroacoustics - Issues and Methods, AIAA J. 33 (1995) 1788–1796. doi:10.2514/3.12728.

[6] C. Bogey, C. Bailly, A family of low dispersive and low dissipative explicit schemes for flow and noise computations, J. Comput. Phys. 194 (2004) 194–214. doi:10.1016/j.jcp.2003.09.003.

[7] G. Alfonsi, On Direct Numerical Simulation of Turbulent Flows, Appl. Mech. Rev. 64 (2011) 020802. doi:10.1115/1.4005282.

[8] V.L. Wells, R.A. Renaut, Computing Aerodynamically Generated Noise, Annu. Rev. Fluid Mech. 29 (1997) 161–199. doi:10.1146/annurev.fluid.29.1.161.

[9] M. Wang, J.B. Freund, S.K. Lele, Computational Prediction of Flow-Generated Sound, Annu. Rev. Fluid Mech. 38 (2006) 483–512. doi:10.1146/annurev.fluid.38.050304.092036.

[10] C.-W. Shu, High order WENO and DG methods for time-dependent convection-dominated PDEs: A brief survey of several recent developments, J. Comput. Phys. 316 (2016) 598–613. doi:10.1016/j.jcp.2016.04.030.

[11] J.A. Ekaterinaris, High-order accurate, low numerical diffusion methods for aerodynamics, Prog. Aerosp. Sci. 41 (2005) 192–300. doi:10.1016/j.paerosci.2005.03.003.

[12] Z.J. Wang, High-order methods for the Euler and Navier–Stokes equations on unstructured grids, Prog. Aerosp. Sci. 43 (2007) 1–41. doi:10.1016/j.paerosci.2007.05.001.

[13] M. Dubiner, Spectral Methods on Triangles and Other Domains, J. Sci. Comput. 6 (1991) 345–390. doi:10.1007/BF01060030.

[14] R.D. Moser, P. Moin, A. Leonard, A Spectral Numerical Method for the Navier-Stokes Equations with Applications to Taylor-Couette Flow, J. Comput. Phys. 52 (1983) 524–544. doi:10.1016/0021-9991(83)90006-2.

[15] M.Y. Hussaini, T.A. Zang, Spectral Methods in Fluid Dynamics, Annu. Rev. Fluid Mech. 19 (1987) 339–367. doi:10.1146/annurev.fl.19.010187.002011.

[16] B. Cockburn, S.-Y. Lin, C.-W. Shu, TVB Runge-Kutta Local Projection Discontinuous Galerkin Finite Element Method for Conservation Laws III: One-Dimensional Systems, J. Comput. Phys. 84 (1989) 90–113. doi:10.1016/0021-9991(89)90183-6.

[17] B. Cockburn, C.-W. Shu, The Runge–Kutta Discontinuous Galerkin Method for Conservation Laws V: Multidimensional Systems, J. Comput. Phys. 141 (1998) 199–224. doi:10.1006/jcph.1998.5892.

[18] J. Qiu, M. Dumbser, C.-W. Shu, The discontinuous Galerkin method with Lax–Wendroff type time discretizations, Comput. Methods Appl. Mech. Eng. 194 (2005) 4528–4543. doi:10.1016/j.cma.2004.11.007.

[19] J. Zhu, X. Zhong, C.-W. Shu, J. Qiu, Runge–Kutta discontinuous Galerkin method using a new type of WENO limiters on unstructured meshes, J. Comput. Phys. 248 (2013) 200–220. doi:10.1016/j.jcp.2013.04.012.

[20] S.K. Lele, Compact Finite Difference Schemes with Spectral-like Resolution, J. Comput. Phys. 103 (1992) 16–42. doi:10.1016/0021-9991(92)90324-R.

[21] X. Zhong, High-Order Finite-Difference Schemes for Numerical Simulation of Hypersonic Boundary-Layer Transition, J. Comput. Phys. 144 (1998) 662–709. doi:10.1006/jcph.1998.6010.

[22] K. Mahesh, A Family of High Order Finite Difference Schemes with Good Spectral Resolution, J. Comput. Phys. 145 (1998) 332–358. doi:10.1006/jcph.1998.6022.

[23] R.K. Shukla, X. Zhong, Derivation of high-order compact finite difference schemes for non-uniform grid using polynomial interpolation, J. Comput. Phys. 204 (2005) 404–429. doi:10.1016/j.jcp.2004.10.014.

[24] R.K. Shukla, M. Tatineni, X. Zhong, Very high-order compact finite difference schemes on non-uniform grids for incompressible Navier–Stokes equations, J. Comput. Phys. 224 (2007) 1064–1094. doi:10.1016/j.jcp.2006.11.007.

[25] P.C. Chu, C. Fan, A Three-Point Combined Compact Difference Scheme, J. Comput. Phys. 140 (1998) 370–399. doi:10.1006/jcph.1998.5899.

[26] H.C. Yee, N.D. Sandham, M.J. Djomehri, Low-Dissipative High-Order Shock-Capturing Methods Using Characteristic-Based Filters, J. Comput. Phys. 150 (1999) 199–238. doi:10.1006/jcph.1998.6177.

[27] A. Harten, High resolution schemes for hyperbolic conservation laws, J. Comput. Phys. 49 (1983) 357–393. doi:10.1016/0021-9991(83)90136-5.

[28] A. Harten, B. Engquist, S. Osher, S.R. Chakravarthy, Uniformly high order accurate essentially non-oscillatory schemes, III, J. Comput. Phys. 71 (1987) 231–303. doi:10.1016/0021-9991(87)90031-3.

[29] X.-D. Liu, S. Osher, T. Chan, Weighted Essentially Non-oscillatory Schemes, J. Comput. Phys. 115 (1994) 200–212. doi:10.1006/jcph.1994.1187.

[30] G.-S. Jiang, C.-W. Shu, Efficient Implementation of Weighted ENO Schemes, J. Comput. Phys. 126 (1996) 202–228. doi:10.1006/jcph.1996.0130.

[31] Y.-X. Ren, M. Liu, H. Zhang, A characteristic-wise hybrid compact-WENO scheme for solving hyperbolic conservation laws, J. Comput. Phys. 192 (2003) 365–386. doi:10.1016/j.jcp.2003.07.006.

[32] L. Zhang, W. Liu, L. He, X. Deng, H. Zhang, A class of hybrid DG/FV methods for conservation laws I: Basic formulation and one-dimensional systems, J. Comput. Phys. 231 (2012) 1081–1103. doi:10.1016/j.jcp.2011.06.010.

[33] L. Zhang, W. Liu, L. He, X. Deng, H. Zhang, A class of hybrid DG/FV methods for

conservation laws II: Two-dimensional cases, J. Comput. Phys. 231 (2012) 1104–1120. doi:10.1016/j.jcp.2011.03.032.

[34] J.J. Choi, Hybrid spectral difference/embedded finite volume method for conservation laws, J. Comput. Phys. 295 (2015) 285–306. doi:10.1016/j.jcp.2015.04.013.

[35] Y. Liu, M. Vinokur, Z.J. Wang, Spectral difference method for unstructured grids I: Basic formulation, J. Comput. Phys. 216 (2006) 780–801. doi:10.1016/j.jcp.2006.01.024.

[36] Z.J. Wang, Y. Liu, G. May, A. Jameson, Spectral Difference Method for Unstructured Grids II: Extension to the Euler Equations, J. Sci. Comput. 32 (2007) 45–71. doi:10.1007/s10915-006-9113-9.

[37] A. Balan, G. May, J. Schöberl, A stable high-order Spectral Difference method for hyperbolic conservation laws on triangular elements, J. Comput. Phys. 231 (2012) 2359–2375. doi:10.1016/j.jcp.2011.11.041.

[38] Z.J. Wang, Spectral (Finite) Volume Method for Conservation Laws on Unstructured Grids: Basic Formulation, J. Comput. Phys. 178 (2002) 210–251. doi:10.1006/jcph.2002.7041.

[39] Y. Liu, M. Vinokur, Z.J. Wang, Spectral (finite) volume method for conservation laws on unstructured grids V: Extension to three-dimensional systems, J. Comput. Phys. 212 (2006) 454–472. doi:10.1016/j.jcp.2005.06.024.

[40] Y. Sun, Z.J. Wang, Y. Liu, Spectral (finite) volume method for conservation laws on unstructured grids VI: Extension to viscous flow, J. Comput. Phys. 215 (2006) 41–58. doi:10.1016/j.jcp.2005.10.019.

[41] Z.J. Wang, Y. Liu, Extension of the spectral volume method to high-order boundary representation, J. Comput. Phys. 211 (2006) 154–178. doi:10.1016/j.jcp.2005.05.022.

[42] Z. Haras, S. Ta'asan, Finite difference schemes for long-time integration, J. Comput. Phys. 114 (1994) 265–279. doi:10.1006/jcph.1994.1165.

[43] G. Ashcroft, X. Zhang, Optimized prefactored compact schemes, J. Comput. Phys. 190 (2003) 459–477. doi:10.1016/S0021-9991(03)00293-6.

[44] R. Hixon, Prefactored Small-Stencil Compact Schemes, J. Comput. Phys. 165 (2000) 522–541. doi:10.1006/jcph.2000.6631.

[45] J.W. Kim, D.J. Lee, Optimized Compact Finite Difference Schemes with Maximum Resolution, AIAA J. 34 (1996) 887–893. doi:10.2514/3.13164.

[46] X. Liu, S. Zhang, H. Zhang, C.-W. Shu, A new class of central compact schemes with spectral-like resolution I: Linear schemes, J. Comput. Phys. 248 (2013) 235–256. doi:10.1016/j.jcp.2013.04.014.

[47] P.C. Chu, C. Fan, A Three-Point Sixth-Order Nonuniform Combined Compact Difference Scheme, J. Comput. Phys. 148 (1999) 663–674. doi:10.1006/jcph.1998.6141.

[48] Y.G. Bhumkar, T.W.H. Sheu, T.K. Sengupta, A dispersion relation preserving optimized upwind compact difference scheme for high accuracy flow simulations, J. Comput. Phys. 278 (2014) 378–399. doi:10.1016/j.jcp.2014.08.040.

[49] C. Cheong, S. Lee, Grid-Optimized Dispersion-Relation-Preserving Schemes on General Geometries for Computational Aeroacoustics, J. Comput. Phys. 174 (2001) 248–276. doi:10.1006/jcph.2001.6904.

[50] M.K. Rajpoot, T.K. Sengupta, P.K. Dutt, Optimal time advancing dispersion relation preserving schemes, J. Comput. Phys. 229 (2010) 3623–3651. doi:10.1016/j.jcp.2010.01.018.

[51] T.K. Sengupta, V. Lakshmanan, V.V.S.N. Vijay, A new combined stable and dispersion relation preserving compact scheme for non-periodic problems, J. Comput. Phys. 228 (2009) 3048–3071. doi:10.1016/j.jcp.2009.01.003.

[52] C.K.W. Tam, J.C. Webb, Dispersion-Relation-Preserving Finite Difference Schemes for Computational Acoustics, J. Comput. Phys. 107 (1993) 262–281. doi:10.1006/jcph.1993.1142.

[53] G. Cunha, S. Redonnet, On the effective accuracy of spectral-like optimized finite-difference schemes for computational aeroacoustics, J. Comput. Phys. 263 (2014) 222–232. doi:10.1016/j.jcp.2014.01.024.

[54] X. Zhong, M. Tatineni, High-order non-uniform grid schemes for numerical simulation of hypersonic boundary-layer stability and transition, J. Comput. Phys. 190 (2003) 419–458. doi:10.1016/S0021-9991(03)00282-1.

[55] S. Pirozzoli, On the spectral properties of shock-capturing schemes, J. Comput. Phys. 219 (2006) 489–497. doi:10.1016/j.jcp.2006.07.009.

[56] S. Pirozzoli, Numerical Methods for High-Speed Flows, Annu. Rev. Fluid Mech. 43 (2011) 163–194. doi:10.1146/annurev-fluid-122109-160718.

[57] C.-W. Shu, High Order Weighted Essentially Nonoscillatory Schemes for Convection Dominated Problems, SIAM Rev. 51 (2009) 82–126. doi:10.1137/070679065.

[58] D.J. Hill, D.I. Pullin, Hybrid tuned center-difference-WENO method for large eddy simulations in the presence of strong shocks, J. Comput. Phys. 194 (2004) 435–450. doi:10.1016/j.jcp.2003.07.032.

[59] E.M. Taylor, M. Wu, M.P. Martín, Optimization of nonlinear error for weighted essentially non-oscillatory methods in direct numerical simulations of compressible turbulence, J. Comput. Phys. 223 (2007) 384–397. doi:10.1016/j.jcp.2006.09.010.

[60] M.D. Salas, A Shock-Fitting Primer, CRC Press, 2009.

[61] A. Prakash, N. Parsons, X. Wang, X. Zhong, High-order shock-fitting methods for direct numerical simulation of hypersonic flow with chemical and thermal nonequilibrium, J. Comput. Phys. 230 (2011) 8474–8507. doi:10.1016/j.jcp.2011.08.001.

[62] P.S. Rawat, X. Zhong, On high-order shock-fitting and front-tracking schemes for numerical simulation of shock–disturbance interactions, J. Comput. Phys. 229 (2010) 6744–6780. doi:10.1016/j.jcp.2010.05.021.

[63] W.S. SARIC, GORTLER VORTICES, Annu. Rev. Fluid Mech. 26 (1994) 379–409. doi:10.1146/annurev.fluid.26.1.379.

[64] W.S. Saric, H.L. Reed, E.J. Kerschen, Boundary-layer receptivity to freestream disturbances, Annu. Rev. Fluid Mech. 34 (2002) 291–319. doi:10.1146/annurev.fluid.34.082701.161921.

[65] W.S. Saric, H.L. Reed, E.B. White, Stability and transition of three-dimensional boundary layers, Annu. Rev. Fluid Mech. 35 (2003) 413–440. doi:10.1146/annurev.fluid.35.101101.161045.

[66] P.J. Schmid, Nonmodal stability theory, Annu. Rev. Fluid Mech. 39 (2007) 129–162. doi:10.1146/annurev.fluid.38.050304.092139.

[67] Y.S. KACHANOV, PHYSICAL-MECHANISMS OF LAMINAR-BOUNDARY-LAYER TRANSITION, Annu. Rev. Fluid Mech. 26 (1994) 411–482. doi:10.1146/annurev.fluid.26.1.411.

[68] T. HERBERT, SECONDARY INSTABILITY OF BOUNDARY-LAYERS, Annu. Rev. Fluid Mech. 20 (1988) 487–526.

[69] P. Durbin, X. Wu, Transition beneath vortical disturbances, Annu. Rev. Fluid Mech. 39 (2007) 107–128. doi:10.1146/annurev.fluid.39.050905.110135.

[70] M.E. GOLDSTEIN, L.S. HULTGREN, BOUNDARY-LAYER RECEPTIVITY TO LONG-WAVE FREE-STREAM DISTURBANCES, Annu. Rev. Fluid Mech. 21 (1989) 137–166. doi:10.1146/annurev.fl.21.010189.001033.

[71] I. TANI, BOUNDARY-LAYER TRANSITION, Annu. Rev. Fluid Mech. 1 (1969) 169-. doi:10.1146/annurev.fl.01.010169.001125.

[72] H.L. Reed, W.S. Saric, D. Arnal, Linear stability theory applied to boundary layers, Annu. Rev. Fluid Mech. 28 (1996) 389–428. doi:10.1146/annurev.fl.28.010196.002133.

[73] S.P. Schneider, Flight data for boundary-layer transition at hypersonic and supersonic speeds, J. Spacecr. Rockets. 36 (1999) 8–20. doi:10.2514/2.3428.

[74] S.P. Schneider, Effects of high-speed tunnel noise on laminar-turbulent transition, J. Spacecr. Rockets. 38 (2001) 323–333. doi:10.2514/2.3705.

[75] S.P. Schneider, Laminar-turbulent transition on reentry capsules and planetary probes, J.

Spacecr. Rockets. 43 (2006) 1153–1173. doi:10.2514/1.22594.

[76] S.P. Schneider, Erratum on Laminar-Turbulent transition on reentry capsules and planetary probes (vol 43, pg 1153, 2006), J. Spacecr. Rockets. 44 (2007) 464–484. doi:10.2514/1.30727.

[77] S.P. Schneider, Effects of roughness on hypersonic boundary-layer transition, J. Spacecr. Rockets. 45 (2008) 193–209. doi:10.2514/1.29713.

[78] S.P. Schneider, Development of hypersonic quiet tunnels, J. Spacecr. Rockets. 45 (2008) 641–664. doi:10.2514/1.34489.

[79] S.P. Schneider, Summary of Hypersonic Boundary-Layer Transition Experiments on Blunt Bodies with Roughness, J. Spacecr. Rockets. 45 (2008) 1090–1105. doi:10.2514/1.37431.

[80] S.P. Schneider, Hypersonic Boundary-Layer Transition with Ablation and Blowing, J. Spacecr. Rockets. 47 (2010) 225–237. doi:10.2514/1.43926.

[81] A. Fedorov, Transition and Stability of High-Speed Boundary Layers, in: Davis, SH and Moin, P (Ed.), Annu. Rev. FLUID Mech. VOL 43, ANNUAL REVIEWS, 4139 EL CAMINO WAY, PO BOX 10139, PALO ALTO, CA 94303-0897 USA, 2011: pp. 79–95. doi:10.1146/annurev-fluid-122109-160750.

[82] L.M. MACK, LINEAR-STABILITY THEORY AND PROBLEM OF SUPERSONIC BOUNDARY-LAYER TRANSITION, AIAA J. 13 (1975) 278–289. doi:10.2514/3.49693.

[83] L. KLEISER, T.A. ZANG, NUMERICAL-SIMULATION OF TRANSITION IN WALL-BOUNDED SHEAR FLOWS, Annu. Rev. Fluid Mech. 23 (1991) 495–537.

[84] J. Qiu, C.-W. Shu, Hermite WENO schemes and their application as limiters for Runge–Kutta discontinuous Galerkin method: one-dimensional case, J. Comput. Phys. 193 (2004) 115–135. doi:10.1016/j.jcp.2003.07.026.

[85] J. Qiu, C.-W. Shu, Hermite WENO schemes and their application as limiters for Runge–Kutta discontinuous Galerkin method II: Two dimensional case, Comput. Fluids. 34 (2005) 642–663. doi:10.1016/j.compfluid.2004.05.005.

[86] J. Zhu, J. Qiu, Hermite WENO Schemes and Their Application as Limiters for Runge-Kutta Discontinuous Galerkin Method, III: Unstructured Meshes, J. Sci. Comput. 39 (2009) 293–321. doi:10.1007/s10915-009-9271-7.

[87] D.S. Balsara, C. Altmann, C.-D. Munz, M. Dumbser, A sub-cell based indicator for troubled zones in RKDG schemes and a novel class of hybrid RKDG+HWENO schemes, J. Comput. Phys. 226 (2007) 586–620. doi:10.1016/j.jcp.2007.04.032.

[88] H. Luo, J.D. Baum, R. Löhner, A Hermite WENO-based limiter for discontinuous Galerkin method on unstructured grids, J. Comput. Phys. 225 (2007) 686–713. doi:10.1016/j.jcp.2006.12.017.

[89] H. Luo, Y. Xia, S. Li, R. Nourgaliev, C. Cai, A Hermite WENO reconstruction-based discontinuous Galerkin method for the Euler equations on tetrahedral grids, J. Comput. Phys. 231 (2012) 5489–5503. doi:10.1016/j.jcp.2012.05.011.

[90] H. Luo, Y. Xia, S. Spiegel, R. Nourgaliev, Z. Jiang, A reconstructed discontinuous Galerkin method based on a Hierarchical WENO reconstruction for compressible flows on tetrahedral grids, J. Comput. Phys. 236 (2013) 477–492. doi:10.1016/j.jcp.2012.11.026.

[91] S.-C. Chang, The Method of Space-Time Conservation Element and Solution Element—A

New Approach for Solving the Navier-Stokes and Euler Equations, J. Comput. Phys. 119 (1995) 295–324. doi:10.1006/jcph.1995.1137.

[92] S.-C. Chang, X.-Y. Wang, W.-M. To, Application of the Space-Time Conservation Element and Solution Element Method to One-Dimensional Convection-Diffusion Problems, J. Comput. Phys. 165 (2000) 189–215. doi:10.1006/jcph.2000.6610.

[93] Z.-C. Zhang, S.T.J. Yu, S.-C. Chang, A Space-Time Conservation Element and Solution Element Method for Solving the Two- and Three-Dimensional Unsteady Euler Equations Using Quadrilateral and Hexahedral Meshes, J. Comput. Phys. 175 (2002) 168–199. doi:10.1006/jcph.2001.6934.

[94] D. Shyam Sundar, K.S. Yeo, A high order meshless method with compact support, J. Comput. Phys. 272 (2014) 70–87. doi:10.1016/j.jcp.2014.04.010.

[95] H. Nishikawa, A first-order system approach for diffusion equation. I: Second-order residual-distribution schemes, J. Comput. Phys. 227 (2007) 315–352. doi:10.1016/j.jcp.2007.07.029.

[96] H. Nishikawa, A first-order system approach for diffusion equation. II: Unification of advection and diffusion, J. Comput. Phys. 229 (2010) 3989–4016. doi:10.1016/j.jcp.2009.10.040.

[97] H. Nishikawa, First-, second-, and third-order finite-volume schemes for diffusion, J. Comput. Phys. 256 (2014) 791–805. doi:10.1016/j.jcp.2013.09.024.

[98] H. Nishikawa, First, second, and third order finite-volume schemes for advection-diffusion, J. Comput. Phys. 273 (2014) 287–309. doi:10.1016/j.jcp.2014.05.021.

[99] T.J. Poinsot, S.K. Lele, Boundary conditions for direct simulations of compressible viscous flows, J. Comput. Phys. 101 (1992) 104–129. doi:10.1016/0021-9991(92)90046-2.

[100] Z. Tao, F. Li, J. Qiu, High-order central Hermite WENO schemes: Dimension-by-dimension moment-based reconstructions, J. Comput. Phys. 318 (2016) 222–251. doi:10.1016/j.jcp.2016.05.005.

[101] Z. Bai, X. Zhong, New very high-order upwind multi-layer compact (MLC) schemes with spectral-like resolution for flow simulations, J. Comput. Phys. 378 (2019) 63–109. doi:10.1016/j.jcp.2018.10.049.

[102] B. Boroomand, A.A. Tabatabaei, E. Oñate, Simple modifications for stabilization of the finite point method, Int. J. Numer. Methods Eng. 63 (2005) 351–379. doi:10.1002/nme.1278.

[103] J. Fang, A. Parriaux, A regularized Lagrangian finite point method for the simulation of incompressible viscous flows, J. Comput. Phys. 227 (2008) 8894–8908. doi:10.1016/j.jcp.2008.06.031.

[104] C.S. Chew, K.S. Yeo, C. Shu, A generalized finite-difference (GFD) ALE scheme for incompressible flows around moving solid bodies on hybrid meshfree–Cartesian grids, J. Comput. Phys. 218 (2006) 510–548. doi:10.1016/j.jcp.2006.02.025.

[105] D.L. Young, Y.C. Lin, C.M. Fan, C.L. Chiu, The method of fundamental solutions for solving incompressible Navier-Stokes problems, Eng. Anal. Bound. Elem. 33 (2009) 1031–1044. doi:10.1016/j.enganabound.2009.03.003.

[106] E. OÑATE, S. IDELSOHN, O.C. ZIENKIEWICZ, R.L. TAYLOR, A FINITE POINT METHOD IN COMPUTATIONAL MECHANICS. APPLICATIONS TO

CONVECTIVE TRANSPORT AND FLUID FLOW, Int. J. Numer. Methods Eng. 39 (1996) 3839–3866. doi:10.1002/(SICI)1097-0207(19961130)39:22<3839::AID-NME27>3.0.CO;2-R.

[107] E. Oñate, S. Idelsohn, O.C. Zienkiewicz, R.L. Taylor, C. Sacco, A stabilized finite point method for analysis of fluid mechanics problems, Comput. Methods Appl. Mech. Eng. 139 (1996) 315–346. doi:10.1016/S0045-7825(96)01088-2.

[108] D. Sridar, N. Balakrishnan, An upwind finite difference scheme for meshless solvers, J. Comput. Phys. 189 (2003) 1–29. doi:10.1016/S0021-9991(03)00197-9.

[109] V.P. Nguyen, T. Rabczuk, S. Bordas, M. Duflot, Meshless methods: A review and computer implementation aspects, Math. Comput. Simul. 79 (2008) 763–813. doi:10.1016/j.matcom.2008.01.003.

[110] T. Belytschko, Y.Y. Lu, L. Gu, Element-free Galerkin methods, Int. J. Numer. Methods Eng. 37 (1994) 229–256. doi:10.1002/nme.1620370205.

[111] Y.Y. Lu, T. Belytschko, L. Gu, A new implementation of the element free Galerkin method, Comput. Methods Appl. Mech. Eng. 113 (1994) 397–414.

[112] R. Löhner, C. Sacco, E. Oñate, S. Idelsohn, A finite point method for compressible flow, Int. J. Numer. Methods Eng. 53 (2002) 1765–1779. doi:10.1002/nme.334.

[113] J.H. Seo, R. Mittal, A high-order immersed boundary method for acoustic wave scattering and low-Mach number flow-induced sound in complex geometries, J. Comput. Phys. 230 (2011) 1000–1019. doi:10.1016/j.jcp.2010.10.017.

[114] H. Luo, R. Mittal, X. Zheng, S.A. Bielamowicz, R.J. Walsh, J.K. Hahn, An immersed-

boundary method for flow-structure interaction in biological systems with application to phonation, J. Comput. Phys. 227 (2008) 9303–9332. doi:10.1016/j.jcp.2008.05.001.

[115] R. Samulyak, X. Wang, H.-C. Chen, Lagrangian particle method for compressible fluid dynamics, J. Comput. Phys. 362 (2018) 1–19. doi:10.1016/j.jcp.2018.02.004.

[116] N.L. Mundis, A.K. Edoh, V. Sankaran, Highly-Accurate Filter-Based Artificial-Dissipation Schemes for Stiff Unsteady Fluid Systems, in: 54th AIAA Aerosp. Sci. Meet., American Institute of Aeronautics and Astronautics, San Diego, California, 2016: pp. 1–22. doi:10.2514/6.2016-0072.

[117] A.K. Edoh, N.L. Mundis, A.R. Karagozian, V. Sankaran, The Role of Dispersion and Dissipation on Stabilization Strategies for Time-Accurate Simulations, in: 54th AIAA Aerosp. Sci. Meet., American Institute of Aeronautics and Astronautics, San Diego, California, 2016: pp. 1–26. doi:10.2514/6.2016-0071.

[118] S. Hu, X. Zhong, Linear stability of viscous supersonic plane Couette flow, Phys. Fluids. 10 (1998) 709–729. doi:10.1063/1.869596.